Galactic archaeology and its application to the galactic center

Govind Nandakumar

UNIVERSITÉ CÔTE D'AZUR

ÉCOLE DOCTORALE
SCIENCES FONDAMENTALES ET APPLIQUÉES

THÈSE DE DOCTORAT

L'archéologie galactique et son application au centre galactique

Govind NANDAKUMAR

Laboratoire J-L. Lagrange - Observatoire de la Côte d'Azur

Présentée en vue de l'obtention du grade de docteur
en Sciences de la Planéte et de l'Univers
d'Université Côte d'Azur

Thése dirigée par: Mathias Schultheis

Soutenue le: 14 Septembre 2018

Devant le jury, composé de :

Mme.	Vanessa Hill	Chargée de recherche CNRS - HDR	Président
Mme.	Livia Origlia	Chercheur Rang A	Rapporteur
M.	Karl Menten	Professeur	Rapporteur
Mme.	Nadine Neumayer	Docteur en Astronomie	Examinateur
Mme.	Elena Valenti	Docteur en Astronomie	Examinateur
M.	Mathias Schultheis	Astronome	Directeur de thèse

L'archéologie galactique et son application au centre galactique

Jury :

Président du Jury:
Mme. Vanessa Hill, Chargée de recherche CNRS - HDR, Université Côte d'Azur

Rapporteurs:
Mme. Livia Origlia, Chercheur Rang A, Observatoire Astronomique de Bologne (Italie)
M. Karl Menten, Professeur, Ste Max-Planck (Allemagne)

Examinateurs:
Mme. Nadine Neumayer, Docteur en Astronomie, Ste Max-Planck (Allemagne)
Mme. Elena Valenti, Docteur en Astronomie, Observatoire européen austral (Allemagne)

Résumé : L'archéologie galactique consiste à disséquer et analyser les nombreuses composantes de la Voie Lactée afin de mettre en évidence et distinguer les processus physiques qui contribuent à sa formation et son évolution. Ceci est possible grâce à une estimation précise des positions, des vitesses ainsi que des propriétés de l'atmosphère stellaire des étoiles individuelles qui appartiennent aux différents populations stellaires qui composent chacune de ces composantes. De ce fait, ce domaine dépend non seulement d'observations photométriques, astrométriques et spectroscopiques permettant de mesurer en détail les propriétés stellaires mentionnées mais également de modèles théoriques précis afin de les confronter avec les données observationnelles. Au cours de cette thèse, j'ai mené une étude détaillée sur les effets de fonction de sélection sur les abondances métalliques en utilisant des sondages spectroscopiques aux grandes échelles, suivi d'observations spectroscopiques de petites et grandes résolutions sur les parties internes de la Voie Lactée afin de caractériser la nature chimique du bulbe galactique ainsi que le taux de formation stellaire dans la zone centrale moléculaire (CMZ).

Avec les présents et futurs grands sondages dédiés à l'archéologie galactique tels que APOGEE, RAVE, LAMOST, GALAH, etc..., il est essentiel de connaître la fonction de sélection spécifique qui est associée à la stratégie de ciblage de chacun de ces sondages. En utilisant des champs communs et des lignes de visée similaires entre APOGEE, LAMOST, GES et RAVE, et tout en considérant des modèles de synthèse de population stellaire, J'ai étudié les effets de fonction de sélection sur la fonction de distribution de la métallicité (MDF) et sur le gradient vertical de métallicité dans le voisinage solaire. Mes résultats indiquent qu'il y a un négligeable effet de fonction de sélection sur la MDF ainsi que sur le gradient vertical de métallicité. Ces résultats suggèrent alors que différents sondages spectroscopiques (de différentes résolutions et de longueurs d'onde) peuvent Ãªtre combinés dans des études similaires à condition que les métallicité soient placées sur la mÃªme échelle.

Tandis que de plus en plus d'observations spectroscopiques des régions externes du bulbe de la Voie Lactée révèlent la complexité de sa morphologie, sa cinétique et de sa nature chimique, les études détaillées sur les abondances chimiques de la région interne du bulbe (400-500 pc) font en revanche défaut. Je présenterai alors des spectres de haute résolution dans la bande K d'étoiles géantes K/M issues de cette région obscure et obtenus à partir du spectrographe de haute résolution dans l'infrarouge, CRIRES (R-50,000) situé au VLT. Je discuterai ensuite la MDF et les abondances chimiques détaillées de notre échantillon dans cette région et également la symétrie Nord-Sud dans la MDF le long du petit axe du bulbe.

Un enjeu majeur dans les modèles d'évolution chimique est le manque de connaissance vis à vis de l'histoire et du taux de la formation stellaire de la Voie Lactée. La partie centrale de la Voie Lactée (<200 pc), appelée communément la zone centrale moléculaire, possède un grand réservoir de gaz moléculaire avec des indications d'activités de formation stellaire durant les 100 000 dernières années. J'ai utilisé des spectres KMOS (VLT) de petite résolution afin d'identifier et analyser les objects stellaires jeunes et massifs (YSOs) et afin d'estimer le taux de formation stellaire dans la CMZ en utilisant la méthode de contage YSO.

Mots clefs: Voie Lactée, populations stellaires, sondages spectroscopiques, archéologie galactique. Etoiles: abondances, "tardive" , pré-séquence principale, massive, diagramme C-M. Galaxie: bulbe, centre, contenu stellaire.

Abstract : Galactic archaeology deals with dissecting the Milky Way into its various components with the objective to disentangle processes contributing to the Milky Way formation and evolution. This relies on precise estimation of positions, velocities as well as stellar atmosphere properties of individual stars belonging to different stellar populations that make up each of these components. Thus this field relies on photometric, astrometric and spectroscopic observations to measure the above mentioned stellar properties in detail in addition to accurate models to compare the observed results with. In this thesis, I have carried out a detailed study of selection function effects on metallicity trends using larges scale spectroscopic surveys, followed by high and low resolution spectroscopic observations towards the inner Milky Way to characterise the chemical nature of the inner Galactic bulge and to measure the star formation rate in the central molecular zone (CMZ), respectively.

With ongoing and upcoming large Galactic archaeology spectroscopic surveys such as APOGEE, RAVE, LAMOST, GALAH etc, it is essential to know the specific selection function which is related to the targeting strategy of each of them. By using common fields along similar lines of sight between APOGEE, LAMOST, GES and RAVE, and together with stellar population synthesis models, I investigate the selection function effect on the metallicity distribution function (MDF) and the vertical metallicitiy gradients in the solar neighborhood. My results indicate that there is negligible selection function effect on the MDF and the vertical metallicity gradients. These results suggest that different spectroscopic surveys (different resolutions and wavelength range) can be combined for such studies provided their metallicities are put on the same scale.

While more and more spectroscopic observations of the outer bulge regions reveal the complex morphological, kinematic and chemical nature of the Milky Way bulge, there is a lack of detailed chemical abundances studies in the inner bulge region (400-500 pc). I will present high resolution K-band spectra of K/M giants in this highly obscured region obtained using the high resolution infrared spectrograph, CRIRES (R-50,000), on VLT. I will discuss the MDF and detailed chemical abundances of our sample in this region as well as the North-South symmetry in MDF along the bulge minor axis.

A major challenge in the chemical evolution models is the lack of knowledge about the star formation history and the star formation rate in the Milky Way. The inner 200 pc of the Milky way, the so called central molecular zone, has a large reservoir of molecular gas with the evidence of star formation activity during the last 100,000 years. I used low resolution KMOS spectra (VLT) to identify and analyse massive young stellar objects (YSOs) and estimated the star formation rate in the CMZ using the YSO counting method.

Keywords: Milky Way, stellar populations, spectroscopic surveys, Galactic archaeology. Stars:abundances, late-type, pre-main sequence, massive, C-M diagrams. Galaxy: Bulge, center, stellar content.

Acknowledgements

Following the Indian tradition, I start by thanking my amma achan (parents), Lekha and Nandakumar. The ideals and value of hard work they have instilled in me and my brother are the primary reason why we have gotten this far. I am well aware of the sacrifices you have endured to build up this family, and I hope to make you proud with the way I live my life. My brother, kannettan, had always been my best friend and a mentor, who had always been there to inspire and motivate me. I am thankful to my dearest grandparents, muthu, ammu and Rukmani ammoomma, who have always showered their blessings, love and affection on me. I still remember the inspiring letter from my uncle, Arummaan, when I joined for my Masters. I have also looked up to my aunt, Dimmaay, for the way she has determinedly pursued to obtain her masters. Kochachan and Devi chitta have also been silent supporters through all these years. In addition, I have been blessed with an extended family of cousins, aunts and uncles from both my mother's and father's side, who have all been very supportive in my 3 year pursuit towards doctorate. I wish to thank them all for their support.

I believe that after parents, it is guru (teacher), who play an important role in developing the personality, ideals, principles and work ethics of a child. I am thankful to my teachers in the school I studied for 14 long years for their guidance and correction (some of them by means of painful beatings). I thank Devdas sir for guiding me and a lot of other students to love mathematics. I wish to thank the friends I have made during my Engineering college days (Akshay, Ashok, Deepak, Gayathri, Jaise, Jaseel, Neetu, Nishad, Pattu, Sankaran, Seban, Sidharth, Sreeyesh, Vinay, Vineetha etc) for their life long friendship and experiences that have helped me grow and learn more about life. I also thank Radhamani aunty, who treated us three like her own children I am thankful to the professors - Sarita, Anandmayee, Anand, Samir, Jagdheep and Resmi of Indian Institute of space science and Technology, who introduced me to Astrophysics and observational astronomy, and were always ready to clear my doubts. I am extremely grateful to Sarita maam for her invaluable guidance during my 1 year masters thesis and Anandmayee maam for her invaluable support during the whole masters program. I also wish to express my gratitude to Anandmayee maam for introducing me to Mathias, and recommending me for the PhD program in Nice. I can't thank Veena chechi enough for her support and guidance during masters, in writing the masters paper as well as during my PhD when I pestered her with my silly doubts.

I have no words to thank Mathias for his continuous support and guidance during these three years. Starting from the email interactions when I was in India, trying to tackle the Visa issues, he proved to be a man of unlimited patience. From the day I landed in Nice, he was at the forefront in helping me settle down, driving me around to the bank, apartment and introducing me to the beautiful city, Nice. Professionally, he was always there, either in person or through emails, to clear my doubts or for discussion. He never thought twice in offering me a ride up to the observatory in his car every morning, and I believe the discussions we had in those brief 10-15 minutes have been the source of inspiration and motivation that had driven me forward every day during my PhD. He also showed confidence in me to be part of the observing proposal, go to Chile and carry out the observations, which had induced so much confidence in me as well. Thus I have learned and gained both professionally as well as

personally from his positive attitude, helping mentality and research temperament. I would also like to thank his wonderful family, Agnes, Arianna and Sibi (ofcourse!) who have hosted me in their home in more than one occasion.

The Galactic Archaeology group (GAG) meetings have been helpful in developing my science communication skills. It also provided a platform for discussing other interesting papers as well as my work with the team. I would like to thank the team, comprising Alejandra, Vanessa, Patrick, Georges and Sebastian for their support during these three years. They have all been very welcoming and supportive. I also thank Oliver for the persistence with which he organised the Journal club and inspired me to read papers outside my research domain. Those sessions have given me a broader perspective.

I could not have survived these three years without the support of the friends I made in Nice. Srivatsan was the first, without whose friendship I couldn't have survived the first few months in such a culturally new place (for me). Then there was my first office mate Alvaro, whose work ethics inspired me to follow his work routine (being the first to reach OCA and the last one to leave). I have to thank Nastya first and foremost for her support and help during our trip to a conference in the west coast of France (me with no bank card or local sim card) when all the trains were cancelled due to floods. I owe it to her for having reached there in one piece. Then came Marina and Katherina, with whom I shared the office for few months and made me realise my fortune to have been in a very lively office. The rude Marina (:-p) has later on become a very good friend. I still remember the initial days of ping pong and tandoori with Alkis, Alvaro, Andrea, Gerardo, Sergei and Srivatsan, that were real stress busters. With in the first year itself, my friend circle became larger as time progressed with the arrival of Michael I, Edouard and Remi. The movie nights and dinners in Michael I's place, hikes and French sessions with Remi and Whiskey evenings with Edouard deserve special mention and will be remembered. It always feels good to speak the mother tongue, and enter Vishnu in the French class, where we spoke more malayalam than French. His company was very important during these years, and I thank him for introducing me to the Cricket club MCCC, through which I made more friends, Ashok paaji, paramjit, Somnath, Rohan, Redwan etc. Tandoori Flame is a name and restaurant that I will remember, not only for the Indian food, but also for the loving attitude with which they served it to us. I have to thank Ashok paaji and Arpan bhai for that. With second year, new adventures and trips started with the arrival of new friends, Francesco, Michael II and Surabhi. I thank them for their company during the hiking trips and road trips we had, that helped me relax during a difficult second year. It was also at this time that I was totally surprised by the gift presented to me for my birthday. I will remember it as the first time that I got such a thoughtful and considerate birthday gift, thanks to Michael II for the idea and hardwork, Nastya for the wonderful design, Surabhi and Francesco for the Tiramisu and all those who contributed the songs. I got a similar surprise again this year and it still reminds me of the wonderful friends I have made.

I thought the three months (during the start of my third year) that I spend in Lund would be the most difficult time I will have during my PhD, first due to the cold climate and second due to the fact that I only knew Nils and Brian there, whom I met in a conference. But those months turned out to be very productive as I learned a lot and I really enjoyed my stay in

Lund, all thanks to the wonderful company of Nils and Brian.

On returning to Nice and during my third year, I had a new office mate, Emma, with whom I have had a lot of stimulating scientific discussions and many other topics (even few words in spanish!). I thank her for being so kind, considerate and for her support during the stressful time I was applying for postdocs and writing this thesis. I would also like to thank Pablo who became a close friend in a very short time. I definitely have to mention the really competitive ping pong sessions I had with Emma, Francesco, Mathias, Pablo and Patrick during the last few months, during which time I was writing the thesis and preparing for the thesis defense. These sessions refreshed me, giving more energy and made me more active to work harder. I also went out to the sea most during this time, thanks to Nastya and Edouard. Talking about stress busters and times of relaxation, I will rank the one hour long amazing lunch in the cantine with the amazing view at the top of the list, thanks to the chef Khaled and the cantine staffs. I have to owe it to Khaled for a lot of French (most of them, profanity) that I have learned. It is during this lunch time that I have met other PhDs, postdocs, permanent staffs and interns in CION and other buildings in the campus. I thank them - Alexis, Andy, Brynna, Clement, Cosmin, Elena, Eric, Florian, Gabriele, Go, Jeremy, Jun, Laurent, Louic, Mateus, Michael III, Rafael, Saverio, Sofia, Tobias, Tomas, Umberto, Vincent, Vitalie Ximena (to name a few) for the interesting discussions and fun lunch conversations.

I would also like to acknowledge the co authors of my papers for their support and invaluable contribution to them. I thank Anja for her help while preparing observations and reducing KMOS spectra. I thank Sophie Rousset, Sylvie Goletto, other administrative and IT staffs in the Lagrange laboratory for their help and support. I also thank EDSFA for funding my PhD.

Finally, as per the Indian tradition, I thank the God (all 33 million of them).

Contents

Chapter 1

Introduction

Contents

In this chapter, a brief overview of the Milky Way galaxy is given, with a little of its history from observational perspective and in detail, the different components that constitute the Milky Way. The main topic of this thesis, Galactic archaeology, is introduced focusing on various observational surveys and certain models used for the Galactic excavation. The inner kpc of the Milky Way, the region I explored in this thesis work, is introduced. Finally, I present the goals of this thesis and the list of published works during this thesis.

1.1 An overview of the Milky Way Galaxy

The first image that comes to our mind on hearing the name "Milky Way" is the dim but glowing band of light with dark patches arching across the dark night sky. This band of light is our host Galaxy in which our star, the Sun, is just one among ~10^{11} stars. In addition to these stars, various phases of gas as well as dust are part of the Milky way seen as diffuse light patches and dark shady patches, respectively. The inherent curiosity of humans have led to continuous efforts and advancements to decipher the Milky Way, and these investigations are still ongoing. It is interesting to map the way our understanding of the Milky Way changed from generations to generations. I present a brief history of such findings, followed

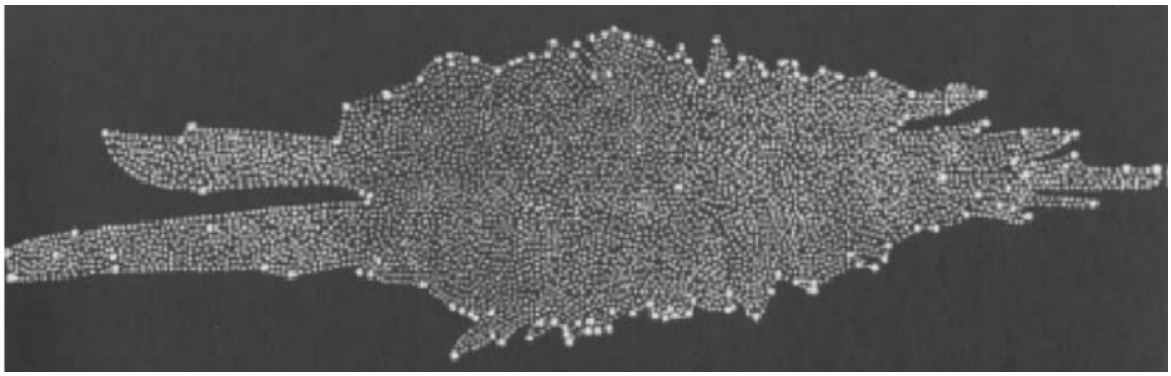

Figure 1.1: The Galaxy model made by William Herschel based on star counts in different directions. Image courtesy : Longair (2008)

by the current understanding that we have about the morphological structure and the stellar populations constituting the different components of the Milky way.

1.1.1 A brief history : Milky Way from observations

Milky Way and its origin had a place in the mythology of ancient civilizations all over the world. May that be the Hindu mythology - the story of the churning of the ocean of milk, *samudra manthan*, that appears in ancient Hindu scriptures like *Srimad Bhagavatam*, *the Mahabharata* and *the Vishnu Purana*. The more popular ones from the Greek Mythology include the Milky Way being created by the Greek gods, not to mention the origin of the word Galaxy from the greek word for milk, *galaktos*. There are numerous other old beliefs and stories showing the interest and subsequent imaginations that the Milky Way has generated in humans.

In the early 17^{th} century, the father of modern observational astronomy, Galileo Galilei, discovered that this nebulous band consists of innumerable stars based on his observations through the telescope. This was followed up with speculative theories about solar systems, orbiting of the Sun around the 'Divine Centre' of the star system and hierarchical or fractal models of the Universe by René Descartes (*The World*; 1636), Thomas Wright (*An Original Theory or New Hypothesis of the Universe*; 1750), Immanuel Kant (1755) and Johann Lambert (1761), respectively. All of these theories lacked observational validation.

A detailed observational study of the Milky Way star distribution was carried out by William Herschel towards the end of the 18^{th} century. He assumed that the stars observed in different directions had the same intrinsic luminosities. Based on this, he presented his famous picture of the structure of the Milky Way with a flattened disc of stars and the Sun located close to its center, as shown in the Figure 1.1 His assumption of constant luminosity for all stars was countered by John Mitchell, who advocated the existence of binary systems as well as star clusters which would lead to a dispersion in intrinsic luminosities of stars. Finally, William Herschel had to agree with John Mitchell's conclusion when he measured the magnitudes of visual binary stars in 1802.

Meanwhile, there have been speculations about the objects that show a diffuse or fuzzy

appearance, differing from the stars. Most of them were considered to be 'island universes' similar to the Milky Way that are too distant to be resolved. Charles Messier started cataloguing many of these bright nebulae and the catalogue contains a mixture of brightest Galactic and extra-galactic nebulae, commonly referred to by their Messier numbers. William Herschel and his sister Caroline also started a similar cataloguing of nebulae, continued by his son John Herschel, which resulted in the publication of the *General Catalogue of Nebulae and Clusters of Stars* in 1864. John Dreyer followed this up with the *New General Catalogue of Nebulae and Clusters of Stars* in 1888, the objects of which are commonly referred to by their NGC numbers.

It was in the year 1900 that the Milky Way was given the spiral arms for the first time by Cornelius Easton, though his model galaxy was small and Sun-centered. Harlow Shapley (1918, 1919) presented a much larger sized Galaxy, calculating the distances to globular clusters using the period-luminosity relation discovered by Henrietta Leavitt for Cepheid variable stars. He found the most distant globular cluster to be located at a distance of 67 kpc. In addition, this meant that the spiral nebulae could hardly be comparable galactic systems, rather they should belong to the enormously large Milky Way galaxy. At the same time, Heber Curtis's Milky Way was only 10 kpc across, with the Sun located at 3 kpc from the center. He was also suggesting the spiral nebulae to be island universes citing the resemblance of the spectrum of the average spiral nebula to that of the integrated spectrum of the Milky Way. The questions about the true nature of the spiral nebulae (island universes or Milky Way subsystems) together with that about the size/structure of the Milky Way, lead to the famous 'The Great Debate' between Harlow Shapley and Heber Curtis in 1920.

The size/structure of the Milky Way was investigated by Jacobus Katpeyn with the determination of the luminosity function of stars near the Sun based on star counts in different directions without accounting for absorption by dust. His model of the Milky Way had a flattened structure with the thickness of 1500 pc and extending about 8 times this size in the Galactic plane, with the Sun located slightly off from the center. Though the debate was unable to throw any significant light upon the issues, Edwin Hubble established that the spiral nebulae are indeed distant extragalactic systems based on his observations of cepheid variables in the Andromeda nebula. This was followed up with his finding in 1929 that the extragalactic nebulae are moving away from the Milky Way with velocities that are proportional to the distance from the Milky Way (Hubble, 1929). This discovery lead to the theory of Big Bang cosmology and eventually the lambda cold dark matter (λ-CDM) models which describes our current understanding of the formation of the expanding Universe and the structures in it. I will summarise them in the context of Galaxy formation in the section 1.1.2.

1.1.2 Lambda Cold Dark Matter model

According to the Big Bang cosmology, the Universe must have started from a hot and dense state (Lemaître, 1931) and experienced inflation (a period of rapid exponential expansion ~picosecond after the Big Bang) that lead to the primordial density enhancements in the form of quantum fluctuations to become the seeds of all structure formation. Various observations in the 20^{th} century contributed to the validation of the Big Bang picture of formation and

evolution of the Universe : the discovery of the expansion of galaxies by Hubble, the observational evidence of the cosmic microwave background radiation (CMB, the cooled remnant of the Universe's very hot early phases; Penzias and Wilson (1965); Dicke et al. (1965)) and the finding that the Big Bang nucleosynthesis could account for the cosmic abundances of the light isotope of helium, ^{3}He, deuterium, D, and lithium, ^{7}Li.

The temperature fluctuations/intensity distributions in the CMB gave an insight into the density fluctuations at the epoch of recombination (formation of neutral hydrogen from electrons and protons; z~1100) that lead to the proposal of two processes by which the present structures in the Universe formed. Both the processes agreed that the very small anisotropies in the CMB could not support a pure-baryonic universe from which the galaxies form (Sunyaev and Zeldovich, 1970). Around the same time, Rubin and Ford (1970) found a flat rotation curve for Andromeda, M31, indicating the presence of non interacting matter or 'dark matter'. One of the process was the hot dark matter model/top-down process of galaxy formation in which the Universe was dominated by neutrinos in the pre-recombination era and they were relativistic when they decoupled from the primordial plasma. In this model, the small-scale structures formed by the fragmentation of the larger scale structures and galaxies, stars etc formed at relatively later epochs (Doroshkevich et al., 1980a,b). The other process was the cold dark matter model/bottom-up process in which matter was cold, meaning they decoupled from the thermal background once they became non-relativistic. Based on this model, small-scale structures came together to form larger structures by hierarchical clustering and stars, galaxies etc form at much earlier epochs.

The evidence of the accelerating universe from the cosmological distance estimates of Type 1a supernovae (Riess et al., 1998; Perlmutter et al., 1999) lead to the inclusion of the cosmological constant, λ, in the CDM models representing the influence of the 'dark energy' in the acceleration. In addition, the detailed power spectrum of the fluctuations in the CMB from WMAP (Bennett et al. 2003; Spergel et al. 2003) helped to determine the cosmological parameters. The latest values of cosmological parameters have been determined by the Planck observations of temperature and polarization anisotropies of the CMB (Planck Collaboration et al., 2016) : Hubble constant, H_0 = 67.81±0.92, density parameters, Ω_λ = 0.692±0.012, Ω_m = 0.308±0.012, and age of 13.799±0.038 Gyr.

Thus the λCDM model was widely accepted to explain the current structure formation from the tiny fluctuations in the cold dark matter density distribution, that formed cold dark matter halos through mergers and accretion. These halos provide deep gravitational potential wells driving the baryons to collapse onto them, eventually evolving into structures that we see today as stars, galaxies and clusters. There are still unresolved issues in the λCDM model like the *missing satellites problem* where the models predict larger number of satellite galaxies than it has been observed around the Milky Way (Klypin et al., 1999).

Now that the general picture of structure formation in the Universe is introduced, I will move on to the different structural components of the Milky Way that are considered to be the relics of the Galaxy's formation and evolution processes.

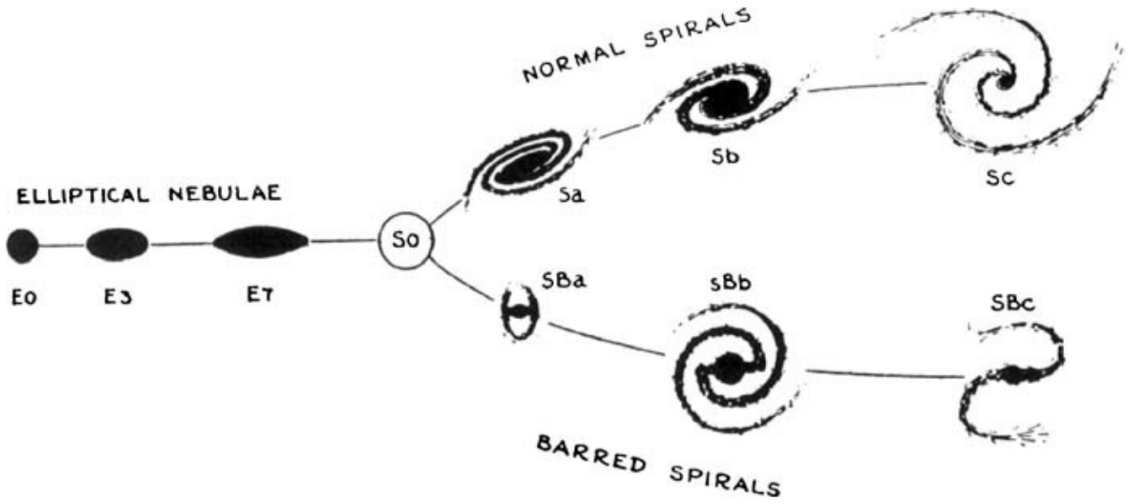

Figure 1.2: The Hubble sequence of galaxies as presented in *The Realm of the Nebulae*.

1.1.3 Components of the Milky Way

From the observations of the spiral nebulae, Edwin Hubble designed the Hubble sequence or the tuning fork diagram showing the morphological scheme of galaxies in *The Realm of the Nebulae* (Hubble, 1936), as shown in the Figure 1.2. The Milky Way was identified to be a SBb type barred spiral galaxy according to the Hubble sequence.

Currently we know that the Milky Way is one among the two dominant spiral galaxies in the Local Group. The Local Group is a collection of spiral and dwarf galaxies, which in turn is a part of the Virgo supercluster of galaxies. Currently, the Milky Way is also found to be interacting with atleast three satellite galaxies : Sagittarius dwarf galaxy (Sgr), small and large magellanic clouds (SMC and LMC). The total stellar mass of the Milky Way has been estimated to be $\sim 5\times10^{10}$ $\mathrm{M}_{\odot}$ (Bland-Hawthorn and Gerhard, 2016). This stellar mass is distributed among four components that resulted from the different stages of the Galaxy's formation process : halo, bulge, thin and thick disc. These components are considered to be axisymmetric, while bars and spiral arms are two main non-axisymmetric and rotating components of the Milky Way. Figure 1.3 shows the rough schematic of the edge-on view of the Milky Way as per our current understanding. The IAU standard for the distance of the Sun from the Galactic center is $\mathrm{R}_{\odot}$=8.5 kpc, while I have used the value of $\mathrm{R}_{\odot}$=8.0 kpc (Boehle et al., 2016; Gillessen et al., 2017) in this thesis.

In the following subsections, I will give a brief overview of the structural details of the Milky Way components, their approximate morphology and the nature of their encompassing stellar populations as inferred from observations as well as comparisons with extensive models.

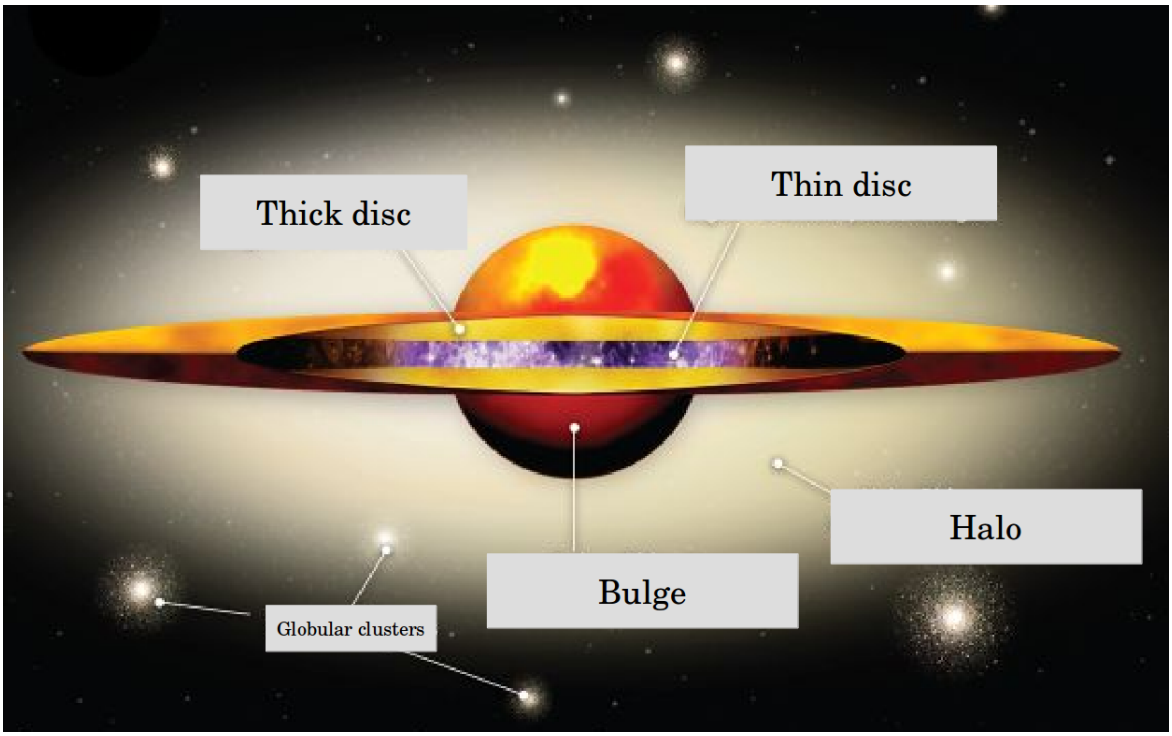

Figure 1.3: A rough diagram showing the components of the Milky Way. Image courtesy : SolStation.com

Halo

The stellar halo of the Milky Way is considered to be one of the oldest components, composed of old stars (RR Lyrae, blue horizontal branch stars etc) moving on eccentric orbits and globular clusters with the metallicities of local halo stars peaking at ~-1.6 dex and extending below [Fe/H]~-3 dex (Ryan and Norris, 1991). There are also evidences of past mergers of satellite galaxies, in the form of numerous stellar streams and overdensities (Helmi, 2008; Bell et al., 2008).

In general, the stellar halo is believed to have formed during the initial dissipative collapse of gaseous cloud (Eggen et al., 1962), followed by the subsequent mergers of satellite galaxies (Searle and Zinn, 1978). The Milky Way halo can be divided into inner and outer halo based on their spatial stellar distribution, kinematics, chemical abundance distribution, age gradient and their inferred formation scenario. The inner halo has a flattened but smooth structure with stars distributed within 15 to 20 kpc from the Galactic center and ~3 kpc from the Galactic mid-plane. Meanwhile, the outer halo stars show a spheroidal distribution at distances of 20 kpc away from the Galactic center at similar heights as the inner halo. The stars in the inner halo exhibit a slight prograde rotation and exhibit a peak metallicity, [Fe/H] = -1.6 dex while within the outer halo, stars rotate in a retrograde fashion with metallicities peaking at [Fe/H] = -2.2 dex (Carollo et al., 2007; Fernández-Alvar et al., 2015). In addition, an age gradient is observed with the inner halo being older having formed during the dissipative collapse of initial gas clouds and younger outer halo population, formed via mergers and

accretion of satellite galaxies (Santucci et al., 2015; Carollo et al., 2016; Das et al., 2016).

In addition to the field halo stars, old globular clusters have been commonly used in the determination of the above mentioned global properties, to interpret the formation scenarios of the halo as well as to distinguish between the inner and outer halo (Searle and Zinn, 1978; Deason et al., 2011). The estimated mass of the stellar halo from main sequence stars and mass-to-light ratio of globular clusters, within radial distance of ~45 kpc, is about from 4-7×10^8 $M_\odot$ (Bell et al., 2008; Deason et al., 2011).

Bulge

The Milky Way bulge is located within 3 – 4 kpc from the Galactic center and on average harbors old stars (Ortolani et al., 1995; Clarkson et al., 2008; Rich, 2013; Origlia, 2014; Ness and Freeman, 2016; Zoccali and Valenti, 2016; Bernard et al., 2018). The estimated stellar mass is around 1.2 – 1.6 × 10^{10} $M_\odot$ and constitutes nearly 15% of the total luminosity (Portail et al., 2015). At the same time, the bulge does not show the spheroidal morphology of the classical bulge, as would have been expected for a structure built through dissipative collapse of a primordial gas cloud or through early mergers. Instead, boxy/peanut shaped (B/P) or X-shaped morphology is exhibited by the stellar populations in the bulge (red clump stars in particular) as revealed by photometric surveys (COBE/DIRBE: Weiland et al. 1994, 2MASS: McWilliam and Rich 1994, OGLE-III: Nataf et al. 2010, VVV: Wegg and Gerhard 2013; Valenti et al. 2016). The X-shape of the bulge gets prominent at a height of 400 pc from the Galactic mid-plane (Nataf et al., 2010; Wegg and Gerhard, 2013; Gonzalez et al., 2015a) in the form of the bimodal distance distribution of red clump stars representing the near and far-sides of the peanut shaped bulge. Within the bulge, there is a longer and flatter bar oriented at an angle between 20° and 30° with respect to the Sun-Galactic center direction (Shen et al., 2010; Wegg and Gerhard, 2013). The B/P or X-shaped morphology of the bulge is considered to be the manifestation of the stellar bar that evolved secularly after buckling (Combes and Sanders, 1981; Athanassoula, 2005; Ness et al., 2012; Di Matteo et al., 2014).

The bulge stars show multi modal metallicity distribution with [Fe/H] between -1.5 dex and 0.6 dex (Ness et al., 2013a; Rojas-Arriagada et al., 2017; Zoccali et al., 2017) indicating the presence of multiple components of stellar populations. The different proportion of these multiple components with height above the Galactic mid-plane has also resulted in the finding of a vertical metallicity gradient (Zoccali et al., 2008b; Gonzalez et al., 2011; Ness et al., 2013a). The bulge stars are also found to be α enhanced suggesting a rapid chemical enrichment(Zoccali et al., 2017). Meanwhile, the cylindrical rotation exhibited by bulge stars in the outer bulge fields (BRAVA: Kunder et al. 2012, ARGOS: Ness et al. 2013b, GIBS: Zoccali et al. 2014) have been successfully reproduced using N-body simulations of pure thin-disc models (Shen et al., 2010; Martinez-Valpuesta and Gerhard, 2011; Gardner et al., 2014; Di Matteo et al., 2015) as the result of secular evolution of disc. Thus, this scenario is able to explain not only the morphology but also the chemical and kinematic properties of bulge stars with [Fe/H] >-0.5 dex to an extent, whereas it is unable to account for the metal-poor bulge ([Fe/H] <-0.5 dex) stars that shows an extended, centrally concentrated spheroidal distribution (Zoccali et al., 2017). However, Di Matteo et al. (2014, 2015); Di Matteo (2016);

Fragkoudi et al. (2017) have suggested using N-body simulations that the Milky Way bulge is the result of the mapping of the "thin + thick" disc of the Galaxy into the boxy/peanut-shaped structure and thus also explain the origin of metal-poor stars to be from the thick disc metal-poor population (and see also Athanassoula et al. (2016); Debattista et al. (2017) for similar findings using hydrodynamic simulations). To summarise, it can be assumed that the bulge formation and evolution have been very complex with contributions from more than any one of the above mentioned processes. Thus, the Milky bulge is a very active research field explored in detail using observations as well as models. A part of this thesis will be focusing on a comparatively unexplored region of the bulge, the inner bulge ($|b|<3°$), where high dust extinction prevents optical observations. I will introduce this region in the Section 1.3 and discuss my work in more detail in the Chapter 3.

Disc(s)

The Galactic disc hosts the maximum of the baryonic content in the Milky Way in the form of gas as well as stars located in the spiral arms. The disc mass was estimated to be ~10^{11} $M_\odot$ by Kafle et al. (2014) using the kinematic data of K-giant stars from the Sloan Extension for Galactic Understanding and Exploration (SEGUE).

Initial investigations of the disc morphology and structure have been carried out based on the stellar density/star counts and luminosity profiles of disc stars in the vertical and radial directions for the Milky Way as well as external galaxies. Based on the photometric observations of disc stars in the vertical direction towards the North and South Galactic poles (Yoshii, 1982; Gilmore and Reid, 1983), it was found that an exponential profile could fit the observed stellar density profile but with an extra component to account for the excess of the observed stars/light emission. Thus the disc was decomposed into two components : thin and thick discs, with scale heights of ~300 pc and ~1450 pc respectively (Gilmore and Reid, 1983). Later, Jurić et al. (2008) refined the scale height of thick disc to ~900 pc based on the density profiles of M dwarfs from SDSS. Bland-Hawthorn and Gerhard (2016) compiled the main papers on the scale height, scale length estimates at $R_\odot$ finding 0.3 ,2.6 kpc and 0.9 , 2.0 kpc as the scale height and scale length for thick and thin discs, respectively.

However, these classifications into thin and thick discs were purely based on geometry, and it was important to include the abundance as well as kinematic information of the stars in this classification to shed some light on the disc formation and evolution. Thus later studies found the thick disc to be older (Bensby et al., 2005), kinematically hotter (Gilmore et al., 2002; Kordopatis et al., 2013), more metal poor and enhanced in α abundances (Reddy et al., 2006; Haywood, 2008; Recio-Blanco et al., 2014) compared to that of the thin disc. Using mono abundance populations of dwarfs in SEGUE, Bovy et al. (2012) showed that the thick disc corresponds to the high [α/Fe], low [Fe/H] population with longer scale height and shorter scale length (~2 kpc), while the low [α/Fe], high [Fe/H] population with shorter scale height and longer scale length (~3.6 kpc) represents the thin disc. But the variation of [α/Fe] sequence in the [α/Fe] vs [Fe/H] plane across the disc from inner to outer parts of the Milky Way (Hayden et al., 2015) have shown that the chemical patterns found at the Solar radius are not representative of the whole disc. Very recently, Hayden et al. (2017)

argued that the current chemical definitions of thin and thick discs are misleading as they found significant age overlap of low and high α sequences for main sequence turn off and sub giant stars in the solar neighbourhood. They attribute this to the radial mixing (through churning and/or blurring, Sellwood and Binney 2002; Schönrich and Binney 2009) of stellar populations from inner and outer discs at the solar position as suggested by Haywood et al. (2013). These results suggests that the thin-thick disc naming convention is valid only in the geometrical context, while the chemical patterns in the [α/Fe] vs [Fe/H] plane suggest the division of disc into inner and outer disc.

An inside-out formation scenario for the disc with old stellar population dominating the inner disc and younger stellar population in the outer disc is supported by observations. Still, the existence of the geometrical thick disc component raises a question about the disc formation and evolution. Adhering to the hierarchical structure formation in the λCDM paradigm, several external mechanisms have been invoked to explain the thick disc formation : accretion of dwarf galaxies and stars from a disrupted satellite galaxy (Statler, 1988; Abadi et al., 2003), minor merger resulting in the heating of pre-existing thin disc (Quinn et al., 1993; Villalobos and Helmi, 2008) or merger induced star formation (Brook et al., 2004). Internal formation mechanisms like radial migration (Sellwood and Binney, 2002; Schönrich and Binney, 2009) and clumpy disc or turbulence dominated disc evolution (Bournaud et al., 2009) have also been introduced to explain the thick disc.

The disc formation and evolution is not discussed in detail in this thesis. I will focus on the vertical metallicity gradient as well as the metallicity distribution function of the disc stellar population in the solar neighbourhood in the chapter 2 in the context of Galactic archaeology and related surveys (see Section 1.2 below)

1.2 Galactic archaeology

As described in the Section 1.1.3 above, our understanding about the Milky Way formation, evolution, the contribution of various Milky Way components and their exact order of formation is still intuitive. Galactic archaeology deals with dissecting the Milky Way into its various components (Freeman and Bland-Hawthorn, 2002) with the objective to disentangle processes contributing to the Milky Way formation and evolution. This relies on precise estimation of stellar atmosphere properties of individual stars belonging to different stellar populations that make up each of these components. Stellar atmospheres retain the composition of chemical elements present in the interstellar medium at the time and place of their formation. Their orbital distributions, kinematics and ages are other reliable parameters that encode the evidences about the various physical processes that contribute to the formation and evolution of individual Milky Way components. Thus tracing chemical abundances of individual stars combined with their kinematic properties, ages and current phase-space distribution is an important part of the Galactic archaeology.

Galactic archaeology studies rely on all sky photometric, astrometric and large scale spectroscopic surveys to measure the detailed properties, i.e., six dimensional phase-space distribution, age and elemental abundances of a large number of stars. We also need stellar

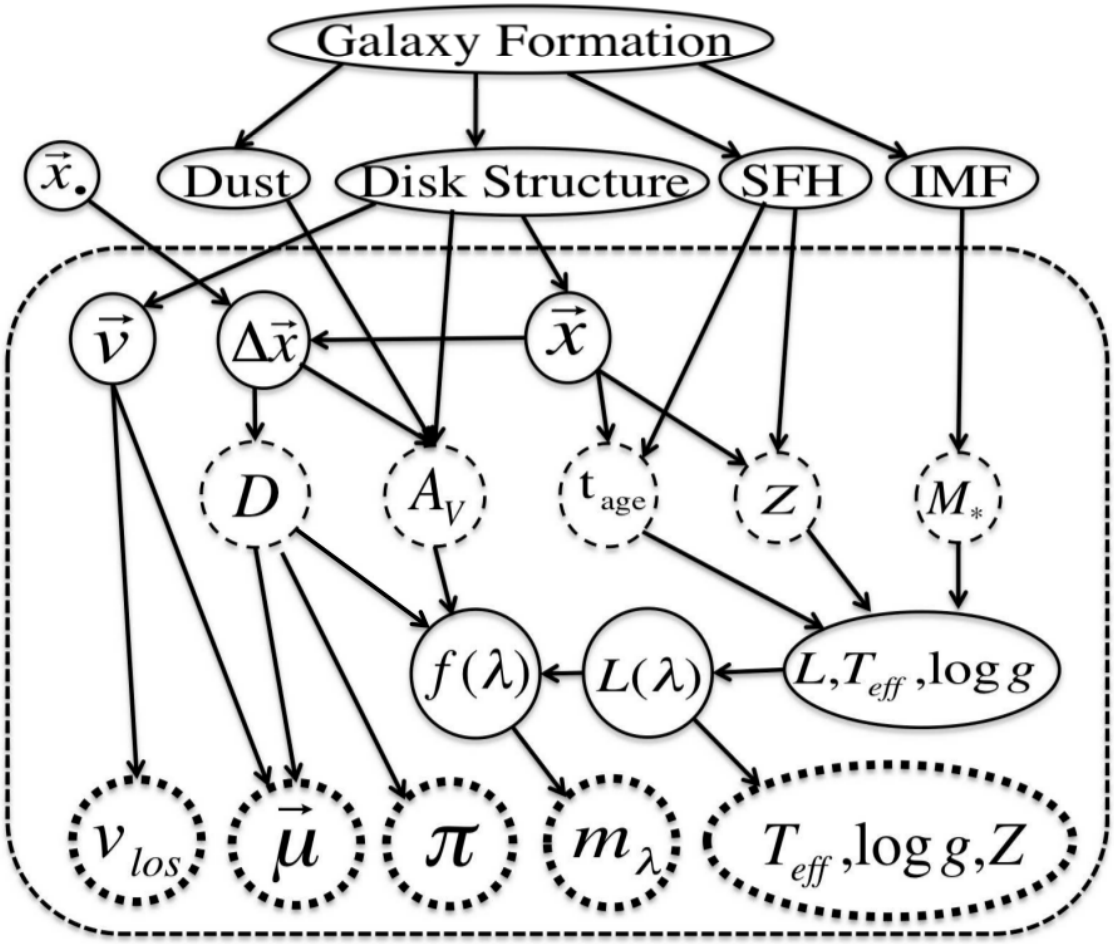

Figure 1.4: A schematic overview showing the logical dependencies between the stellar observables in Galactic surveys (thick dotted ovals) and the main desired parameters for each star (thin dashed ovals). The desired properties of each star include distance from the Sun (D), dust extinction (A_V), age (t_{age}), abundances (Z) and mass (M_*). The basic observables are line-of-sight-velocity (v_{los}) , proper motions (μ), parallax (π), multi-band photometry (m_λ) and photospheric parameters derived from spectra ($T_{\rm eff}$, $\log g$, abundances, Z). Stellar isochrones and stellar atmospheric models are used to determine the probability of the stellar observables for a given set of desired properties, for which prior probabilities are obtained from our notions about star formation (e.g. IMF), the the Galaxy structure and various constraints on the dust distribution. This model still makes a number of simplifications. Image and caption courtesy : Rix and Bovy (2013)

population synthesis models to account for the target selection biases in these surveys, and chemical evolution models to test various Galactic formation and evolution scenarios. These models in turn depends on our approximate idea about the star formation rate (SFR), star formation history (SFH), initial mass function (IMF), age-metallicity relations, isochrones and stellar atmosphere models. A rough schematic overview from Rix and Bovy (2013) is shown in the Figure 1.4 describing the way stellar parameters are constrained from observables in Milky Way surveys.

In the following subsections, I will introduce various photometric and spectroscopic surveys which have been used in this thesis as well as a few other current and ongoing surveys. A brief description about stellar population synthesis and chemical evolution models are also given.

1.2.1 Photometric surveys

There are many imaging and photometric surveys of the Milky Way covering multiple ranges of wavelengths, that estimate flux density of point sources and provide detailed catalogs. These catalaogs can be used as input photometric catalogs for target selection in complementary Milky Way spectroscopic surveys. In this subsection, I will introduce few surveys that have been used as input photometric catalog for spectroscopic surveys listed in subsection 1.2.2, which in turn have been used for my study involving the selection function in Chapter 2. I will also introduce a few mid and near infrared photometric catalogs that are not part of big surveys, but have been used in detail in the Chapters 3 and 4.

2MASS

The Two-Micron All Sky Survey (2MASS) is an all sky near infrared photometric survey covering JHK bands with 10σ Vega-based limiting magnitudes of J = 15.8, H = 15.1 and K = 14.3 with a spatial resolution of 4" (Skrutskie et al., 2006). Observations were carried out using 1.3 m telescopes at Mt. Hopkins and CTIO, Chile. 2MASS provides full sky coverage ($\geq$ 10,000 square degree) and the 2MASS point source catalogue contains positional and photometric information for nearly half a billion sources (mostly stars). The 2MASS photometric catalog have been used as input catalog for spectroscopic surveys like APOGEE.

SDSS

The Sloan Digital Sky Survey (SDSS) is an imaging + spectroscopy survey that focused on galaxy evolution, quasars etc, with the photmetric survey covering uptoone quarter of the celestial sphere in the north Galactic cap and a smaller area of ~225 square degree in the southern Galactic hemisphere (York et al., 2000; Stoughton et al., 2002). Observations are carried out in five optical bands, *ugriz*, in AB_ν system with completeness of ~99.3% at the bright end, dropping down to 95% at magnitudes of 22.1, 22.4, 22.1, 21.2 and 20.3 in *u*,*g*,*r*,*i* and *z* respectively with approximate spatial resolution of 1".

VHS

The VISTA Hemisphere Survey (VHS) is a near infrared survey of the southern hemisphere covering an area of ~20,000 square degrees in J and K_S wavebands with 5σ Vega-based point source limits of J = 20.2 and K_S = 18.1, resulting in a depth 30 times fainter than the 2MASS in the same bands and a spatial resolution of 0.339″per pixel. An area of ~5000 square degrees in the South Galactic cap is imaged more deeply including H band with 5σ limits of J = 20.6, H = 19.8 and K_S = 18.5 (McMahon et al., 2013). As the name indicates, the survey is being carried out using the 4.1 m Visible and Infrared Survey Telescope (VISTA) located at the Paranal Observatory in Chile. VHS is used as input photometric catalog for Gaia ESO survey (GES).

VVV

The Vista Variables in the Vía Láctea (VVV) is an infrared variability survey of the Milky Way bulge and a part of the disc, performed at the 4.1 m VISTA in five passbands : Z, Y, J, H, K_S (Minniti et al., 2010). VVV provide photometry for 10^9 point sources, among which there are 10^6 expected variable sources with repeated observations over 2010-2015. Using RR Lyrae stars as distance calibrators, VVV will provide the 3D map of its surveyed region, in addition to variable source detection, search for micro lensing events, estimate dust extinction etc (Saito et al., 2012). VVV is also used in the photometric selection function and ancillary photometric catalogs of the Gaia-ESO survey bulge felds.

Spitzer GLIMPSE and MIPSGAL

Infrared Array Camera (IRAC; Fazio et al. 2004) and Multiband Imaging Photometer (MIPS; Rieke et al. 2004) are two instruments onboard the *Spitzer Space Telescope* (Werner et al., 2004), which is a space-borne telescope with 0.85 m aperture. IRAC obtains simultaneous broadband images at 3.6, 4.5, 5.8 and 8 μm. All four detector arrays in the camera are 256 × 256 pixels in size, and the FWHM of the point spread function are 1".6, 1".6, 1".8 and 1".9 at 3.6, 4.5, 5.8 and 8.0 μm, respectively. MIPS covers longer wavelengths with imaging bands at 24, 70 and 160 μm and very low resolution spectral energy distribution (SED) spectroscopy from 52 to 100 μm. MIPS achieves telescope-limited resolutions of 6", 18" and 40" at 24, 70 and 160 μm, respectively.

The Galactic Legacy Infrared Mid-Plane Survey Extraordinaire (GLIMPSE; Churchwell et al. 2009a) is one of the legacy programs of the *Spitzer Space Telescope* that uses IRAC observations to get a deeper understanding of the physics of interstellar dust, star formation, and the large-scale structure of the Milky Way as traced by stars. GLIMPSE consists of three surveys : GLIMPSE I covering an area of 220 deg^2 of the Galactic plane from longitudes |l| = 10° to 65°, GLIMPSE II fully imaging the inner 20° of the Galactic plane and GLIMPSE 3D extending the GLIMPSE I & II latitude coverage to ±3° at nine selected latitudes and to ±4° within 2° of the Galactic center.

MIPSGAL (Carey et al., 2009) is another legacy program of the *Spitzer Space Telescope* that covers 278 deg^2 of the inner Galactic plane using the 24 and 70 μm bands of the

MIPS instrument. MIPSGAL provides far-infrared/submillimeter measurements for both point sources and diffuse emission, complementary to their observations in near infrared regime using 2MASS and GLIMPSE.

1.2.2 Spectroscopic surveys

Spectroscopic surveys of the Milky Way focusing on Galactic archaeology mainly observe in narrow spectral bands covering optical to near infrared wavebands chosen depending on their science goals and the area/component of the Milky Way being studied. The spectral resolution and quality of the spectra obtained from these surveys vary depending upon the instruments they use and the time they dedicate for observations respectively. Many of the latest surveys observe multiple targets simultaneously using dedicated multi-fiber observing plates and have dedicated pipelines to carry out spectral data reduction. They also provide final catalogs containing the reduced stellar parameters like effective temperature ($T_{\rm eff}$), surface gravity ($\log g$) and abundances for various elements (iron peak elements, alpha elements, odd-z elements etc). Below, I will briefly explain various surveys focusing mainly on few spectroscopic surveys whose data have been used in this thesis (see Chapter 2)

APOGEE

The Apache Point Observatory Galactic Evolution Experiment (APOGEE; Majewski et al. 2017) is one of the four programs in the Sloan Digital Sky Survey III (SDSS-III; Eisenstein et al. 2011), which performed a three-year survey of our Galaxy using the Sloan 2.5 m Telescope at the Apache Point Observatory (APO). APOGEE observed in the near-infrared H-band ($1.5\,\mu$m – $1.7\,\mu$m) at high spectral resolution ($R \sim 22500$) and high signal-to-noise ratios, S/N (>100). APOGEE was designed to obtain precise and accurate radial velocities and chemical abundances for ~10^5 red giant branch stars, red clump stars and asymptotic giant branch stars in the dust-enshrouded Galactic mid plane and inner Galaxy regions, typically ignored by optical surveys.

The survey made use of the standard SDSS plugplates designed with holes for 300 APOGEE fibers, with ~230 fibers placed on science targets and ~70 fibers reserved for telluric absorption calibrators and airglow emission calibration positions. Each plate has a field of view (FOV) ranging from 1-3°; the number of visits per field varied from 1 to ~24 depending on the type and location of the field. The targeting strategy of APOGEE involved grouping of stars into sets based on their apparent H-band magnitudes, called "cohorts", with the aim of obtaining desired S/N for all the stars in the cohort. Cohorts are categorised into short, medium and long in the increasing order of their number of visits. The brightest set of stars belong to the short cohorts, implying fewer number of visits than fainter ones that are in the medium and long cohorts. Each plate is drilled with a "design", made up of a particular combination of cohorts, which is associated with only one field (Zasowski et al., 2013). I will explain the color and magnitude cuts used for APOGEE target selection in the Chapter 2.

The APOGEE Stellar Parameters and Chemical Abundances Pipeline (ASPCAP; García Pérez et al. 2016) is used to determine the stellar parameters and chemical abundances of up

to 15 elements based on a χ^2 minimization between observed and synthetic model spectra. There have been 5 public data releases of APOGEE starting from DR10 to DR14. In this work, I use the DR13 catalogue of APOGEE.

The APOGEE-2 survey (Majewski et al., 2016) is part of the Sloan Digital Sky Survey IV (SDSS-IV) and a successor to APOGEE, with the plan to observe the Northern (APOGEE-2N) and Southern (APOGEE-2S) hemispheres. The APOGEE-2N survey is carried out by the same telescope and instrument as the APOGEE, while a second observing station, the du Pont 2.5-m telescope at Las Campanas Observatory (LCO) with a similar spectrograph have been used for APOGEE-2S. Thus APOGEE-2 aims to expand the original APOGEE sample in both distance and spatial coverage, in addition to the inclusion of diverse target objects and scientific goals.

RAVE

The RAdial Velocity Experiment (RAVE) (Steinmetz et al., 2006) is a multi-fibre spectroscopic survey that covers the entire southern celestial hemisphere except at low $|b|$ and $|l|$. The observations were carried out at the Anglo-Australian Observatory (AAO) in Siding Spring, Australia, using the 1.2 m UK Schmidt telescope. A 6° field multi-object spectrograph was used to obtain the spectra in the infrared CaII-triplet region (8410 Å$< \lambda <$ 8795 Å) with a spectral resolution of R~7500. Three field plates with 150 robotically positioned fibers have been used in turn for observations.

RAVE was designed to decipher the chemical and dynamical evolution of the Galaxy, using the local dwarfs as well as giant stars. The limiting magnitude of I~12 limit the most apparently bright targets to the thin and thick discs. RAVE was designed to be a precursor to *Gaia*, with the RAVE wavelength range matching to that of the *Gaia* Radial Velocity Spectrometer. In addition to the Ca II IR triplet lines, there are iron, silicon, magnesium and titanium lines that provide an estimate of the alpha element abundance, [α/Fe], as well as overall metallicity, [Fe/H]. RAVE data have been used to advance our understanding of the Milky Way disc (Kordopatis, 2014), to estimate the Milky Way mass from extreme high velocity stars (Piffl et al., 2014b), determine the local dark matter density (Piffl et al., 2014a), to detect signatures of radial migration (Wojno et al., 2016) etc.

RAVE provides radial velocities and stellar parameters complementing the surveys that focus on astrometric information. The stellar atmospheric parameters were estimated using the pipeline designed for the RAVE spectra (Kordopatis et al., 2011, 2013) making use of the MATrix Inversion for Spectral SynthEsis algorithm (MATISSE, Recio-Blanco et al. 2006) and the DEcision tree alGorithm for AStrophysics (DEGAS). There have been 5 data releases of RAVE providing the stellar atmospheric parameters, radial velocities and individual abundances for more than 400,000 unique stars. I use the DR4 version of the RAVE data in this work.

GES

The Gaia-ESO survey (GES) is a ESO spectroscopic survey aimed at targeting ~10^5 stars covering the major components of the Milky way (Gilmore et al., 2012). The observations are carried out using the Fibre Large Array Multi Element Spectrograph (FLAMES) (Pasquini et al., 2002) on the Very Large Telescope array (VLT) in Cerro Paranal, Chile. This fibre facility has a FoV of 25 arcmin diameter for two different spectrographs, GIRAFFE and UVES.

GES was designed to advance our knowledge of the Galactic and stellar evolution by quantifying the kinematic and multi-element chemical abundance distribution functions of the Milky Way components (bulge, halo, thin and thick discs). Blue F stars in the halo, redder F stars in the thick disc and K giants in the bulge fields as well as outer thin disc, warp, flare etc. have been targeted. The Field survey has been carried out mainly with GIRAFFE for ~10^5 stars to V<20 mag, making use of its two mid resolution setups, HR10 (Ca II IR triplet) and HR21 (~540 nm), that include a number of Fe I and Fe II lines as well as lines of several α-elements such as Ca, Mg etc. UVES, with its red (300-500 nm) and blue (420-1100 nm) high resolution setups, have been used in parallel to observe ~10^4 G-type stars to V<15 mag. GES also observed a significant sample of open cluster populations of all accessible cluster ages and stellar masses. UVES fibers have been allocated to pre-main sequence or zero age main sequence G and K-type cluster members, while GIRAFFE fibers targeted K and M-type cluster members.

The stellar parameters were derived by different nodes (using MATISSE, SME: Valenti and Piskunov 1996 and FERRE: Allende Prieto et al. 2006 codes for GIRAFFE spectra, and about a dozen different methods for UVES spectra). The final recommended GES parameters come from a careful homogenization and calibration of the different results for a given star. There have been four public data releases of GES, DR1 to DR4, with data from DR4 used in this thesis.

LAMOST

The Large Sky Area Multi-Object Fiber Spectroscopic Telescope (LAMOST) is another extensive ground-based spectroscopic survey of the Galaxy being carried out with the Guo Shou Jing reflecting Schmidt Telescope. It is equipped with 16 low resolution spectrographs capable of recording the spectra of up to 4000 objects simultaneously in a FOV of 5°, covering all optical wavelengths with a spectral resolution of ~1800 (Cui et al., 2012; Zhao et al., 2012). The survey contains the LAMOST ExtraGAlactic Survey (LEGAS) and the LAMOST Experiment for Galactic Understanding and Exploration (LEGUE : Deng et al. 2012; Smith et al. 2012), which itself is composed of three separate surveys with different input catalogues and target selection criteria.

Stars have been targeted using bright, medium and faint plates, with limiting magnitudes set at $14 \leq r \leq 16.3$, $16.3 \leq r \leq 17.8$ and $17.8 \leq r \leq 18.5$. Restricted number of faint plates have been observed constrained by the observing condition at the site. The main survey goals include determining the basic stellar parameters of nearly 7 million stars belonging to

thin, thick discs and halo, map out the star density distribution for Galactic disc and halo in multi dimensional phase space, identify possible phase-space substructures and decipher the contributions of mergers and accretion to the Galactic stellar spheroid, measure the local dark matter density in the solar neighborhood etc. (Liu et al., 2015).

The LAMOST survey has collected more than 5 million low resolution stellar spectra and provides basic parameters, including radial velocity, effective temperature, surface gravity and metallicity determined with the LAMOST Stellar Parameter Pipeline (LASP) (Wu et al., 2011). There have been three public data releases of LAMOST, and I use the data from the DR2 catalog in this thesis.

GIBS

The GIRAFFE Inner Bulge Survey (GIBS) is carried out using the GIRAFFE spectrograph of the FLAMES instrument at the ESO Very Large Telescope (VLT) targeting red clump stars in the Milky Way Bulge (Zoccali et al., 2014). The survey aims top derive the metallicity and radial velocity of bulge stars located in the in the region of Galactic longitude range ~ -10° to +10° and latitude range ~ -10° to +5°, same as those mapped by the VVV survey. Hence the targets of 200–400 stars for the 31 fields are selected from the VVV survey catalog. Majority of fields are located at negative latitudes, with only ~5 fields at b = 4°. The LR8 setup (R ~ 6500, centred on the CaT spectral feature at ~ 8500 Å, S/N per pixel ~ 50) of the FLAMES GIRAFFE have been used for observing stars in all fields except those at b = -4°. The stars in this latitude fields have been observed with the HR13 setup (R ~ 22,500, centred at ~ 6500 Å, S/N per pixel ~ 100) to measure iron and light element abundances. The survey continues to give results that have been used to constrain the chemodynamical properties of the Galactic bulge (Gonzalez et al., 2015b; Zoccali et al., 2017)

GALAH

The Galactic Archaeology with HERMES (GALAH) survey is a large-scale Milky Way stellar spectroscopic survey designed with the aim of understanding the Galaxy's history by means of chemical tagging (De Silva et al., 2015). GALAH makes use of the High Efficiency and Resolution Multi-Element Spectrograph (HERMES) at the 3.9-m Anglo-Australian Telescope, which provide multi-object (~392) high resolution (~28000) spectra. The survey aims to provide elemental abundances for up to 30 elements in four optical windows. The GALAH targets are chosen within magnitude range of 12<V<14 and Galactic latitude $|b| > 10°$, with roughly two-thirds of the targets being dwarf stars and the rest, red giant branch stars located at kpc-scale distances from the solar neighborhood.

GALAH targets are in the magnitude range wherein the *Gaia* parallaxes and proper motions are accurate as well as complete. Moreover, GALAH will be highly complementary, in terms of different magnitude ranges and regions of the Galaxy observed, to the existing spectroscopic surveys like APOGEE and GES. The latest data release, DR2, provides stellar atmosphere parameters and element abundances for more than 300,000 stars (Buder et al., 2018). GALAH aims to obtain spectra for several million stars by the end of the survey run.

WEAVE

The WHT Enhanced Area Velocity Explorer (WEAVE) survey is a multi-object survey that makes use of the WEAVE spectrograph which will equip the prime focus of the 4.2-m William Herschel Telescope (WHT) at the Observatorio del Roque de los Muchachos, on La Palma in the Canary Islands. This instrument will enable astronomers to observe and obtain optical spectra of up to ~1000 targets over a two-degree field of view in a single exposure (MOS). The same field can be observed using 20 deployable mini integral-field units (mIFUs) of 11" × 12", with 1.3" spaxels. Finally, there is a large fixed integral-field unit (LIFU) with a field of view of 1.3" × 1.5" and 2.6" spaxels to study extended objects. The WEAVE spectrograph has two arms, red and blue, offering spectroscopic resolutions of 5000 and 20000 respectively (Bonifacio et al., 2016). The science goals and targets of WEAVE are broad and diverse, some of which are Galactic archaeology, stellar physics, Galaxy clusters, QSOs etc. WEAVE is expected to start operations in 2019.

MOONS

The Multi-Object Optical and Near-infrared Spectrograph (MOONS; Cirasuolo et al. 2014) on the 8.2 m VLT, with it's 1000 object multiplex capability and medium to high resolution set ups (9000 in the optical and 20000 in the infrared) covering near-IR wavelength range, has Galactic archaeology in the bulge as one of the main science goals. The observations, to start in 2019, will be able to provide accurate radial velocities, metallicities and chemical abundances for bulge stars in highly extincted regions, thus enabling to shed light on the chemo-dynamical characteristics of the bulge.

4MOST

The 4-metre Multi-Object Spectroscopic Telescope (4MOST) is a fibre-fed spectroscopic survey facility on the VISTA telescope with a hexagonal field-of-view of 4 square degrees and ability to simultaneously observe and obtain spectra for ~2400 objects . The fibers will feed one high-resolution (~20,000) and two medium resolution (~5000) spectrographs with fixed 3-channel designs and identical 6k × 6k CCD detectors. The science goals of 4MOST are broad ranging from Galactic Archaeology and stellar physics to high-energy physics, galaxy evolution, and cosmology (de Jong et al., 2016). The survey science operations are expected to start in 2021.

1.2.3 Stellar population synthesis models

The observations carried out using various photometric and spectroscopic surveys have given us a global view of the Milky Way and its various components. The data products from these surveys have enabled us to visualise the Milky Way components not only in terms of their star counts/density distributions but also from chemical, dynamical as well as chronological perspective.

Similarly, there have been a progressive increase in the models of the Milky Way, from simple empirical models fitting star counts along few lines of sights to dynamically self consistent population synthesis models. Stellar population synthesis models make use of Galaxy formation and evolution scenarios along with various physical assumptions (star formation histories (SFH), initial mass functions (IMF), age-metallicity relations (AMR) etc.) to generate a picture of the Milky Way in different photometric systems. Their prime objective is to compare as well as interpret different observational data currently available and to test the theories on which the models are based. Besançon (Robin et al., 2003) and TRILEGAL (Girardi et al., 2005) are two of the commonly used stellar population synthesis models, while Galaxia (Sharma et al., 2011) provides a numerical framework to create such models, successfully tested for Besançon. These models make use of suitable stellar isochrones that takes into account our knowledge about the stellar structure evolution and link it with the Galactic component properties like SFH, IMF, density profiles etc.

In the following subsections, I will briefly introduce the two stellar population synthesis models, TRILEGAL and Galaxia/Besançon, that have been used to create mock catalogs for certain spectroscopic surveys as explained in the Chapter 2.

1.2.3.1 TRILEGAL

The TRI-dimensional modeL of the GALaxy (TRILEGAL) is essentially a Monte Carlo simulation in which stars across small sky areas towards an element of galactic coordinates (*l,b*) and solid angle dΩ, in a given bin of apparent magnitude [m_λ,m_λ + dm_λ] are generated for a specific passband, λ, according to the following fundamental equation of stellar statistics (Bahcall, 1986):

$$N(m_\lambda, l, b) = dm_\lambda \int_0^\infty dr\, r^2 \rho(\mathbf{r}) \phi(M_\lambda, \mathbf{r}) d\Omega \tag{1.1}$$

Here, r is the line of sight distance, $\phi(M_\lambda, \mathbf{r})$ is the intrinsic luminosity function of the stars considered at $\mathbf{r}$, $\rho(\mathbf{r})$ is the stellar density as a function of the position $\boldsymbol{r}$ = (*l,b,r*). r (pc) is related to the absolute magnitude (M_λ), apparent magnitude (m_λ) and interstellar absorption (A_λ) by the formula :

$$M_\lambda = m_\lambda - 5logr - A_\lambda(r) + 5 \tag{1.2}$$

One major assumption is that ρ or stellar density can be separated into distinct components like that of thin disc, thick disc, halo and bulge. The number of stars in each distance modulus bin is predicted using Equation 1.1, and the age, metallicity and mass for each simulated star is obtained from the SFR, AMR and IMF defined for the corresponding component to which the star belongs. The age, metallicity and mass are then used to derive the corresponding absolute magnitude, $T_{\rm eff}$, $\log g$ etc via interpolation in the isochrone grids.

A user interactive mode is available for TRILEGAL, for which the input model parameters like IMF, SFR, local surface density of stars etc can be modified. A default version is also provided that is advocated in Girardi et al. (2005). The default IMF is a log-normal function from Chabrier (2001). The thin disc is not locally isothermal (scale height, h_d, a function of

stellar age), has a radially decreasing mass density and is not isolated. The TRILEGAL web interface provides two choices of SFH for thin disc : one with a constant SFR up to an age of 11 Gyr and the other, a two-step SFH with a 1.5 times enhancement in the SFR between the ages of 1 and 4 Gyr (Gao et al., 2013). The scale height of the thick disc, h_t, is not a function of stellar age with the SFH taken to be constant over an age range of 11-12 Gyr with metallicity, [Fe/H] = -0.67±0.1 dex and α enhancement of [α/Fe] ~ 0.3 dex. TRILEGAL assumes a de Vaucouleurs $r^{1/4}$ (de Vaucouleurs, 1959) or oblate $r^{1/4}$ spheroid (Gilmore and Reid, 1983) mass density profile for the halo, with a constant SFH over an age range of 12–13 Gyr, peak metallicity of -1.6±1 dex and α enhancement of [α/Fe] ~ 0.3 dex. The bulge is modeled as a triaxial one, with a single bursts of age of 10 Gyr and peak metallicity of +0.3 dex. The detailed description of the model is given in Girardi et al. (2005), and the specific details of the input parameters used for this work is given in Chapter 2.

TRILEGAL have been used in different studies comparing the model output with the observed characteristics of the Milky Way as well as external galaxies. Vanhollebeke et al. (2009) used TRILEGAL to study the characteristics of the stellar populations and the metallicity distribution in the Galactic bulge. The color cut used in the APOGEE target selection was chosen and justified based on the comparison with the CMDs simulated using TRILEGAL (Zasowski et al., 2013). Miglio et al. (2013) used TRILEGAL to simulate the red giant population in two disc fields from the *Corot* sample by using their selection cuts and understand the observed mass distribution. TRILEGAL have been used to model external galaxies as well (Rubele et al., 2012, 2015).

1.2.3.2 Galaxia/Besançon

The Galaxia code provides a framework for modeling the Galaxy based on analytic distribution functions of stellar populations that make up the individual Milky Way components. Like TRILEGAL, the distinct components include the thin disc, the thick disc, the stellar halo and the bulge. Each of these components is defined by the following distribution function :

$$f_i = f_j(\mathbf{r}, \mathrm{v}, \tau, \mathrm{Z}, m) \tag{1.3}$$

where **r** represents the position, v the velocity, τ the age, Z the metallicity and *m* the mass of star belonging to the component labelled *j*. This function can be written as the product of individual functions, that depend mostly on age, τ, and in some cases the spatial position, **r**. These are the star formation rate ($\psi(\tau)$), IMF ($\varepsilon(m,\tau)$), present day spatial distribution of stars (f_{pos}(**r**,τ)), velocity distribution (f_{vel}(Z,**r**,τ)), metallicity distribution (f_Z(Z,**r**,τ)). Equation 1.3 then becomes :

$$f_i = \frac{\psi(\tau)}{< m >} \varepsilon(m,\tau) f_{pos}(\mathbf{r},\tau) f_{vel}(Z,\mathbf{r},\tau) f_Z(Z,\mathbf{r},\tau) \tag{1.4}$$

<m> represents the mean mass of the stars of a simple stellar population with the prescribed age dependent IMF. Detailed description of these individual distribution functions can be found in Sharma et al. (2011).

Once the distribution laws are fixed, the next step is to sample position and age coordinates for stars using an adaptive Von Neumann rejection technique, which is much more efficient and computationally less expensive compared to the standard Von Neumann rejection technique. The metallicity and velocity distributions can then be easily generated from age and spatial distribution, followed by the mass from IMF. A synthetic library of isochrones can be used to constrain the basic stellar parameters like $T_{\rm eff}$,$\log g$,bolometric luminosity etc. via interpolation. Galaxia makes use of the Padova isochrones (Marigo et al., 2008).

The properties of other main ingredients like SFR, age-velocity relation, density profiles etc for each of the Milky Way components are adopted from the Besançon model (Robin et al., 2003). The Besançon model is dynamically self consistent, constraining the scale height of populations (assumed to be isothermal and relaxed) by its velocity dispersion and Galactic potential. Among the four main populations, the thin disc is divided into seven age components (0 to 10 Gyr) and has a two-slope IMF. The thick disc has a mean metallicity of -0.78 dex simulated as a single burst of age 11 Gyr, while the halo (mean metallicity ~ -1.78 dex) and bulge (mean metallicity ~ 0.0 dex) are simulated as single bursts of ages of 14 and 10 Gyr, respectively. Robin et al. (2012) updated the model by using two components to define the bulge/bar. The main component is boxy S-shape, triaxial with mass ~ 6.1×10^9 $\mathrm{M}_\odot$, age around 8 Gyr and approximately solar metallicity. The second one is of similar age, more extended and triaxial with poorer metallicity ~ -0.35 dex. Instead of the Schlegel extinction maps (Schlegel et al., 1998) used by Galaxia to calculate the extinction along a given line of sight, the more sophisticated model of the 3D dust distribution provided by Drimmel et al. (2003) is chosen for this work.

The Galaxia code has been used to evaluate the statistical significance of the Aquarius stellar stream in the RAVE data (Williams et al., 2011). Boeche et al. (2013) investigated the influence of selection effects on the chemical radial gradients in the Galactic disc with RAVE data using Galaxia model. Some of the ongoing as well as planned surveys (GALAH, 4MOST etc.) also made use of the Galaxia code to simulate the input catalog and produce the expected output from the complete run of these surveys, to evaluate the science capabilities of these surveys.

1.2.4 Chemical evolution models

Stellar atmospheres retain the composition of chemical elements present in the interstellar medium at the time and place of their formation. Thus the determination of chemical abundances in stellar atmospheres can help us in reconstructing the star forming history of the Milky Way. Chemical evolution models play an important role in interpreting the abundances of various chemical elements from stellar atmospheres belonging to different Milky Way components. It is possible to constrain initial conditions of the interstellar medium, star formation history as well as possible stellar yields from star formation and evolution processes by comparing the results from chemical evolution models with observational data.

To build a Galactic chemical evolution model, there are many basic ingredients, starting from certain initial conditions. These include the definition of the system, i.e., whether it is closed (no infall and/or outflow) or open, and also if the system has primordial or chemically

enriched gas. Following this, the stellar birth rate function needs to be defined as follows :

$$B(m,t) = \psi(t)\psi(m)\,dt\,dm \tag{1.5}$$

where $\psi(t)$ is the rate at which stars form from the available gas and $\psi(m)$ is the mass distribution of the stars at birth. As Equation 1.5 suggests, the stellar birth rate function is the product of these two independent functions.

In addition, it is necessary to know how different elements are produced in stars via nuclear burning inside stellar interiors during its lifetime, and the amount of each element being restored into the interstellar medium by means of mass loss or especially at the time of death of the star. This is termed as the stellar yields and is another crucial ingredient in the chemical evolution models. There are other ingredients like gas flows in the form of galactic winds, radial flows and infall of extragalactic gas that are considered to be supplementary (Matteucci, 2014).

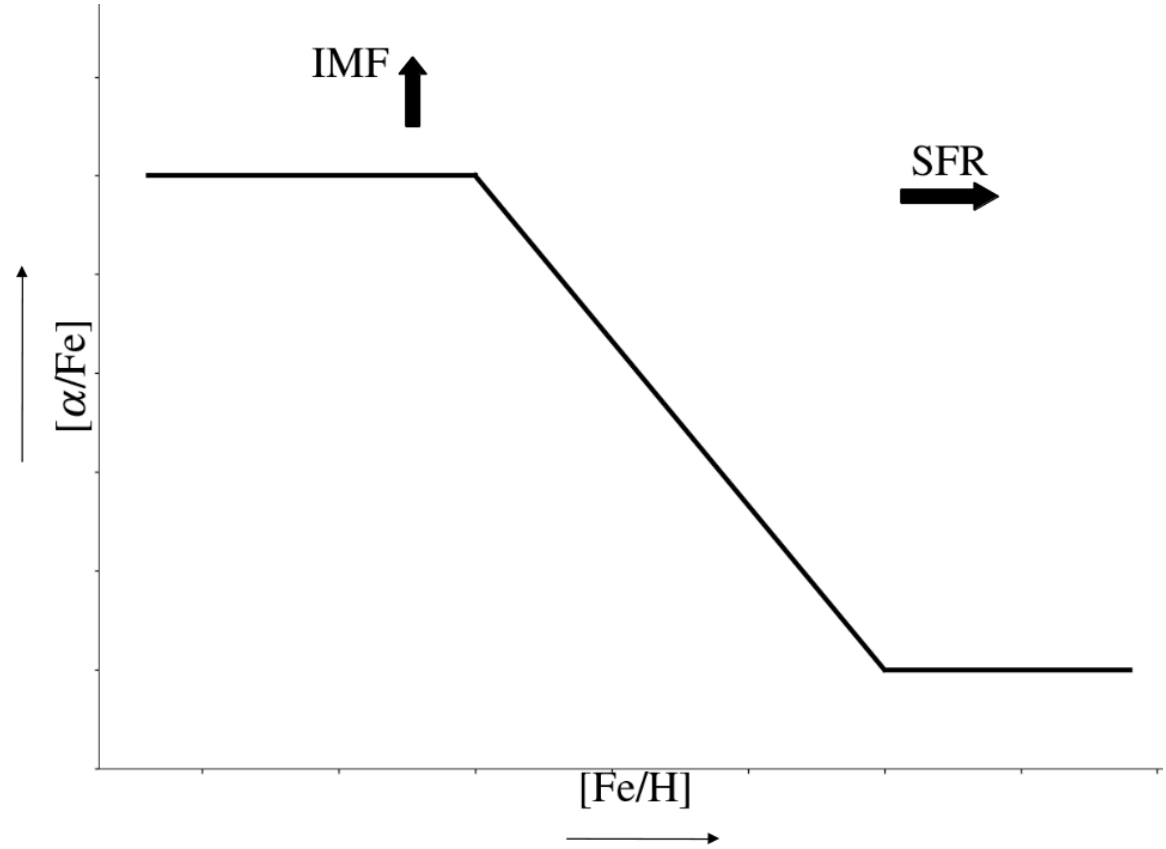

Figure 1.5: The [α/Fe] versus [Fe/H] plot showing the usual observed pattern followed by stars belonging to different components.The arrows indicate how the IMF and SFR affect the variation of plateau level of [α/Fe] and the variation of the location of the knee respectively.

The chemical enrichment of the ISM with elements heavier than H, He and small amounts of Li (all from Big Bang) can be traced back to their production in different types of supernovae. Core collapse type II supernovae (SN II) explosions have massive stars (M > $10\mathrm{M}_{\odot}$)

as progenitors and nucleosynthesis calculations have indicated that most of the O, other α-elements (Ne, Mg, Si, S, Ca, Ti), and some iron are produced in these events. Meanwhile, the type Ia supernovae (SN Ia) explosions have lower mass stars (M < $8M_{\odot}$) as progenitors producing large quantities of iron-peak elements (Vn, Cr, Mn, Fe, Co, Ni). Due to their short lifetimes, massive stars drive the early evolution of the gas enrichment, polluting the gas with α-elements from SN II explosions. The SN Ia supernovae, arising from lower mass stars, takes much longer time and thus iron enrichment of the ISM is expected to be delayed. This delay between chemical enrichment of the ISM gas lead to the proposal of the time-delay model, which can be used to interpret the behaviour of [α/Fe] versus [Fe/H] measured in stars of different Milky Way components as shown in the Figure 1.5. Thus the initial high level of the [α/Fe] is determined by the fraction of massive stars born initially in the system, i.e., initial mass function (IMF). The plateau of the [α/Fe] will be at a higher level if there are more massive stars initially. Small amount of iron production from SN II together with the not so dominant SN Ia ensures that the metallicity, [Fe/H] , also increases as the chemical enrichment proceeds. The plateau will end up in a "knee" once the SN Ia explosions become prominent and the [α/Fe] value decreases with increasing metallicity from this point. The location of the knee is controlled by the star formation rate (SFR) as higher SFR will result in the knee to move to higher metallicities.

Multiple chemical evolution models have been made with different assumptions. One of the earliest model is based on only one episode of infall, during which first the halo formed and then the disc (Matteucci and Francois, 1989, 1992). Another model was based on the parallel formation with the simultaneous formation of halo, thick and thin disc but at different rates (Pardi et al., 1995). A more recent model is the two infall episode scenario (Chiappini et al., 1997) with a short time scale for the first infall episode during which the inner halo and bulge are formed and the thick disc is assembled. The thin disc is formed inside out during the second infall episode with a relatively longer time scale.

In this thesis, I have not used any chemical evolution models to compare my results with. But I have carried out a detailed observational study to estimate the SFR in the inner Milky Way (central molecular zone, CMZ) as discussed in detail in Chapter 4. As I have mentioned, SFR is an important ingredient in the Galactic chemical evolution models. I will briefly introduce the IMF and SFR which are the primary ingredients that make up the stellar birth rate function.

The majority of the chemical evolution models assume the SFR to be a function of the surface gas density, σ_g, following the Schmidt (1959) law :

$$\psi(t) = A\,\sigma_g^k \tag{1.6}$$

where *k* varies from 1 to 2 (Kennicutt, 1989) obtained by the best fit to the observational data on spiral disks and starburst galaxies, and A is the efficiency of star formation expressed as the inverse of the timescale of star formation. Observational results of Dopita and Ryder (1994) suggested the inclusion of the total surface mass density, induced by supernovae feedback, besides the surface gas density, resulting in the following formulation :

$$\psi(t) = A\,\sigma_g^k\,\sigma_{tot}^k \tag{1.7}$$

Other Schmidt-like formulations of SFR include that from Kennicutt (1998) including the angular rotation speed of gas, Ω_g :

$$\psi(t) = 0.017\,\sigma_g\,\Omega_g \tag{1.8}$$

Meanwhile, these relations with surface gas density are not found to reproduce the SFR in the CMZ, and we need other methods to determine the SFR to constrain the chemical evolution models in the CMZ, as shown in Chapter 4.

The variation of the SFR over a certain period of time (e.g. the evolution time of the Galaxy) is known as star formation history (SFH). It is very difficult to unravel SFH as it is closely tied up with the nature and mechanism of gas accretion, infall history, re-accretion of outflowing gas etc. which are still not completely understood. Snaith et al. (2015) have tried to reconstruct the SFH of the Milky Way using a chemical evolution model making use of the age-metallicity relations and [α/Fe] vs [Fe/H] relations estimated for the solar neighbourhood stars. Their best fit SFH showed that there was an intense phase of star formation between 9 and 13 Gyr ago, followed by a rapid drop for about 1 Gyr (related to quenching) and continues at a lower intensity from ~7 Gyr ago upto the present. Bernard et al. (2018) have used the CMD fitting technique to reconstruct the SFH of the Galactic bulge that revealed nearly 60-70% of stars being old (>10 Gyr) but also found recent star formation ~1 Gyr ago. Thus determining SFH is very crucial to decipher the formation history of the Milky Way and chemical evolution models are needed to decipher and validate them.

The IMF is a probability distribution function that provides a convenient way to parametrize the relative number of stars as a function of their mass. From the definition, the IMF can be estimated by counting stars within a limited volume as a function of mass. But low mass stars are more numerous than high mass stars, thus requiring large volumes to construct samples with significant samples of high mass stars. Moreover, massive stars have shorter lifetimes than lower mass stars and thus the present day mass function (PDMF), constructed by counting the stars in a population spanning a large range of ages, need to be corrected for the loss of the previous generations of high mass stars. Finally, stellar multiplicity, in the form of undetected binary stars, need to be taken into account (Bastian et al., 2010).

Salpeter (1955) introduced a one-slope power law form for the IMF :

$$\psi(m) = A\,m^{-(1+x)} \tag{1.9}$$

where x = 1.35 and A is the normalization constant, with the IMF normalized as :

$$\int_0^\infty m\psi(m)\,dm = 1 \tag{1.10}$$

Chabrier (2003) found the IMF to depend weakly on the environment and present a general formula that follows a power-law form for m > 1 $M_\odot$, and a lognormal form below 1 $M_\odot$,

$$\psi_c(m) = A_c exp^{-\frac{(-logm-logm_c)^2}{2\sigma^2}} \text{ if } m < 1\mathrm{M}_\odot \tag{1.11}$$

$$\psi_c(m) = B_c m^{-1.3} \text{ if } m > 1\mathrm{M}_\odot \tag{1.12}$$

Here logm_c denote the mean mass and σ^2 the variance in logm.

Kroupa (2001) introduced a three-slope function for the IMF determined based on the study of stelllar clusters :

$$\psi(m) = Am^{-2.3} \text{ for } 0.5M\odot \leq m \leq 120M\odot \tag{1.13}$$

$$\psi(m) = Bm^{-1.3} \text{ for } 0.08M\odot \leq m \leq 0.5M\odot \tag{1.14}$$

$$\psi(m) = Cm^{-0.3} \text{ for } 0.01M\odot \leq m \leq 0.08M\odot, \tag{1.15}$$

where A, B, and C are scaling factors. The Kroupa IMF has been used to determine the SFR in the CMZ as described in the Chapter 4.

1.3 The inner Milky Way

The inner Milky Way, in this thesis, refer to the inner 200 pc region across the Galactic major axis (Galactic mid plane or longitude) and 400-500 pc around the Galactic center along the Galactic minor axis (Galactic latitude). This region is characterized by the presence of very high stellar density of stars and star forming molecular clouds that are largely extincted in the optical wavelength regimes by the huge amount of dust. This region hosts the supermassive black hole (SMBH), Sgr A*, the so called nuclear bulge encompassing the nuclear star cluster (NSC), nuclear stellar and molecular discs, as well as the unusually dense molecular cloud complex, also known as the central molecular zone (CMZ) (Launhardt et al., 2002). Figure 1.6 shows the nuclear bulge region of the Milky Way using the RBG color composite image made combining the *Herschel* 250 μm (FIR), *Spitzer* IRAC 8 μm (MIR) and *Spitzer* IRAC 3.6 μm (NIR) maps each of which traces the cold dust emission, warm dust + UV excited polycyclic aromatic hydrocarbon (PAH) emission and the stellar emission respectively. Major molecular clouds and stellar cluster features in the CMZ are also shown in the figure.

The initial identification of the Galactic center was through radio observations that uncovered the Sgr A (Piddington and Minnett, 1951), and later confirmed by the discovery of the unresolved source Sgr A* or the SMBH of the Milky Way at (l,b) = (-0.056°, -0.046°) (Balick and Brown, 1974; Reid and Brunthaler, 2004). The mass of the SMBH was estimated to be 4.2±0.2 × 10^6 $\mathrm{M}_\odot$ compiled from various studies (Bland-Hawthorn and Gerhard 2016 and references therein).

Astrometric and spectroscopic studies using high angular resolution infrared observations aided by adaptive optics have enabled the identification as well as kinematic characterisation of the highly dense population of stars orbiting the SMBH. These stars include a complex population of young hot, early type stars, Wolf-Rayet stars, older and lower mass giants as well as O and B-type main sequence, giants and super giants within the central parsec that

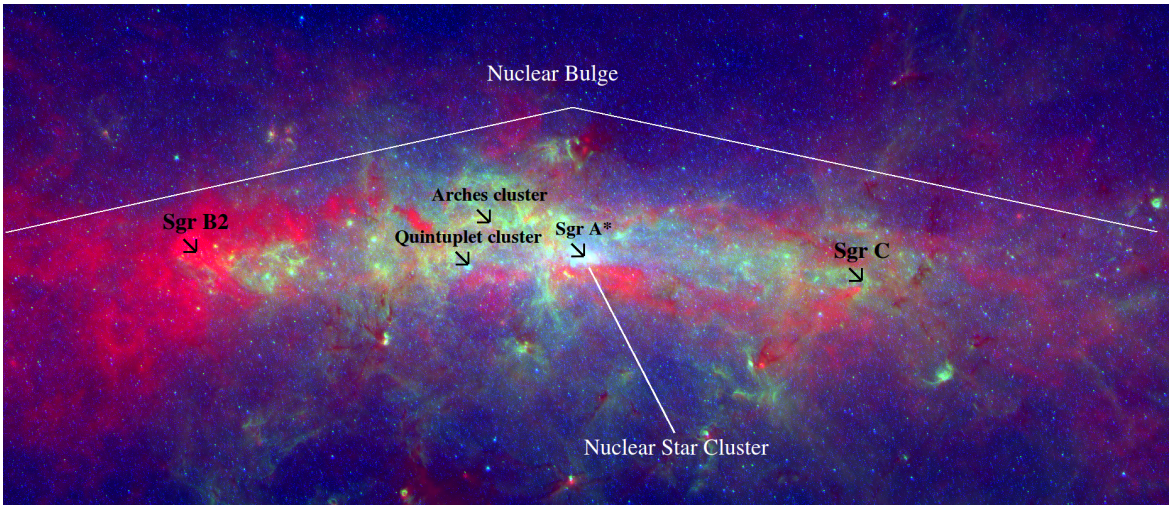

Figure 1.6: The RGB map of the inner Milky Way with red diffuse emission showing the cool dust emission as traced by *Herschel* 250 μm (FIR), green extended emission representing the warm dust+ PAH emission as traced by *Spitzer* IRAC 8 μm (MIR) and blue point source emission tracing the stellar emission from *Spitzer* IRAC 3.6 μm (NIR) maps. Sgr A* is the location of the supermassive black hole (SMBH) of the Milky Way. The bright emission seen very close around Sgr A* represent the nuclear star cluster (NSC), a cluster of young massive stars. Other well studied molecular clouds as well as clusters are also indicated in the map that are all concentrated in the Galactic mid plane. The whole region shown in the map is the so called Nuclear Bulge (Launhardt et al., 2002). The central molecular zone (CMZ) includes these features and is a bit more extended in longitude. The region in the map is ~2° (275 pc) in longitude and ~1° (140 pc) in latitude.

belong to the NSC which was discovered by Becklin and Neugebauer (1968). Schödel et al. (2014) found the NSC (earlier assumed spherically symmetric) to be elliptical and flattened with a half light radius of 4.2 ± 0.4 pc, luminosity at 4.5 μm of 4.1±0.4 × 10^7 $L_\odot$ and mass of 2.5±0.4 × 10^7 $M_\odot$. Feldmeier et al. (2014) extracted the kinematics of individual stars as well as from integrated light in near infrared spectrum and found the kinematic axis to be misaligned with respect to the photometric axis. Feldmeier-Krause et al. (2015) observed the central >4 pc^2 of the Galactic centre and found that early-type stars (>100 of them) are centrally concentrated favouring the *in situ* formation of early-type stars. Støstad et al. (2015) mapped a smaller area within 0.28-0.92 pc from SgrA* and found a break in the distribution of young stars at 0.52 pc. These authors concluded that this break possibly indicated an outer edge to the young stellar cluster in the Galactic centre, which is expected in the case of *in situ* star formation.

In addition to the NSC, most of the stellar mass of the nuclear bulge is constrained in the nuclear stellar disc (NSD), dominating the stellar mass distribution between ~30 pc and ~230 pc with estimated mass of ~1.4±0.6×10^9 $M_\odot$ (Launhardt et al., 2002). From their detailed multi wavelength study using the photometric data covering the NIR to radio wavelength range (IRAS, COBE, IRAM), Launhardt et al. (2002) also established the presence of a nuclear molecular disc (NMD) composed of an inner (<120 pc) warm disk and outer cold torus of dust and gas.

Above mentioned molecular gas clouds, stellar clusters and disc structures are all encompassed within the innermost few hundred pc radius region, i.e., the CMZ. It is a giant molecular cloud complex with an asymmetric distribution of molecular clouds (see e.g. Morris and Serabyn 1996; Martin et al. 2004; Oka et al. 2005). It has also been evident from observations that roughly the distribution of molecular gas as well as their kinematics are strongly assymetrical with roughly three quarters of molecular emission coming from positive longitudes. The prominent features detected at 24 μm using the MIPS map in the central 2.5° × 2° region are shown in the Figure 1.7. This prodigious reservoir of molecular gas is in an active region of star formation, where there is evidence of starburst activity during the last 100,000 years (Yusef-Zadeh et al., 2009). The gas pressure and temperature are higher in the CMZ than in the Galactic disc; these conditions favour a larger Jeans mass for star formation and an initial mass function (IMF) biased towards more massive stars (see Serabyn and Morris 1996; Fatuzzo and Melia 2009). In addition, the tidal force from the SMBH, shocks from the rotating inner spiral arms etc must regulate/feed the star formation in this region. Amidst these unique conditions, the exact star formation rate in the CMZ poses an intriguing question, which will be discussed in detail in the Chapter 4.

While severe extinction and reddening prevents large scale observations in the inner Milky Way especially across the Galactic mid plane, there are similar observational limitations upto a certain height above and below the Galactic plane. This has hindered our understanding of the characteristics of the stellar populations in the inner bulge, which is the region that lies within ~400-500 pc around the Galactic center or within $|b| \sim 3°$. Figure 1.8 shows the A_{Ks} extinction map estimated using extinction coefficients from Nishiyama et al. (2009) calculated with the methods described in Gonzalez et al. (2012). The bulge outline from the COBE/DIRBE estimate (Weiland et al., 1994) is also shown. In section 1.1.3, I

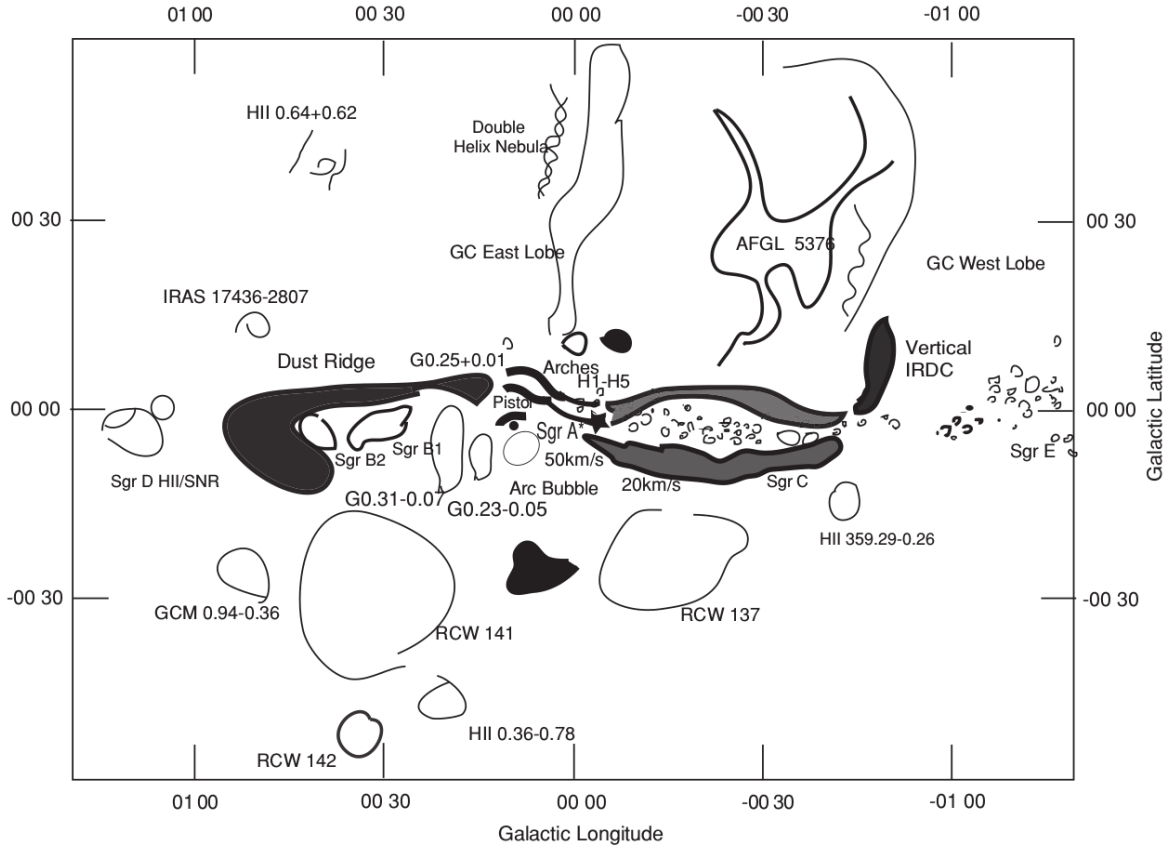

Figure 1.7: A schematic diagram of prominent features detected at 24 μm (MIPS) from the central 2.5° × 2°. Image courtesy : Yusef-Zadeh et al. (2009)

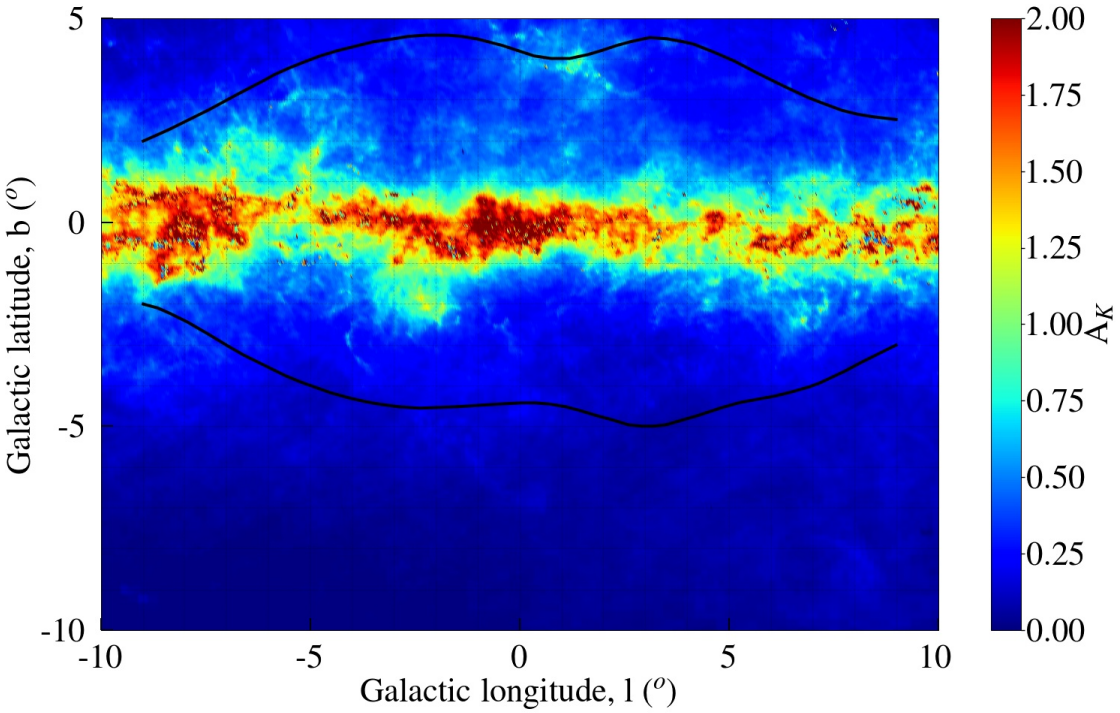

Figure 1.8: The mean extinction map, calculated from Gonzalez et al. (2012) using extinction coefficients from Nishiyama et al. (2009), is overlaid on the figure to show the level of obscuration in our observed fields. The bulge outline is the COBE/DIRBE bulge envelope (Weiland et al., 1994).

mentioned several large scale surveys that explore the morphology, chemistry and kinematics of stellar populations in the outer bulge (|b|>3°). Meanwhile chemical characterisation of inner bulge regions mainly rely on small scale spectroscopic surveys covering only a handful of sources. A detailed review of previous studies in the inner bulge region is carried out in the Chapter 3.

1.4 Goals of this thesis

This thesis involves the use of data from the currently available spectroscopic surveys as well as observations with low and high resolution spectroscopic instruments to explore the metallicity trends in the solar neighbourhood and derive chemical abundance relations using late type stars as well as estimate SFR in the Galactic center region. Our understanding of the present day SFR is an important input parameter in chemical evolution models. The derived chemical abundances of stellar populations also are crucial to understand the Galaxy formation scenario and to reconstruct the SFH by comparing the observed abundance relations with the outputs of chemical evolution models. Thus chemical evolution models link the SFR and chemical abundances both as means to develop such models as well as to validate and improve them. In this thesis, I attempt

- to understand the selection function effect in the metallicity trends using Galactic archaeology surveys, focusing on the solar neighbourhood.
- to derive accurate chemical abundances for late type stars in the inner bulge region from their high resolution spectra, explore the North-South symmetry in MDF as well as determine the abundance relations that can be used to confront the chemical evolution models with.
- to carry out spectroscopic identification of young stellar objects (YSOs) in the CMZ, and estimate the present day SFR in the CMZ, which can be used as input parameter in the chemical evolution models to explore CMZ's evolutionary history.

Thus this thesis aims to contribute to the Galactic archaeological endeavor by making use of available data and observing facilities, especially in the comparatively unexplored Galactic center region.

1.5 Published works

The works presented in this thesis have been published in peer reviewed journals. There are three first author papers that have come out of this thesis, in the broad context of Galactic archaeology, focusing on large scale spectroscopic surveys and small scale spectroscopic observations towards the inner Milky Way. I have also contributed to few other related published research works. All of them are listed below.

First author papers from the thesis

- **Nandakumar, G.**; Schultheis, M.; Hayden, M.; Rojas-Arriagada, A.; Kordopatis, G.; Haywood, M. (2017) **A&A 606, A97** *Effects of the selection function on metallicity trends in spectroscopic surveys of the Milky Way*. Presented in Chapter 2. This paper was chosen as A&A highlight.

- **Nandakumar, G.**; Schultheis, M.; Feldmeier-Krause, A.; SchÃ¶del, R.; Neumayer, N.; Matteucci, F.; Ryde, N.; Rojas-Arriagada, A.; Tej, A. (2018) **A&A 609, A109** *Near-infrared spectroscopic observations of massive young stellar object candidates in the central molecular zone*. Presented in Chapter 4

- **Nandakumar, G.**; Ryde, N.; Schultheis, M.; Thorsbro, B.; JÃ¶nsson, H.; Barklem, P. S.; Rich, R. M.; Fragkoudi, F. (2018) **MNRAS.tmp.1201N** *Chemical Characterization of the Inner Galactic bulge: North-South Symmetry*

Other first author papers unrelated to the thesis

- **Nandakumar, G.**; Veena, V. S.; Vig, S.; Tej, A.; Ghosh, S. K.; Ojha, D. K. (2016) *Star-forming Activity in the H II Regions Associated with the IRAS 17160-3707 Complex*

Other contributions

- Schultheis, M.; Ryde, N.; **Nandakumar, G.** (2016) **A&A 590, A6** *Temperatures and metallicities of M giants in the Galactic bulge from low-resolution K-band spectra*

- Schultheis, M.; Rojas-Arriagada, A.; GarcÃa PÃ©rez, A. E.; JÃ¶nsson, H.; Hayden, M.; **Nandakumar, G.**; Cunha, K.; Allende Prieto, C.; Holtzman, J. A.; Beers, T. C.; Bizyaev, D.; Brinkmann, J.; Carrera, R.; Cohen, R. E.; Geisler, D.; Hearty, F. R.; Fernandez-Tricado, J. G.; Maraston, C.; Minnitti, D.; Nitschelm, C.; Roman-Lopes, A.; Schneider, D. P.; Tang, B.; Villanova, S.; Zasowski, G.; Majewski, S. R. (2017) **A&A 600, A14** *Baade's window and APOGEE. Metallicities, ages, and chemical abundances*

CHAPTER 2

Selection function effects on metallicity trends

Contents

In this chapter, I investigate the effect of the selection function on the metallicity distribution function (MDF) and on the vertical metallicity gradient by studying similar lines of sight using four different spectroscopic surveys (APOGEE, LAMOST, RAVE, and Gaia-ESO), which have different targeting strategies and therefore different selection functions. I use common fields between the spectroscopic surveys of APOGEE, LAMOST, RAVE (ALR) and APOGEE, RAVE, Gaia-ESO (AGR) and use two stellar population synthesis models, GALAXIA and TRILEGAL, to create mock fields for each survey. I apply the selection function in the form of colour and magnitude cuts of the respective survey to the mock fields to replicate the observed source sample. I make a basic comparison between the models to check which best reproduces the observed sample distribution. I carry out a quantitative comparison between the synthetic MDF from the mock catalogues using both models to understand the effect of the selection function on the MDF and on the vertical metallicity gradient.

2.1 Selection function

During the last decade, the number of low, medium, and high resolution spectroscopic surveys of stellar populations in our Galaxy have increased drastically (Wyse, 2016). As mentioned in Section 1.2.2, there are several multi-object spectroscopic surveys that have been completed or are underway. They differ in spectral resolution, wavelength coverage, and in their selected targets (giant stars, dwarf stars, clusters, etc.) based on their science goals. These unique target selection schemes can lead to biases in which stellar populations are observed, and affect measurements of the observed properties of the Milky Way; these targeting biases are known as the selection function. The selection function is defined as the fraction of objects in a certain colour and magnitude range successfully observed spectroscopically compared to the underlying stellar populations, and determines how representative the observed sample is compared to the full existing stellar population of the Milky Way.

Each spectroscopic survey targets and observes a limited number of stars belonging to certain populations based on the colour and magnitude limits imposed during target selection. Moreover, the location of the telescope decide the part of the sky being covered for observation. In addition, the field of view of the instrument and the plate design limits the field size. Taking all this into account and according to the definition in the previous paragraph, the selection function of a spectroscopic survey can be formulated as follows (Bovy et al., 2012; Wojno et al., 2017) :

$$S \; \alpha \; S_{select}(l, b, magnitude, colour) \tag{2.1}$$

$$S_{select}(l, b, magnitude, colour) = \frac{N_{Survey}(l, b, magnitude, colour)}{N_{input}(l, b, magnitude, colour)} \tag{2.2}$$

where N_{Survey} is the number of observed stars with valid spectroscopic parameters observed in a field centered on (l,b) limited in magnitude and colour by the target selection criterion in the respective colour magnitude diagram. N_{input} is the total number of stars from the input photometric catalog in the same field and within the colour and magnitude cuts, representing the total number of targets available for target selection and observation.

The target selection schemes limit the coverage of parameter space of $T_{\rm eff}$, log g, and $[\mathrm{Fe/H}]$ that could potentially lead to biases while carrying out analysis that measure the gradients and metallicity distributions of certain stellar populations. Cheng et al. (2012) and Schlesinger et al. (2012) used different weighting schemes to correct for the metallicity bias introduced by the target selection in their sample of SEGUE main-sequence turn-off stars, and G and K dwarf stars, respectively. Meanwhile, Bovy et al. (2012) determined a plate-dependent selection function for a G-dwarf sample along ~150 lines of sight in SEGUE using the dereddened colour-magnitude boxes. The selection effects in the APOGEE red clump (RC) sample is discussed in Bovy et al. (2014) and Nidever et al. (2014) using the much simpler and well-defined target selection algorithm of APOGEE (Zasowski et al., 2013). Sharma et al. (2014) constrained the kinematic parameters of the Milky Way disc using stars from RAVE and the Geneva–Copenhagen Survey (GCS; Nordström et al. 2004) using kinematic analytic models. The RAVE selection function was taken into account while modelling using

GALAXIA (Sharma et al., 2011). On comparing the temperature and colour distributions of RAVE stars with that predicted using GALAXIA, they found a reasonably good match except for colours in J–K for stars at low Galactic latitudes. An extinction correction was performed to correct this. Wojno et al. (2017) described the RAVE selection function in detail and studied the selection function effect on the RAVE metallicity and velocity parameters. For this, they created a mock-RAVE catalogue using the GALAXIA stellar population synthesis model. They found that RAVE stars do not show any selection effects in terms of kinematics and metallicities using the selection cuts in magnitude and colour of RAVE. Anders et al. (2016) created a mock sample of more than 600 solar-like oscillating red giant stars observed by both CoRoT and APOGEE based on their selection functions. They found some small systematic biases of $\pm 0.02\,\mathrm{dex}$ in the radial gradient, most notably in the age bin 2–4 Gyr. Recently, there have been many more attempts to provide a detailed description of the selection function for other major spectroscopic surveys showing the importance of the knowledge of the selection function (e.g. GES: Stonkutė et al. 2016; LAMOST: Yuan et al. 2015, Carlin et al. 2012).

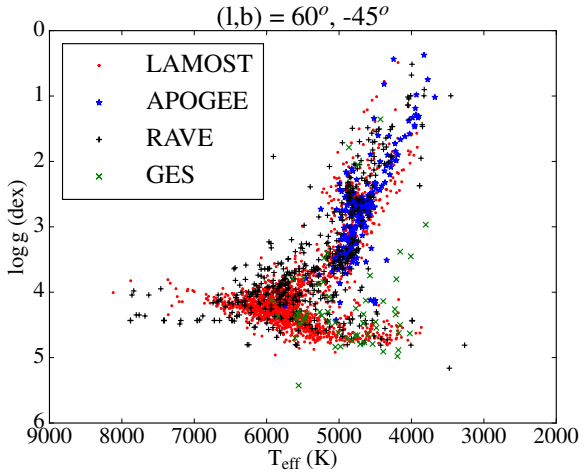

Figure 2.1: $T_{\rm eff}$ vs log g diagram of sources for the four surveys in the field located towards (l,b) ~ (60 °, -45 °).

For this study, I use four different spectroscopic surveys (APOGEE, LAMOST, RAVE, and Gaia-ESO), the selection function of each of which are described in detail below. In Figure 2.1, I show the Hertzsprung-Russell diagram for the sources in the field common to all four surveys located towards (l,b)~ 60°, -45°. This figure shows how different surveys observe different stellar populations located in the same part of the sky (the same field) depending on their target selection schemes and how the number of observed targets differ depending on their respective field sizes. The location of LAMOST and RAVE sources are mainly concentrated along the main-sequence and the turn-off stars, while APOGEE traces mainly giant stars and red clump stars. The lowest density comes from GES tracing mainly main-sequence stars.

APOGEE selection function

APOGEE has a well-defined input catalogue and colour selection scheme, as described in Zasowski et al. (2013). The 2MASS Point Source Catalog is used as the base catalogue, and the targets are chosen based on their H-band magnitude and a colour limit to the dereddened $(J\text{-}K_S)_0$ colour (Zasowski et al., 2013). The extinction corrections are derived using the Rayleigh Jeans Colour Excess (RJCE) method (Majewski et al., 2011), which calculates the reddening values combining the 2MASS photometry with mid-IR data (Spitzer-IRAC Galactic Legacy Infrared Mid-Plane Survey (Benjamin et al., 2003; Churchwell et al., 2009b) and Wide-field Infrared Survey Explorer (Wright et al., 2010)), as

$$A(K_S) = 0.918 \times (H - [4.5\mu] - (H - [4.5\mu]_0) \tag{2.3}$$

$$E(J - K_S) = 1.5 \times A(K_S) \tag{2.4}$$

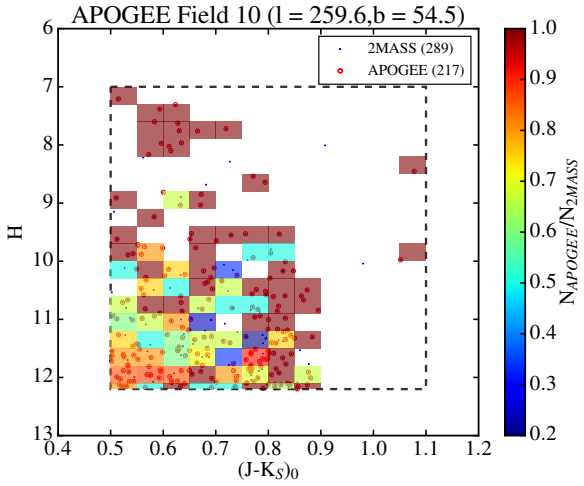

Figure 2.2: $(J\text{-}K_S)_0$ vs H showing the selection function for one of the fields located towards l~259.6 °, b~54.5 °. The bins are colour-scaled based on the N_{APOGEE}/N_{2MASS} with bin sizes of 0.05 mag in $(J\text{-}K_S)_0$ colour and 0.3 mag in H. The dashed box shows the overall colour and magnitude cuts used for APOGEE.

A colour cut at $(J\text{-}K_S)_0 \geq 0.5$ mag was used to include stars cool enough that the stellar parameters and abundances can be reliably derived by ASPCAP, and to lower the fraction of nearby dwarf star 'contaminants' in the sample. For the halo fields (|b|>16 °), the limit is extended to a bluer colour cut of 0.3 mag (Zasowski et al., 2013). In addition, for some dwarf-dominated halo fields, Washington+DDO51 photometry [1] was used to choose more giants stars than dwarfs. The bit 7 of the APOGEE_TARGET1 flag is set for sources that fulfil the Washington+DDO51 photometric giant star criteria (see Zasowski et al. 2013). The general H-magnitude limit is taken to be 7≤H≤13.8, though the upper limit varies depending on the field and the plate design.

[1] acquired with the Array Camera on the 1.3 m telescope of the U.S. Naval Observatory, Flagstaff Station

Using the input 2MASS sample and their respective A(K_S) values for our fields of interest, we estimated the fraction of the observed stars with respect to 2MASS stars in small rectangular bins in the CMD. Figure 2.2 shows a typical example where we see that the selection function shows variations along the CMD. For the full field the fraction of observed stars to the 2MASS sample is ~0.75. However, with the rectangular binning in the CMD, we see a lower fraction for fainter stars (H > 11) and for bluer stars (J-K_S)$_0$ < 0.7.

We use the DR13 catalogue which has 164 558 sources (Albareti et al., 2017). We select only main survey targets, removing calibration, telluric, and ancillary targets, for a total sample of 109 376 stars. APOGEE provides also 'calibrated' stellar parameters which were calibrated using a sample of well-studied field and cluster stars, including a large number of stars with asteroseismic stellar parameters from NASA's Kepler mission. Using calibrated parameters implies a limit in $\log g < 3.8$. Nearly 16% of the sample lacks calibrated surface gravities and nearly 4% of the sources have no calibrated effective temperature and metallicity values. For this reason, we chose the uncalibrated ASPCAP values of fundamental stellar parameters for this study.

GES selection function

The GES selection function is defined in Stonkutė et al. (2016) based on the VHS magnitudes. We obtained the VHS catalogue for our fields of interest from the ESO archive by searching using the field centre and a search radius of 0.2^o. We used the APERMAG4 magnitude in the VHS catalogue for the corresponding J, H, and K magnitudes as it gives the closest magnitudes to those provided in the GES catalogue.

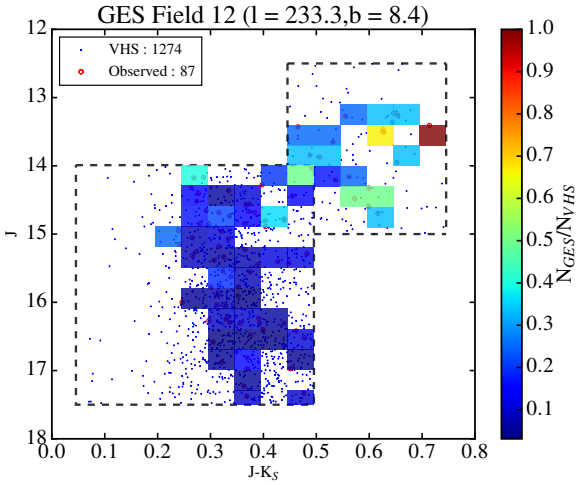

Figure 2.3: (J-K_S) vs J (CM diagram) showing the selection function for field 12 located approximately towards l~233.3 °, b~8.4 °. The bins are colour-scaled based on the N_{GES}/N_{VHS} with bin sizes of 0.05 mag in (J-K_S) colour and 0.3 mag in J. The dashed box shows the overall colour and magnitude cuts for red and blue boxes used for GES.

The target selection scheme of GES is built on stellar magnitudes and colours by defining two boxes, one blue and one red. The blue box is used for the selection of the turn-off and main-sequence targets, while the red box is for the red clump targets (Stonkutė et al., 2016). The colour and magnitude cuts for the blue and red boxes are given below:

- Blue box : 0.0 ≤ (J - K_S) ≤ 0.45 for 14.0 ≤ J ≤ 17.5
- Red box : 0.4 ≤ (J - K_S) ≤ 0.70 for 12.5 ≤ J ≤ 15.0

That said, the actual target selection scheme also takes into account the extinction by shifting the boxes by 0.5×E(B - V), where E(B - V) is taken as the median reddening in the field measured from the Schlegel et al. (1998) maps. Furthermore, additional targets were assigned by relaxing the red edge of the colour-cut if enough targets were not available within the colour cuts (e.g. high latitude Milky Way fields). Thus, the target selection scheme becomes

- Blue box: 0.5E(B - V) + [0.0 ≤ (J - K_S) ≤ 0.45] for 14.0 ≤ J ≤ 17.5
- Red box: 0.5E(B - V) + [0.4 ≤ (J - K_S) ≤ 0.70] for 12.5 ≤ J ≤ 15.0
- Extra box: 0.5E(B - V) + [0.0 ≤ (J - K_S) ≤ 0.45 + $\triangle_G$] for J≥ 14.0 and J + 3×((J - K_S) - 0.35) ≤ 17.5

where $\triangle_G$ is the right-edge extension of the extra box, and the values of $\triangle_G$ and E(B - V) are provided in Table 1 of Stonkutė et al. (2016) for the required fields. Figure 2.3 shows the selection scheme for field 12, which is a low latitude field with a higher stellar density, that leads to a lower selection fraction. In this field, we found no stellar parameters for about 15% of the GES sources. This fraction can increase to about 40% in other fields.

For this study, we chose the sources observed using GIRAFFE with two set-ups, HR10 (λ = 5339-5619 Å, R~19,800) and HR21 (λ = 8484-9001 Å, R~16,200). We used the homogenized set of parameters from the three nodes in DR4, which are available on the public ESO webpage [2], and were left with 29 591 sources.

RAVE selection function

For RAVE, the selection function is defined based on the I magnitude and (J-K_S) colour cut. The initial target selection is based on the apparent I-band magnitude, for 9<I<12, but the input sample is not obtained from a single catalogue. For the regions towards the Galactic disc and bulge (Galactic latitude $|b| < 25^\circ$), a colour criterion J-$K_S \geq 0.5$ is imposed to select cool giant stars (Kordopatis et al., 2013). The original input catalogue for earlier data releases of RAVE was constructed by deriving I magnitudes from the Tycho-2 catalogue (Høg et al., 2000), photographic I magnitudes from the SuperCOSMOS Sky Survey (Hambly et al., 2001), and later using the Gunn I-band photometry from the DENIS catalogue (Epchtein et al., 1997). The latest DR4 release includes observations drawn from a new input catalogue

[2] http://www.eso.org/gi/

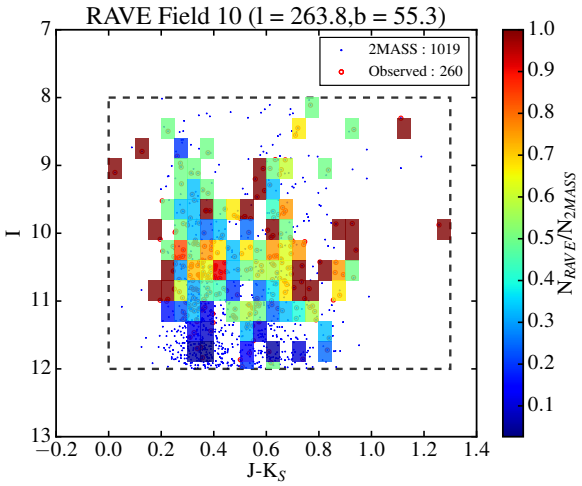

Figure 2.4: (J-K$_S$) vs I (CMD) showing the selection function for one of the fields located towards l~263.8 °, b~55.3 °. The bins are colour-scaled based on the N$_{RAVE}$/N$_{2MASS}$ with bin sizes of 0.05 mag in (J-K$_S$) colour and 0.3 mag in I. The dashed box shows the overall colour and magnitude cuts for RAVE.

based on DENIS DR3 (DENIS Consortium, 2005) cross-matched with the 2MASS point source catalogue. We adopted the same strategy as Wojno et al. (2017) by choosing 2MASS as the input catalogue, and calculated an approximate I$_{2MASS}$ magnitude via the following formula:

$$I_{2MASS} - J = (J - K_S) + 0.2 \times e^{\frac{(J-K_S)-1.2}{0.2}} + 0.12 \tag{2.5}$$

For our fields of interest, we searched for 2MASS sources using the approximate field centres (Tables 2.2 and 2.3) with a radius of 2.85°, and used the above-mentioned formula to calculate the I$_{2MASS}$ magnitude. We used the same approach as in the case of APOGEE to determine the selection function for each field, i.e. by defining selection bins in the CMD, (J-K$_S$) vs I$_{2MASS}$. We used sources with I$_{2MASS}$ between 8 and 12 magnitude as the I$_{2MASS}$ distribution for DR5 is shown to be broader than I$_{DENIS}$ (Wojno et al., 2017). Figure 2.4 shows the CMD for one such field located towards high galactic latitude. Here again, a clear drop in the selection fraction to about 0.1-0.2 is seen for the fainter magnitudes (I > 11).

We use the DR5 catalogue of RAVE, which has more than ~ 520 000 sources (Kunder et al., 2017). There are repeated observations (~15%) with the same RAVEID, DENIS_ID, and 2MASS_ID, but which differ in the stellar parameters. In these cases, we chose the sources with the highest S/N. For this study, we used the calibrated fundamental stellar parameters which are labelled with the suffix '_N_K' (e.g. TEFF_N_K, LOGG_N_K, etc.; Kunder et al. 2017).

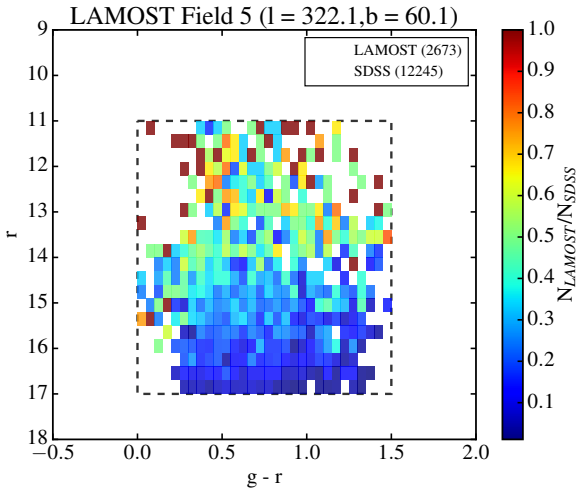

Figure 2.5: (g-r) vs r (CM diagram) showing the selection function for one of the fields located towards approximate l~322.1^o, b~60.1^o. The bins are colour-scaled based on the N_{LAMOST}/N_{SDSS} with bin sizes of 0.05 mag in (g - r) colour and 0.3 mag in r. The dashed box shows the overall colour and magnitude cuts used for LAMOST.

LAMOST selection function

Like RAVE, LAMOST does not make use of a single input catalogue and unlike the other three surveys, LAMOST uses *ugriz* photometry for their target selection. Catalogues such as UCAC4 (Zacharias et al., 2013) and Pan-STARRS 1 (Tonry et al., 2012) have been used to select targets for the observing plates in the main survey regions. To make sure that we use a homogeneous photometric input sample, we use only the SDSS photometry[3] in order to define the selection function. For the respective fields, we searched for SDSS sources within a radius of 2.5^o around the field centres. We use only those fields where we have the full SDSS footprint covered.

The targeting algorithm for LEGUE designed by Carlin et al. (2012) was not applied, due to the sparse stellar sampling. This results from the limited dynamic range of magnitudes observed on a single LAMOST plate and from the brighter r magnitude limit at the faint end compared to the designed goal (Liu et al., 2017). Finally, the target selection was carried out on a plate-by-plate basis with different plates covering 9 < r < 14, 14 < r < 16.8, r < 17.8, and r < 18.5.

Based on the distribution of LAMOST sources of each field in the g-r vs r CMD, we used the following colour and magnitude cuts : 0.0 < g-r < 1.5 and 11 < r < 17.8. We neglected the small fraction of very red (g-r>1.5) and blue (g-r<0.0) sources. Figure 2.5 shows a typical example for a field towards l = 322.1 °, b = 60.1 °. Statistically, LAMOST is more prominent than the other three surveys, and this is seen in the dramatic rise in the number of masks within the colour and magnitude range. The gradual decrease in the selection fraction towards fainter magnitudes is seen here as well.

[3]2MASS was more complete in each field, but the LAMOST sources are fainter than the reliable magnitude limits (~14.3) of 2MASS pass band magnitude.

We use the DR2 catalogue, which includes the calibrated stellar parameters for 2 207 803 sources estimated using the LAMOST Stellar Parameter Pipeline (LASP, Wu et al. 2011).

2.2 Comparison of stellar parameters

Despite the large amount of spectroscopic data available, few studies exist (e.g. Schultheis et al. 2017, Kunder et al. 2017, Lee et al. 2015, Chen et al. 2015, Kordopatis et al. 2013) comparing stellar parameters and chemical abundances of the same stars. Lee et al. (2015) studied common stars between APOGEE DR12 (Alam et al., 2015) and the LAMOST DR2 catalogue. They found that the LAMOST photometrically calibrated $T_{\rm eff}$ were consistent with the spectroscopic $T_{\rm eff}$ from APOGEE, but found systematic biases in log g and $[\rm Fe/H]$ for common stars in the APOGEE DR12 and LAMOST DR2 catalogues. Lee et al. (2015) applied the SEGUE Stellar Parameter Pipeline (SSPP : Allende Prieto et al. 2008; Lee et al. 2008a,b; Smolinski et al. 2011; Lee et al. 2011) to the spectra from LAMOST and compared the stellar parameters with the common stars in APOGEE (DR12), RAVE (DR4), and SEGUE. For the RAVE DR5 release a detailed comparison of the derived stellar parameters in RAVE with that of APOGEE, GES, and LAMOST for the common stars has been obtained as a part of the external RAVE DR5 verification (Kunder et al., 2017).

Table 2.1: Median offset and dispersion estimated for the comparison of fundamental stellar parameters in APOGEE - RAVE and APOGEE - LAMOST.

APOGEE - RAVE (907)		
	Median Offset	Dispersion
$T_{\rm eff}$ (K)	-109.4	229.2
Log g (dex)	0.02	0.60
$[\rm Fe/H]$ (dex)	0.10	0.16

APOGEE - LAMOST (11 203)		
	Median Offset	Dispersion
$T_{\rm eff}$ (K)	-42.3	170.4
Log g (dex)	-0.04	0.34
$[\rm Fe/H]$ (dex)	0.05	0.09

Recently, a data-driven approach known as *The Cannon* (Ness et al., 2015) has been introduced. *The Cannon* uses stellar spectra along with the derived stellar parameters from well-characterized stars (estimated with pipelines using synthetic model spectra) in higher resolution surveys as a training set to derive stellar parameters. This method was used to derive the stellar parameters for around 450 000 giant stars in LAMOST (low spectral resolution survey) by bringing them to the scale of APOGEE (high spectral resolution), showing that two very different spectroscopic surveys can be combined together (Ho et al., 2017).

But still there are limitations in this data-driven approach, as the accuracy of *the Cannon* depends on the chosen training set. In the cases of APOGEE and LAMOST, which target different populations – red giants stars for APOGEE vs dwarf stars for LAMOST – only a limited training set is available. *The Cannon* was also used to re-analyse the RAVE spectra and a new catalogue (RAVE-on) of stellar parameters and abundances was produced (Casey et al., 2017). The training set for red giant stars was made using common stars in APOGEE DR13 (Albareti et al., 2017), while the stars in common in K2/EPIC catalogue (Huber et al., 2016) made up the main-sequence and subgiant branch training set.

For our study, we need to make sure that systematic offsets between surveys are corrected. This is accomplished by comparing the derived stellar parameters for the common sources between the surveys. We have arbitrarily chosen the APOGEE data set as a reference frame due to its high spectral resolution and S/N. We used a cross-identification radius of 2" to identify the common sources of the three surveys with respect to APOGEE.

In this section, we investigate the systematic offsets seen in $T_{\rm eff}$, log g, and $[\mathrm{Fe/H}]$[4] between APOGEE and the other data sets, RAVE, GES, and LAMOST, respectively. We found only six sources in common between GES and APOGEE, making any comparison difficult. Therefore, we carried out the comparison only between APOGEE and RAVE and between APOGEE and LAMOST. Table 2.1 lists the median offsets and the standard deviation estimated for APOGEE - RAVE and APOGEE - LAMOST.

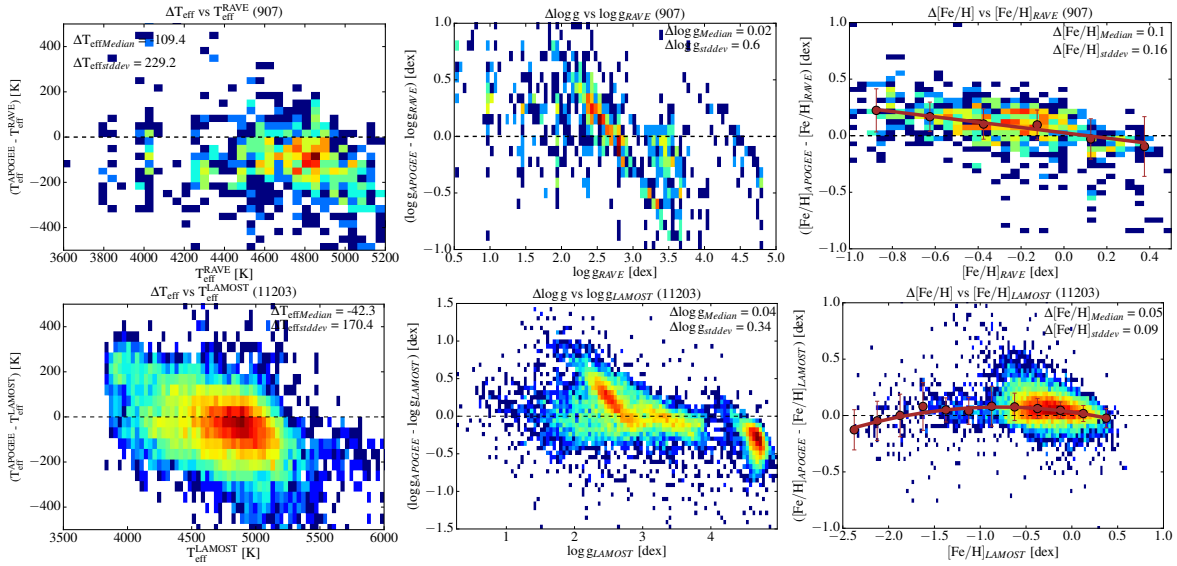

Figure 2.6: Comparison of common sources in APOGEE and RAVE (Top), and APOGEE and LAMOST (Bottom) for $T_{\rm eff}$ (left), log g (middle), and [Fe/H] (right). For the metallicities, the median of the difference in parameters and its dispersion is also shown as red circles with error bars in the plots. $[\mathrm{Fe/H}]$ here denote the global metallicity for APOGEE and RAVE (see footnote 4).

[4]APOGEE, RAVE, and GES use the $[\mathrm{M/H}]$ notation for the overall content of metallic elements, rather than $[\mathrm{Fe/H}]$. However, throughout this paper, we use $[\mathrm{Fe/H}]$ as the the global metallicity, i.e. $[\mathrm{Fe/H}] = [\mathrm{M/H}]$. For LAMOST, only $[\mathrm{Fe/H}]$ is provided in the catalogue.

APOGEE-RAVE

There are 907 sources in common between APOGEE and RAVE. Figure 2.6 (top panel) shows the comparison of the stellar parameters. We find that RAVE has systematically higher temperatures than APOGEE with a median difference of about 110 K. The log g values show a peculiar shape (Figure 2.6, top middle panel), which has been already noted by Kunder et al. (2017). They consider this behaviour to be the consequence of degeneracies in the Ca IR triplet region that affects the determination of log g (Kordopatis et al., 2011). Overall we see a large dispersion (0.6 dex) for log g between APOGEE and RAVE. In terms of the metallicity comparison, we note that APOGEE gives higher metallicities for metal-poor stars ($[\mathrm{Fe/H}]$ < -0.2 dex), while much lower metallicities for metal-rich stars ($[\mathrm{Fe/H}]$ > 0.2 dex) in comparison with RAVE. We have calculated the median offsets in bins of 0.25 dex in RAVE metallicities (indicated by the red points) and did a linear fit to them, as indicated by the red line.

APOGEE-LAMOST

LAMOST has 11 203 sources in common with APOGEE, which is statistically the highest number. The plots used for comparison are shown in the bottom panel of Figure 2.6. The median offset of T_{eff} between LAMOST and APOGEE is about 42 K with a dispersion of 170 K. A slight trend with T_{eff} is visible in the sense that for stars hotter than 5000 K LAMOST predicts higher temperatures. However, the APOGEE pipeline is more adapted to getting stellar parameters for cooler stars below 5000 K (Holtzman et al., 2015). The log g correlation shows distinct behaviour for the APOGEE values above and below ~ 4.0 dex. Below 4.0 dex we see in general good agreement except around log g ~ 2.5, the area where the red clump is dominant. The log g values above 4.0 dex are underestimated in APOGEE because of the lack of reliable calibrators for stars with high surface gravity values (Holtzman et al., 2015). This can be seen in the behaviour of difference in log g with log g_{LAMOST} for log g > 4.0 dex. Hence, we estimate the median offset and dispersion for log g_{APOGEE} < 4.0 dex. Overall, the median offset is negligible (~ -0.04 dex), but with a large dispersion (~0.34 dex). In the case of metallicity, the median offset between APOGEE and LAMOST for sources within -1 < $[\mathrm{Fe/H}]$ < 0.5 is 0.05 dex with a dispersion of 0.14 dex. Here again, we added correction terms for the metallicities by calculating the median offset in bins of 0.25 dex in metallicity and fitting a second-degree polynomial to them (red points and line).

2.3 ALR and AGR

We have chosen to select common fields distributed along similar lines of sight to study the effect of the selection function on the observed MDF and the vertical gradient. In total, there are only three common fields between the four surveys, which provide a relatively small sample size, and for this reason we have chosen to restrict ourselves to the common fields between three surveys at a time: APOGEE, LAMOST, and RAVE (hereafter ALR)

Table 2.2: Details of the ALR fields. The field numbers assigned by us, mean of field centres of each field for three surveys, along with the number of observed sources in each field are listed. The number of observed sources having their distances calculated (based on availability of derived $T_{\rm eff}$, log g, $[{\rm Fe/H}]$, and photometric magnitudes) are indicated in parentheses alongside the observed source numbers. There are overlapping fields for certain surveys, indicated by _1, _2, or _3.

Field	Mean(l °,b °)	N(APOGEE)	N(RAVE)	N(LAMOST)
5	(320.7, 59.4)	222 (222)	497 (495)	2844 (2677)
10_1	(262.6,55.2)	221 (221)	277 (277)	503 (475)
10_2	(259.1,55.4)	—	—	1306 (1175)
13_1	(58.7,-45.5)	228 (228)	566 (566)	719 (709)
13_2	(61.7,-46.5)	—	—	1185 (1160)
14	(312.4,59.1)	225 (225)	250 (248)	1208 (777)
15_1	(292.1,59.6)	221 (221)	362 (362)	994 (898)
15_2	(293.2,60.7)	—	—	990 (846)
20_1	(331.6,58.6)	227 (227)	306 (306)	2822 (2488)
20_2	(330.7,60.7)	—	—	3021 (2870)
25_1	(273,58.3)	252 (252)	282 (282)	2668 (2500)
25_2	(269.9,57.9)	263 (262)	—	385 (360)
25_3	(270.7,58.8)	260 (260)	—	1542 (1460)
32	(254,51.4)	225 (225)	300 (300)	1793 (1698)

and APOGEE, GES, and RAVE (AGR). We found eight common fields in the ALR case and ten in AGR. Tables 2.2 and 2.3 list the common fields in each survey of ALR and AGR, respectively, with the approximate mean field centres and number of sources in each field.

2.4 Distances

Distances for the sources in each survey are estimated by isochrone fitting as described in Rojas-Arriagada et al. (2017), which is similar to other methods in the literature (e.g. Zwitter et al. 2010) using the derived stellar parameters $T_{\rm eff}$, log g, $[{\rm M/H}]$ together with the J, H, K_S (for APOGEE, RAVE, and GES) or SDSS u,g,r,i photometry (for LAMOST). A set of PAdova and TRieste Stellar Evolution Code (PARSEC) isochrones with ages ranging from 1 to 13 Gyr in 1 Gyr step and metallicities from -2.2 dex to +0.5 dex in 0.1 dex step are chosen for this. PARSEC is the stellar evolutionary code used to compute sets of stellar evolutionary

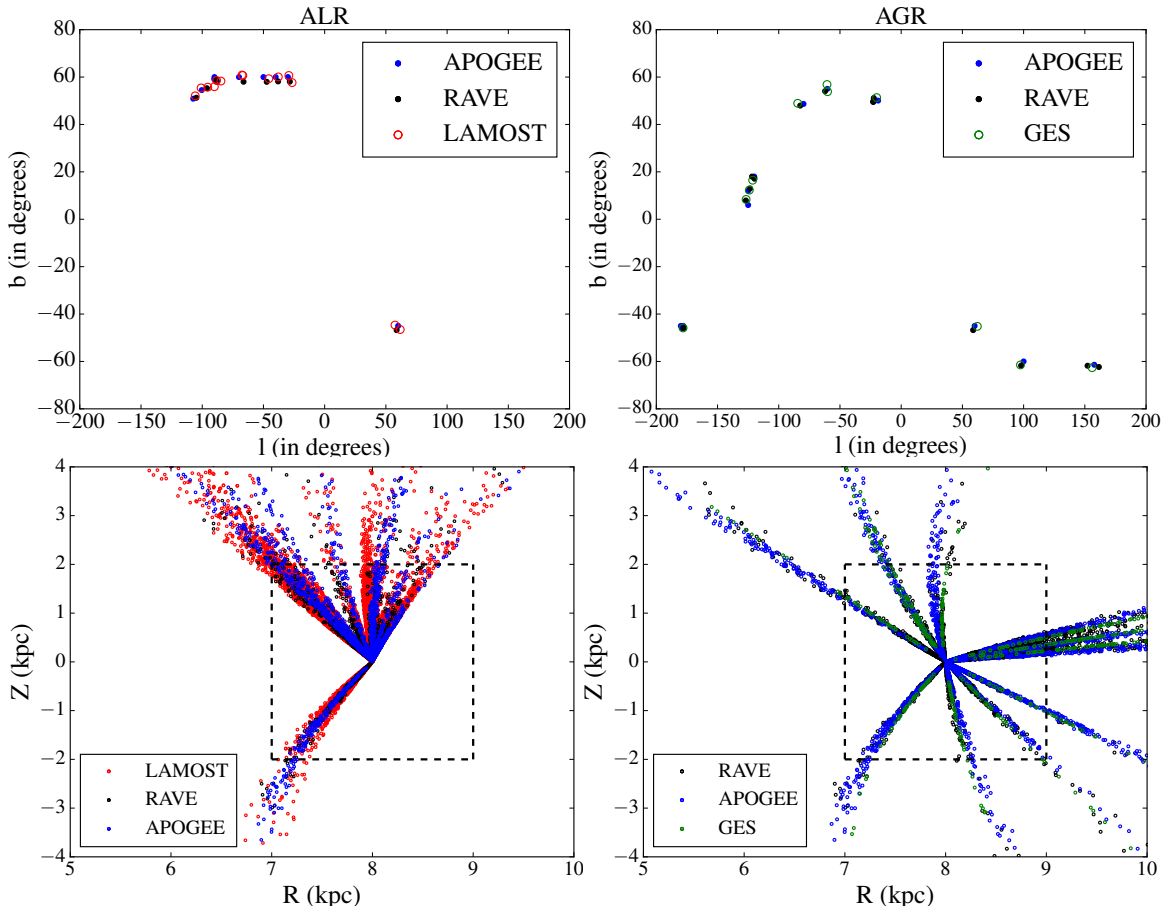

Figure 2.7: Distribution of the common fields in ALR and AGR shown in the Galactic plane (top); the R-Z distribution of the sources in those fields with the dashed box indicating the 7≤R≤9 kpc and |Z| ≤ 2 kpc range we chose to select the sources for our study (bottom).

Table 2.3: Details of the AGR fields. The columns are the same as in Table 2.2

Field	Mean(l °,b °)	N(APOGEE)	N(RAVE)	N(GES)
1_1	(339.6,50.8)	228 (228)	485 (485)	103 (54)
1_2	(337.1,49.7)	—	521 (521)	—
1_3	(337.2,49.5)	—	534 (534)	—
3	(182,-45.6)	222 (222)	155 (155)	91 (47)
4_1	(158.4,-62.1)	259 (259)	389 (389)	82 (45)
4_2	(152.2,-61.8)	—	233 (233)	—
5_1	(239.6,17.2)	230 (230)	614 (614)	104 (81)
5_2	(238.2,18)	—	479 (479)	—
8	(60.3,-45.7)	228 (228)	566 (566)	103 (59)
10	(277.7,48.5)	220 (220)	582 (582)	102 (51)
12	(233.8,7.4)	229 (229)	801 (801)	104 (87)
14	(235.9,12.4)	229 (229)	451 (451)	108 (88)
23	(98.4,-61.1)	279 (279)	320 (320)	86 (47)
31_1	(299.1,54.3)	231 (231)	348 (348)	108 (60)
31_2	(299.4,56.9)	—	—	96 (54)

tracks for stars of different intial masses, evolutionary phases, and metallicities. Isochrones in several photometric systems are derived from these tracks (Bressan et al., 2012). The distance of the observed star to the set of all model stars from the whole set of isochrones is calculated in the $T_{\rm eff}$-log g-$[{\rm Fe/H}]$ parameter space. This distance is weighted to account for the evolutionary speed and non-uniformity of model stars along the isochrone tracks. Using these weights, the most likely values of absolute magnitudes of the star in each band is calculated as the weighted mean or median of the model stars' absolute magnitudes. We also compute the line-of-sight reddening from the observed and theoretical colours. Finally, we compute the distance modulus and the line-of-sight distance in each passband from the absolute magnitudes and the estimated reddening (Rojas-Arriagada et al., 2017). We use the average value of the distances from different passbands as the final line-of-sight distance of each source. Using the same approach to calculate the distances for each of the four surveys makes sure that no biases are introduced. The typical uncertainty of the distances is in the order of $\sim 20\%$. The Galactocentric distance R (kpc) and the vertical height Z (kpc) from

the Galactic mid-plane for the sources are calculated by assuming the Sun to be located at R~8.0 kpc. The distribution of the fields in the Galactic plane and that of the sources in the R-Z plane are shown in Figure 2.7. We see from the R-Z distribution in the bottom panel of Figure 2.7 that there is a wide range of Z allowing us to determine the vertical gradient (see Section 2.7), while the range in the radial gradient is limited. Even though the range in R is broader in AGR than that in ALR, to be consistent between the two cases and to minimize the impact of any radial gradient on the vertical gradient, we restrict the samples in R from 7 to 9 kpc and |Z| from 0 to 2 kpc for our study (see the dashed box in the bottom panel of Figure 2.7).

2.5 MOCK fields using SPS models

As mentioned in the Chapter 1, stellar population synthesis models make use of Galaxy formation and evolution scenarios along with some physical assumptions to generate a picture of the Milky Way in different photometric systems. Their prime objective is to compare and interpret different observational data currently available and also to test the theories on which the models are based. I also introduced in the Chapter 1 GALAXIA (Sharma et al., 2011) and TRILEGAL (Girardi et al., 2005), the two most commonly used population synthesis models differing in their assumed component parameters, density laws, star formation history, stellar libraries, and other dynamical constraints. We chose them to create the respective mock fields for each survey with the aim of understanding the selection function effect in the MDFs and to attempt a basic comparison of the models. We chose two stellar population synthesis models with different input physics to test the robustness of our analysis. We generate the mock catalogues along each line of sight using the field centre and the field radius of the respective surveys for each of the model. The 2MASS+SDSS photometric system was used for both the models.

2.5.1 Applying uncertainties and related checks on the models

Both GALAXIA and TRILEGAL predict the stellar parameters and photometric magnitudes for each star at a given line of sight. Each of the four surveys has intrinsic errors in the measured stellar parameters and observed photometric magnitudes, which should be simulated accordingly in the model in order to make it more realistic. Since we use only the metallicity values from the models to compare the MDFs and vertical gradients, we do this only for the metallicity among the stellar parameters in the model. In order to simulate the metallicity errors, we have fitted a fourth-degree polynomial in the $\sigma_{[\mathrm{Fe/H}]}$ vs $[\mathrm{Fe/H}]$ plane for LAMOST, and GES and a third-degree polynomial for APOGEE. For RAVE, we used the same metallicity error description as described in Kordopatis et al. (2013). We apply a Gaussian filter to the metallicities of the mock catalogues.

$$\sigma_{[Fe/H]_{APOGEE}} = 0.023 - 0.015[Fe/H] - 0.001[Fe/H]^2 - 0.005[Fe/H]^3 \tag{2.6}$$

$$\sigma_{[Fe/H]_{GES}} = 0.072 + 0.047[Fe/H] + 0.150[Fe/H]^2 + 0.034[Fe/H]^3 - 0.004[Fe/H]^4 \quad (2.7)$$

$$\sigma_{[Fe/H]_{LAMOST}} = 0.164 - 0.122[Fe/H] + 0.048[Fe/H]^2 + 0.013[Fe/H]^3 - 0.004[Fe/H]^4 \quad (2.8)$$

Similarly we need to apply uncertainties to the photometric 2MASS or SDSS magnitudes provided by each model. We used an exponential function for 2MASS and a third-degree polynomial for SDSS to define the relation between the mag vs σ_{mag}, which we model as a Gaussian for each model source, as mentioned earlier.

$$\sigma_J = 0.019 + e^{0.537J - 10.530} \quad (2.9)$$

$$\sigma_H = 0.025 + e^{0.612H - 10.736} \quad (2.10)$$

$$\sigma_K = 0.028 + e^{0.728K - 11.963} \quad (2.11)$$

$$\sigma_g = 9.079 - 2.287g + 0.213g^2 - 0.009g^3 \quad (2.12)$$

$$\sigma_r = 14.273 - 3.502r + 0.319r^2 - 0.013r^3 \quad (2.13)$$

In addition, we have simulated errors in the distance distribution in the model to verify the percentage of souces lost or gained, due to our limiting R-Z cut. The typical errors in the spectro-photometric distances are in the order of 20% (see Hayden et al. 2015, Schultheis et al. 2015). We carried out ten trials, each time introducing a 20% error in distance calculated by the models to check whether this drastically affects the number of sources at the boundaries of the R-Z range that are thrown out or that come in. We have found that a 20% error in the distances would affect less than 5% of stars in the selected R-Z ranges. This is a relatively small change in the sample size, but to make the mock sample realistic, we kept the 20% distance uncertainty in the models.

2.5.2 Comparison between GALAXIA and TRILEGAL

In Section 2.1, we show the CMDs for each survey with their respective colour and magnitude cuts that were used to select the target sample. We carry out the same exercise for the mock fields generated using the models. The masks (in the form of small rectangular boxes within the selection box) are used to denote the bins in colour and magnitude where the sources are observed. Figure 2.8 shows an example of our method for the APOGEE field located towards l~259.6^o and b~54.5^o for both GALAXIA and TRILEGAL. The masks are colour-coded with the fractional percentage of model sources compared to the input photometric sample (2MASS or SDSS). We find that TRILEGAL predicts more sources at the faint end

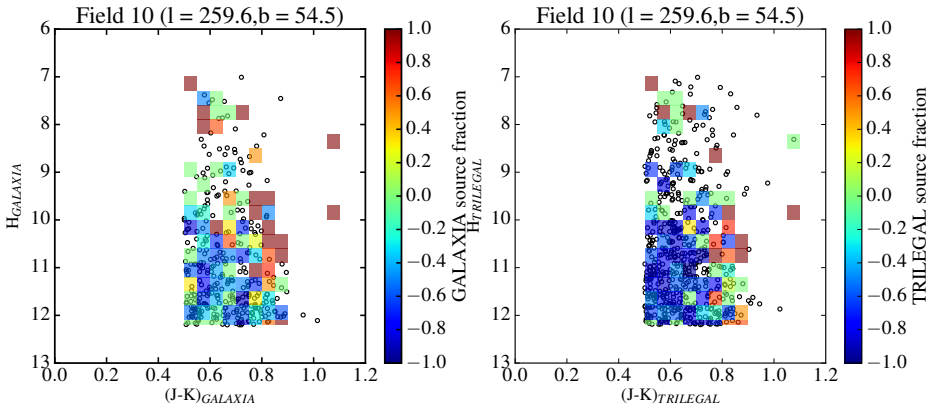

Figure 2.8: CMD diagrams for the APOGEE field located towards l,b~59.6^o, 54.5^o with GALAXIA and TRILEGAL source distribution shown in the left and right panels, respectively. The open circles in each panel represent the respective model sources. The rectangular boxes are the masks where the real observed sources are, each colour-coded with the fraction (N_{2MASS} - N_{model})/N_{2MASS} if $N_{2MASS} > N_{model}$ or (N_{2MASS} - N_{model})/N_{model} if $N_{2MASS} < N_{model}$. The redder colours indicate that the 2MASS sources are in equal number or greater than the number of model sources, while bluer colours denote more model sources. From the colours of the bins, there are more TRILEGAL sources than GALAXIA sources towards the faint magnitudes.

than does GALAXIA. A very similar trend is seen for the simulated RAVE, LAMOST, and GES fields.

Using the masks in the CMD we force each model to have the same fraction ($N_{observed}/N_{photometricsample}$) as the real targeted and observed sample. To understand which model best replicates the observed MDF, we compare the mask and the observed sample MDFs combining all common fields for each survey in ALR and AGR, restricted in the R-Z range of $7 \leq R \leq 9$ kpc and $|Z| \leq 2$ kpc, as shown in Figures 2.9 and 2.10. Each model uses different stellar libraries and stellar evolutionary tracks, which could lead to systematic offsets in the abundance scale between the models and observations. However, as discussed in Sections 2.6 and 2.7, we investigate the selection effect within each model.

Except for APOGEE and GES, GALAXIA predicts a slightly higher number of sources, while TRILEGAL overestimates the star density for all four surveys. This difference in the number of predicted sources with respect to the observed sample could be explained by the different assumption in the density normalization of the two models. The fractional percentage of mask sources compared to the observed sources is listed in Table 2.4, where the differences between the two models can be clearly seen.

The MDFs are binned in 0.1 dex metallicity bins and then normalized by the total number of sources. The fit of the distributions are carried out using a Gaussian mixture model (GMM) (as in Rojas-Arriagada et al. 2017). A mixture model (M) is a weighted sum of a number of probability distribution functions, while the mixture in a GMM in 2D is defined by a sum of bivariate normal distributions. For a given data structure composed of certain underlying substructures/features, the parameters (μ, σ, etc.) that define the best mixture model with a given number of modes is determined using the expectation-maximization algorithm

Table 2.4: Fractional percentage of mask sources compared to the observed sources for GALAXIA and TRILEGAL in ALR and AGR.

ALR	APOGEE (%)	RAVE (%)	LAMOST (%)
GALAXIA	-20.16	+1.32	+10.06
TRILEGAL	+34.41	+68.72	+111.23
AGR	**APOGEE (%)**	**RAVE (%)**	**GES (%)**
GALAXIA	-15.62	+0.41	-39.07
TRILEGAL	+45.04	+65.74	+49.10

that maximizes the likelihood function of the mixture. Since we do not know a priori the exact number of components in the data, we use the Bayesian Information Criterion (BIC) as a cost function to assess the relative fitting quality between different proposed mixtures and determine the best solution (the one with the lowest BIC value) to the number of Gaussian components that constitutes the distribution.

In order to quantify the differences between the observed and the mask MDFs, we estimate and compare the quartile values for each distribution as in Wojno et al. (2017). The quartile values designated as Q1, Q2, Q3 represent the $25th$, $50th$ and $75th$ percentiles of the distribution, respectively, as indicated in each panel of Figures 2.9 and 2.10. We choose 0.1 dex (considered to be the general metallicity uncertainty) as the threshold for the difference between the respective quartiles of samples below which the distributions are considered to agree. We note the following results by comparing the mask and observed MDFs for each survey (see Figures 2.9 and 2.10) :

- Both models show a significant metal-poor tail in the mask MDF compared to the APOGEE MDF, which is more prominent in the case of GALAXIA but absent in the observations. This can be seen in the difference in Q1 quartile between GALAXIA and APOGEE distributions, exceeding the adopted threshold of 0.1 dex.
- For RAVE, TRILEGAL matches the observed distribution very well for both AGR and ALR. In GALAXIA the mask MDF is distributed as broadly as the RAVE MDF, though there are subtle differences in the source fraction throughout.
- For LAMOST, the observed MDF has a broad peak that is skewed towards subsolar metallicities, which both the models are unable to replicate. The difference in Q1 and Q2 quartiles exceed the 0.1 dex threshold between TRILEGAL and LAMOST distributions.
- The small sample size in the case of GES makes it hard to decipher the exact shape of the MDFs, especially for GALAXIA. The majority of the 0.1 dex bins in the GALAXIA MDF have fewer than 15 sources, except for the bins closer to the peak with more than

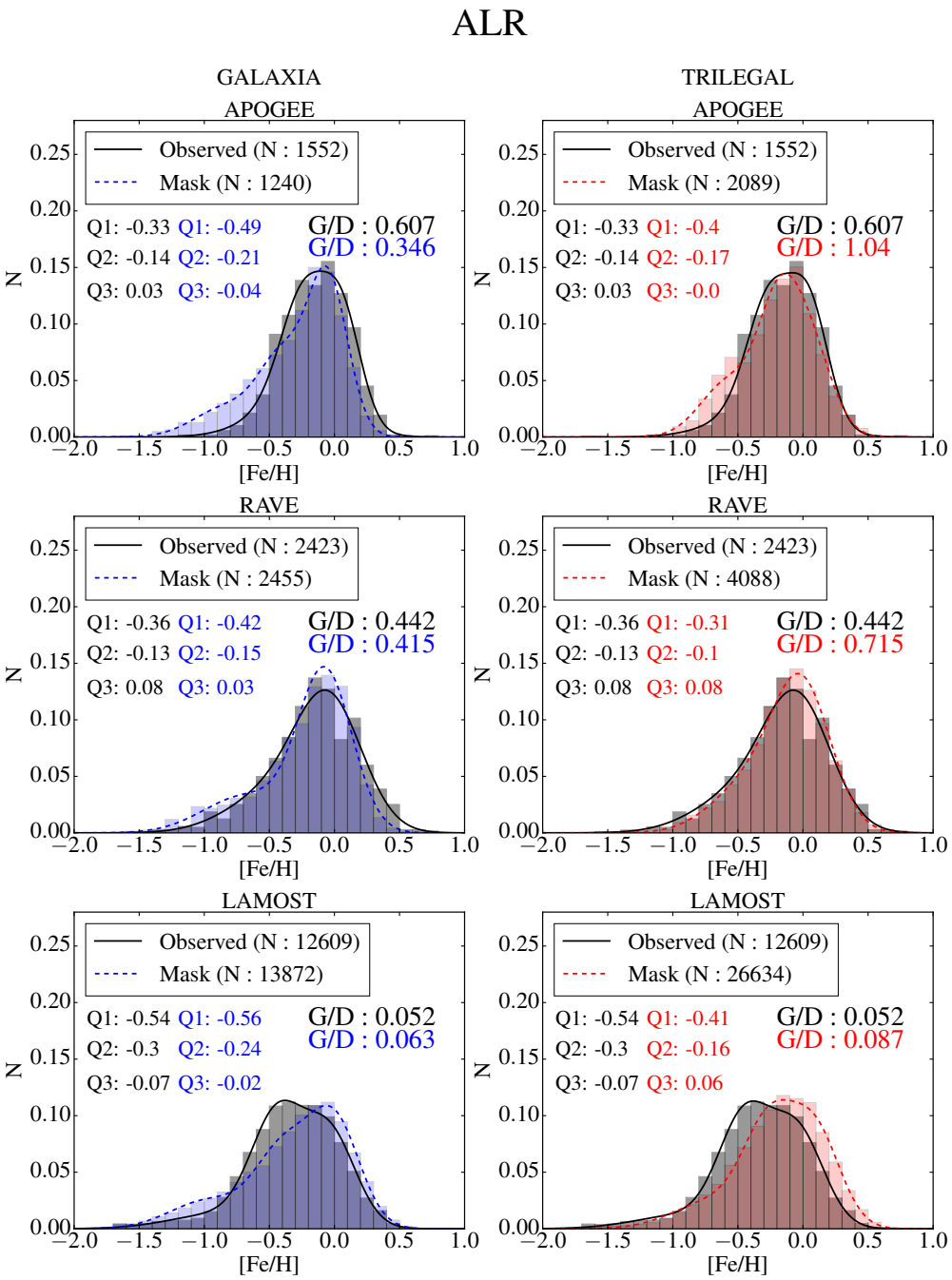

Figure 2.9: Mask and observed normalized MDF for ALR in the R-Z range of 7≤ R ≤ 9 kpc and 0≤ |Z| ≤ 2 kpc. The survey histograms are in black, while GALAXIA and TRILEGAL histograms are in blue and red, respectively. Histograms are normalized by dividing the counts in each 0.1 dex bin by the total number of sources. The distributions in black line represent the observed MDF, while those in blue and red lines represent the mask MDF for GALAXIA and TRILEGAL, respectively. APOGEE and RAVE distributions are shown in the top and middle rows, respectively, and the LAMOST in the bottom row. Quartile values for both distributions are given in each panel colour-coded according to the distribution. Indicated is also the giant-to-dwarf ratio for mask and observed samples of each survey for both models.

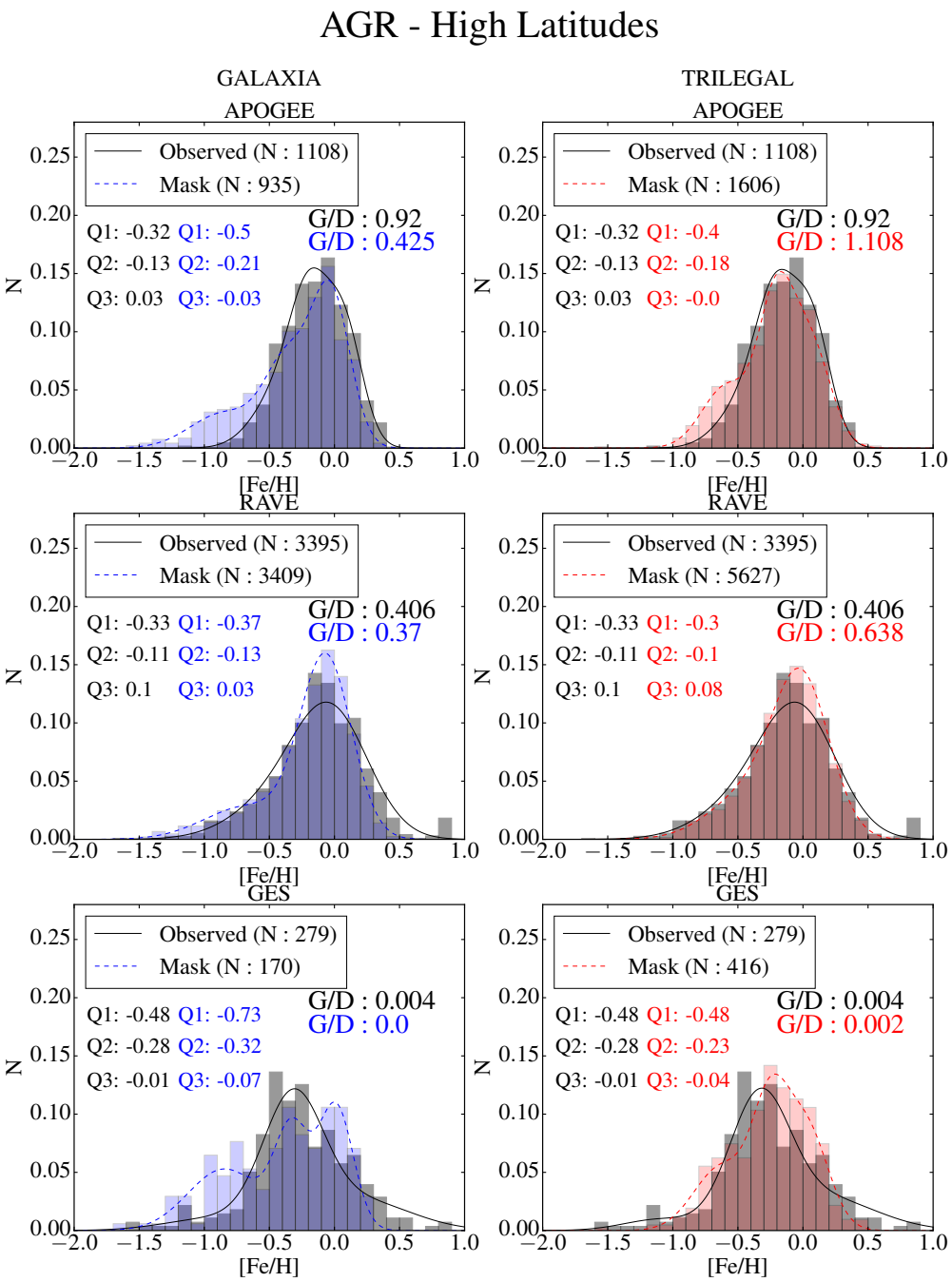

Figure 2.10: Same as in Figure 2.9 for AGR high latitude fields.

25 sources. Thus the normalized GALAXIA mask MDF is dominated by noise in the form of multiple peaks, which we are not able to properly fit using GMM. The TRILEGAL mask MDF has better statistics, resulting in significantly less noise in the distribution. This is also evident in the quartile analysis for GALAXIA, with the Q1 quartile difference between GALAXIA and GES distributions exceeding 0.1 dex, which is not the case with TRILEGAL.

We also estimated the giant-to-dwarf ratio in the model and observed samples in all cases. The giants and dwarfs are separated based on their log g value, i.e. dwarfs : log g>3.5 dex and giants : log g<3.5 dex. These ratios show how well each model is able to replicate the observed stellar population. Among the four surveys, the giant fraction is highest in APOGEE followed by RAVE, LAMOST, and GES. We find that both models are unable to represent the ratio we find in the observed sample for APOGEE as GALAXIA gives a lower value, while TRILEGAL overpredicts the ratio by a factor of ~2 in ALR. The prediction by TRILEGAL is close to the observed case for APOGEE in AGR, although still slightly overpredicted. For RAVE, we find the ratio in GALAXIA to be very close to that of the observed case, while TRILEGAL again gives comparatively higher values for both ALR and AGR. The giant-to-dwarf ratios predicted by both GALAXIA and TRILEGAL are quite similar for LAMOST and for GES, though the sample size is quite limited for the GES mask in GALAXIA.

Overall, neither model is able to reproduce both the MDF and the giant-to-dwarf ratio of the APOGEE sample. Both conditions are found to be very consistently satisfied by GALAXIA in the case of RAVE. Even though the shape of the MDFs are slightly different from the observed MDF, we find consistency in the MDF and giant-to-dwarf ratio between GALAXIA and TRILEGAL for LAMOST. In the case of GES, TRILEGAL reproduces the observed MDF better than GALAXIA, likely because of the lack of targets in the latter model.

2.6 Selection function effects on MDF

With the models described above, we are able to study the effect of the selection function on the MDF for the sample from the common fields of each survey in ALR and AGR. We categorize the sources in the mock fields by the limiting magnitude of the respective surveys and restricted in R-Z range as the parent population. This represents the underlying sample from which the selection function in the form of colour and magnitude cuts are applied to create a subset of mask sources. These mask sources in turn represent the observed sources. Thus by comparing the MDF of the underlying sample, hereafter called the magnitude limited sample, with that of the mask sample, we can assess the effect of the selection function, if any, on the underlying MDF for each survey. For ALR and AGR, we restrict both the magnitude limited and mask sample in the R-Z range of $7 \leq R \leq 9$ kpc and $|Z| \leq 2$ kpc and all fields are combined together. The $|Z|$ values for sources in the three low latitude fields in AGR do not exceed 1 kpc for the selected R range. As these low latitude fields have different selection cuts and low numbers of stars, we restrict our analysis only towards high latitude fields.

We compare the magnitude limited MDFs and the effect of the selection function on the

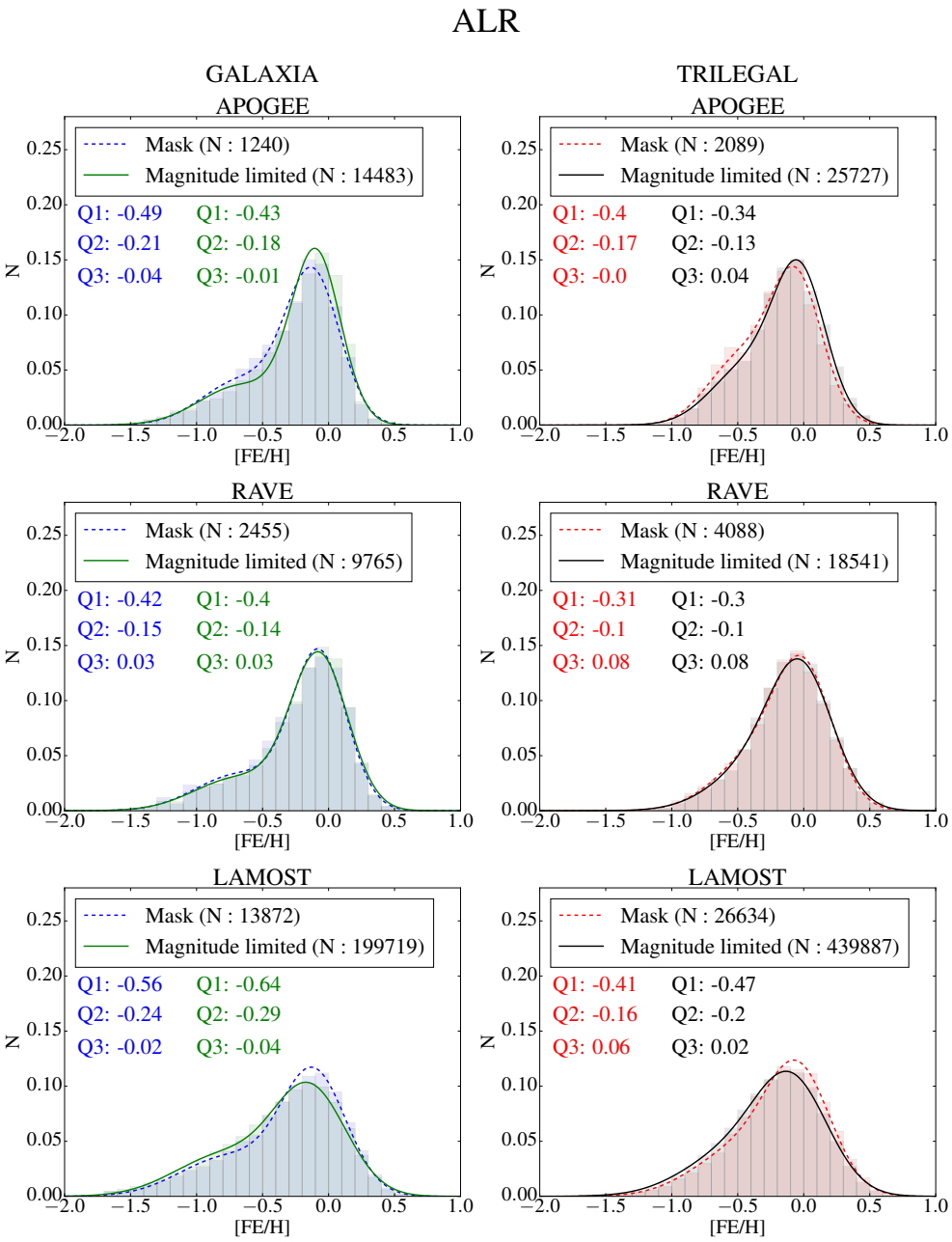

Figure 2.11: MDFs of magnitude limited and mask sample for the high latitude fields of each survey in ALR. The GALAXIA and TRILEGAL MDFs are shown respectively in the left and right columns of each panel. The histograms are normalized by dividing the counts in each 0.1 dex bin by the total number of sources (mentioned in each panel). The blue and red lines represent the mask distribution, while the green and black lines for the magnitude limited distribution fitted using GMM for GALAXIA and TRILEGAL respectively. APOGEE and RAVE distributions are shown in the top and middle rows, respectively, and the LAMOST (left) and GES (right) in the bottom row. Quartile values for the two distributions are given in each panel, colour-coded according to the distribution.

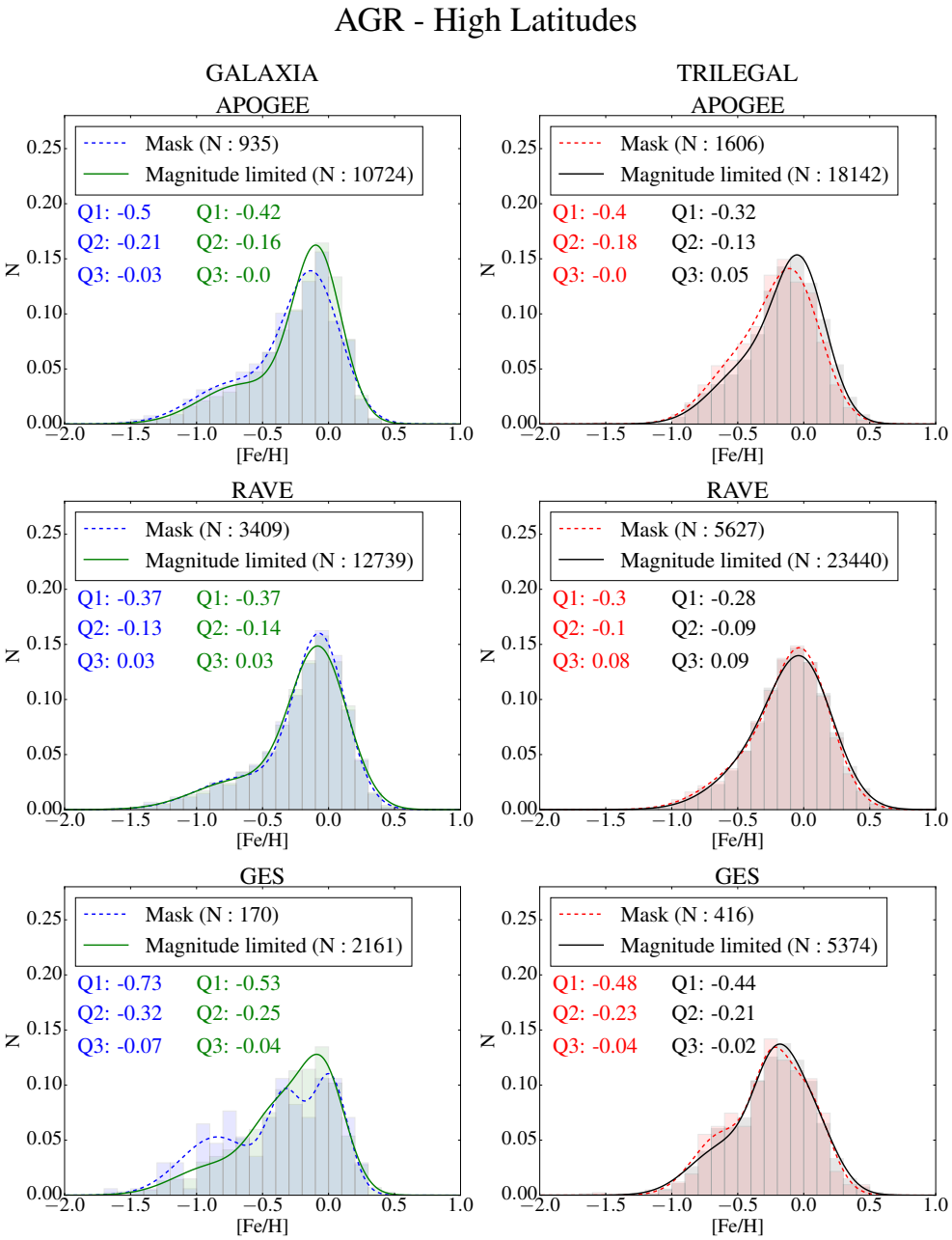

Figure 2.12: Same as in Figure 2.11 for AGR.

MDF for ALR and AGR in Figures 2.11 and 2.12 respectively. Here again we use the GMM method to fit the multiple number of Gaussians to the MDF. In addition, we use the quartile values to carry out a quantitive comparison of two distributions. Wojno et al. (2017) carried out a similar comparison of distributions using the quartile values for RAVE. As mentioned in Section 2.5.2, we choose 0.1 dex as the threshold for the difference between the respective quartiles of samples below which the distributions are considered to agree thus implying that the selection function has a minimal effect on the MDF. The quartile values for mask and magnitude limited samples are listed in the respective panels in Figure 2.11. We find that all the quartile values estimated for the mask and the magnitude limited sample in GALAXIA are more metal-poor than those in TRILEGAL.

2.6.1 AGR vs ALR

As APOGEE and RAVE are the common surveys in ALR and AGR, we check the consistency of the quartile values of their mask and magnitude limited distributions. Since we are using only high latitude fields, the colour and magnitude cuts are consistent for both surveys in ALR and AGR. As a first step, we compare the quartile values of mask and magnitude limited distributions of APOGEE in ALR and AGR for each model separately. The same model-wise quartile comparison is carried out for RAVE in ALR and AGR. We find that model-wise, the individual quartiles differ only by a maximum of ~0.03 dex for both surveys between ALR and AGR. This ensures that APOGEE and RAVE distributions in ALR and AGR are consistent.

To quantitively compare the mask and magnitude limited distributions of each model in ALR and AGR, we check for differences in their individual quartiles:

- For APOGEE, we find the differences in Q1 to be ~0.05-0.08 dex, for Q2 ~0.03-0.05 dex, and for Q3 ~0.03-0.05 dex. Thus, although we find the quartile differences to vary widely, they are all within the 0.1 dex difference threshold, implying no large selection function effect. As mentioned in the APOGEE selection function, there are certain halo fields in APOGEE where the giant targets are preselected using the Washington+DDO51 photometry. These photometric bands are not available in the two the models we use, so we attempted an approximate simulation of this preselection for such fields in our mask sample by using the APOGEE_TARGET1 flag. We estimated the observed giant-to-dwarf fraction in each small rectangular bins, which we tried to replicate in the models by choosing approximately the same giant fraction. We carried out the comparison of mask and magnitude limited samples with this approximate giant preselection using quartiles. We find there is an overselection of metal-poor stars in the -0.5 to -1.0 dex range in $[\mathrm{Fe/H}]$ in GALAXIA, which is not evident in TRILEGAL. The Q1 quartiles for mask and magnitude limited samples show differences higher than 0.1 dex in such fields for GALAXIA, but in Figures 2.9 and 2.10, we find that GALAXIA already (i.e. without any giant preselection) overpredicts the metal-poor stars in the same $[\mathrm{Fe/H}]$ regime compared to the observed APOGEE MDF. It is likely that this selection effect seen in such giant dominated fields is the result of

model parameterization, as it already significantly overpredicts contributions from the metal-poor populations.

- For RAVE, the individual quartile differences are minimal: ~0.0-0.02 dex. Thus we find the RAVE MDF to be least affected by the selection effect. Wojno et al. (2017) have found very similar result for the RAVE DR5 sample, for separate giant, main-sequence, turn-off samples of stars and for a mixed population sample and at different distance bins from the Galactic mid-plane.
- Like APOGEE, the individual quartile differences in LAMOST show some variations (Q1: ~0.06-0.08 dex, Q2: ~0.04-0.05 dex, and Q3: ~0.03 dex). However, as per our criteria, the selection function effect is not prominent.
- In the case of GES, we find inconsistency in the quartiles between GALAXIA and TRILEGAL. The quartile differences of the mask and magnitude limited sample in TRILEGAL agrees within the 0.1 dex threshold (Q1: ~0.04 dex, Q2: ~0.02 dex, and Q3: ~0.02 dex), but the Q1 values in GALAXIA differ by ~0.2 dex. We find that GALAXIA masks do not have enough sources in the metal-poor regime (170 stars in total), making this difference highly susceptible to Poisson noise.

2.7 Selection function effects on vertical metallicity gradients

We use stellar population synthesis models as described in Section 2.6 to simulate any influence of the selection function on the vertical metallicity gradient.

Here we estimate and compare the vertical metallicity gradients for the mask and magnitude limited sample of each survey. In both models, the gradient in metallicity in the vertical direction is not incorporated as an input parameter. Instead, the mean metallicity of different Galaxy components like thin and thick discs, combined with their different scale heights, leads to the vertical metallicity gradient. In TRILEGAL, this is found to be shallow (~ -0.1 dex kpc^{-1}), while that in GALAXIA is steeper (~ -0.4 dex kpc^{-1}). This can be attributed to the wide range of the age–metallicity relation for thin disc in GALAXIA (~-0.01 to -0.37 dex Sharma et al. 2011). Thus the two models differ largely in their vertical metallicity gradients. We use only the ALR sample to carry out our simulations to ensure sufficient statistics.

As mentioned in Section 2.5.2, the mask sample is made by randomly choosing the model sources within each 0.05 mag by 0.3 mag bins in the CMD. The slopes of the gradients are measured by finding the median metallicity in 0.2 kpc bins in |Z| and then using a linear least-squares regression fit to the median values. Unlike in the case of MDF, we find that the source distribution in the |Z|-[Fe/H] plane is sensitive to the random distribution of stars calculated by the models for the mask sample. We find that the mask gradient varies each time the model is run since the location of mask sample stars at the high Z boundaries keep varying. In order to account for this, we performed ten different mask samples for each survey in ALR. We use the median value of the vertical metallicity gradient and its error estimated from all ten trials as the final gradient for the mask sample. If there is a major influence of the selection

Table 2.5: Vertical metallicity gradients measured for mask and magnitude sample for GALAXIA and TRILEGAL in ALR.

Model	Survey	Mask (dex kpc^{-1})	Mag limited (dex kpc^{-1})
GALAXIA	APOGEE	-0.359±0.033	-0.382±0.025
	LAMOST	-0.396 ± 0.019	-0.378 ± 0.017
	RAVE	-0.438 ± 0.047	-0.424 ± 0.042
TRILEGAL	APOGEE	-0.085±0.018	-0.054±0.01
	LAMOST	-0.037 ± 0.005	-0.044 ± 0.005
	RAVE	-0.121 ± 0.019	-0.103 ± 0.016
	GES	-0.075 ± 0.039	-0.072 ± 0.011

function, we expect to find different metallicity gradients between the mask and magnitude limited samples. Table 2.5 gives the fitted values of the metallicity gradient for ALR using GALAXIA and TRILEGAL. We find that the variation in the gradient estimated between the mask and magnitude limited samples are consistent within the 1-σ limit for all three surveys (see Table 2.5). This indicates that the selection function does not have a strong impact on the vertical metallicity gradient. We investigate this further in the following section using the vertical metallicity gradients estimated for the observed sample from each survey.

2.7.1 Vertical metallicity gradients for the observed sample

To estimate the vertical metallicity gradient and compare them between the different surveys, we have to ensure that the metallicities of the different surveys are on the same scale. We applied a small offset to the RAVE and LAMOST metallicities with respect to our reference sample APOGEE using the linear and second-degree polynomial functions that we fitted in Section 2.2. While estimating the functional relation of metallicity offsets of RAVE and LAMOST with respect to APOGEE, we make sure that the relation holds true seperately for both high and low S/N samples of RAVE and LAMOST. So we can proceed without any major quality cuts for each survey, ensuring a statistically significant sample for our study.

Here again we restrict our study to the high latitude fields. Figure 2.13 shows the vertical metallicity gradients plotted separately for ALR and AGR. We follow the same fitting routine mentioned in the previous section to estimate the slopes. Table 2.6 lists the slopes of the gradients calculated for each survey in ALR and AGR, along with the slope of the combined sample. We also list the mean vertical metallicity gradient estimated from combined samples of ALR and AGR in the last row of the table.

We measured the vertical gradients of -0.235 ± 0.025 dex kpc^{-1} and -0.229 ± 0.026 dex kpc^{-1} for APOGEE in ALR and AGR, respectively. Hayden et al. (2014) measured a slightly steeper slope of -0.31 ± 0.01 dex kpc^{-1} for their APOGEE DR10 sample located within the solar neighbourhood, 7<R<9 kpc and |Z| < 2 kpc. Their sample in the solar neighbourhood is more complete and homogeneous than the volume limited sample we are dealing with. We used the same criterion in Hayden et al. (2014) to distinguish the α-poor and α-rich sources in

Table 2.6: Vertical metallicity gradients measured for ALR and AGR high latitude fields.

Survey	$\frac{d[\mathrm{Fe/H}]}{dZ}$ (dex kpc^{-1})
APOGEE	-0.235±0.025
LAMOST	-0.224 ± 0.024
RAVE	-0.225 ± 0.025
ALR	**-0.225± 0.024**
APOGEE	-0.229±0.026
GES	-0.202 ± 0.095
RAVE	-0.274 ± 0.025
AGR	**-0.256 ± 0.015**
Mean $\frac{d[\mathrm{Fe/H}]}{dZ}$	**-0.241± 0.028**

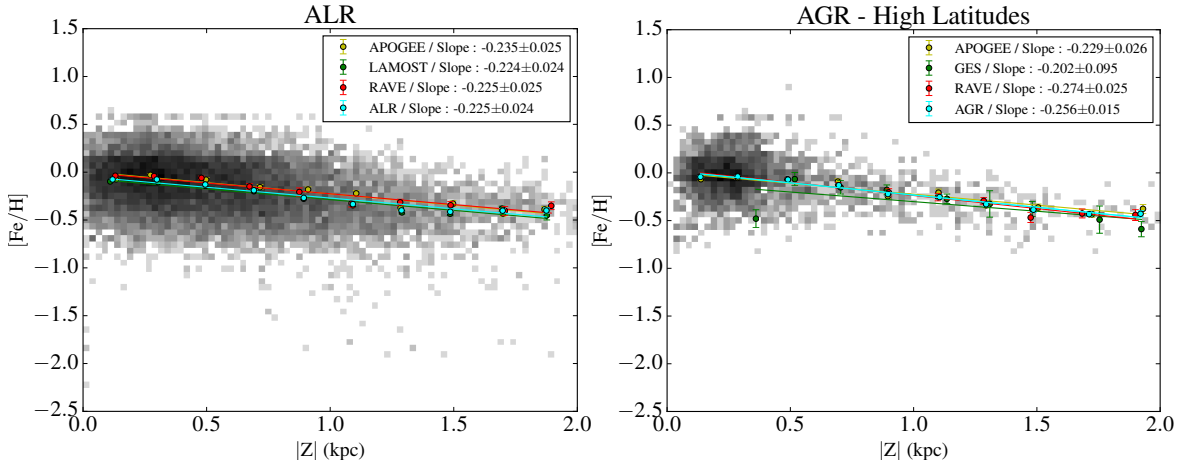

Figure 2.13: Vertical metallicity gradients calculated for all sources in each survey belonging to ALR (left) and AGR (right). The slope estimated for each survey is also shown in the plots. The gradient for the combined sample of surveys is shown for ALR and AGR.

our sample, and measured $\frac{d[\mathrm{M/H}]}{dZ}$ = -0.175 ± 0.045 dex kpc^{-1} and -0.164 ± 0.035 dex kpc^{-1} for the low-α samples in ALR and AGR, respectively. Hayden et al. (2014) measured a slightly steeper gradient of -0.21 ± 0.02 dex kpc^{-1} for their set of low-α samples. Meanwhile, the low number statistics of the high-α sources in our sample prevented us from calculating the same. The vertical metallicity gradient for the DR13 APOGEE sources in the same R-Z range was recalculated and found to be consistent with our slope (Hayden et al. 2017 in prep.).

The RAVE vertical metallicity gradient calculated for ALR and AGR are also similar, with slopes of -0.225 ± 0.025 dex kpc^{-1} and -0.274 ± 0.025 dex kpc^{-1}, respectively. The steeper slope in AGR could be due to the comparatively low number statistics in the bins at high $|Z|$ with respect to that in ALR, which makes the slope steeper. Boeche et al. (2014) used

giants stars in the RAVE DR4 sample and measured a shallower slope of $\frac{d[\mathrm{Fe/H}]}{dZ}$ = -0.112 ± 0.007 dex kpc^{-1} for ~ 10511 stars (RC sample) in the region extending from 7.5 to 8.5 kpc in R and |Z| ≤ 2 kpc. They have also carried out a study of the gradients seen in the α-poor and α-rich sample, but we were not able to identify any clear separation in the [α/Fe] vs [Fe/H] plane to define a α-poor and α-rich sample.

The low number statistics of GES is a significant issue when analysing metallicity trends. Since we use only the high latitude fields, there are no sources populated in the first 0.2 kpc bins of |Z|. We also find a comparatively metal-poor median metallicity value in the 0.2–0.4 kpc |Z| bin, which leads to a very high uncertainty of ~ 0.1 dex kpc^{-1} in the estimated gradient. We calculated $\frac{d[\mathrm{Fe/H}]}{dZ}$ of -0.202 ± 0.095 dex kpc^{-1}, which is still inside 1-σ with respect to APOGEE and RAVE. Mikolaitis et al. (2014) measured vertical metallicity gradients of -0.079 ± 0.013 and -0.046 ± 0.010 dex kpc^{-1} for thin and thick-disc FGK stars separately in the solar circle (7≤R≤9 kpc and |Z| ≤ 3.5 kpc), which are much shallower than our measurements. They use the first internal data release of the GES (GES iDR1) and chemically differentiate the thin and thick discs based on their α abundances, whereas our sample is made using the iDR4 release and we do not make any separation based on the α-abundances.

The vertical metallicity gradient measured for LAMOST is steep, -0.224 ± 0.024 dex kpc^{-1}, but within the 1-σ limit with respect to APOGEE and RAVE. Using nearly 70 000 red clump stars covering 7≤R≤14 kpc and |Z| ≤ 3 kpc from the LAMOST Spectroscopic Survey of the Galactic Anti-Centre (LSS-GAC) survey, Huang et al. (2015) measured the radial and vertical metallicity gradients. Our estimate is steeper than their slopes of -0.146 ± 0.012 dex kpc^{-1} and -0.149± 0.012 dex kpc^{-1} measured for the sample in 7≤R≤8 kpc and 8≤R≤9 kpc, respectively. Xiang et al. (2015) measured a vertical metallicity gradient that is in the range of ~ -0.2 to -0.3 dex kpc^{-1} in the R bin of 8 to 9 kpc and |Z| < 2 kpc, for a sample of main-sequence turn-off stars from LSS-GAC, which is consistent with our value.

Our mean vertical metallicity gradient from the combined samples of ALR and AGR is -0.241±0.028 dex kpc^{-1}. Among recent studies, Schlesinger et al. (2014) carried out a detailed study of the vertical metallicity gradient using over 40 000 G-dwarf stars from the SEGUE DR9 catalogue, volume complete in the range of 6.7 to 9.5 kpc in R and 0.27 to 1.62 kpc in |Z|. Their range in R-Z is very close to the coverage of our samples. They estimated the gradient to be $-0.243^{+0.039}_{-0.053}$ dex kpc^{-1}, which is in good agreement with our derived mean value. Very recently, Duong et al. (2018) estimated the vertical metallicity gradient to be -0.22±0.01 dex kpc^{-1} for stars within 7.9≤R≤9.5 kpc and |Z| ≤4 kpc from the GALAH pilot survey, which is again consistent with our measured mean value.

In addition to the results from the surveys used in our analysis, there are other studies calculating the vertical metallicity gradients near the solar circle, Chen et al. (2003): -0.295 ± 0.005 dex kpc^{-1}, Borkova and Marsakov (2003): -0.29 ± 0.06 dex kpc^{-1}, Soubiran et al. (2008): -0.31 ± 0.03 dex kpc^{-1} for thin disc clump giants within |Z| ≤ 1 kpc, Ak et al. (2007): -0.22 ± 0.03 dex kpc^{-1} for G-type stars in |Z| ≤ 3 kpc. All these gradients are very close to the gradients we estimated for each survey. Vertical gradients have been measured for thick discs alone; Chen et al. (2011) have measured a gradient of -0.22 ± 0.07 dex kpc^{-1} for RHB stars in 1 ≤ |Z| ≤ 3 kpc, and Carrell et al. (2012) -0.113 ± 0.010 dex kpc^{-1} for SEGUE FGK dwarf stars in 1 ≤ |Z| ≤ 3 kpc. Kordopatis et al. (2011) have estimated a vertical metallicity

gradient of -0.14 ± 0.05 dex kpc^{-1} using roughly 700 stars at $1 \leq |Z| \leq 4$ kpc from the solar neighbourhood towards the Galactic coordinates (l~ 277 °, b~ 47 °).

While there is a large variation in the vertical metallicity gradient in the literature, we find consistent measurements of the vertical gradient in the four spectroscopic surveys analysed in this paper. This implies that the effect of the selection function on the vertical metallicity gradient is very small, if any at all.

As seen in Section 2.7 the metallicity gradients for the mask sample in both models (Table 2.5) do not match the observed metallicity gradient (see Table 2.6). However, as we compare the magnitude limited sample and the mask sample for each model separately to study the influence of the selection effect, we neglect the discrepancy between the observed gradient and both models. Nevertheless, it shows that both models need to be improved in order to reproduce the observed quantities (e.g. metallicity gradient).

Thus, using the models and the observed sample, we find negligible selection function effects on the vertical metallicity gradient. This in turn means that it is indeed possible to merge different spectroscopic surveys to obtain a broader Z range that traces the vertical metallicity gradient to higher precision, provided they are on the same metallicity scale.

2.8 Summary and conclusions

We investigated the effect of the selection function on the MDF and on the vertical metallicity gradient using common fields between APOGEE-LAMOST-RAVE (ALR) and APOGEE-GES-RAVE (AGR) around the solar neighbourhood. Our results can be summarized as follows:

We compared and discussed stellar parameters of the common sources between APOGEE, RAVE, and LAMOST. In order to bring the surveys to the same metallicity scale, we applied corrections for $[\mathrm{Fe/H}]$ with respect to APOGEE, which we used as the reference sample. Distances were calculated for all four surveys and we restricted our sample in R from 7 to 9 kpc and |Z| from 0 to 2 kpc allowing the determination of the MDF and vertical metallicity gradient.

We generated mock fields using two commonly used population synthesis models, GALAXIA and TRILEGAL, to investigate the selection effect in MDFs. We divided the corresponding CMDs into small bins (called masks) which we applied to each model trying to replicate the observed MDF. Based on the comparison of the shape of mask MDFs and giant-to-dwarf ratio we find that

- for APOGEE, both models have a dominant metal-poor tail absent in the observed MDF. In addition, GALAXIA underestimates the giant-to-dwarf ratio while TRILEGAL overestimates it;
- GALAXIA traces both the shape of the MDF and the giant-to-dwarf ratio of the RAVE sample better than TRILEGAL;
- for LAMOST there is good consistency between the giant-to-dwarf ratio of mask samples and observed samples, even though the shape of the mask MDF relative to the

observed is found to be different in the two models.

To understand the selection function effect in MDF, we compared the mask MDF with the magnitude limited MDF for the survey-replicas of both models using quartiles. We found APOGEE, RAVE, and LAMOST to have negligible selection effects using both models, while GES suffers from number statistics that are too low to be conclusive.

We simulated the vertical metallicity gradient with the two models, and they both failed to reproduce our observed metallicity gradient; clearly some improvements in both models are necessary. However, when we compare the vertical metallicity gradients between mask and magnitude limited samples for APOGEE, RAVE, and LAMOST, which are sensitive to the selection function, we did not find any significant difference. In addition, the agreement found in our observed values of the metallicity gradient between the four different surveys again strengthens the argument that the selection effect plays a negligible role when determining the metallicity gradient.

We scaled the metallicity values in RAVE and LAMOST to that in APOGEE and compared the vertical metallicity gradients for combined fields for each survey in ALR and AGR. The estimated vertical metallicity gradient for each survey is consistent within 1-σ indicating the negligible effect of selection function. Finally, we estimated a mean vertical metallicity gradient of -0.241$\pm$0.028 dex kpc^{-1}.

We conclude that in the era of rising large spectroscopic surveys, in principle common fields of the surveys could be combined once they are put on the same metallicity scale. This will increase significantly the statistics without imposing any selection effect when studying the MDF and the metallicity gradient. With the forthcoming Gaia data releases, we plan to extend this study to a much larger volume .

Chapter 3

Chemical characterization of the inner Galactic bulge

Contents

In this chapter, we carry out the data reduction and analysis of high resolution K band CRIRES spectra of 72 M giant stars in the inner Galactic bulge. The stars are distributed in six fields along the bulge minor axis (l = 0°) covering latitudes, b = 0°, ±1°,, ±2° and +3°. We derive the fundamental stellar parameters ($T_{\rm eff}$, $\log g$, [Fe/H], radial velocities and [α/Fe] (Si and Mg) abundances of all the stars in our sample, with the aim to estimate the nature of the MDF in the inner bulge region and do a comparison to its nature in the outer bulge. We also intend to investigate the North-South symmetry/asymmetry in the MDF as well as chemical abundance patterns in the inner bulge regions.

3.1 (Lack of) Observations in the inner Galactic bulge

As mentioned in the Section 1.1.3, the Milky Way bulge is on average one of the older components of the Milky Way, located within $\sim 3-4$ kpc from the Galactic center and harbors most likely multiple stellar populations. Its structure, formation, and evolution scenarios have been under debate in recent years owing to a large increase of observational data allowed by the advancements in telescope sizes, instrumentation as well as observing techniques. These general advances derive from observations of bulge stars in regions of relatively low optical extinction. However, much of the *mass* of the bulge, that lies within ~400-500 pc around the Galactic center or within $|b| \sim 3°$, has escaped investigation due to the obscuration in the line-of-sight toward the inner bulge. Observations at infrared wavelengths mitigates this problem, enabling us to peer further and deeper through the highly extincted inner regions of the Milky Way.

One of the first observations and metallicity determination for stars in the inner bulge region along the bulge minor axis ($0°1 < \mathrm{b} < -2\overset{\circ}{.}8$) was carried out by Frogel et al. (1999) using IRCAM (Persson et al., 1992). These authors derived mean metallicities from the slope of giant branches in CMDs and estimated a slope of -0.085±0.033 dex deg^{-1} for -0°.8≤b≤-2°.8. Follow up low resolution (R~1300-4800) spectroscopic observations of around 100 M giants in the same fields were carried out by Ramírez et al. (2000b). These authors determined metallicities for their sample from the equivalent widths of three features in these spectra, EW(Na), EW(Ca), and EW(CO), and found no evidence for a metallicity gradient along the minor or major axes of the inner bulge (R_G ~560 pc). Carr et al. (2000) and Ramírez et al. (2000a) have carried out a detailed abundance analysis using high resolution spectra (R~40,000) to estimate a mean metallicity of +0.12±0.22 dex for 10 cool luminous super giants stars in the Galactic center (GC). The same stars were re-analysed by Cunha et al. (2007) with a slightly higher resolution (R~50,000) and they estimated a similar mean metallicity.

Rich et al. (2007) did one of the first detailed abundance analysis of 17 M giants located at (l,b)=($0°, -1°$) from their high resolution (R~25,000) spectra and found a mean iron abundance of [Fe/H]=-0.22 with a $1\,\sigma$ dispersion of 0.14 dex. Rich et al. (2012) then proceeded to carry out a consistent analysis of 30 M giants at (l,b)=($0, -1\overset{\circ}{.}75$) and ($1°, -2\overset{\circ}{.}75$) that were observed with the same instrument and estimated mean iron abundances of -0.16 ± 0.12 dex and -0.21 ± 0.08 dex respectively. These authors also combined their analysis of 14 M giants in Baade's Window (l=$1\overset{\circ}{.}02$, b=$-3\overset{\circ}{.}93$) using the same instrument and found no major vertical abundance or abundance gradient in the inner most 150 pc to 600 pc region. Babusiaux et al. (2014) determined metallicities for ~100 red clump (RC) stars at (l,b) = ($0°$,+$1°$) using low resolution spectra (R~6,500) and found a mean metallicity very similar to that of Ramírez et al. (2000b) and Rich et al. (2007) at (l,b) = ($0°, -1°$) suggesting symmetry between Northern and Southern inner bulge fields. APOGEE data (Majewski et al., 2017) presented evidence of a significant metal-poor component in the inner one degree (Schultheis et al., 2015). Ryde and Schultheis (2015) analyzed 9 field giants in the vicinity of the Nuclear Star Cluster (NSC), finding a broad, metal-rich component at [Fe/H]~+0.1 and a lack of metal-poor stars. Their α abundances are found to be low following the trends from studies in the

outer bulge, resembling a bar-like population. Grieco et al. (2015) made a detailed chemical evolution model of the center region to compare with these data. They conclude that this region experienced a main, early, strong burst of star-formation, with a high star-formation efficiency, no late in-fall of gas, and some indications of a top-heavy Initial-Mass Function (IMF). Ryde et al. (2016a) presented an abundance study of 28 M giants in fields located within a few degrees south of the Galactic Center using high resolution (R ~50,000) spectra and determine the metallicity distribution functions and α element trends. They find a large range of metallicities, with a narrower range towards the center, and a large similarity of the α element trends among the different fields and that of the outer bulge, suggesting a homogeneous bulge regarding the enrichment processes and star-formation history. Recently, Zoccali et al. (2017) derived metallicities of stars from the GIRAFFE Inner Bulge Survey (GIBS) in fields close to the Galactic plane, at b = -2° and b = -1°. They find a clear bimodal Metallicity Distribution Function (MDF). Meanwhile, García Pérez et al. (2018) identify more than two components by arranging the red giant stars in the APOGEE DR12 bulge sample by projected Galactocentric distance and distance from the Galactic mid-plane. Fragkoudi et al. (2018), using derived metallicities from the more recent data release of APOGEE (DR13), compare the observed MDF, including that in the inner bulge with that obtained from N-body simulations of a composite (thin+thick) stellar disc. These authors find the MDF trends to be reproduced by the models, and argue their consistency with bulge formation from the secular evolution of disc.

It is clear from the overview of the literature that almost all focus has been on the less extincted Southern fields of the inner bulge. Here, I present the first comprehensive data set of high resolution spectroscopic data of 72 stars in fields sampling the full inner bulge within $|b| \sim 3°$, thus both at Southern and Northern latitudes, all analyzed in a homogeneous way. My study is the first comparative study of stars in inner fields of the bulge of both sides of the Galactic Plane. With this study, I aim to estimate the nature of the MDF in the inner bulge region and do a comparison to its nature in the outer bulge. I also intend for the first time to investigate the symmetry in MDF between Northern and Southern latitudes, which has not been studied before. With our limited sample, I also try to understand how the mean metallicity changes with different latitudes away from the Galactic mid-plane. In addition, O also estimate α-element abundances for the observed stars, and show the [α/Fe] vs [Fe/H] trend in the inner bulge region. Finally, I have measured radial velocities of our stars with the aim of exploring correlations between kinematics and metallicity. All these studies are needed to constrain the formation of the Milky Way bulge.

3.2 Data

In order to determine the MDF and the α-element trends for stellar populations in the optically obscured inner bulge, we have observed M giants in six different fields at high spectral resolution in the K band. We succeeded in securing useful spectra of 72 bulge giants along the Northern and Southern minor axes within 3 degrees[1] of the Galactic Center. We have

[1]This corresponds to approximately 450 pc in projected distance

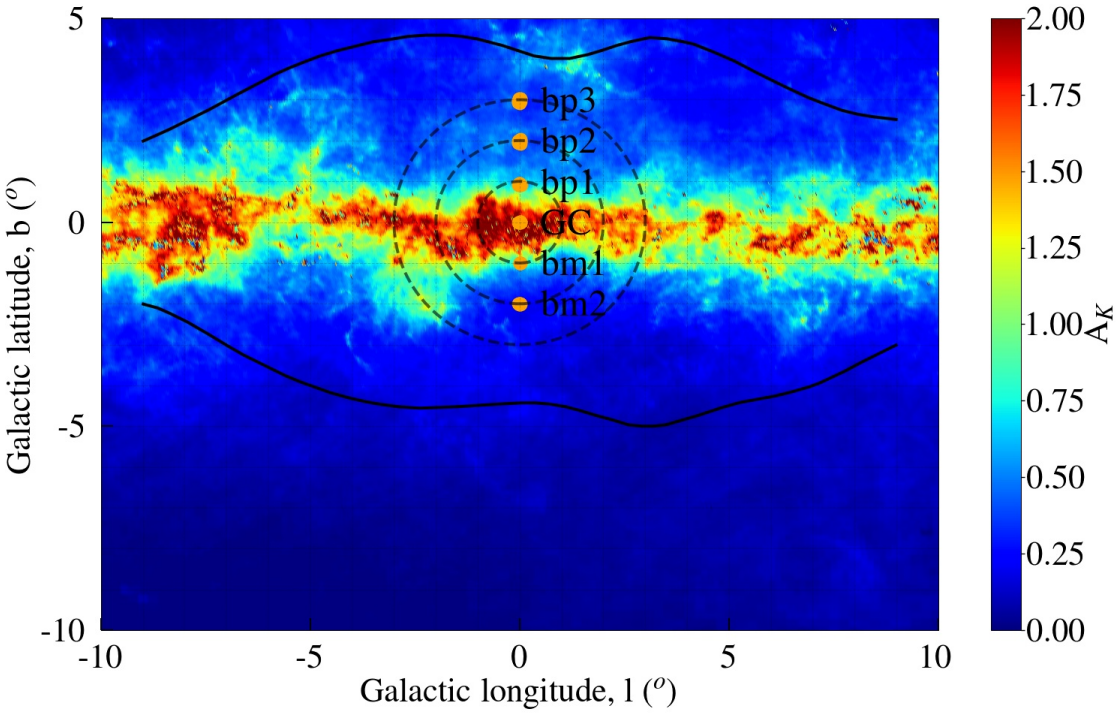

Figure 3.1: Our inner bulge fields in galactic coordinates. The individual stellar coordinates (orange) are plotted, which shows the concentration within each field. The mean extinction map, calculated from Gonzalez et al. (2012) using extinction coefficients from Nishiyama et al. (2009), is overlaid on the figure to show the level of obscuration in our observed fields. The bulge outline is the COBE/DIRBE bulge envelope (Weiland et al., 1994).

included a Galactic Center field at $2\farcm5 - 5\farcm5$ North of the Galactic Center, thus avoiding the Nuclear Star Cluster[2]. In Figure 3.1 the stars are plotted on a sky projection showing how they sample the inner minor axis both to the North and to the South of the Galactic Plane. We observed the stars in the infrared K-band at $2.1\,\mu\mathrm{m}$, in order to overcome the extreme optical extinction towards the inner regions.

All stars were observed at both high- and low spectral resolution. The high resolution spectra, recorded with the CRIRES spectrograph (yielding a resolving power of $R \sim 50,000$; Käufl et al., 2004; Käufl et al., 2006; Moorwood, 2005) mounted on UT1 of the *Very Large Telescope*, VLT, were used to determine the metallicity and abundances of the α elements, while the low resolution spectra, recorded with the ISAAC spectrograph ($R \sim 1000$; Moorwood et al., 1998a) on UT3 of the VLT and the SOFI instrument ($R \sim 1000$ Moorwood et al., 1998b) on the NTT telescope at La Silla, were used to determine the effective temperatures of the stars via low resolution spectroscopy of the 2.2 μm CO bands, following the method described in Schultheis et al. (2016) (see Section 3.3.3).

44 of the observed giants that are located in the Northern fields were observed with CRIRES during the period 20 April - 16 September 2013 in Service Mode and with SOFI during 13-17 July 2013 in Visitor Mode (program ID 091.B-0369). 28 of the remaining giants are located in the Galactic Center field and the Southern fields and were observed with both the CRIRES and ISAAC spectrographs in Visitor Mode during 27-29 June 2012 (program ID 089.B-0312). The 44 bulge giants in the Northern fields are presented for the first time here, whereas the 28 giants in Southern and Center fields are reanalysed here for consistency, but were first published in Ryde and Schultheis (2015) and Ryde et al. (2016b). In Tables 3.1 and 3.2 the coordinates and total exposure times for all the stars are provided.

3.2.1 Target selection

We selected our M giant sample in the Northern fields in the same way as it was done for the Southern fields (Ryde et al. 2016b) to ensure consistency of the North and South samples. We used the dereddened color-magnitude diagram, which covers the full $(J-K)_0$-colour range for all the fields except the Galactic center field, where we use the $(H-K)_0$-colour. Figure 3.2 shows the corresponding colour-magnitude diagrams for the northern and southern fields together with our selected targets. Interstellar extinction is less severe than in the Southern fields, especially for the field located at b=+1° is well known for its low and homogeneous interstellar extinction, which has been the subject of many studies (see e.g. Omont et al. 2003a, van Loon et al. 2003, Babusiaux et al. 2014). Our input catalog for the Northern field is the 2MASS catalog, as the Nishiyama et al. (2009) catalog is not available for the Northern fields. We again checked our extinction values with the 3D high-resolution interstellar extinction map from Schultheis et al. (2014).

In addition, we used the surface-gravity index, as outlined in Ramírez et al. (2000b), based on measured equivalent widths (W) of the Na I- and Ca I-features, as well as the first overtone, CO bandhead in our low-resolution spectra. This is done to ensure that none of

[2]An abundance analysis based on high-resolution spectra of stars in the Nuclear Star Cluster is performed in Ryde et al. (2016a); Rich et al. (2017)

Table 3.1: The coordinates, dereddened magnitudes and exposure time for the observed stars in the Northern fields.

Star	RA (J2000) (h:m:s)	Dec (J2000) (d:am:as)	H	K	H_0	K_0	exp. time [s]
Northern field at $(l, b) = (0°, +3°)$							
bp3-01	17:34:05.20	-27:19:58.20	10.04	9.55	9.31	9.10	1500
bp3-02	17:34:19.24	-27:20:42.70	11.48	10.99	10.69	10.50	1200
bp3-04	17:34:09.23	-27:22:38.00	10.97	10.39	10.22	9.23	1200
bp3-05	17:34:00.71	-27:18:59.60	10.47	9.96	9.78	9.53	1200
bp3-06	17:34:07.13	-27:22:28.90	11.71	11.21	10.97	10.75	1200
bp3-07	17:34:24.09	-27:23:16.70	11.52	10.97	10.77	10.51	1200
bp3-08	17:34:16.44	-27:24:34.30	10.43	9.82	9.69	9.36	1200
bp3-10	17:34:13.70	-27:24:31.00	11.50	11.03	10.75	10.57	1200
bp3-11	17:33:58.67	-27:20:30.20	10.10	9.59	9.44	9.18	720
bp3-12	17:34:06.61	-27:19:29.30	10.13	9.61	9.40	9.16	720
bp3-13	17:34:08.21	-27:22:58.70	10.25	9.66	9.50	9.20	720
bp3-14	17:33:57.31	-27:21:07.60	10.27	9.67	9.61	9.26	1200
bp3-15	17:34:06.52	-27:22:30.20	10.30	9.77	9.56	9.31	1200
bp3-16	17:34:15.46	-27:22:30.90	10.39	9.78	9.63	9.31	1200
bp3-17	17:34:03.57	-27:18:49.60	10.31	9.82	9.60	9.38	1200
Northern field at $(l, b) = (0°, +2°)$							
bp2-01	17:37:49.64	-27:51:05.50	11.21	10.66	10.42	10.17	1800
bp2-02	17:38:02.25	-27:52:31.40	11.11	10.64	10.33	10.16	1800
bp2-03	17:37:58.65	-27:51:40.90	10.93	10.37	10.15	9.89	1200
bp2-04	17:38:02.12	-27:52:49.80	10.86	10.38	10.08	9.90	1800
bp2-05	17:37:53.31	-27:52:01.10	11.39	10.88	10.60	10.39	1800
bp2-06	17:37:51.19	-27:54:01.70	11.48	11.03	10.72	10.56	1200
bp2-07	17:37:58.13	-27:53:42.60	11.30	10.87	10.55	10.40	1800
bp2-08	17:37:56.88	-27:51:52.80	10.87	10.29	10.08	9.80	1200
bp2-09	17:37:50.52	-27:54:24.60	10.89	10.36	10.14	9.89	1200
bp2-10	17:38:01.25	-27:55:38.40	10.60	10.03	9.86	9.57	1800
bp2-11	17:38:00.03	-27:55:45.00	10.62	10.02	9.88	9.56	1200
bp2-12	17:38:02.01	-27:53:30.70	10.55	10.03	9.78	9.56	2400
bp2-13	17:38:02.54	-27:55:42.50	11.52	11.06	10.78	10.60	1200
bp2-14	17:38:01.74	-27:55:56.10	11.16	10.55	10.42	10.09	1200
bp2-15	17:38:13.55	-27:53:41.40	10.67	10.15	9.93	9.69	600
Northern field at $(l, b) = (0°, +1°)$							
bp1-01	17:41:57.26	-28:28:46.50	11.91	11.17	10.87	10.53	1200
bp1-02	17:41:57.62	-28:28:51.60	11.46	10.86	10.41	10.21	1200
bp1-03	17:41:58.61	-28:28:46.80	11.38	10.65	10.31	9.99	1800
bp1-04	17:41:55.92	-28:27:03.80	11.56	10.93	10.60	10.34	1200
bp1-05	17:41:59.76	-28:27:36.20	11.70	10.95	10.68	10.32	1200
bp1-06	17:41:57.66	-28:27:07.20	11.79	11.11	10.82	10.51	1200
bp1-07	17:42:03.59	-28:27:18.20	11.68	11.08	10.63	10.43	1200
bp1-08	17:41:58.51	-28:26:18.70	11.61	10.81	10.53	10.15	1800
bp1-09	17:42:04.43	-28:26:55.60	11.61	10.81	10.58	10.17	1800
bp1-10	17:42:06.49	-28:27:09.10	11.43	10.69	10.36	10.03	1800
bp1-11	17:41:59.06	-28:26:03.90	11.64	11.08	10.70	10.50	1200
bp1-12	17:41:58.72	-28:25:58.80	11.50	10.90	10.56	10.32	1800
bp1-13	17:42:05.96	-28:26:59.10	11.03	10.43	9.98	9.78	1200
bp1-14	17:42:10.05	-28:25:36.90	11.47	10.83	10.48	10.22	1800

Table 3.2: The coordinates, dereddened magnitudes and exposure time for the observed stars in the Southern fields.

Star	RA (J2000) (h:m:s)	Dec (J2000) (d:am:as)	H	K	H_0	K_0	exp. time [s]
Galactic Centre field at $(l, b) = (0^\circ, 0^\circ)$							
GC1	17:45:35.43	-28:57:19.28	14.74	11.90	10.48	9.40	3000
GC20	17:45:34.95	-28:55:20.17	14.47	11.87	10.21	9.37	3600
GC22	17:45:42.41	-28:55:52.99	13.41	11.54	9.15	9.04	3600
GC25	17:45:36.34	-28:54:50.41	14.35	11.60	10.09	9.10	2400
GC27	17:45:36.72	-28:54:52.37	14.31	11.64	10.05	9.14	3600
GC28	17:45:38.13	-28:54:58.32	14.08	11.67	9.82	9.17	3000
GC29	17:45:43.12	-28:55:37.10	14.39	11.59	10.13	9.09	3600
GC37	17:45:35.94	-28:58:01.43	13.77	11.50	9.51	9.00	3600
GC44	17:45:35.95	-28:57:41.52	13.78	11.74	9.52	9.24	3600
Southern field at $(l, b) = (0^\circ, -1^\circ)$							
bm1-06	17:49:33.42	-29:27:28.75	11.84	11.04	10.58	10.26	1800
bm1-07	17:49:34.58	-29:27:14.82	12.22	11.44	10.95	10.66	2400
bm1-08	17:49:34.34	-29:26:57.98	11.22	10.40	9.95	9.62	1200
bm1-10	17:49:34.45	-29:26:48.68	10.92	10.12	9.65	9.34	1920
bm1-11	17:49:32.57	-29:26:30.75	11.26	10.41	10.00	9.63	1200
bm1-13	17:49:37.12	-29:26:40.24	10.91	10.25	9.65	9.47	1080
bm1-17	17:49:37.08	-29:26:21.67	11.70	10.94	10.43	10.16	1800
bm1-18	17:49:37.83	-29:26:19.19	12.23	11.42	10.96	10.64	1800
bm1-19	17:49:36.93	-29:26:10.51	12.11	11.34	10.84	10.56	3600
Southern field at $(l, b) = (0^\circ, -2^\circ)$							
bm2-01	17:53:29.06	-29:57:46.22	11.44	11.11	11.08	10.89	2400
bm2-02	17:53:24.59	-29:59:09.48	10.78	10.44	10.41	10.21	1920
bm2-03	17:53:27.61	-29:58:36.39	11.30	10.93	10.94	10.70	2400
bm2-05	17:53:33.20	-29:57:25.88	10.07	9.51	9.70	9.28	2280
bm2-06	17:53:30.68	-29:58:15.75	10.01	9.71	9.65	9.48	1200
bm2-11	17:53:31.50	-29:58:28.51	10.20	9.91	9.83	9.68	1680
bm2-12	17:53:31.74	-29:58:22.94	10.67	10.32	10.30	10.09	480
bm2-13	17:53:31.14	-29:57:32.76	10.86	10.52	10.50	10.29	2400
bm2-15	17:53:30.23	-29:56:42.74	10.43	9.96	10.07	9.74	1200
bm2-16	17:53:29.54	-29:57:22.71	10.93	10.57	10.56	10.35	1200

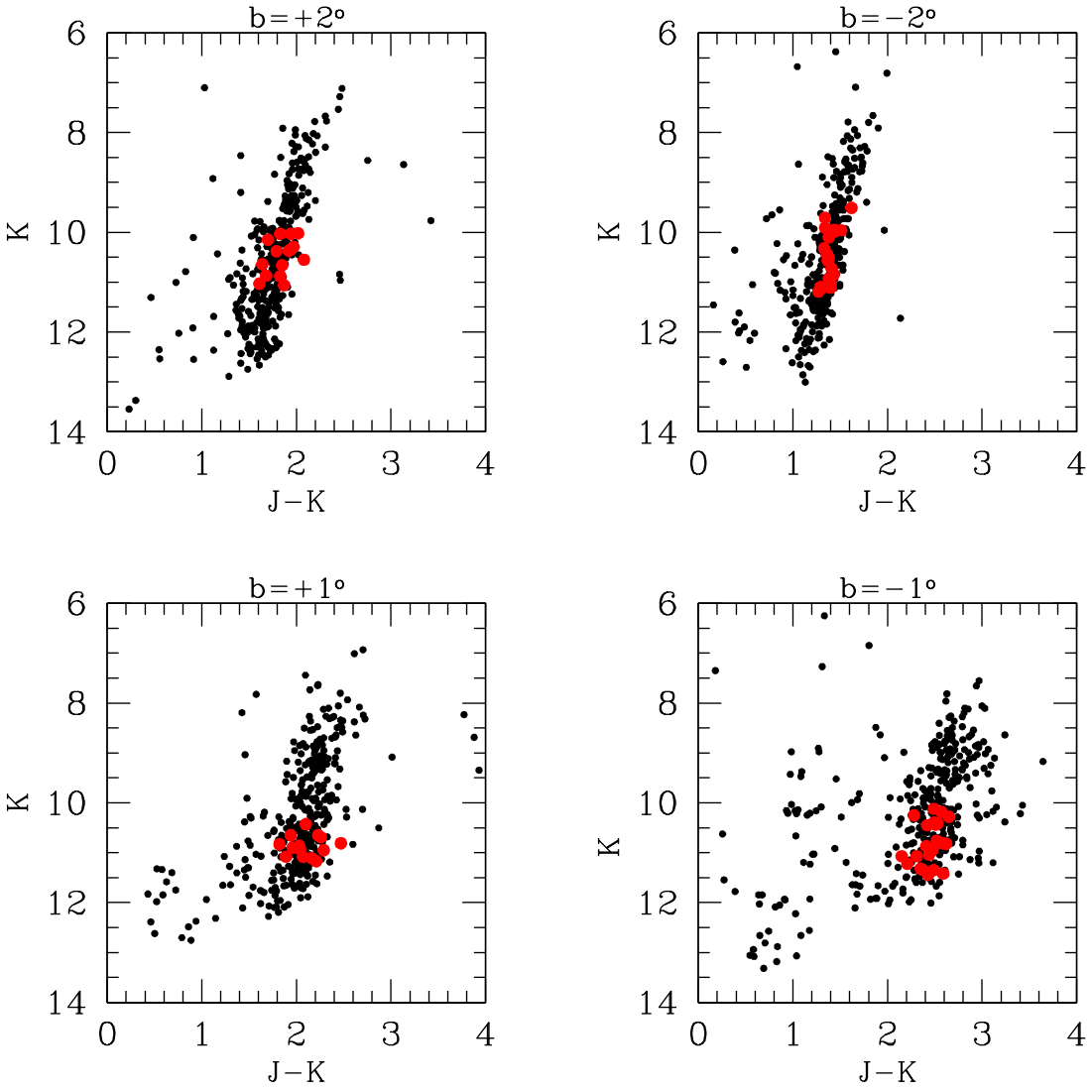

Figure 3.2: 2MASS K vs . J–K diagram for the Northern and Southern fields. The filled red points show our selected targets.

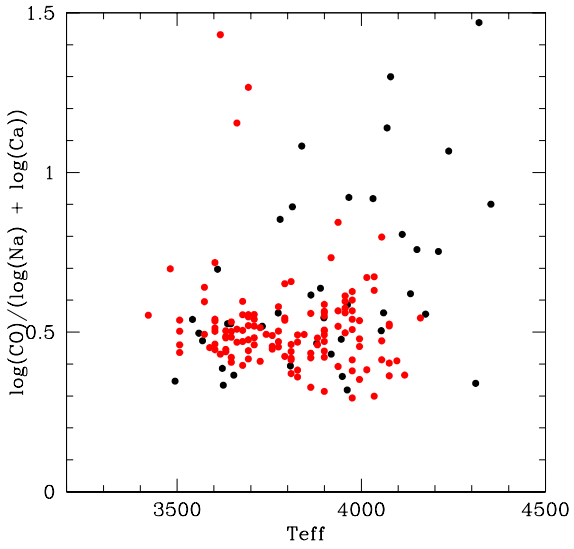

Figure 3.3: Effective temperatures based on the ^{12}CO first overtone bandhead vs. log g sensitive spectral index log(CO)/(log(Na)+log(Ca)). Black filled circles show our sample while the red filled circles are those of Ramírez et al. (2000a).

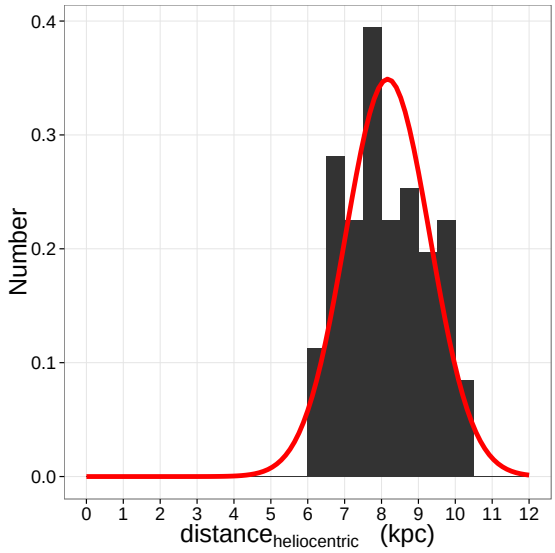

Figure 3.4: Histogram of the heliocentric distances of our stars using the isochrone method from Rojas-Arriagada et al. (2014) and Schultheis et al. (2017)

our stars actually is a foreground dwarf star. Ramírez et al. (2000b) demonstrated nicely that this index is a very good discriminator to distinguish dwarf stars from giant stars. Figure 3.3 shows our sample of M giant stars in black and the comparison sample of Ramirez et al. (1997) in red. Dwarf stars are supposed to lie at about $\log$ [((CO)/((Ca) + (Na))]~ 0. We see clearly that our stars are indeed M giants.

We have also calculated the heliocentric distances for our sample by using the stellar parameters $T_{\rm eff}$, $\log g$ and [Fe/H] (determined in Sections 3.3.3 and 3.3.4) and taking the closest point in the PARSEC isochrones (Bressan et al., 2012), by assuming a typical age between 5 and 10 Gyr. A more detailed explanation of the procedure can be found in Rojas-Arriagada et al. (2014) and Schultheis et al. (2017). Figure 3.4 shows the histogram of our derived distances. Our distance distribution shows clearly that our stars belong to the bulge and that we can exclude any foreground contamination.

All our targeted stars are M giants (3300 K< $T_{\rm eff}$<4300 K and 0.5 < $\log g$ < 2.0), for which we will determine the metallicities, [Fe/H], and the abundances of the α-elements, Mg and Si. The apparent magnitudes of our stars lie in the range of K=$9.5-12.0$. The H and K-band magnitudes, as well as the dereddened H_0- and K_0-magnitudes are presented in Table 3.1 and 3.2.

In the following section, we give some details about the specific observations of our targets.

3.2.2 Observations

High spectral resolution VLT/CRIRES observations

When possible, we used the *Adaptive Optics* (AO) MACAO system when observing with the CRIRES spectrometer, concentrating the light into our slit. Special care was thus taken to find an optimal AO guide star, sufficiently bright in the R band (the band in which the wavefront sensing is done, with $R < 14$ required), and within $15''$ of our science target, in order for an optimal performance of the MACAO system.

Furthermore, special care was also taken to individually determine the position angles of the slit for every target star in these crowded fields. This is done in order to ensure that we only record the target star on the $40''$ long slit, also when nodding along the slit and jittering to reduce the sky background, following standard procedures (Smoker, 2007). Figure 3.5 shows an example of a finding chart in the K band, used at the observations, with the target and the AO-guide stars marked. The crowding of stars in these regions and the size of the long, narrow slit of the CRIRES spectrometer is illustrated nicely in the Figure and demonstrates the challenges in observing in the inner bulge.

A slit width of $0\farcs4$, which we used, yields a resolving power of $R \sim 50,000$. For the CRIRES observations, we used a standard setting ($\lambda_{\rm vac}^{\rm ref}$ = 2105.5, order=27) with an unvignetted spectral range covering $20818 - 21444$ Å, with three gaps (20 Å) between the four detector arrays. Exposure times of $0.5 - 1$ hour per star provide a signal-to-noise ratios per pixel of typically 50-100.

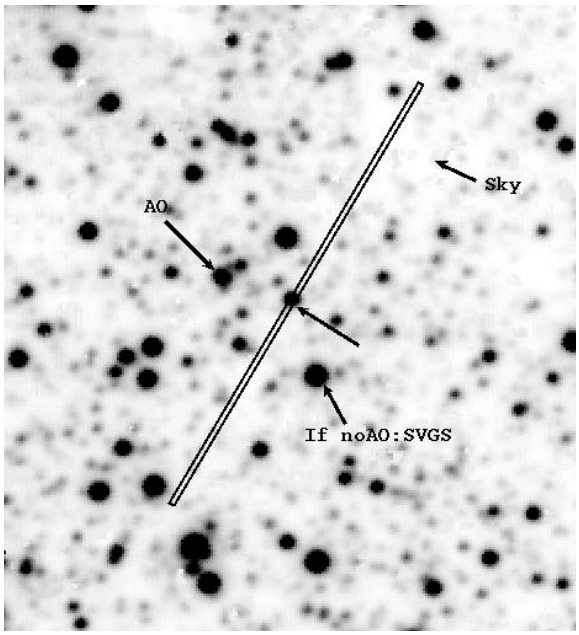

Figure 3.5: An example of a finding chart from our observing run with VLT/CRIRES. The underlying image is a DR9, UKIDSS K-band image (Lawrence et al., 2013). The observed giant star GC37, lies in the Galactic Center field. East is to the left and North straight down. The slit is $40''$.

The reduction of all of the CRIRES observations was accomplished by following standard methods (Smoker et al., 2012) using Gasgano (Klein Gebbinck et al., 2012). Subsequently, we used IRAF (Tody, 1993) to normalize the continuum, eliminate obvious cosmic hits, and correct for telluric lines (with telluric standard stars).

Low spectral resolution VLT/ISAAC observations

We obtained spectra using the red grism of the ISAAC spectrograph (ESO,VLT) covering the wavelength range between $2.00 - 2.53\,\mu\mathrm{m}$. The slit width is $1''$ providing a resolving power of $\mathrm{R} \sim 2000$ and the typical S/N ratio is about 100.

We observed B dwarfs (typically 6-8 stars per night) close to the airmass range of our targets, to use as telluric standard stars to correct for the instrumental and atmospheric transmission. We used IRAF to reduce the ISAAC spectra. We removed cosmic ray events, subtracted the bias level, and then divided all frames by a normalized flat field. We used the traces of stars at two different positions (AB) along the slit to subtract the sky. After extracting and co-adding the spectra, we calibrated wavelengths using the Xe-lamp. The r.m.s of the wavelength calibration is better than 0.5 Å. The spectra were rebinned to a linear scale with a dispersion of ~ 7 Å and a wavelength range from 2.0 μm to 2.51 μm. Each spectrum has been divided by a telluric standard star observed closest in time and in airmass.

Low spectral resolution NTT/SOFI observations

We used the Red Grism of the SOFI spectrograph, covering 1.50–2.53 μm, to observe our M giant sample. We took the spectra with a 1″ slit providing a resolving power of R ~ 1000. We obtained a $K_{\rm S}$-band acquisition image before each spectrum to identify the source and place it on the 90″ slit. We used UKIDSS finding charts for source identification and to choose 'empty' sky positions for optimal sky subtraction.

We observed B dwarfs (typically 6-8 stars per night), close to the airmass range of our targets, as telluric standard stars to correct for the instrumental and atmospheric transmission. We used `IRAF` to reduce the SOFI spectra. We removed cosmic ray events, subtracted the bias level, and then divided all frames by a normalized flat-field. We used the traces of stars at two different (AB) positions along the slit to subtract the sky. After extracting and co-adding the spectra, we calibrated wavelengths using the Xe-lamp. The r.m.s of the wavelength calibration is better than 1 Å. We re-binned the spectra to a linear scale, with a dispersion of ~ 10 Å/pixel. We then divided each spectrum by the telluric standard observed closest in time and in airmass (airmass difference < 0.05). We then normalized the resulting spectra by the mean flux between 2.27 and 2.29 μm.

3.3 Analysis

In order to determine the abundances from our spectra, we first have to determine the fundamental parameters of the stars. These are the effective temperatures ($T_{\rm eff}$), surface gravities ($\log g$), metallicities ([Fe/H]), and microturbulences ($\xi_{\rm micro}$). With these parameters, we can synthesize model spectra for the stars, based on spherical model atmospheres and an appropriate line list with atomic and molecular lines. In the following sections, we will describe the procedure to determine the fundamental stellar parameters and the abundances of iron (metallicity), silicon, and magnesium from our spectra.

3.3.1 SME

We have used the package Spectroscopy Made Easy (SME) (Valenti and Piskunov 1996, 2012; Piskunov and Valenti 2017) for the spectral synthesis and the abundance analysis. Among the model libraries available with the SME, a grid of MARCS spherical-symmetric, LTE model atmospheres (Gustafsson et al., 2008) have been used in this work to generate synthetic spectra for a given set of fundamental, stellar parameters. SME has two main components : the graphical user interface (GUI) written in IDL and solver that performs the calculations, either the spectral synthesis or the fit to an observed spectrum. The GUI expects the user to provide as input, the global stellar parameters ($T_{\rm eff}$, $\log g$, metallicity, and radial velocity), line data (see Section 3.3.2), spectral intervals, and line broadening parameters (macro- and micro-turbulence, *v*sini, and instrumental profile). Synthetic spectra are generated by solving for molecular and ionization equilibrium, radiative transfer equations as well as computing continuous and line opacities. The procedure to fit observed spectrum with SME is explained below.

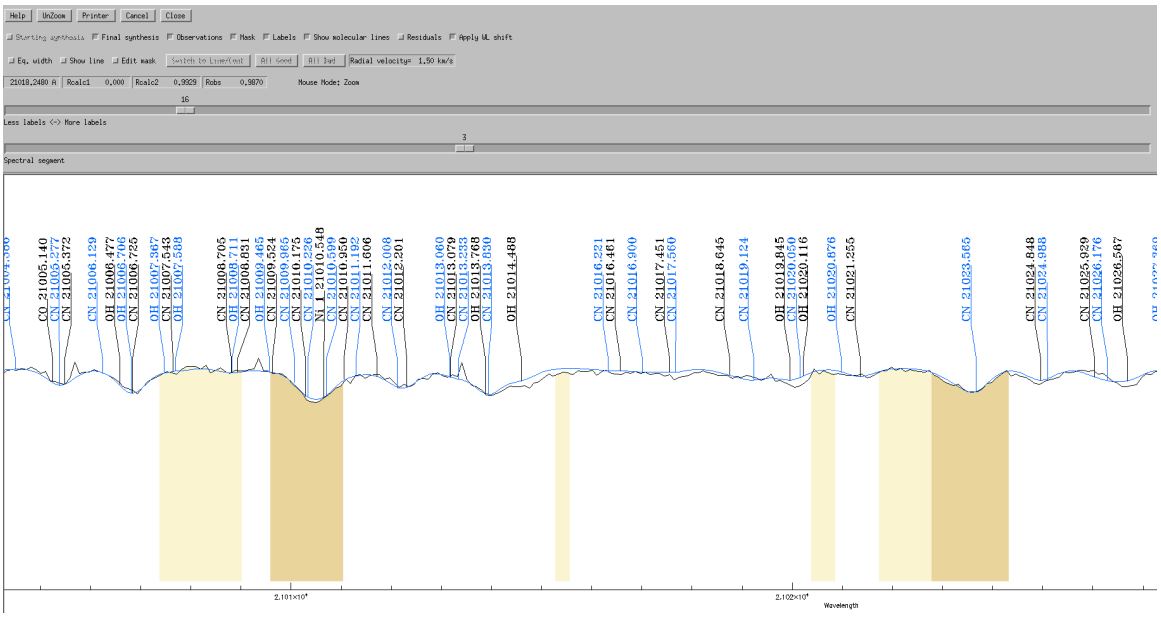

Figure 3.6: The SME interface with the synthetic spectrum fit (blue line) to a typical observed spectrum (black line). The dark orange coloured regions represent the masks used to define the chosen lines of interest and those in light orange colour represent the chosen continuum regions.

The spectral lines of interest are marked with masks to indicate the parts of the lines that should be modeled and compared with the observed spectra. In a similar fashion, we also marked regions, around the lines being analyzed with masks, that should be treated by the SME as continuum regions. These are used for a final, local continuum normalization. Figure 3.6 shows the synthetic spectrum fit for a typical observed spectrum in the SME interface and the masks used to define the chosen lines of interest as well as the continuum regions. Abundances or any other parameters to be determined are set as free variables, for which SME synthesizes spectra in an iterative manner following an approach that minimizes the χ^2 by comparing the synthesized with the observed spectrum.

3.3.2 K-band line list

The line list used in the K band is based on an extraction from the VALD3 database (Piskunov et al., 1995; Kupka et al., 1999; Ryabchikova et al., 1997; Kupka et al., 2000; Ryabchikova et al., 2015), but with updated values of wavelengths and line-strengths from recent experimentally and theoretically determined atomic line-strengths of Mg (Civiš et al., 2013; Pehlivan Rhodin et al., 2017), as well as of Si (Pehlivan et al., 2018, in prep.). Furthermore, astrophysical $\log gf$-values are determined and wavelengths corrections are applied by fitting the solar center intensity atlas of Livingston and Wallace (1991). Of approximately 700 interesting spectral lines for cool stars identified in the K band, 570 lines have been assigned new values.

The Fe, and Si abundances are determined from between 2-6 lines depending on star, telluric lines, radial velocities, and spectral quality. The Mg abundance is determined from

two quite strong spectral features consisting of two fine-structure groups of 4f-7g lines at 21059 – 21061 Å. Since the pressure-broadening obviously affects this feature, we made calculations based on the Kaulakys method (Kaulakys (1985, 1991)), as described in Osorio et al. (2015). The line broadening cross section, σ, at a relative speed of 10^4 m s^{-1} (see Anstee and O'Mara, 1991; Barklem and O'Mara, 1998; Barklem et al., 2000) is found to be 2917 au [atomic units], expected to be accurate to 20-50%, and the calculations indicate a roughly a flat temperature dependence, which was adopted in the calculations.

In the abundance analysis, we also include molecular line lists of the CN molecule (Sneden et al., 2014).

3.3.3 Stellar parameters

We determined stellar parameters in a similar way as for the Southern fields in Ryde et al. (2016b) using the relation between effective temperature and the ^{12}CO band-head at 2.3 μm. This tight relation between $T_{\rm eff}$ and ^{12}CO is based on the low resolution (ISAAC) spectroscopic observations of 20 well studied M giant stars in the Galactic bulge (Schultheis et al., 2016). This relation is as follows :

$$T_{\rm eff} = 4974.85 - 56.53 \times^{12} CO(3-1) \tag{3.1}$$

where ^{12}CO$(3-1)$ represent the equivalent width of the ^{12}CO band-head at 2.3 μm measured using the Blum et al. (2003) bandpasses and continuum points. In addition we determined photometric effective temperatures from the dereddened J_0 and K_0 photometry for stars that have no low resolution observations.

The surface gravities were determined by the iterative method described in Rich et al. (2017), who demonstrated that this method determines surface gravities with a precision better than 0.3 dex compared to an APOGEE data set. In short, we proceed as follows: we start off from a rough photometric estimate of the surface gravity by using H and K band photometry, extinction values (quite uncertain) from Gonzalez et al. (2012), and bolometric corrections from Houdashelt et al. (2000). For this, we assumed a solar value of $\rm T_{\odot}$=5770 K, $\log g_{\odot}$=4.44, $\rm M_{\odot}^{bol}$ =4.75, and a mass of our giants of 1.0 $M_{\odot}$. With this surface gravity, a first metallicity estimate can be determined from our high-resolution CRIRES spectra as explained in the section 3.3.4. A better estimate of the $\log g$ is subsequently found from the isochrone for a given $T_{\rm eff}$ and [Fe/H]. We then use this new $\log g$ to redetermine the [Fe/H] value. This procedure is iterated a few times until it converges. A schematic block diagram of the procedure to determine the stellar parameters is shown in the Figure 3.7 and an example in the corresponding HR diagram in the Figure 3.8.

The microturbulence, $\xi_{\rm micro}$, that takes into account the small-scale, non-thermal motions in the stellar atmospheres, is important for saturated lines, influencing their line strengths. We estimate this parameter from an empirical relation with the surface gravity based on a detailed analysis of spectra of five red giant stars ($0.5 < \log g < 2.5$) by Smith et al. (2013), as described in Rich et al. (2017). Our derived stellar parameters for all our stars are given in Tables 3.3 and 3.4.

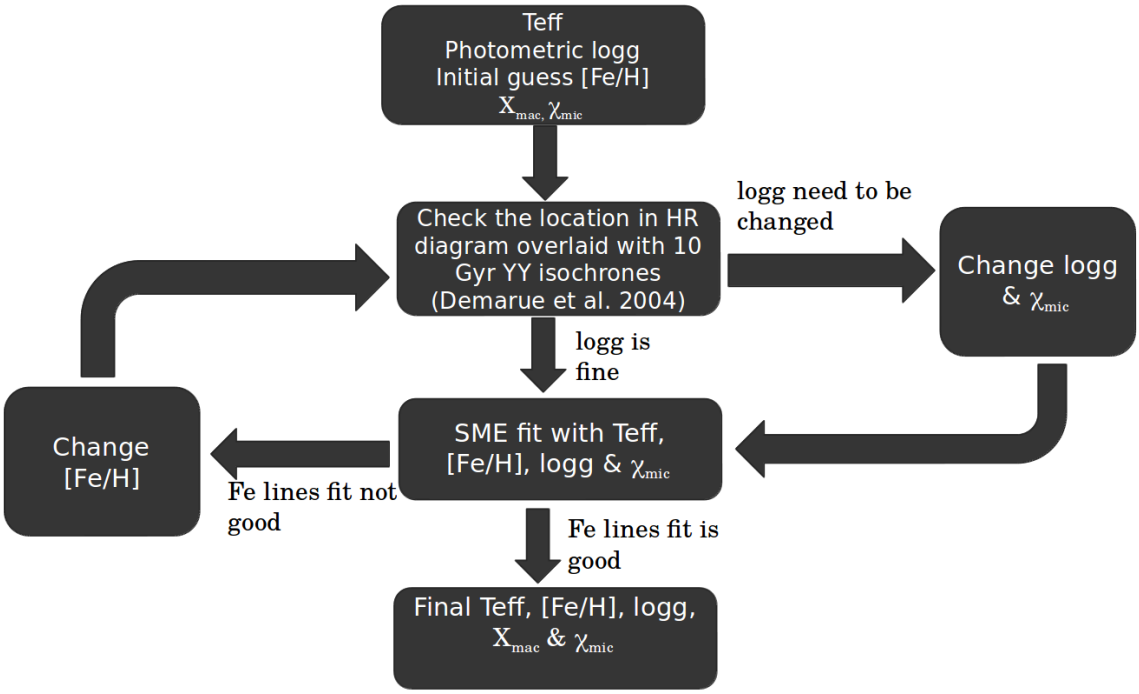

Figure 3.7: Schematic block diagram of the procedure to determine the stellar parameters.

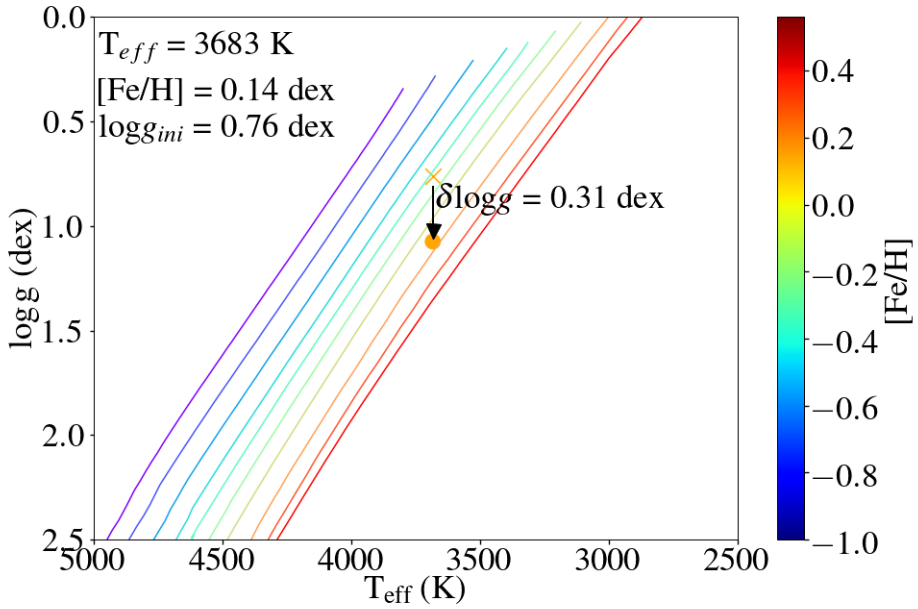

Figure 3.8: Example HR diagram showing the case where the assumed initial value of $\log g$ has to be increased by 0.31 dex so that the star lies on the correct isochrone track.

Table 3.3: The derived stellar parameters and abundances for the observed stars in the Northern fields.

Star	RA (J2000) (h:m:s)	Dec (J2000) (d:am:as)	$T_{\rm eff}$ [K]	$\log g$ (cgs)	[Fe/H]	$\xi_{\rm macro}$ [km s^{-1}]	[Si/Fe]	[Mg/Fe]
Northern field at $(l, b) = (0°, +3°)$								
bp3-01	17:34:05.20	-27:19:58.20	3780	0.79	−0.60	6.7	+0.20	+0.20
bp3-02	17:34:19.24	-27:20:42.70	4111	1.90	+0.20	5.6	−0.12	−0.10
bp3-04	17:34:09.23	-27:22:38.00	3623	0.94	+0.10	7.3	+0.05	0.00
bp3-05	17:34:00.71	-27:18:59.60	3879	1.55	+0.30	5.4	−0.20	−0.10
bp3-06	17:34:07.13	-27:22:28.90	3755	0.68	−0.70	5.8	+0.20	+0.30
bp3-07	17:34:24.09	-27:23:16.70	3962	1.70	+0.30	4.9	−0.10	0.00
bp3-08	17:34:16.44	-27:24:34.30	3637	1.12	+0.30	4.9	−0.20	0.00
bp3-10	17:34:13.70	-27:24:31.00	4052	1.70	+0.10	5.3	−0.10	+0.10
bp3-11	17:33:58.67	-27:20:30.20	3542	0.66	+-0.10	6.8	−0.10	0.00
bp3-12	17:34:06.61	-27:19:29.30	3966	1.45	−0.05	7.2	0.00	+0.10
bp3-13	17:34:08.21	-27:22:58.70	3625	0.74	−0.20	5.2	−0.05	0.00
bp3-14	17:33:57.31	-27:21:07.60	3569	0.92	+0.20	9.2	−0.20	−0.10
bp3-15	17:34:06.52	-27:22:30.20	3610	0.56	−0.50	6.3	+0.20	+0.10
bp3-16	17:34:15.46	-27:22:30.90	3654	0.85	−0.10	8.4	+0.10	+0.20
bp3-17	17:34:03.57	-27:18:49.60	3946	1.52	+0.10	7.5	−0.10	−0.10
Northern field at $(l, b) = (0°, +2°)$								
bp2-01	17:37:49.64	-27:51:05.50	4054	1.95	+0.40	6.1	−0.10	−0.05
bp2-02	17:38:02.25	-27:52:31.40	3838	1.60	+0.50	5.9	−0.20	−0.10
bp2-03	17:37:58.65	-27:51:40.90	3889	1.70	+0.60	7.4	−0.10	−0.25
bp2-04	17:38:02.12	-27:52:49.80	4134	1.74	−0.10	6.5	0.00	+0.05
bp2-05	17:37:53.31	-27:52:01.10	4079	1.40	−0.50	4.9	+0.20	+0.40
bp2-06	17:37:51.19	-27:54:01.70	3962	1.17	−1.80	7.8	+0.20	+0.40
bp2-07	17:37:58.13	-27:53:42.60	4320	1.84	−0.50	5.8	+0.10	+0.10
bp2-08	17:37:56.88	-27:51:52.80	3808	1.38	+0.25	4.0	−0.15	+0.20
bp2-09	17:37:50.52	-27:54:24.60	3813	0.70	−0.80	6.2	+0.15	+0.20
bp2-10	17:38:01.25	-27:55:38.40	3774	1.28	+0.20	4.8	0.00	0.00
bp2-11	17:38:00.03	-27:55:45.00	3645	1.26	+0.50	5.3	−0.30	+0.10
bp2-12	17:38:02.01	-27:53:30.70	4032	1.54	−0.10	8.4	0.00	0.00
bp2-13	17:38:02.54	-27:55:42.50	3899	1.12	−0.40	5.5	+0.15	+0.30
bp2-14	17:38:01.74	-27:55:56.10	3559	1.00	+0.30	5.4	−0.10	0.00
bp2-15	17:38:13.55	-27:53:41.40	4237	1.69	−0.50	6.7	+0.13	+0.20
Northern field at $(l, b) = (0°, +1°)$								
bp1-01	17:41:57.26	-28:28:46.50	3918	1.54	+0.20	5.6	0.00	0.00
bp1-02	17:41:57.62	-28:28:51.60	4311	1.89	−0.40	6.0	+0.10	+0.10
bp1-03	17:41:58.61	-28:28:46.80	3948	1.75	+0.40	4.8	−0.10	−0.20
bp1-04	17:41:55.92	-28:27:03.80	4060	1.66	+0.00	6.6	−0.15	0.00
bp1-05	17:41:59.76	-28:27:36.20	3731	1.30	+0.30	4.6	−0.10	+0.20
bp1-06	17:41:57.66	-28:27:07.20	3863	1.50	+0.30	7.4	−0.06	−0.10
bp1-07	17:42:03.59	-28:27:18.20	4209	1.58	−0.60	5.9	+0.10	+0.30
bp1-08	17:41:58.51	-28:26:18.70	4242	1.63	−0.60	7.2	+0.14	+0.30
bp1-09	17:42:04.43	-28:26:55.60	3494	0.79	+0.20	5.2	−0.10	−0.15
bp1-10	17:42:06.49	-28:27:09.10	3879	1.50	+0.20	5.7	−0.13	+0.10
bp1-11	17:41:59.06	-28:26:03.90	4352	1.90	−0.50	7.3	+0.18	+0.20
bp1-12	17:41:58.72	-28:25:58.80	4175	1.95	+0.10	6.4	0.00	+0.05
bp1-13	17:42:05.96	-28:26:59.10	4151	1.47	−0.60	6.9	+0.10	+0.20
bp1-14	17:42:10.05	-28:25:36.90	4070	1.70	+0.00	5.4	−0.06	+0.10

Table 3.4: The derived stellar parameters and abundances for the observed stars in the Southern fields.

Star	RA (J2000) (h:m:s)	Dec (J2000) (d:am:as)	$T_{\rm eff}$ [K]	$\log g$ (cgs)	[Fe/H]	$\xi_{\rm macro}$ [km s^{-1}]	[Si/Fe]	[Mg/Fe]
Galactic Centre field at $(l, b) = (0^\circ, 0^\circ)$								
GC1	17:45:35.43	-28:57:19.28	3668	1.25	+0.40	5.0	−0.17	+0.10
GC20	17:45:34.95	-28:55:20.17	3683	1.33	+0.50	7.3	−0.17	−0.10
GC22	17:45:42.41	-28:55:52.99	3618	1.00	+0.20	5.5	−0.10	+0.10
GC25	17:45:36.34	-28:54:50.41	3340	0.54	+0.20	7.6	−0.20	−0.20
GC27	17:45:36.72	-28:54:52.37	3404	0.64	+0.20	7.2	−0.05	−0.05
GC28	17:45:38.13	-28:54:58.32	3773	1.20	+0.10	5.9	−0.10	+0.20
GC29	17:45:43.12	-28:55:37.10	3420	0.65	+0.18	8.1	−0.25	−0.10
GC37	17:45:35.94	-28:58:01.43	3754	1.33	+0.30	7.2	−0.08	−0.05
GC44	17:45:35.95	-28:57:41.52	3465	0.89	+0.40	7.5	−0.20	−0.10
Southern field at $(l, b) = (0^\circ, -1^\circ)$								
bm1-06	17:49:33.42	-29:27:28.75	3814	1.56	+0.50	4.6	−0.30	−0.20
bm1-07	17:49:34.58	-29:27:14.82	3873	1.38	+0.08	5.7	−0.06	+0.10
bm1-08	17:49:34.34	-29:26:57.98	3650	1.10	+0.24	4.2	−0.05	−0.05
bm1-10	17:49:34.45	-29:26:48.68	3787	1.09	−0.10	7.3	+0.05	+0.20
bm1-11	17:49:32.57	-29:26:30.75	3812	1.35	+0.20	4.1	−0.10	0.00
bm1-13	17:49:37.12	-29:26:40.24	3721	0.46	−0.91	6.1	+0.20	+0.50
bm1-17	17:49:37.08	-29:26:21.67	3775	0.65	−0.79	7.3	+0.25	+0.40
bm1-18	17:49:37.83	-29:26:19.19	3780	1.28	+0.18	3.3	−0.10	0.00
bm1-19	17:49:36.93	-29:26:10.51	3958	1.77	+0.40	5.0	−0.20	−0.10
Southern field at $(l, b) = (0^\circ, -2^\circ)$								
bm2-01	17:53:29.06	-29:57:46.22	3946	1.33	−0.19	4.3	+0.10	+0.30
bm2-02	17:53:24.59	-29:59:09.48	4013	1.51	−0.10	6.8	−0.10	+0.15
bm2-03	17:53:27.61	-29:58:36.39	3668	1.25	+0.40	4.9	0.00	—
bm2-05	17:53:33.20	-29:57:25.88	3450	0.64	+0.10	6.3	−0.05	−0.05
bm2-06	17:53:30.68	-29:58:15.75	4208	1.26	−1.00	6.8	+0.20	+0.50
bm2-11	17:53:31.50	-29:58:28.51	4005	1.20	−0.60	7.2	+0.25	+0.30
bm2-12	17:53:31.74	-29:58:22.94	4003	1.67	+0.15	6.3	−0.30	−0.15
bm2-13	17:53:31.14	-29:57:32.76	3727	0.94	−0.17	6.9	+0.13	+0.40
bm2-15	17:53:30.23	-29:56:42.74	3665	1.09	+0.20	5.6	0.00	+0.30
bm2-16	17:53:29.54	-29:57:22.71	3886	1.38	+0.06	3.14	−0.02	—

3.3.4 Stellar abundances

As mentioned above, once we have determined the $T_{\rm eff}$, an approximate [Fe/H], initial photometric $\log g$-estimate, and the corresponding $\xi_{\rm micro}$ for our stars, we made use of our high resolution spectra to iteratively determine their final metallicities. Subsequently we can then determine the α-element abundances (Si and Mg).

Since SME compares the strengths and forms of observed spectral lines with the synthesized ones (within the defined masks), the line profiles have to be accurately characterized and the line broadening well determined. Extra broadening not accounted for by the synthesis, is the *stellar* macroturbulence $\xi^{\rm stellar}_{\rm macro}$, but also the instrumental profile, which is set by the instrumental resolution. We estimate this extra *total* broadening (which is a convolution of the both) for each of our stars by fitting a few selected well-formed, medium-weak lines while setting '$\xi_{\rm macro}$' as a free parameter in a SME run and assuming both broadening profiles to be Gaussian in shape. We then get the total macroturbulences for our stars, $\xi_{\rm macro}$, which are given in Tables 3.3 and 3.4.

Subsequently, we ran SME for each star with the above mentioned parameters, letting SME perform a χ^2 minimization to fit Fe lines in the spectra that are of sufficient quality, in shape and form (due to their strengths for a given SNR), for retrieving an abundance. We then adjusted the [Fe/H] value based on the fit, simultaneously changing to a new $\log g$-estimate based on the position on the isochrone tracks, and a corresponding $\xi_{\rm micro}$ from the Smith et al. (2013) relation. This is repeated until the stellar parameters are consistent with the corresponding isochrone in the HR diagram. Figure 3.9 shows the HR diagram with the locations of our stars on the 10 Gyr YY isochrones (Demarque et al., 2004), color coded with their determined metallicities. With the fundamental stellar parameters thus determined, we proceeded to determine the [Si/Fe] and [Mg/Fe] using SME with similarly selected Si and Mg lines.

The final metallicities and Si and Mg abundances are given in Tables 3.3 and 3.4.

3.3.5 Uncertainties

It has been shown in Rich et al. (2017); Ryde et al. (2016b) that the uncertainties in the derived metallicities arise partly from the fitting procedure and partly from the uncertainties in the derived stellar parameters like $T_{\rm eff}$, $\log g$, and $\xi_{\rm micro}$. The systematic uncertainties due to the noise in the spectra, telluric residuals and the uncertainty in continuum level is assumed to be of the order of 0.15 dex. When observing our stars we aimed for a S/N of 60-70 per pixel, which means that the uncertainties are of similar magnitudes for all the stars. For a few stars (e.g. GC25 and GC44) the S/N is lower, and these uncertainties can therefore be larger.

Even though the above mentioned studies have explored the uncertainty in metallicity due to a variation in stellar parameters for individual stars of a given $T_{\rm eff}$ and metallcity, the variation of the uncertainty in metallicity determination for a range of metallicities and $T_{\rm eff}$ has been relatively unstudied. We have carried out such an investigation in Section 3.3.5.2.

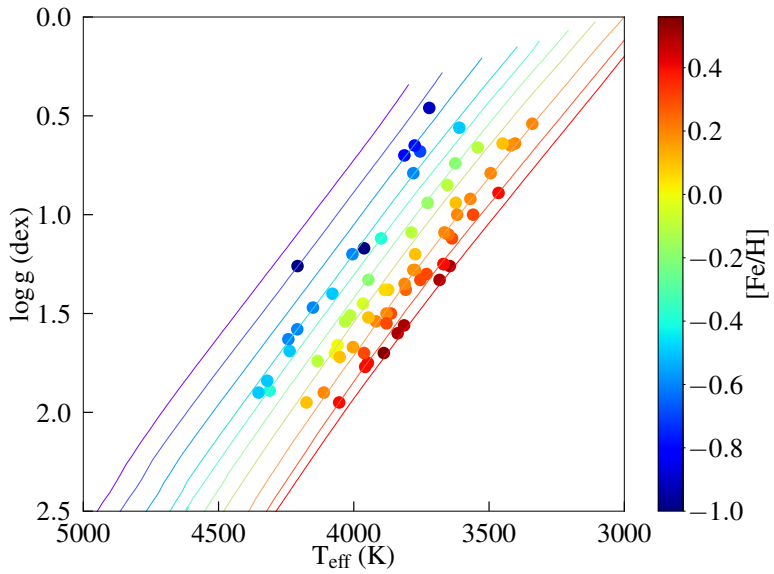

Figure 3.9: $T_{\rm eff}$ vs $\log g$ diagram showing the position of our sample of stars on different metallicity tracks of the 10 Gyr YY isochrone (Demarque et al., 2004). Each star is color coded with their determined [Fe/H] values.

3.3.5.1 General uncertainties

The abundance is given by the line strength, which is the contrast between the continuum and the line center. Not only the determination of the continuum level in the observations, which can be difficult depending on SNR and spurious feature in the spectrum, is crucial, but also the calculation of the continuous opacity in the generation of the synthetic spectra is important. For a typical star in our sample, the continuous opacity is due to H^- free-free opacity, which is affected by the electron density. This is given by the major electron donors in the line-forming regions of the star, which are magnesium (1/2 of all electrons), iron (1/3 of electrons), and Si (1/10). Thus, it is especially important to know the magnesium abundance for an accurate abundance determination of any element. We have taken the general α-element trend vs. metallicity for bulge stars into account in order to minimize this effect. Also, special care has been taken to find good continuum points.

As described above, the way SME works by fitting the shape of the line, the determined abundance is sensitive to the line broadening adopted, most importantly the macroturbulence but also the pressure broadening for strong lines, like the Mg lines used in this study. We have therefore invested considerable effort to estimate the broadening as accurately as possible.

Most line strengths in our line list, are determined from the solar spectrum (astrophysical gf-values). We have also tested the list against the spectra of the metal-poor, ~4800 K giant α Boo, and the metal-rich giant μ Leo. There might, however, be non-LTE, saturation, or 3D effects that are not taken into account which might affect different type of stars differently, see Rich et al. (2017) for a discussion. We have avoided spectral lines that we suspect are affected by these issues.

As mentioned above, we estimate the total uncertainty due to the fitting procedure to approximately 0.15 dex.

3.3.5.2 Uncertainties related to stellar-parameters

We synthesized a grid of test spectra of similar spectral resolution as that of our observed spectra, with metallicities of -0.8, -0.5, -0.3, 0.0, 0.3, 0.5 dex, each with $T_{\rm eff}$ of 3500, 3900, 4300 K. For each of these test spectra, we determined the surface gravities and the corresponding microturbulence in the same way as for our observed spectra (see Section 3.3.3).

For each of the test spectra, we varied $T_{\rm eff}$ by the typical uncertainty from the low-resolution, CO-bandhead estimate, namely ±150 K, changed $\log g$ as well as $\xi_{\rm micro}$ correspondingly, and then ran SME with these parameters, setting [Fe/H] as free parameter. This exercise was carried out for each of the three $T_{\rm eff}$ cases for all six [Fe/H] values, thus covering the full range of fundamental stellar parameters of our observed sample. The difference between the actual [Fe/H] and that estimated by SME gives us the typical uncertainty in [Fe/H] that arises from the combination of errors in $T_{\rm eff}$, $\log g$, and $\xi_{\rm micro}$. The same exercise was carried out to estimate the typical uncertainty in [Mg/Fe] by setting Mg as the free parameter. Table 3.5 lists the final estimated error in [Fe/H] and [Mg/Fe] , and we plot them in Figure 3.10. The typical change in $\log g$ ranges from ±0.25 to 0.37 dex and in $\xi_{\rm micro}$ from -0.2 to $+0.2$ km s^{-1}, for a ±150 K change in $T_{\rm eff}$. The maximum values of [Fe/H] uncertainties are of the order of 0.2 dex, found partly at the lowest metallicity and partly at low $T_{\rm eff}$, whereas the maximum uncertainty of [Mg/Fe] of the same order, is found at supersolar metallicities.

Indeed, one could suspect that there should be a systematic trend in the uncertainties due to the line strength. Lines tend to get weaker for more metal-poor stars ($T_{\rm eff}$ and $\log g$ may, however, also play a role). Thus, for a given SNR, metal-poor stars might have weaker lines, and therefore more uncertainty in the derived abundances.

Furthermore, the cooler the star, the stronger the molecular features are, and therefore the quality of the molecular line list is increasingly important. In addition, the continuum determination might be more uncertain. In no case were the molecular lines so dense as to prevent us from identifying continuum points. Hence we do not require pseudo-continua, i.e. a situation where the true continuum is not found but many weak lines blend into each other forming flat regions, resembling a continuum.

Also, for more metal-rich stars, there might be a problem with saturation of the lines, especially for the strong Mg lines, which get increasingly saturated and therefore less abundance sensitive.

However, from Table 3.5 and Figure 3.10 we see that the uncertainties do *not dramatically* increase neither towards the metal-poor regime, nor the metal-rich one, which is reassuring. Nevertheless we find that warmer stars have generally lower abundances uncertainties, less than 0.1 dex.

We conclude that apart from more systematic uncertainties (e.g. continuum placement) the typical abundance uncertainties are due to errors in the stellar parameters, which are ~<0.1 dex. We have somewhat higher errors for stars with [Fe/H]<-0.5 dex, and further, the

Table 3.5: Uncertainties in the derived metallicities and magnesium abundances due to uncertainties in $T_{\rm eff}$ of ± 150 K, corresponding change in $\log g$ and $\xi_{\rm micro}$. This was estimated using synthetic spectra with metallicities in the range of -0.8, -0.5, -0.3, 0.0 ,0.3 and 0.5 dex each with $T_{\rm eff}$ of 3500, 3900 and 4300 K, that represent the stars in our sample.

[Fe/H]	$T_{\rm eff}$	$\delta\, T_{\rm eff}$	$\delta \log g$	$\delta\, \xi_{\rm micro}$	δ [Fe/H]	δ [Mg/Fe]
-0.8	3900	-150	-0.27	+0.1	-0.07	-0.04
		+150	+0.27	-0.2	+0.19	+0.10
	4300	-150	-0.27	0.0	+0.01	+0.07
		+150	+0.28	-0.1	+0.09	+0.06
-0.5	3500	-150	-0.25	+0.1	-0.06	+0.03
		+150	+0.25	-0.2	+0.03	-0.01
	3900	-150	-0.27	+0.1	-0.09	-0.04
		+150	+0.28	-0.2	+0.07	+0.11
	4300	-150	-0.28	+0.1	-0.07	-0.03
		+150	+0.29	0.0	+0.06	+0.01
-0.3	3500	-150	-0.24	+0.1	-0.10	0.00
		+150	+0.25	-0.2	-0.02	-0.06
	3900	-150	-0.27	+0.1	-0.14	-0.11
		+150	+0.28	-0.1	-0.03	-0.06
	4300	-150	-0.28	+0.1	-0.09	-0.04
		+150	+0.29	0.0	+0.05	-0.02
0.0	3500	-150	-0.24	+0.1	+0.02	+0.10
		+150	+0.26	-0.2	+0.05	-0.01
	3900	-150	-0.28	+0.1	-0.01	-0.05
		+150	+0.28	0.0	+0.02	-0.17
	4300	-150	-0.30	0.0	-0.06	+0.04
		+150	+0.31	-0.1	+0.07	0.00
0.3	3500	-150	-0.25	-0.1	0.00	+0.06
		+150	+0.26	-0.2	+0.17	+0.08
	3900	-150	-0.27	0.0	-0.01	+0.18
		+150	+0.28	-0.1	+0.04	-0.05
	4300	-150	-0.31	+0.1	-0.06	+0.06
		+150	+0.36	0.0	+0.08	-0.06
0.5	3500	-150	-0.26	+0.1	-0.05	+0.06
		+150	+0.26	-0.1	+0.06	+0.11
	3900	-150	-0.27	+0.1	-0.04	+0.09
		+150	+0.27	0.0	+0.06	-0.07
	4300	-150	-0.32	+0.1	-0.07	+0.09
		+150	+0.37	0.0	+0.08	-0.07

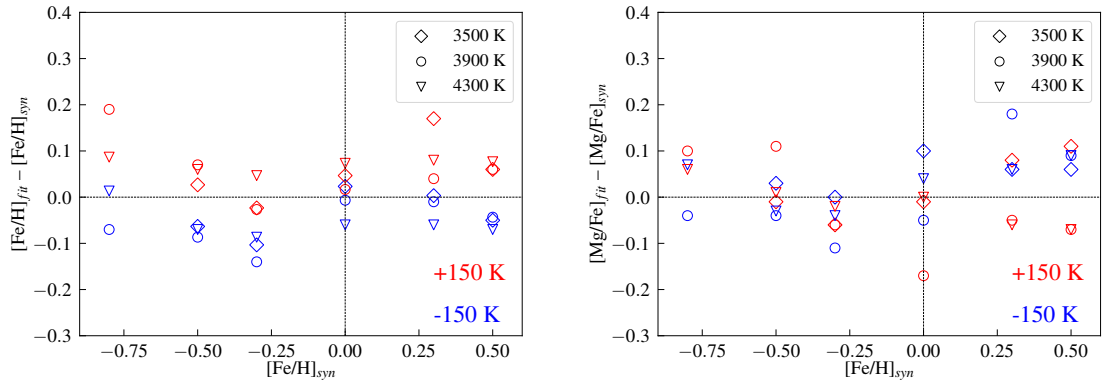

Figure 3.10: Plots showing the trend of [Fe/H] and [Mg/Fe] uncertainties as a function of metallicity for the case of different temperatures covered by our sample. Left panel shows the differences in SME estimated metallicities vs actual metallicities due to uncertainties in $T_{\rm eff}$ of $\pm\,150$ K, corresponding change in $\log g$ and $\xi_{\rm micro}$. Right panel shows the same for magnesium abundances. This was estimated using synthetic spectra with metallicities in the range of -0.8, -0.5, -0.3, 0.0,0.3 and 0.5 dex each with $T_{\rm eff}$ of 3500, 3900 and 4300 K, that represent the stars in our sample.

Mg abundances for the coolest and most metal rich stars are uncertain by ~0.15 dex.

A grand total uncertainty is thus mainly due to systematic fitting errors (Section 3.3.5.1), which leaves us with a total estimate of approximately 0.15 dex.

As a further note of caution, we would also like to point out that isochrones are poorly calibrated at super solar metallicity, i.e., they are mostly extrapolated from the sub-solar regime, especially at old ages. Hence, constraining stellar parameters based on these isochrones can suffer from systematics that cannot be properly quantified yet. In addition, a few tenths of a dex lower gravities for super solar metallicity stars in our sample can lower their metallicities by a few tenths of a dex.

3.4 Homogeneous Analysis of the North-South sample

The 44 giants in the Northern fields are analysed here for the first time. The 28 stars in the Southern fields were first published in Ryde and Schultheis (2015); Ryde et al. (2016b), but are reanalysed here in the same manner as the Northern-field giants, to allow for the whole sample to be analysed as consistently as possible. This will minimize the relative uncertainties and will allow for a comparison between properties of the stars in different fields.

Specifically, the 9 stars in the Galactic center field were first published in Ryde and Schultheis (2015), and the 9 stars at $(l, b) = (0, -1°)$, and 10 stars at $(l, b) = (0, -2°)$ were published in Ryde et al. (2016b). The largest difference between the analyses in these publications and our analysis, is the method we use to determine the surface gravities of the stars. Here, we force the stars to be consistent with isochrones, following the method outlined in

Sections 3.3.3 and 3.3.4, instead of the more uncertain method of assuming the stars to be at a certain distance (8 kpc) and dereddening the photometry. Differences as large as $\Delta \log g$ =0.6 can be found. As described in Schultheis et al. (2017) the latter method can give large uncertainties, since the Galactic bulge shows an intrinsic depth ($\sim 1-2\,\mathrm{kpc}$) which can result in large uncertainties in log g, especially for M giants. We refer here for a more detailed discussion to Schultheis et al. (2017). The new surface-gravity determinations can account for most of the changes in the derived abundances. Furthermore, for a few of the stars a different value of the macroturbulence is determined. Due to the way the χ^2 minimization is done in line masks, the derived abundances are quite sensitive to the broadening fit of the lines. For yet another few stars, most notably GC25 and GC44, the abundance sensitive lines in the spectra are affected by so much noise that the determination is quite uncertain. This was not the case for most of our sample, however.

Thus, we are confident that we can make a comparative study of the stellar properties and the metallicity distributions in the different location along the minor axes, i.e. metallicity gradients, and the symmetries of the Northern fields compared to the Southern fields.

3.5 Results

The final reduced spectra and fitted synthetic spectra for one star in each field are shown in Fig 3.11. The location of several Fe, Si and Mg lines used for our abundance estimation are also shown in the plots. The necessity of requiring high resolution spectra for abundance analysis can be evidently seen, as we are able to clearly separate the molecular CN lines in our spectra. These features can lead to more blending in Fe and Si lines in lower resolution spectra. The stellar parameters for all stars belonging to the Northern and Southern fields along with their derived α-element abundances of [Si/Fe] and [Mg/Fe] are listed in Tables 3.3 and 3.4. They are normalized to the solar abundances of Grevesse et al. (2007).

We plot the MDF of our entire sample in bins of 0.15 dex as shown in Figure 3.12 together with the kernel density estimate (KDE) of the MDF with a bandwidth of 0.15 dex. We see clearly a bimodal distribution, one at metallicity of ~+ 0.3 dex and the other at ~-0.5 dex. An outlier with metallicity of -1.8 dex leads the KDE estimate to find a small peak at this metallicity. Keeping this star aside, the metallicity of our entire inner bulge sample along the bulge minor axis is in the range of -1.0 <[Fe/H] < 0.6 dex.

In Figure 3.13, we show the [Si/Fe] and [Mg/Fe] trends as a function of the metallicity for the entire sample, with the typical uncertainty of 0.15 dex. We find the expected trend of supersolar α-abundances for metal-poor stars, while metal-rich stars show subsolar α-abundances. Though the [Si/Fe] abundances follow this trend, they are systematically lower than [Mg/Fe] values in the subsolar metallicity range. The [Si/Fe] abundances show a lower dispersion than [Mg/Fe] abundances which is most likely due to the fact that we use several Si lines for the Si-abundance while for Mg we use only one line feature. We see clearly that for supersolar metallicities the Si and Mg abundances decrease with increasing metallicity.

In addition, we measured the approximate heliocentric radial velocity, V_R of each star by estimating the difference in the wavelength position of a strong line in their observed spectra

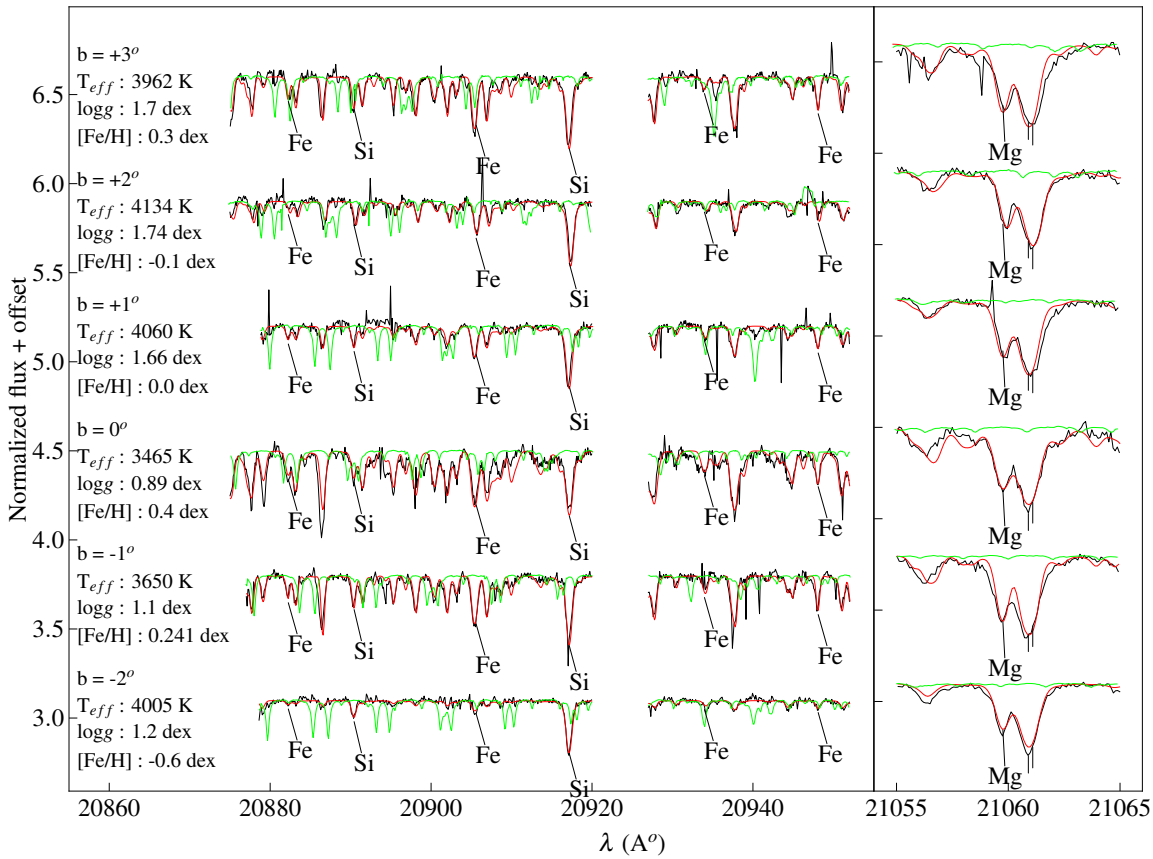

Figure 3.11: Spectra of wavelength regions covering a few Fe lines used for the abundance determination. The latitudes and their stellar parameters of each star are indicated beside each spectrum. Synthetic spectra are shown in red and the telluric lines, shown in green, indicate the areas where they hit the spectrum. Also indicated are two Si lines used in the determination of Si abundance. Rest of the features seen in the spectra are mostly CN molecular lines. This shows how well they are separated from our lines of interest (Fe and Si) indicating the advantages of high resolution spectra and the quality of molecular CN line-lists from Sneden et al. (2014).

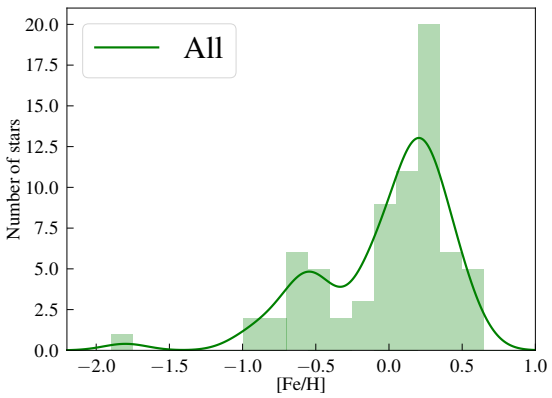

Figure 3.12: MDF for our entire sample in bins of 0.15 dex, overlaid with kernel density estimate (KDE) with bandwidth of 0.5 dex (green line).

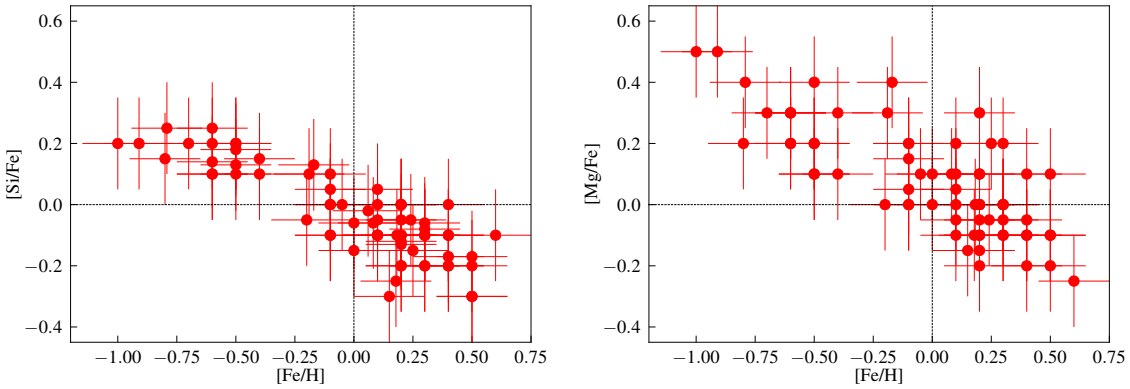

Figure 3.13: The [Si/Fe] (top panel) and [Mg/Fe] (bottom panel) trends as a function of the metallicity for the entire sample, with the typical uncertainty of 0.15 dex

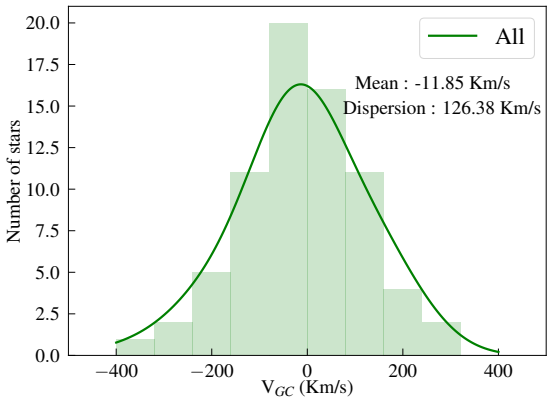

Figure 3.14: Galacotcnetric radial velocity distribution for our entire sample in bins of 80 kms^{-1}, overlaid with KDE with the same bandwidth. The mean and dispersion estimated for the sample are indicated in the plot.

with that from the laboratory measurement (Mg line at 21061.095 nm). Based on spectral resolution, one pixel in velocity space corresponds to ~3 kms^{-1}, which can be considered to be the typical uncertainty in V_R. We converted this to Galactocentric radial velocity, V_{GC}, by adopting the local standard of rest velocity at the Sun to be 220 kms^{-1} and a solar peculiar velocity of 16.5 kms^{-1} in the direction (l,b) = (53°,5°) (Ness et al., 2013b).

$$V_{GC} = V_R + 20\,[\sin(l)\cos(b)] + 16.5[\sin(b)\sin(25) + \cos(b)\cos(25)\cos(l-53)] \quad (3.2)$$

We show the Galactocentric radial velocity distribution for our entire sample in Figure 3.14. We find a mean value of -12 kms^{-1} with a dispersion of 126 kms^{-1}.

3.6 Discussion

Here, we will discuss and compare our results with other literature studies carried out in the inner and outer Galactic bulge fields. We also investigate for the first time, the symmetry in MDF and α abundance trends between the Northern and Southern fields of inner Galactic bulge.

3.6.1 MDF

From Figure 3.12, we find that the inner bulge MDF shows a bimodal distribution or the presence of two components. On the other hand, Rich et al. (2007, 2012) did not find a bimodal metallicity distribution based on their detailed abundance analysis of 61 M giants located at (l, b)=$(0°, -1°)$, $(0°, -1.°75)$, $(0°, -2.°75)$ and Baade's window fields for the combined case as well as for individual fields. They find a mean metallicity of around -0.2 dex with a typical dispersion of 0.15 dex. A different targeting strategy could be the reason for their absence of metal-rich stars. Babusiaux et al. (2014) also found no clear bimodality in the MDF of red clump stars located at the Northern field, (l, b) = $(0°$,+$1°)$. However their spectra were of much lower spectral resolution ($R \sim 6500$), with low signal-to-noise ratio and the individual [Fe/H] measurement errors were larger, of the order of at least 0.2 dex. In general, a larger sample would be required to assert bimodality; moreover, one would expect correlation with some additional physical parameter, such as radial velocity, proper motion, or composition.

The Baade Window field, one of the most observed Galactic bulge fields in terms of chemical abundances and global metallicities, reveals two components in their MDF (Schultheis et al. 2017; Hill et al. 2011) but these components are not established by other physical properties. Bimodality in the MDF is also seen in recent studies using much larger samples of stars in the inner and outer bulge fields (Zoccali et al. 2017; Rojas-Arriagada et al. 2017). Zoccali et al. (2017), using red clump stars in GIBS survey, also at a lower spectral resolution ($R \sim 6500$), using the Calcium II triplet (CaT) feature at ~ 9000 Å, found a bimodality in their MDF for fields similar to b=$-1°$ and b=$-2°$, though we do not have enough number statistics in each field to reproduce and compare it with. These authors also found a bimodal MDFs for the outer bulge fields centered at (l, b) = $(0°, -6°)$ and $(0°, -8°)$ with the metal

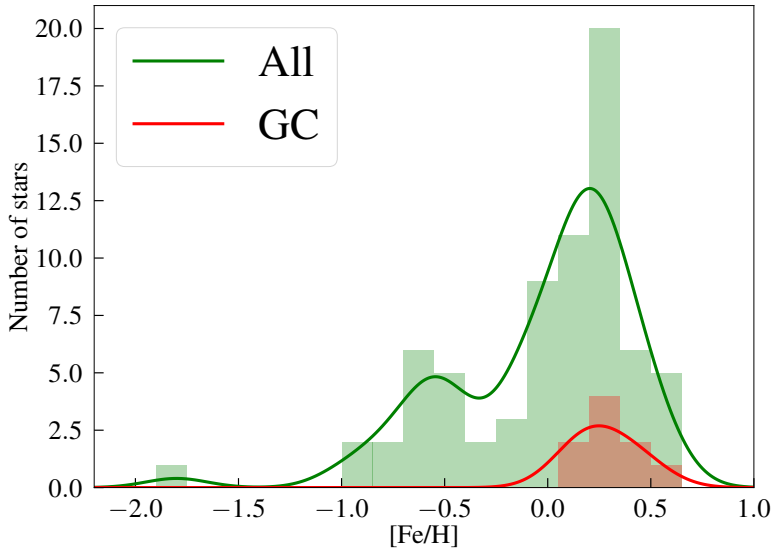

Figure 3.15: MDF of the Galactic center sample (red) in comparsion with that of the entire sample (green). Galactic center stars in our sample are all metal rich. Overlaid KDEs,shown in respective colors, use the same bandwidth as binsizes of the histograms.

rich fraction getting lower as we move away from the Galactic mid-plane. Similar results were obtained by Rojas-Arriagada et al. (2017) using the derived metallicities of red clump stars from the Gaia-ESO survey for the outer bulge fields. Both the above mentioned studies assumed a Gaussian distribution for the bimodal components and used a Gaussian Mixture Model (GMM) to characterize them. Since our sample size is small and the GMM method requires a larger sample size, we prefer to use a simple KDE analysis for our MDF.

We show the entire MDF in Figure 3.15 along with the distribution in red showing the MDF of the Galactic Center sample. We find that all GC stars do have super-solar metallicities with a mean metallicity of ~+0.3 dex and a tight dispersion of ~ 0.10 dex. Our peak metallicity value at the GC is consistent with that from the GC field of APOGEE (Schultheis et al., 2015). A large fraction of super-solar stars has been found by Feldmeier-Krause et al. (2017) based on low-resolution spectra in the nuclear star cluster. We will discuss in a forthcoming paper the chemical similarities as well as differences between the nuclear star cluster, the Galactic Center field population and the inner Galactic bulge. Our high resolution study does not confirm the large number of stars with [Fe/H]> $+0.55$ dex found by Do et al. (2015) and Feldmeier-Krause et al. (2017). We suspect that many abundances derived at low resolution using Bayesian code such as employed in this study will be too high at the metal rich end, perhaps due to a lack of appropriate templates. For cool stars of high metallicity, there is substantial risk of blends, especially with molecules, that can result in spuriously high abundance estimates based on low resolution spectra.

Feldmeier-Krause et al. (2017) do also report stars at low metallicity -1.6 <[Fe/H]< 0.8 dex, whereas we do not find any subsolar metallicty star in our GC sample. However, the APOGEE stars in Schultheis et al. (2015) are mainly located at $|b| > 0.^{\circ}5$ and do not

cover the actual GC region. We also want to stress that our GC sample consists of only nine stars. Clearly more observations are needed to confirm the absence of metal-poor stars in the Galactic center.

We also find the median, over-all metallicity in each field to decrease as we move outward from the Galactic mid-plane. Note, however, that the form of the distribution changes too. This confirms the presence of a negative vertical over-all metallicity gradient in the inner bulge fields as it has been found for the low extinction fields of the outer bulge (Zoccali et al. 2008a; Gonzalez et al. 2011; Ness et al. 2013a). There is one star in our b=+2° field that is very metal poor ([Fe/H]= -1.8) compared to our bulge sample. Our uncertainties, even at this low metallicity are definitely small. Our estimated radial velocity of $-101\,\mathrm{km\,s^{-1}}$ does not unequivocally suggest that it is a halo star passing through the bulge. We note that Schultheis et al. (2015) discovered, as mentioned above, a few stars with metallicities of this magnitude range , suggesting the presence of a metal-poor population. Further, Do et al. (2015) report several stars with [Fe/H] < -1 in the central cluster. Confirmation of the nature of these stars will depend on proper motions and radial velocities.

3.6.2 [α/Fe] vs [Fe/H]

As mentioned in Section 3.5, though we find the expected α-abundance trend, the [Si/Fe] abundances are lower than [Mg/Fe] abundances in the subsolar metallicity regime. In Figure 3.16, we show the outer bulge ($|b| > 2°$) α-element trends seen for micro-lensed dwarf sample in Bensby et al. (2013) and for red giant branch stars in Johnson et al. (2014). We plot each star with their individual uncertainties estimated for [Si/Fe] ,[Mg/Fe] and [Fe/H], from the corresponding tables in Bensby et al. (2013) and Johnson et al. (2014). The α abundance trend with metallicity in Rich et al. (2012) cover only a narrow range in metallicity of ~-0.4 to 0 dex. Hence, it is not possible to make a full metallicity range comparison with our trend though two of our sample fields coincide with theirs in the inner Galactic bulge.

We find that our [Si/Fe] trend is consistent with the outer bulge trend of Johnson et al. (2014) over the full metallicity ranges, apart from a systematic shift of the order of 0.1 dex. This shift is consistent within the 1-σ uncertainty limits of both samples. Both trends seem to continuously decrease with metallicity, even in the supersolar regime. The [Si/Fe] trend of Bensby et al. (2013) in the subsolar metallicity regime, lies consitently in between our and the Johnson et al. (2014) trend. One significant difference is, however, that the supersolar [Si/Fe] trend of Bensby et al. (2013) saturates or levels off and continues at supersolar [Si/Fe] values. Such a scenario is only possible if the rate of Type II supernovae explosions, that produce the majority of α elements, increases sufficiently compared to the Type Ia supernovae explosions or if there is a metallicity dependent yield that increases the Si abundances dramatically, both of which are unexpected. Another possibility is that our studies are considering different stellar populations. Also, generally it should be noted that at supersolar metallicities, there might be a problem with blending atomic or molecular lines, which are not known to exist or whose strengths are unknown. The lines used in abundance analyses are generally checked for blends, but if there are unknown blends which cannot be taken into account, there is a tendency to overestimate the abundance of a spectra line, since

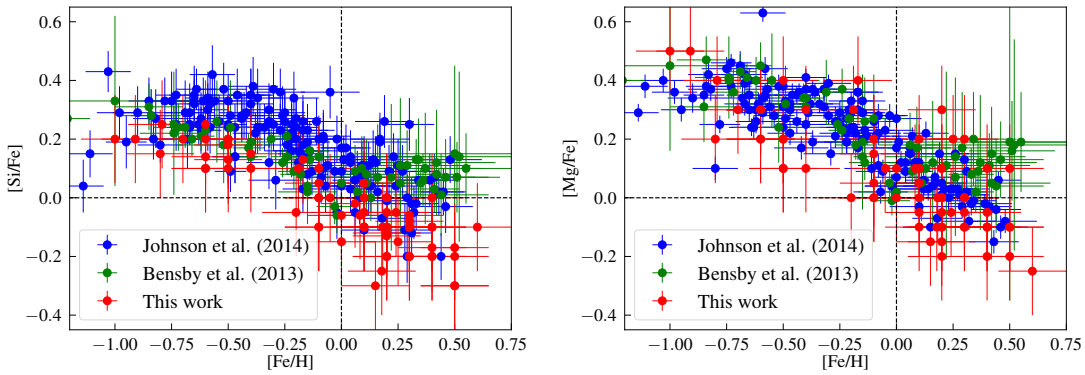

Figure 3.16: [Si/Fe] vs [Fe/H] (left) and [Mg/Fe] vs [Fe/H] (right) trends of our sample (red filled circles) in comparison with that of the micro-lensed dwarf sample in Bensby et al. (2013) (green filled circles) and red giant sample in Johnson et al. (2014) (blue filled circles) in outer bulge fields. We plot our sample with typical uncertainty of 0.15 dex, while the comparison samples are plotted with individual uncertainties of each star estimated in Bensby et al. (2013) and Johnson et al. (2014). Our trends in the subsolar metallicity regime are consistent within the 1-σ uncertainty limit of both samples. In the supersolar metallicity regime, we find subsolar alpha-abundances causing the trend to go down, consistent with Johnson et al. (2014). Meanwhile the trend in Bensby et al. (2013) is leveling off and continuing at the supersolar alpha values, with higher uncertainties.

the unknown blending line is ascribed to the element. Therefore, there is always a risk of overestimating the derived abundances in cool, metal rich stars.

Our [Mg/Fe] trend is consistent with the trends of both Bensby et al. (2013) and Johnson et al. (2014) in the subsolar metallicity regime. Our trend over the entire metallicity ranges is especially consistent with that of Johnson et al. (2014). Still the dispersion in our [Mg/Fe] measurements are higher than the comparison samples which may be due to the fact that there is only one spectral feature that can be used for the abundance determination, namely the group of lines at 21060 Å. In the supersolar metallicity regime, our trend is consistent with that found by Johnson et al. (2014), while the trend in Bensby et al. (2013) is again leveling off and continuing at the supersolar [Mg/Fe] values.

3.6.3 Kinematics

The mean value of the Galactocentric radial velocity that we have estimated for our entire sample within $|b|<3^\circ$ is consistent with the estimates from other studies using much larger sample of stars in the inner and outer bulge fields (Howard et al., 2008; Kunder et al., 2012; Ness et al., 2013b; Zoccali et al., 2014; Babusiaux et al., 2014). The mean values of V_{GC} estimated by BRAVA survey for fields at (l,b) ~ (0°,-2°), (0°,-4°), (0°,-5°), (0°,-6°) and (0°,+4°) ranges from -8 to 14 kms^{-1} (Howard et al., 2008; Kunder et al., 2012). Our mean estimate of -12 kms^{-1} is closer to the values of -9.7, -6.2 and -10.9 kms^{-1} found by Ness et al. (2013b) for their fields at (l,b) = (0°,-5°), (0°,-7°.5) and (0°,-10°) respectively. Babusiaux et al. (2014) also finds a negative mean V_{GC} of -3 kms^{-1} for their sample at (l,b) = (0°,+1°). At the same

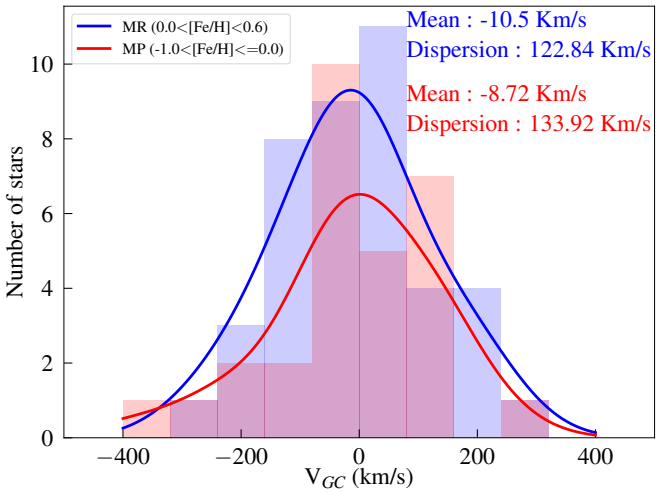

Figure 3.17: The Galactocentric radial velocity distribution for our entire sample divided into metal-poor (MP; red) and metal-rich (MR; blue). Overlaid KDEs of respective colors have similar bandwidth as their binsize. The mean velocity and dispersion for the two samples are listed in the figure.

time, the mean V_{GC} surface in the longitude-latitude plane as derived from the GIBS Survey (Fig. 10 in Zoccali et al. 2014[3]) clearly showed that the mean V_{GC} along the bulge minor axis is in the range of -10 to 0 kms^{-1}. Valenti et al. (2018) measured the mean Galactocentric radial velocity and dispersion from the low resolution MUSE spectra for bulge stars in the fields at (l,b) = (0°,+2°), (0°,-2°), (+1°,-1°) and (-1°,+2°). They find the mean Galactocentric radial velocity for stars in their fields corresponding to our bp2 and bm2 fields to be +9.8 and +19.2,kms^{-1} respectively.

In the case of the Galactocentric radial velocity dispersion, Babusiaux (2016) compiled radial velocity dispersion values along the bulge minor axis (l=0°, |b|<12°) from different literature studies. They showed that the V_{GC} dispersion follows a steep trend that goes down as we move away from the Galactic mid-plane. So, we compare our dispersion estimate with only those studies within |b|<2°. (Howard et al., 2008) estimated the velocity dispersion at (l,b) ~ (0°,-2°) to be 126 kms^{-1}, consistent with our estimate. A higher velocity dispersion of 145 kms^{-1} was calculated by Babusiaux et al. (2014). Zoccali et al. (2014) also found a peak dispersion value closer to 140 kms^{-1} for the GIBS sample at (l,b) ~ (0°,-1°) and (0°,-2°). Valenti et al. (2018) confirmed this result in their study including fields at positive latitudes that were missing in GIBS, also finding a symmetric velocity dispersion about the Galactic plane. Any slight variation of our estimate from the rest of the studies can be attributed to our small sample size due to which we had to combine our entire sample.

Babusiaux (2016) has also shown (see their Fig. 4.) that the dispersion trends for the metal-poor star (-1<[Fe/H] <-0.5) and the metal-rich star sample (0<[Fe/H] <0.) are comparable within |b|<2°. For higher latitudes ($|b| \geq 4°$) there is a strong decrease in velocity dispersion for metal-rich stars while it is flat for metal-poor stars. By dividing the GIBS sample

[3]Assuming symmetry in b

into metal-poor (-0.8<[Fe/H] <-0.1) and metal-rich ([Fe/H] >0.1) populations, Zoccali et al. (2017) also found a similar trend. We also separated our limited sample into metal-poor (-1.0≤[Fe/H] ≤0.0) and metal-rich (0.0<[Fe/H] ≤0.6) populations and estimated their dispersions as shown in Figure 3.17. We find similar velocity dispersions for the two populations which are close to the estimates from the above mentioned studies. However, we suffer from a limited sample size and clearly more observations are needed.

3.6.4 North-South symmetry

The North-South symmetry in bulge kinematics, namely mean Galactocentric radial velocity and dispersion, have already been shown for a range of longitudes by sampling outer bulge fields (Ness et al., 2013b; Zoccali et al., 2014). The rotation and dispersion symmetry along the major axis has been shown by Ness et al. (2013b) using three fields at latitudes of -10° and +10°, and longitudes of -10°, -5° and +10°. Similar results have been obtained by Zoccali et al. (2014) using the GIBS survey fields at b = +4°.5 and -4°.7 covering a range of longitudes, |l|<8°.

Valenti et al. (2016) have shown, using the VVV PSF-fitting photometry, the increase of the RC density distribution in the density profile of the inner bulge towards the Galactic plane. They have also shown symmetries in their RC star counts in the Galactic mid-plane, at l = 0°, b = ±1°, ±2°, ±3° and ±4°. This suggests a North-South symmetry in kinematics and stellar density for the outer bulge and inner bulge regions respectively. We extend this investigation for the North-South symmetry to chemical abundances and the metallicity distribution function.

Four of our fields along the bulge minor axis are located at symmetrically opposite latitudes with respect to the Galactic mid-plane. In addition, we have carried out a consistent analysis of the spectral analysis in both North and South fields. This is crucial in order to explore the symmetry of the MDF between Northern and Southern fields along the bulge minor axis. This is the first time such a study is being carried out, as previously most of the studies in the inner bulge have been concentrated to the southern latitudes.

The Sun is located at a distance of 17±5 pc above the Galactic mid-plane and at a distance of 8.2±0.1 kpc from the Galactic center (Karim and Mamajek, 2017). Based on this, we estimated a very similar distance of ∼145 and 298 pc, above the Galactic mid-plane along the bulge minor axis, corresponding to the North-South latitudes, ±1° and ±2° respectively. Thus we can safely assume that our stars at the North-South latitudes in our sample are located symmetrically with respect to the Galactic mid-plane.

We group the stars in the b=+1°, b=+2° fields together as the North field and those in the b=-1°, b=-2° fields as the South field, and plot their metallicity distributions in Figure 3.19. The metal rich part of both the MDFs are very similar. The overlaid KDE estimate for the North and South fields in the metal-rich regime are similar with approximate matching peaks. Keeping in mind the low number of stars and the abundance uncertainties, the KDE peak in the metal-poor regime for South field do, however, not seem to match with that for the Northern field due to the absence of stars with metallicities in the range of -0.3 to -0.6 dex.

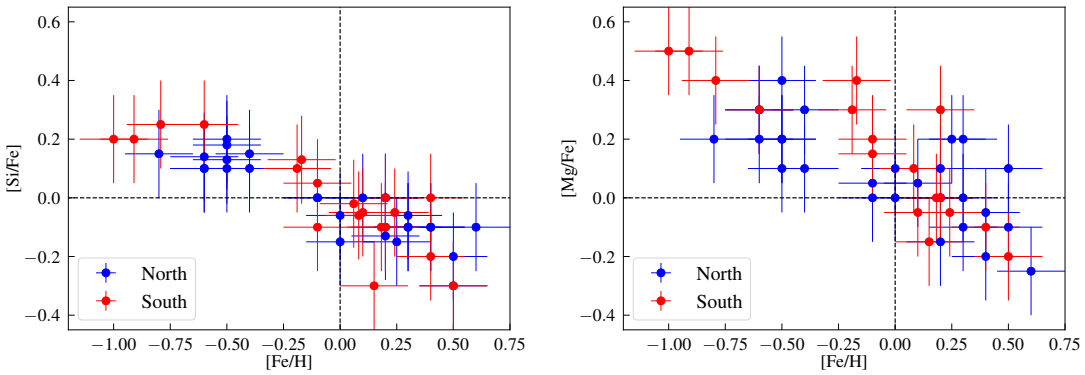

Figure 3.18: [Si/Fe] vs [Fe/H] (left) and [Mg/Fe] vs [Fe/H] (right) trends of stars at b=+1°, +2° (blue filled circles) and those at b=-1°, -2° (red filled circles). The error bars correspond to typical uncertainty of 0.15 dex.

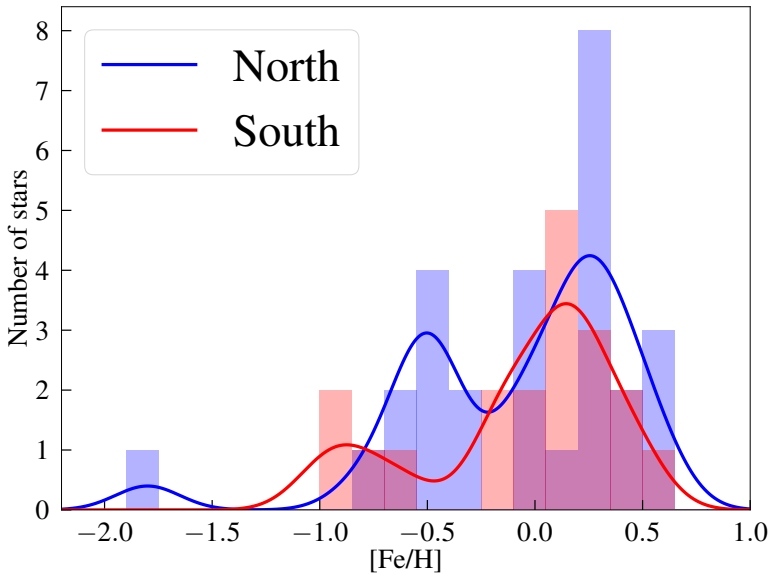

Figure 3.19: MDF of North (blue; b = +1°, +2°) and South (red; b = -1°, -2°) field stars to investigate the North-South symmetry in MDFs. Overlaid KDEs,shown in respective colors, use the same bandwidth as binsizes of the histograms.

The metallicity distribution for the Northern field in the metal-poor regime show a peak in the KDE of around -0.5 dex. We want to stress that we are dealing here with low-number statistics; there are only four stars in the Southern fields with metallicities falling into the metal-poor group. Clearly a larger sample is needed. We can not reject the hypothesis of symmetry based on the distribution of these few stars. It is too early to claim any difference. Testing the full Northern and Southern MDF populations (only excluding the [Fe/H]=-1.8 star) with a Kolmogrov-smirnoff test, we arrive at a p-value of 0.90 suggesting that both distributions, nevertheless, come from the same parent population. Thus, we cannot claim any non-symmetry in the MDFs between Northern and Southern fields based on our data. Most likely the inner bulge is symmetric along the minor axis in its metallicity distributions.

We then proceed to carry out a similar exercise for the [Si/Fe] vs [Fe/H] and [Mg/Fe] vs [Fe/H] trends, as shown in Figure 3.18. As mentioned in the above paragraph, the absence of Southern field stars in the range of -0.3 to -0.6 dex results in insignificant overlap between North-South samples in subsolar metallicity regime. Still, they follow a very similar continuous trend. On the other hand, there is significant overlap and consistency between the [Si/Fe] and [Mg/Fe] values in the supersolar metallicity regime. Thus we cannot reject North-South symmetry in the α-abundance trends based on our data, but we need more data to confirm it.

3.7 Summary and conclusions

We have carried out a consistent spectroscopic analysis of 72 M giant stars in the inner Galactic bulge (|b|<3°) along the minor axis from the high resolution CRIRES spectra. Out of 72 stars, 9 stars are located in the Galactic center, 44 stars are at the Northern latitudes, while 28 at the Southern latitudes. This is the first work to carry out such a systematic analysis in the inner bulge region, especially at symmetric fields along the bulge minor axis.

We find a bimodal MDF in the inner bulge, following that reported for outer bulge samples, but a larger sample will be required for confirmation. Our GC sample is completely supersolar with a mean metallicity of 0.3 dex but with no subsolar metallicities which could be due to our limited sample size. We find that the median overall metallicities in each field to decrease as we move away from the Galactic mid-plane. This is in agreement with the negative vertical metallicity gradient found in outer bulge fields. We find no stars with [Fe/H]> +0.6 dex.

The α-element trends with metallicity show no gradient over the entire minor axis, from far out through the GC and going North. Our [Si/Fe] and [Mg/Fe] trends with [Fe/H] are consistent with outer bulge trends for red giants, showing a gradual decreasing trend with increasing metallicity, as expected from chemical evolution models. We confirm that for the supersolar regime, the [Si/Fe] and [Mg/Fe] abundances decrease as expected from chemical evolution models.

The mean Galactocentric radial velocity and dispersion for our entire sample is consistent within the errors with the study of Howard et al. (2008) and that of the GIBS survey. No difference in the velocity dispersion has been found between the metal-rich and the metal-

poor sample.

Based on our investigation using b = ±1°, ±2° fields, we confirm the expected North-South symmetry in the MDF as well as in the α abundances for the inner bulge region. These results imply that there is chemical homogenity between the northern and the southern fields.

Although we report the largest and highest resolution abundance analysis of giants within 2 degrees of the Galactic center, the sample size remains relativley modest. Upcoming instruments and surveys such as CRIRES+ or MOONS will help to obtain a larger sample of stars in the inner bulge and towards the Galactic Center region. This will allow us to trace the vertical metallicity gradient as well as the full MDF in the GC together with their chemical footprints. It will also be vital to add superior kinematic data. All of this can help in deciphering the formation/evolution scenario of the inner bulge as well as the relation of the inner bulge to the Galactic Center and its nuclear star cluster.

Chapter 4

SFR in the CMZ

Contents

In this chapter, I describe briefly some of the methods commonly used to estimate the present star formation rate, focusing mainly on the YSO counting method. We use this method to estimate the SFR in the CMZ of the Milky Way based on the low resolution near infrared spectroscopic observations of ~100 sources, that are most likely YSO candidates selected based on photometric criteria.

4.1 Estimating SFR

The details about the star formation rate (SFR) and it's importance in the chemical evolution models has been explained in the Section 1.2.4. There are different methods that are used in order to determine the SFR in the Milky Way as well as in other external galaxies.

These methods rely on detailed observations of the region of interest in different wavelength regimes as explained below. I will briefly give an overview of three such methods that rely on cm or mm wavelength observations, mid and far infrared observations and near infrared observations, respectively.

4.1.1 Using cm or mm continuum emission

The young and massive O and B stars (>8–10 $M_\odot$) emit ionising UV radiation ($h\nu$ > 13.6 eV) that ionises the surrounding natal molecular clouds as well as the interstellar medium, producing H II regions. At cm or mm wavelengths, the free-free emission from the ionised gas in H II regions can be traced, enabling the determination of the rate at which ionising photons are being produced, from the free-free luminosity (Murray and Rahman, 2010). Once the ionsing photon rate, Q, is known, the SFR can be estimated using the equation (following Mezger 1978 and McKee and Williams 1997):

$$\dot{M}_* = Q \frac{< m_* >}{< q >} \frac{1}{< t_Q >} \tag{4.1}$$

where $< q >$ is the ionising flux per star averaged over the initial mass function (IMF), $< m_* >$ is the mean mass per star (in solar units) and $< t_Q >$ represents the time at which the ionising flux of a star falls to half its maximum value, averaged over the IMF.

4.1.2 Using infrared luminosity

Another method to estimate the SFR, especially in external galaxies or highly extincted regions of our own Galaxy where individual stars cannot be resolved, is to use the infrared luminosity maps. This method is based on the assumption that the short wavelength emission from the embedded stellar population (mostly young massive stars) is absorbed and then re-emitted at longer infrared wavelengths (where the emission becomes optically thin) by the surrounding dust. Thus, the total infrared luminosity can be considered to directly correspond to the bolometric luminosity from the embedded stellar population. There are many factors of uncertainties to be taken into account, ranging from the measurement uncertainties to high energy photon leakage, dust heating by other sources etc, most of which are difficult to determine with the present available observational technology.

This method makes use of emission maps from surveys like *Spitzer*-GLIMPSE (Churchwell et al., 2009a) and MIPSGAL (Carey et al., 2009), *Herschel* Hi-GAL (Molinari et al., 2010), ATLASGAL (Schuller et al., 2009) etc. covering a range of wavelengths from 3.6 μm to 870 μm. The emission maps have to be smoothed down to that of the lowest resolution one and the integrated flux densities of the region at each wavelength have to be estimated from the corresponding emission map after proper background subtraction. This range of wavelengths cover emission from warm dust (3.6 μm – 70 μm) and from cold dust (70 μm – 870 μm). Hence to measure the bolometric luminosity (as well as dust temperature and column density), the spectral energy distribution (SED) plotted using the integrated flux densities must be fitted with a modified black body model or a two component modified Planck function (Ward-Thompson and Robson, 1990; Battersby et al., 2011; Barnes et al., 2017):

$$S_\nu = \frac{2h\nu^3}{c^2(e^{\frac{h\nu}{kT}} - 1)}(1 - e^{-\tau_\nu}) \tag{4.2}$$

$$\tau_\nu = m_H \mu \, N(H_2) k_\nu \tag{4.3}$$

where S_ν is the flux density at frequency ν, T is the temperature, h is the planck constant, k the Boltzmann constant, $m_H\mu$ is the mean particle mass with m_H representing the mass of a hydrogen atom and μ is 2.8 a.m.u. (atomic mass unit), $N(H_2)$ is the column density of molecular hydrogen and k_ν is the dust mass opacity. The total flux can be measured by integrating the area under the fitted SED, that can be used along with the measurement of the source distance to measure the bolometric luminosity. Following this, there are many monochromatic as well bolometric luminosity - SFR relations that can be used to determine the SFR. A list of various monochromatic as well bolometric SFR conversion factors used in the CMZ region have been compiled in the Table 2 of Barnes et al. (2017), and there is a maximum variation of 0.05 $M_\odot yr^{-1}$ between the estimated SFRs.

4.1.3 YSO counting

The two methods mentioned above makes use of the longer wavelength emission and do not necessarily require very high spatial resolution. Hence they can be used to determine the SFR over global scales in the Milky Way as well as in external galaxies. The YSO counting method, as the name suggests, depends on counting the embedded young stellar population to determine the SFR. This method cannot be used in external galaxies as it requires high spatial resolution to resolve the individual high mass YSOs.

The YSO phase of a massive star is a relatively brief phase in the stellar evolution where the star is surrounded by dense envelopes of gas and dust (Zinnecker and Yorke, 2007). These objects are best identified by their point-source infrared radiation as well as excess flux values in the mid-infrared bands. Young stellar objects are classified in three classes or stages depending on their spectral index (Lada, 1987) and SED (Robitaille et al., 2006). Adams et al. (1987) identified Class I YSOs as protostars with infalling envelopes, Class II YSOs as stars with disks, and Class III YSOs as those stars having the SEDs of stellar photospheres. Analogous to this classification, Robitaille et al. (2006) defined three evolutionary stages based on their derived SED model properties: Stage I objects are young protostars embedded in an opaque infalling envelope, Stage II objects are stars surrounded by an opaque disk and dispersed envelope, and Stage III objects are stars with an optically thin disk. Figure 4.1 shows a rough schematic diagram classifying YSOs based on the infrared excess emission due to the surrounding envelopes of dust and gas as well as proto planetary discs.

In this method, masses of photometrically or spectroscopically confirmed YSOs in the region of interest are estimated either from SED fits or, using the zero-age main sequence (ZAMS) luminosity-mass relations. By assuming an appropriate IMF and extrapolating the stellar IMF down to lower masses, the total embedded stellar population mass of the region can then be estimated. Assuming an average age of 0.5 – 1 Myr for the YSOs, the SFR can be determined by dividing the mass by the average age (see Section 4.7).

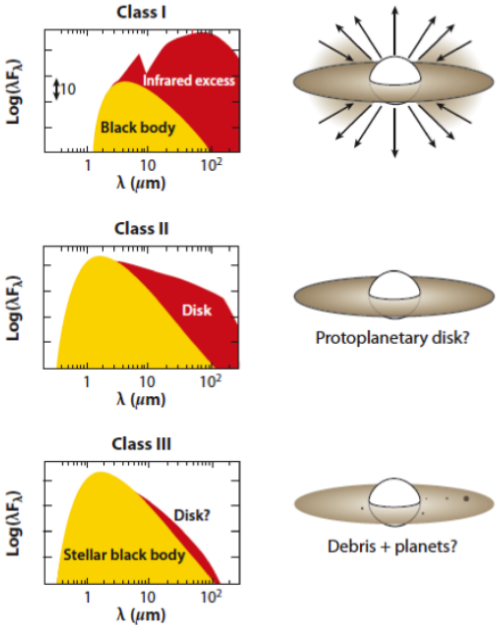

Figure 4.1: Schematic diagram showing the way YSOs are classified based on the presence of surrounding envelopes of dust and gas as well as proto planetary discs that results in infrared excess emission. Image courtesy : http://astronomy.swin.edu.au/ smaddiso/teaching/yso.html

4.2 Identifying YSOs

One of the commonly used ways to identify YSOs involves the use of colour-colour and colour-magnitude diagrams using infrared photometry. Theoretical models of protostellar envelopes and protoplanetary discs were initially used to predict the typical mid-IR colours of YSOs and thereby the zones in colour-colour diagrams wherein YSOs are concentrated(Whitney et al., 2003; Allen et al., 2004), as shown in the left panel of the Figure 4.2. Until recently, most studies of YSOs in the CMZ have also been based on infrared photometry (Felli et al. 2002; Schuller et al. 2006; Yusef-Zadeh et al. 2009). Felli et al. (2002) searched for YSO candidates using the mid-infrared excess derived from Infrared Space Observatory (ISO) photometry at 7 and 15 μm and used a criterion to find a strong concentration of YSO candidates in the inner Galaxy. Schuller et al. (2006) refined this ISO mid-infrared colour criteria based on the 7 and 15 μm ISO colours and spatial extent at 15 μm, and argued that slightly extended mid-infrared sources were more likely to be YSOs than point-like mid-infrared sources. Yusef-Zadeh et al. (2009) (hereafter YHA09) identified YSO candidates using *Spitzer*/IRAC and *Spitzer*/MIPS photometry at 3.6 – 24 μm as shown in the right panel of the Figure 4.2 and their SED fitting techniques associated most of their YSO candidates with Stage I objects.

The CMZ, however, suffers from very large and spatially variable interstellar extinction (A_V = 20 – 40 mag; see e.g. Schultheis et al. 2009). The significant foreground extinction causes evolved stars with circumstellar envelopes, such as mass-losing asymptotic giant

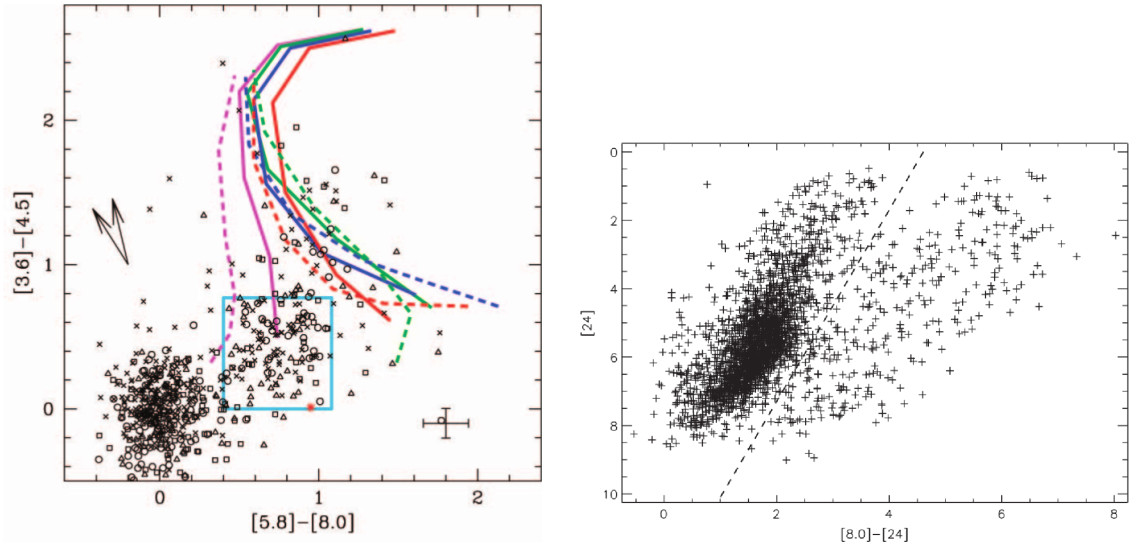

Figure 4.2: (left) [3.6]-[4.5] vs. [5.8]-[8.0] colour-colour diagram showing the IRAC colors for four young cluster members : S140 (squares), Cep C (crosses), S171 (circles), and NGC 7129 (triangles) from the IRAC Guaranteed Time Observer (GTO) embedded clusters survey (Megeath et al., 2004). The light blue square indicates the zone of Class II YSOs based on Allen et al. (2004) models, while the colored lines show the Class I models. The colours magenta, green, blue, and red represent envelope models for a range of central luminosities : 0.1, 1, 10 and 100 L⊙, respectively. Models are plotted for two values of the centrifugal radius, R_c, 50 AU (solid line) and 300 AU (dashed line). Image courtesy : Allen et al. (2004) (Right) [24] vs. [8.0]-[24] colour-magnitude diagram showing the distribution of sources in the region b±10′and -1°.4 < l < 0°. The dashed line is an empirical separator between evolved AGB stars (to the left) and candidate YSOs to the right. Image courtesy : Yusef-Zadeh et al. (2009)

branch (AGB) stars, to have infrared colours similar to those of YSOs. Schultheis et al. (2003) demonstrated that near-infrared spectra are a powerful tool to distinguish YSOs from reddened AGB stars. These authors found that YSO samples in the CMZ selected by photometric colour criteria are heavily contaminated by AGB stars, red giants, and even supergiants (see the Figure 4.3). By contrast, they showed that moderate-resolution spectra in the H and K bands delineate YSOs from evolved stars by the absence or presence (respectively) of CO absorption at ~ 2.3 μm. Detectable YSOs at the distance of the Galactic centre (~8 kpc) are all massive, and thus never show 2.3 μm CO absorption; instead, they are featureless around 2.3 μm or show 2.3 μm CO in emission (Geballe and Persson, 1987; Carr, 1989; Hanson et al., 1997; Bik et al., 2006).

A recent improvement in YSO selection in the CMZ came from *Spitzer*/*IRS* spectra to select YSOs. An et al. (2011), hereafter An11, presented *Spitzer*/*IRS* 5–35 μm spectra of 107 YSO candidates selected from 3.6–8.0 μm *Spitzer* photometry (Ramírez et al., 2008). The authors of An11 identified massive YSOs in the CMZ by the presence of gas-phase absorption from C_2H_2 (13.7 μm), HCN (14.0 μm), and CO_2 (15.0 μm) as well as strong and broad 15.2 μm CO_2 ice absorption. They found that mid-infrared spectra confirm only 33% of YSO candidates selected by their photometric criteria, and confirm 57% of YSO candidates selected photometrically by YHA09. Immer et al. (2012) analysed 5–40 μm *Spitzer*/*IRS* spectra of 57 YSO candidates selected from 7 and 15 μm ISO colours and spatial extent at 15 μm (Schuller et al., 2006). These authors identified 25% of their sources as YSOs and an additional 37% as HII regions. There is disagreement in the YSO classification even among the common sources in An11 and Immer et al. (2012) samples, suggesting uncertainties in spectroscopic YSO classification schemes as well. Koepferl et al. (2015), using radiative transfer models and realistic synthetic observations (with HYPERION (Robitaille, 2011) and the FluxCompensator (Koepferl and Robitaille, 2017)), re-examined the YHA09 YSO sample and showed that embedded main sequence stars contaminate the YHA09 sample. These recent studies demonstrate significant contamination of photometrically selected YSO candidate samples by non-YSOs, which has important implications for CMZ star formation rates derived from photometry (YHA09).

4.3 SFR in the CMZ

As mentioned in Section 1.3, the CMZ is in an active region of star formation with higher gas pressure, temperature and turbulence than in the disc. Thus it is essential to understand the modes of star formation and star formation history in the unique environment of the CMZ, both to gain insight into our own Milky Way and to provide a template for circumnuclear star formation in the closest galactic nuclei.

Longmore et al. (2013a) carried out a detailed study of the variations in star formation across the Galactic plane using observational tracers of dense gas (NH_3(1,1)) and star formation activity (masers, HII regions). These authors showed that there is a deficiency in star formation activity tracers in the CMZ given the large reservoir of dense gas available. On the other hand, they found that various star formation models predict much higher values

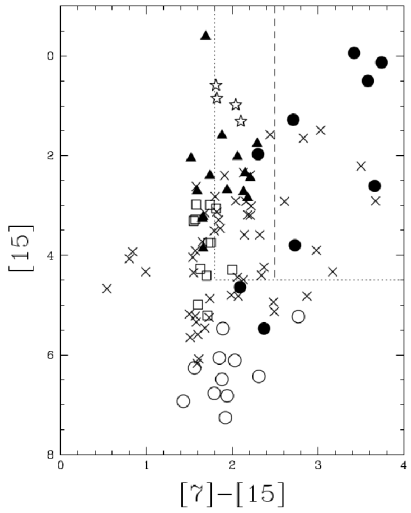

Figure 4.3: [15] vs. [7]-[15] colour-magnitude diagram showing the distribution of sources with mid-IR excesses at 7 and 15 μm from the ISOGAL survey. YSOs are indicated by filled circles (featureless spectra with no CO absorption lines), candidates of red giants by open circles, OH/IR stars (identified by Wood et al. 1998) by filled triangles, Long Period variables (identified by Glass et al. 2001) by open squares, red giant candidates, supergiant candidates by stars and AGB Variables by crosses (based on the strong CO band absorption at $\sim$ 2.3 μm). The dotted line shows the region searched by Felli et al. (2000) for YSO candidates and the long-dashed line indicates a more conservative criterion for identifying YSOs (Felli et al., 2002). Both criteria are unable to effectively distinguish YSOs from other stellar populations. Image courtesy : Schultheis et al. (2003)

of SFR. Barnes et al. (2017) determined the average SFR across the CMZ using a variety of extragalactic luminosity–SFR conversion and found it to be comparable to previous measurements made from YSO counting and free-free emission. Thus, they ruled out systematic uncertainties in the SFR measurements as the reason for low star formation in the CMZ. All these studies point to the necessity of estimating an accurate value of the SFR, that can be used in various star formation as well as chemical evolution models to understand physical mechanism(s) that drive the star formation in the CMZ.

In this work, I present moderate-resolution 2.0–2.5 μm spectroscopic follow-up observations of a sample of 91 photometrically identified YSO candidates in the CMZ using K-band Multi Object Spectrograph (KMOS; Sharples et al. 2013) at VLT-UT1 (Antu). My goal is to distinguish YSOs from evolved late-type stars by their near-infrared spectra. I discuss and show the contaminating evolved late-type stars in different colour-magnitude (CMD) and colour-colour (CCD) diagrams and define a new colour-colour criterion to distinguish these stars using our spectroscopically identified YSO sample. Finally, I estimate the SFR in the CMZ based on the YSO counting method and on SED fitting techniques.

4.4 Data

In this section, the way we obtained the data for this work is described : starting from the target selection, followed by the observations using KMOS and finally the spectral data reduction.

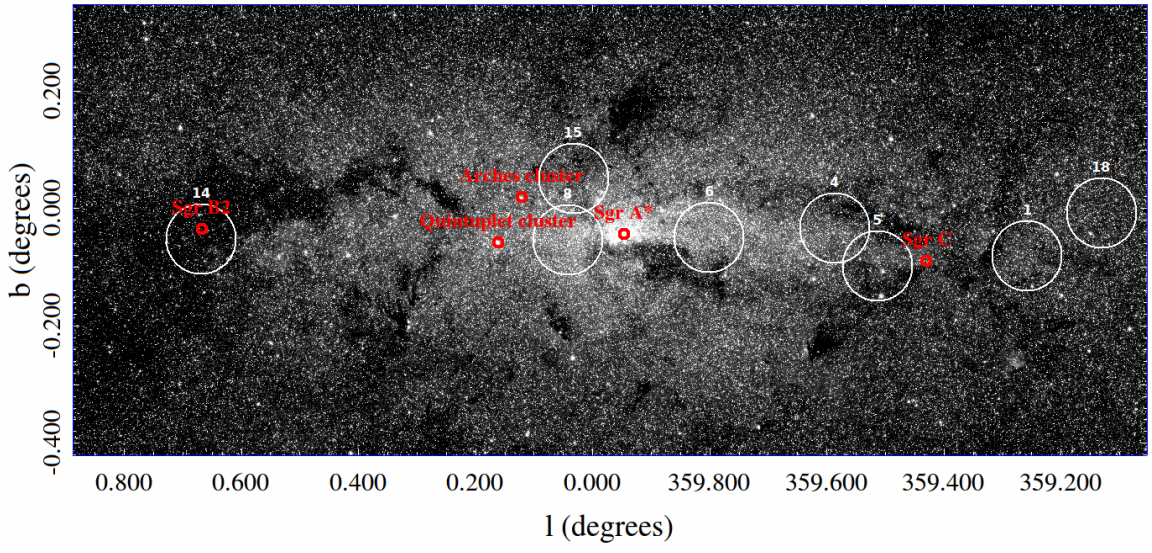

Figure 4.4: Field distribution of our observations overlaid on the 3.6 μm *Spitzer* image (Stolovy et al., 2006). The white circles represent the 7′.2 diameter fields that have been observed. The numbers are assigned to identify the fields, details of which are given in Table 4.1. Shown in red are the locations of prominent sources in the CMZ such as Sgr A*, Sgr B2, Sgr C, Quintuplet, and Arches clusters.

4.4.1 Sample selection

We selected the sample for our observation from the photometric catalogue of SIRIUS (Nishiyama et al., 2006) and point-source catalogue of *Spitzer*/IRAC survey of the Galactic centre (Ramírez et al., 2008). The JHK$_S$ photometry from the SIRIUS catalogue has average 10σ limiting magnitudes of J=17.1, H=16.6 and K$_S$=15.6 mag, while the 3.6, 4.5, 5.8, and 8.0 μm bands from the *Spitzer*/IRAC catalogue has confusion limits of 12.4, 12.1, 11.7, and 11.2 mag, respectively. We divided our sample into three categories of high, medium, and low priorities; the highest priority (priority 1) was given to those sources in our sample that are photometrically identified YSO candidates in YHA09. We divided the rest of the sample into medium (priority 2) and low (priority 3) priorities using the following criteria that select sources exhibiting excess emission in mid-infrared regimes:

Medium priority	Low priority
[3.6]-[4.5] > 0.5	[3.6]-[8.0] > 2
[4.5]-[5.8] > 0.5	K$_S$ < 17
[5.8]-[8.0] > 1	
K$_S$ < 17	

The KMOS consists of 24 integral field units (IFU) that can be arranged in a 7$'$.2 diameter field per configuration, and it is crucial to prevent the 24 IFUs on the 24 pick-off arms from blocking each other. We use the KMOS ARM Allocator (KARMA), which assigns the maximum number of highest priority targets to the 24 pick-off arms, followed by medium and low priority targets thereby leaving as few arms as possible unallocated.

4.4.2 Observations

Our spectroscopic observations were carried out with KMOS at VLT-UT1 (Antu) on June 23, 2016. Each of the 24 IFUs in KMOS has a field of view of 2$''$.8×2$''$.8. The spectral resolution of KMOS is R~4300 with the wavelength range covering 1.925 μm - 2.500 μm. We prepared 22 fields with unique IFU configuration covering a significant part of the CMZ. But owing to bad weather conditions, only eight fields could be observed with an integration time of 900s for each field in the *nod to sky* mode. The observations were carried out under photometric conditions with seeing ~0$''$.8. The observed field positions are shown in Figure 4.4 and the field details with the number of different priority sources in each field are given in Table 4.1.

The fields are in regions with high stellar density as can be seen in the Figure 4.4. Hence, it was not possible to observe sky in each IFU by dithering or nodding to a new position within the respective field. So we observed a dark cloud G359.94+0.17 (α ~ 266°.2, δ ~ -28°.9; Dutra and Bica 2001) in free dither mode with 2$''$.8 dither in between two 900s exposures to carry out a proper sky subtraction. The sky observation was carried out after every two field observations. B and A type stars were observed for telluric corrections after every sky offset.

Table 4.1: Details of the observed fields. The (l,b) of field centres and the number of high, medium, and low priority sources, and the manually allocated sky and random sources for the free arms are listed.

Field No.	l(°)	b(°)	Priority 1	Priority 2	Priority 3	Sky	Random source
1	359.26	-0.08	13	3	3	3	2
4	359.58	-0.03	13	5	4	1	1
5	359.51	-0.09	9	3	11	1	0
6	359.80	-0.05	15	1	7	1	0
8	0.04	-0.05	0	5	18	1	0
14	0.67	-0.05	12	9	3	1	0
15	0.03	0.05	3	9	12	2	0
18	359.13	-0.01	12	1	5	4	2

4.4.3 Data reduction

We used the ESO KMOS Recipe Flexible Execution Workbench (Reflex; Freudling et al. 2013) for data reduction. It organises the science and associated sky and calibration data together based on the calibration source type and their proximity in time to science observations. This is followed by dark level correction of frames, flat fielding, wavelength calibration, spatial illumination correction, telluric correction, sky subtraction, and cube reconstruction of the science data by dedicated pipeline recipes (or stages).

We made use of an IDL routine to remove the Brγ absorption line from each telluric spectrum by fitting the Brγ line with a Lorentz profile and subtracting it from the telluric spectrum. This routine also removes the stellar continuum by dividing it by a blackbody spectrum. We also removed cosmic rays from the final reconstructed object cube with a 3D version of L.A.Cosmic (van Dokkum, 2001).

We extracted spectra from 173 data cubes using *kmos_extract_spec* recipe with the ESO Recipe Execution Tool (EsoRex).The *kmos_extract_spec* recipe extracts a spectrum from a data cube with the option of defining a mask manually or automatically by fitting a normalised profile to the image of the data cube. We identified multiple sources in 53 data cubes and extracted their spectra by defining the mask manually. Finally, we extracted nearly 250 spectra and used IRAF median filtering with seven pixels as filter size to smoothen the spectra. After discarding spectra with a signal-to-noise ratio (S/N) below 20 or having negative flux values, there were 91 spectra left in our sample with good S/N. Among these spectra, there are 15 from data cubes with multiple sources, and we selected the spectrum of the brightest source in the data cube.

4.5 Classification

In this section, we classify our targets as YSOs and late-type stars based on their spectra. Using this classification, we evaluate different photometric YSO classification criteria and suggest a new criterion to distinguish YSOs and late-type stars.

4.5.1 Spectroscopic classification

We classified our spectra mainly based on the presence or absence of the ^{12}CO (2,0)-band at 2.3 μm. CO absorptions bands are typically found in late-type G, K, M giants and AGB stars. In addition, we also used Brγ, found in emission, absorption, or with a P-Cygni-type profile in massive YSOs (Cooper et al., 2013). We carried out background subtraction during data reduction to make sure that the Brγ emission lines are intrinsic to the source. Still, we expect contamination from the OB main sequence or post-main sequence Wolf Rayet stars, some of whose spectra also show Brγ in emission attributed to their stellar wind (Mauerhan et al., 2010a). CO band emission at 2.3 μm is also considered to be an indication for the presence of a dense circumstellar disk and hence a YSO signature (Bik et al., 2006). Some spectra show a featureless continuum at 2.0–2.5 μm; these could be either YSOs (Greene and Lada, 1996) or dusty late-type carbon-type (WC) Wolf–Rayet stars (Mauerhan et al., 2010a).

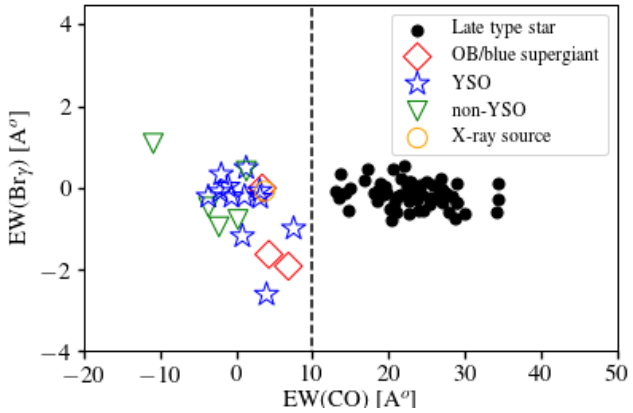

Figure 4.5: Equivalent widths measured for the ^{12}CO (2,0) line and Brγ line for YSOs (blue stars) and late-type stars (black dots). We separate the two populations approximately using the dashed line at EW(CO

) =

10 .$Different symbols and colours represent the classification of the SIMBAD matches to our sources by search$

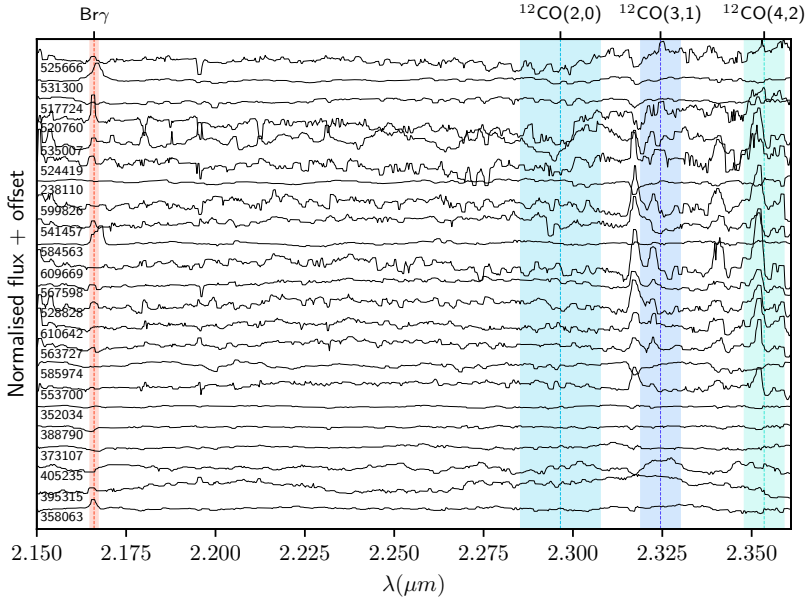

Figure 4.6: Normalised spectra of YSOs classified based on the absence of ^{12}CO (2,0) band absorption line and presence of Brγ emission or absorption line. Dashed lines and shaded areas represent the central wavelengths and range of continuum used for measuring equivalent widths of Brγ, ^{12}CO (2,0), ^{12}CO (3,1), and ^{12}CO (4,2) bands. The SST GC No. for each source is specified adjacent to the corresponding spectra.

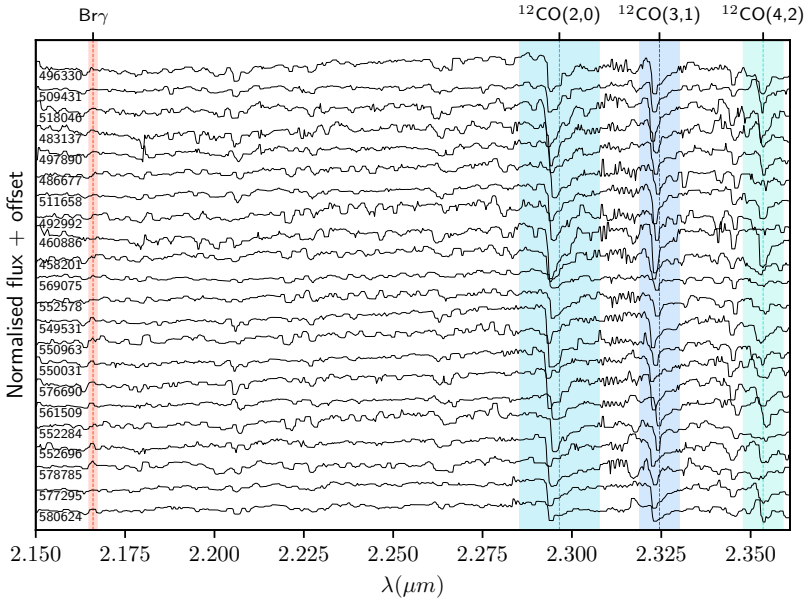

Figure 4.7: Same as Figure 4.6 but for cool late-type stars in fields 8 and 15, classified based on the presence of ^{12}CO (2,0) band absorption line.

Thus we classify the stars to the right of the dashed line as cool, late-type stars and those to the left as YSOs. All cool, late-type stars (represented by filled black circles) lie very close to EW(Brγ) = 0 Å indicating the absence of this particular feature in their spectra. The majority of stars we classify as YSOs also show no Brγ feature, while approximately five stars show Brγ in emission (EW(Brγ) < 1 Å) and only one star shows Brγ in absorption (EW(Brγ) > 1 Å), which also shows CO in emission (EW(CO) = -10 Å).

Based on the above-mentioned classification scheme, there are 23 spectroscopically identified YSOs in our sample. Figures 4.6 and 4.7 show the reduced normalised spectra of YSOs and cool late-type stars, respectively. We searched for previously identified sources in the SIMBAD database with a search radius of 2$''$.0 from each of the 23 YSOs to check their status in the literature. Table 4.2 lists all 23 sources with their SST (*Spitzer Space Telescope*) Galactic centre (GC) number, equatorial coordinates in degrees, distance of the SIMBAD match from the source, source type along with corresponding references, and JHK$_S$ magnitudes from SIRIUS catalogue. There are seven sources in common with An11, out of which only one is confirmed to be YSO and one is considered to be a possible YSO by An11. The remaining five sources have been classified as non-YSOs, with #517724 also classified as an OB super giant star in Mauerhan et al. (2010b) based on absorption lines of Brγ at 2.1661 μm, NIII at 2.115 μm and He I at 2.058, 2.113, and 2.1647 μm. Two other sources (#528828 and #599826) have been classified as possible long period variable stars in Matsunaga et al. (2009) and Glass et al. (2001) based on periods estimated using near-infrared observations, although no clear periodicity was found for them. Two sources (#531300 and #584563) have been classified as blue super giant stars based on weak Brγ emission or absorption features, NIII and CIV contributions, and HeI absorption profiles at 2.058 μm in addition to detected Paschen-α (Pα) excess (Mauerhan et al., 2010a). The counterpart to the source #238110 has been classified as X-ray source in Muno et al. (2003). Three sources (#358063, #395315, and #520760) are in common with the YHA09 sample, out of which #520760 is classified also as a radio source in Dong et al. (2015). The remaining eight sources do not have any counterparts in the SIMBAD database within 2$''$.0.

In Figure 4.5, we show the sources classified in the literature as X-ray sources, OB or blue supergiants, and non-YSOs using separate symbols. Regarding the classification of five sources as non-YSOs by An11, the large pixel sizes of *Spitzer/IRS* spectra can lead to misidentification of sources in high stellar density regions such as in the CMZ. Also one non-YSO (#405235) shows Brγ in absorption and CO in emission, indicating the presence of a dense circumstellar disk and considered to be a massive YSO feature though rarely seen (Bik et al. 2006; Cooper et al. 2013). Thus we stick with our classification scheme for this source. Since no clear periodicity was found for the two sources classified as long period variable stars, we assume that these are YSOs as well. Two blue supergiants (#584563 and #531300) show Brγ in emission, while no clear emission is seen for #517724 classified as OB supergiant. We made an approximate EW measurement of NIII at 2.115 μm and found that all three sources mentioned above as well as the radio source #238110 show a clear emission feature that is not seen in the rest of our YSOs. Thus we consider their classifcation as supergiants to be acceptable. Based on these measurements we conclude that none of the rest of our YSOs are O/B supergiants.

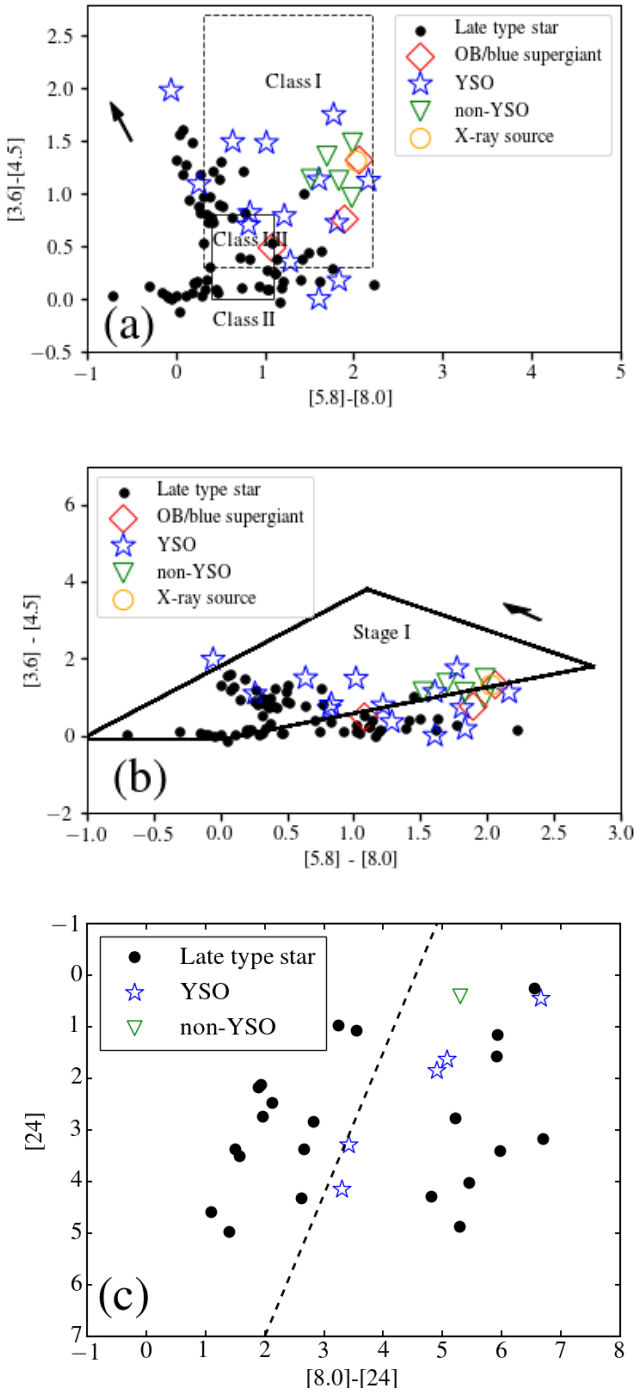

Figure 4.8: (a) [3.6]-[4.5] vs. [5.8]-[8.0] diagram used to identify different classes of YSOs based on the disk and envelope models of low mass YSOs as shown in the Figure 4.2. Class II YSOs are expected to be concentrated in the small box, while Class I YSOs in the bigger box. (b) Same colour-colour diagram as (a) with the region shown by black polygon where Stage I YSOs are expected to lie (Robitaille et al., 2006). (c) [8.0]-[24] vs. [24] diagram showing the criteria used by YHA09 to choose their sample of possible YSO candidates (region to the right of the dashed line). The black arrows in (a) and (b) represent the extinction vector estimated for A_K = 2 mag (typical of the CMZ) using the $\frac{A_\lambda}{A_K}$ relations from Nishiyama et al. (2009). In each diagram, the spectroscopically identified YSOs are shown using blue star symbols and the cool late-type stars using black filled circles. Other symbols and colours represent the classification of the SIMBAD matches to our sources by searching within 2″.0 (see Section 4.5.1)

Table 4.2: Details of the search for previously identified sources within 2″.0 of our spectroscopically identified YSOs in the SIMBAD database. For each source represented by their SST GC number, their equatorial coordinates in degrees, distance from the source, source type along with corresponding references, and JHK_S magnitudes from SIRIUS catalogue are listed. For sources with no counterpart within 2″.0 and no valid photometry in J or H bands, we use '...' for the corresponding column.

SST GC No.	RA (°)	DEC (°)	Distance (in ″)	Source type	J (mag)	H (mag)	K_S (mag)	Field
238110	265.93	-29.67	0.64	X-ray source[a]	17.19	13.64	11.84	18
517724	266.40	-28.89	0.07	OB supergiant[b], non-YSO[c]	15.75	12.80	11.23	15
520760	266.41	-28.89	1.54	radio source[d], YSO[e]	...	15.59	13.17	15
524419	266.41	-28.89	0.50	non-YSO[c]	...	15.86	14.02	15
525666	266.42	-28.89	0.04	non-YSO[c]	...	14.49	12.74	15
531300	266.43	-28.88	0.17	Blue super giant[b]	14.70	11.67	10.11	15
535007	266.43	-28.87	0.05	non-YSO[c]	...	16.05	13.81	15
528828	266.42	-28.91	0.11	Long period variable star[f]	...	...	13.69	8
541457	266.44	-28.91	...	...	...	14.28	12.53	8
553700	266.46	-28.91	...	...	15.11	13.09	12.27	8
563727	266.47	-28.98	...	...	...	14.75	12.97	8
567598	266.48	-28.94	...	...	...	14.71	12.92	8
609669	266.54	-28.92	...	...	...	16.24	14.17	8
610642	266.55	-28.93	0.05	Maybe YSO[c]	...	15.26	12.69	8
584563	266.51	-28.92	0.17	Blue super giant[b]	13.45	10.69	9.12	8
585974	266.51	-28.96	...	...	16.80	11.73	9.42	8
599826	266.53	-28.93	0.52	Long period variable star[f]	...	...	13.87	8
373107	266.18	-29.34	...	...	16.48	13.59	11.94	4
388790	266.20	-29.39	0.40	non-YSO[c]	...	14.12	12.05	5
352034	266.14	-29.39	...	...	...	12.52	10.95	5
395315	266.21	-29.34	0.02	YSO[e]	...	15.95	13.65	4
405235	266.23	-29.26	0.28	non-YSO[c]	...	14.77	12.97	4
358063	266.15	-29.31	0.14	YSO[e]	15.59	13.42	11.79	4

[a] Muno et al. 2003
[b] Mauerhan et al. 2010a
[c] An et al. 2011
[d] Dong et al. 2015
[e] Yusef-Zadeh et al. 2009
[f] Matsunaga et al. 2009; Glass et al. 2001

4.5.2 Classification using photometric criteria

Several previous studies have made use of colour-colour diagrams (CCDs) to define criteria to classify YSOs. We are trying with our spectroscopic sample of YSOs and non-YSOs to establish new and more reliable photometric criteria to distinguish YSOs from non-YSOs. Initially, we made use of some YSO classification criteria using CCDs implemented in the literature to check whether they are able to classify and separate our sample of spectroscopically identified YSOs from late-type stars. For this, we obtained the photometry of point sources at 3.6 μm, 4.5 μm, 5.8 μm, 8.0 μm (Ramírez et al., 2008), and 24 μm from the MIPSGAL

catalogue (Gutermuth and Heyer, 2015), and we merged these with our data by searching within radii of 2.″0. We find 87 sources with valid 3.6 to 8.0 μm photometry and 28 sources with valid 24 μm photometry in our sample.

Figure 4.8 shows two CCDs and a colour-magnitude diagram (CMD) with respective criteria from the literature to classify YSOs. In Figure 4.8(a), we plot [5.8]-[8.0] vs. [3.6]-[4.5] with a small and big box representing the regions belonging to Class II and Class I YSOs, respectively. Those areas come from the disk and envelope models of low mass YSOs as shown in Allen et al. (2004). Figure 4.8(b) shows the same plot, but with a polygon used to define the region enclosing Stage I YSOs as defined in Robitaille et al. (2006). YHA09 used the CMD ([8.0]-[24] vs. [24]) in Figure 4.8(c) to choose their sample of possible YSO candidates in the CMZ by considering all sources lying to the right of the dashed line as YSOs. We estimate and show the extinction vector (black arrow) for the two CCDs, assuming an A_K of 2 mag (corresponding to A_V=30 mag; typical of the CMZ from Schultheis et al. (2009)) using the $\frac{A_\lambda}{A_K}$ relations from Nishiyama et al. (2009). It is clear from each plot that, even after taking the extinction into account, there is severe contamination from the late-type stars in the regions defined to contain YSOs and that there is no clean colour-colour criterion visible.

Hence, we tested various combinations of colours and magnitudes to clearly separate YSOs from cool late-type stars in our sample. We see a clear linear trend followed by the late-type stars only in the CCD H-K_S vs. H-[8.0], as shown in Figure 4.9, while the YSOs exhibit redder H-[8.0] colours and are thus clearly separated. We defined a rough criterion to separate YSOs from cool late-type stars, taking into account the H-K_S cut at 1.5 estimated to remove foreground sources (assuming A_V = 30 mag and using extinction laws of Nishiyama et al. (2009)). A similar H-K_S cut was also suggested by Schödel et al. (2010) to remove foreground sources based on their study towards the central parsec of the Galaxy. We estimate the extinction vector again, as mentioned before, and show that it is almost parallel to the line separating YSOs from late-type stars. Thus the extinction does not greatly affect our criterion. We want to stress that our sample is small and this criterion needs to be confirmed by a larger sample,

$$(H - [8.0]) = 2.75 \times (H - K_S) + 1.75;\ 1.5 < (H - K_S) \leq 5. \tag{4.4}$$

4.6 Mass estimation

In the above section, we spectroscopically identified 23 YSOs from among 91 sources in the CMZ. In this section, we construct their near- and mid-infrared SEDs and fit these soruces using synthetic SED models for YSOs to constrain their stellar parameters (e.g. stellar radius $R_\star$, effective temperature $T_{\rm eff}$, stellar mass $M_\star$, total stellar luminosity $L_\star$, and extinction in V-band A_V).

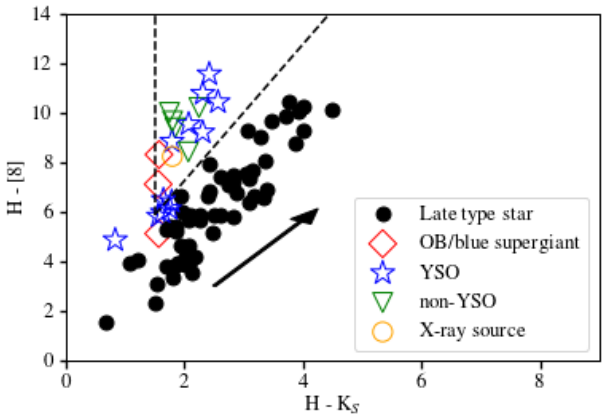

Figure 4.9: H-K_S vs H-[8.0] diagram. This plot shows a clear trend for cool late-type stars separating the YSOs in our sample. The dashed line represents our proposed criterion to separate YSOs and late-type stars. The black arrow represents the extinction vector estimated for A_K = 2 mag (typical of the CMZ) using the $\frac{A_\lambda}{A_K}$ relations from Nishiyama et al. (2009).

4.6.1 Robitaille SED models

Robitaille et al. (2006) presented a set of approximately 20,000 radiative transfer models with corresponding SEDs assuming an accretion scenario with a central star surrounded by an accretion disk, infalling envelope, and bipolar cavities, i.e. YSOs. Robitaille et al. (2007) presented a tool to fit these YSO model SEDs to observations, providing a range in the parameter (e.g. stellar mass, total luminosity, extinction in V-band, envelope accretion rate, and age) space corresponding to a set of best fit models.

These models are largely in use to estimate approximate values of stellar parameters for a photometrically or spectroscopically identified sample of YSOs. YHA09 and An11 used these models to classify YSOs into various evolutionary stages based on the envelope infall rate and disk accretion rate of each source. YHA09 in turn estimate the SFR in the CMZ using masses they obtain from the SED fits.

Recently, Robitaille (2017), hereafter R17, introduced an improved set of SED models for YSOs that covers a much wider range of parameter space and excluding most of model-dependent parameters in addition to several other improvements. Unlike previous models, there are 18 different sets of models with increasing complexity that vary from a single central star to a star in an ambient medium surrounded by accreting disk, infalling envelope, and bipolar cavities as described in detail in R17. We used the latest R17 models to fit the SEDs of sources in our sample to estimate stellar parameter such as stellar radius, luminosity, or effective temperature. We used these parameters to determine the stellar masses of our YSO sample.

4.6.2 SED fits

We construct the SEDs for our sample using wavelengths ranging from 1.25 - 24 μm. As mentioned in Section 4.5.2, we used the JHK_S photometry from the SIRIUS catalogue, 3.6 to 8.0 μm photometry from Ramírez et al. (2008) and 24 μm MIPS photometry from Gutermuth and Heyer (2015). In addition, we use the 15 μm photometry from the ISOGAL point source catalogue (Omont et al. 2003a,b) so that we constrain the SEDs over a large wavelength range. Searching within 2.″0 of YSOs in our sample, we find seven sources in the ISOGAL PSC out of which only two have valid 15 μm magnitudes. Within the same search radius, we find six YSOs with a match in the 24 μm catalogue, all of which have valid photometry.

Thus, among 23 spectroscopically identified YSOs in our sample, in addition to 1.25 - 8.0 μm magnitudes, six sources have only 24 μm magnitudes, two sources have only 15 μm magnitudes, and there are no sources with valid magnitude determined at both 15 μm as well as 24 μm. We find that the SED fitting by the model requires data points at λ>12 μm to give reliable results. For that reason, we carried out SED fits using the SED fitting tool only for these eight sources using the above-mentioned set of photometry.

We assume the source distance to be in the range 7 kpc < R < 9 kpc from the Sun and interstellar extinction along the line of sight to the Galactic centre to be in the range 20 mag < A_V < 50 mag (Schultheis et al., 2009), ensuring that these sources belong to the CMZ. These assumptions ensure that the conditions at the Galactic centre are considered while fitting the model SEDs to our observed SEDs. We assume typical errors of 0.05 mag for JHK_S photometry and 0.1 mag for 3.6 to 8.0 μm photometry, while ISOGAL and MIPSGAL catalogues provide typical errors of ~0.05 mag for 15 μm and 0.1 mag for 24 μm photometry, respectively. To include reasonable fitting results, we selected all SEDs that satisfy χ^2 - $\chi^2_{\rm best}$ < 5 per data points for each source in all 18 model sets. For each model set, $\chi^2_{\rm best}$ represents χ^2 value of the best fit. Thus each source SED is fitted with 18 different model sets, each of which gives a best fit SED with a $\chi^2_{\rm best}$ value. For each source, we selected the model set corresponding to the best fit SED with the lowest $\chi^2_{\rm best}$ value as the one that best represents the evolutionary stage of the source. Figure 4.10 shows typical examples of SED fitting results for eight YSOs in our sample.

4.6.3 Fit parameters and mass

We chose the model set corresponding to the best fit SED with the lowest $\chi^2_{\rm best}$ value as mentioned above and estimate mean values of A_V, $T_{\rm eff}$, and stellar radius, $R_\star$ from all the fits satisfying the χ^2 cut in the chosen model set. We estimated approximate values for the stellar luminosity, $L_\star$, using the Stefan-Boltzmann law from $T_{\rm eff}$ and $R_\star$, assuming solar $T_{\rm eff}$ to be 5772 K. To determine an approximate mass for each YSO, we used the pre-main sequence (PMS) tracks for stars with metallicity of Z = 0.02 and mass range of 0.8 $M_\odot$ to 60 $M_\odot$ from Bernasconi and Maeder (1996). The masses were sampled in a non-uniform manner with stellar tracks provided for 0.8, 1.0, 1.5, 2.0, 3.0, 5.0, 9.0, 15.0, 25.0, and 60.0 $M_\odot$.

We calculated the separation of each source from the stellar track for each mass in the

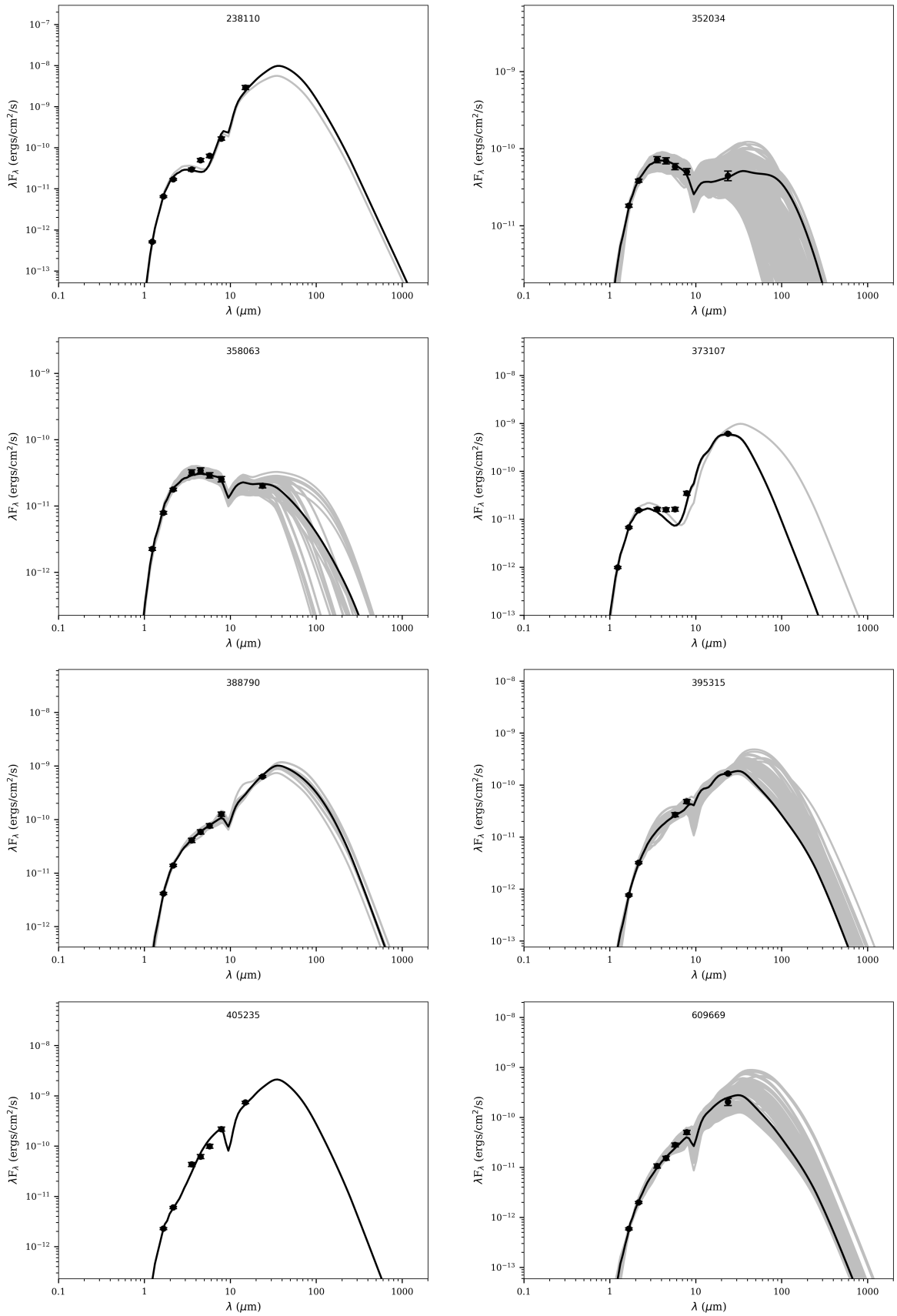

Figure 4.10: SED fits for 8 YSOs in our sample with available photometric data up to 24 μm, performed by the SED fitter tool using different YSO SED models in R17. The best fit is shown using solid black line and grey lines show all other fits that satisfy the criteria : χ^2 - $\chi^2_{\rm best}$ < 5 per data point.

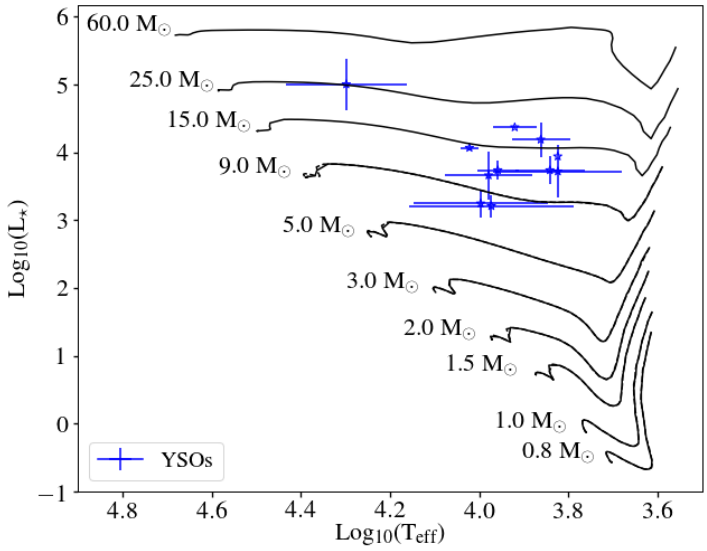

Figure 4.11: $\log_{10}(L_\star)$ vs. $\log_{10}(T_{\rm eff})$ diagram showing the location of YSOs (blue stars) and the pre-main sequence (PMS) stellar tracks from Bernasconi and Maeder (1996) for different masses in black. The errors in $T_{\rm eff}$ and $L_\star$ are also shown.

Table 4.3: Details of the SED fit parameters. For each source represented by their SST GC No., average values of parameters from the model set corresponding to the best fit SED with the lowest $\chi^2_{\rm best}$ value are chosen and listed. The errors or uncertainties for parameters are roughly determined from the standard deviation in mass from all fits. The last column shows the A_V values from the extinction map of Schultheis et al. (2009) within $2'$ of each source.

SST GC No.	Model	N_{data}	N_{fits}	$\chi^2_{\rm best}$	<A_V> (mag)	<$\log_{10}(L_\star)$> ($L_\odot$)	<$T_{\rm eff}$> (K)	<$M_\star$> ($M_\odot$)	$A_{V map}$ (mag)
238110	spubhmi[a]	8	2	96.7	20.5 ± 0.4	4.4 ± 0.0	8329 ± 936	20.0 ± 5.0	25.5 ± 1.1
352034	sp–s-i[b]	7	329	1.1	22.8 ± 2.4	3.7 ± 0.4	6668 ± 2213	12.4 ± 3.8	45.0 ± 11.3
358063	sp–s-i[b]	8	45	30.1	20.3 ± 0.3	3.7 ± 0.1	9091 ± 979	9.4 ± 1.5	32.3 ± 5.8
373107	sp–h-i[c]	8	9	104.5	24.8 ± 0.6	4.1 ± 0.0	10524 ± 499	15.0[*]	31.7 ± 5.1
388790	spubsmi[d]	7	13	0.9	22.2 ± 1.2	3.7 ± 0.2	6946 ± 1255	12.7 ± 2.9	43.0 ± 12.4
395315	spubsmi[d]	5	91	1.9	24.2 ± 3.5	3.2 ± 0.2	9397 ± 3981	7.8 ± 2.0	34.3 ± 4.2
405235	spu-smi[e]	7	1	32.7	20.0	3.9	6671	15.0[+]	37.5 ± 2.5
609669	spubsmi[d]	7	132	8.6	22.8 ± 2.7	3.3 ± 0.2	9932 ± 3436	8.2 ± 1.7	26.7 ± 2.6

[a] A complex model in which the central star with a disk, a variable disk inner radius, and bipolar cavities are enclosed in a rotationally flattened envelope structure surrounded by ambient interstellar medium.
[b] Disks around a central star with a non-variable inner radius. No surrounding envelope or ambient interstellar medium
[c] Same as b except that the disk inner radius is variable.
[d] Same as a except that the disk inner radius is set to the dust sublimation radius.
[e] Same as d except that there are no bipolar cavities
[*] Only one closest stellar track to source position (see Figure 4.11) from all SED fits of the chosen model set
[+] Only one SED fit to the observed photometry by the chosen model set

$\log_{10}(L_\star)$ - $\log_{10}(T_{\rm eff})$ space, and assigned each source the mass corresponding to the track at the least separation. This exercise was carried out for all fits that satisfy the χ^2 cut in the chosen model set and we estimated a mean mass from them. The standard deviation in mass from all SED fits can be used to make a rough estimate of the error. A zero error for mass is obtained when there is only one SED fit or when there is a single closest stellar track to source positions from all SED fits of the chosen model set. We assume their mass uncertainties to be limited by the mass sampling of PMS tracks. Figure 4.11 shows the $\log_{10}(L_\star)$ versus $\log_{10}(T_{\rm eff})$ plot with the stellar tracks and location of 8 spectroscopically identified YSOs. Mass estimates range from ~ 8 to 20 $M_\odot$, as expected for high mass YSOs.

We estimated the uncertainties for $T_{\rm eff}$, $L_\star$, and A_V similarly from standard deviation in their values from all SED fits of the chosen model set. Table 4.3 lists the main model fit parameters and the estimated masses for the YSOs. The A_V values estimated by the SED models are mostly close to the lower end of our constraints (20 mag < A_V < 50 mag), which is not the expected case. So we used the extinction map of Schultheis et al. (2009) to estimate the foreground visual extinction close to the location of our sample, by searching within the radius corresponding to the pixel size of the extinction map (2′). The estimated A_{Vmap} values are listed in the last column of Table 4.3. We find significant difference in A_V from models and A_{Vmap} from the extinction map (mean difference ~ 9.3 mag), suggesting that the models need to be improved. A similar disagreement between A_V from Robitaille et al. (2007) models and A_V from Schultheis et al. (2009) extinction map was estimated by An11 for their spectroscopically identified YSOs.

4.7 SFR estimate

As mentioned in Section 4.1.3, once the masses of YSOs are estimated, by extrapolating the chosen stellar IMF down to lower masses, the total embedded stellar population mass of the region can then be estimated which can in turn be used to estimate the SFR. Owing to the low number of spectroscopically identified YSOs, it is not possible to apply this method to our spectroscopic sample.

However it is possible to use our photometric selection criterion (see Section 4.5.2) based on the H-$K_{\rm S}$ versus H-[8.0] diagram to obtain a much more complete sample of YSOs in the CMZ. For this, we used the the photometric catalogue of SIRIUS towards the Galactic centre from which we selected our observed sample. We combined this sample with 3.6 - 8.0 μm photometry from Ramírez et al. (2008), 24 μm photometry from Gutermuth and Heyer (2015), and 15 μm photometry from ISOGAL PSC. Within |l| < 1°.5 and |b|<0°.5 we find 16,180 sources with valid photometric magnitudes in H, $K_{\rm S}$, and 8.0 μm bands and in either of the two bands: 15 μm or 24 μm. We then applied our criterion (see Equation 4.4), identifying 334 sources as YSOs. As seen in Section 4.5.2, foreground sources were removed by default using this criterion. However, OB supergiants can still contaminate our YSO sample.

Figure 4.12 shows the selected YSOs in H-$K_{\rm S}$ versus H-[8.0] diagram (left panel) and spatial distribution of YSOs in the (l,b) plane colour coded with the number of YSOs in (l,b)

bins of 0.°05 each. The white patch close to ~0.°0 latitude and longitude is an observational artefact from the Gutermuth and Heyer (2015) and the ISOGAL PSC catalogues where data are lacking. As a result, the YSO count is higher at the negative longitudes than in positive longitudes, contrary to the fact that two-thirds of molecular gas is on positive longitudes (Bania 1977; Bally et al. 1988; Morris and Serabyn 1996; Oka et al. 2005 etc.). We performed the SED fitting using R17 models for these 334 sources and we determined approximate masses for these sources as mentioned in section 4.6.3.

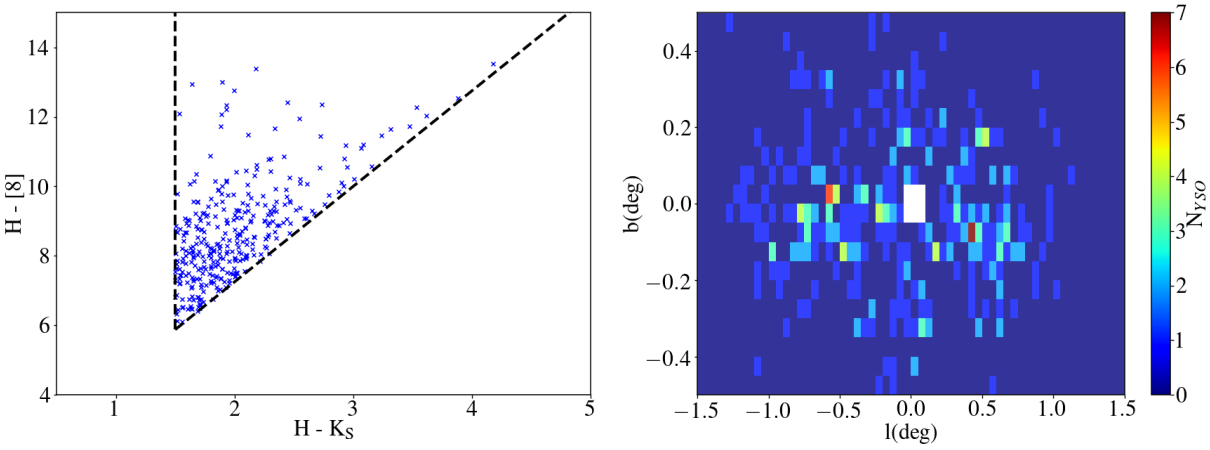

Figure 4.12: Plots showing candidate YSOs in the CMZ selected using our criterion and their distribution in the (l,b) plane. Left: H-K_S vs. H-[8.0] diagram is used to select YSOs from the source sample constructed by combining NIR catalogue of Galactic centre using SIRIUS (Nagashima et al. 1999; Nagayama et al. 2003), 3.6 - 8.0 μm photometry from Ramírez et al. (2008), 24 μm photometry from Gutermuth and Heyer (2015) and 15 μm photometry from ISOGAL PSC. The dashed line represents our proposed criteria to separate YSOs and late-type stars. Right: Spatial distribution of YSOs in the (l,b) plane colour coded with the number of YSOs in (l,b) bins of 0.°05 each. The white patch close to (l,b) ~ (0.°0,0.°0) is the observational artefact from the Gutermuth and Heyer (2015) and the ISOGAL PSC catalogues where data are lacking.

We chose ~ 190 sources with $\chi^2_{\rm best} < 35$ (chosen based on the average value of $\chi^2_{\rm best}$ among the 8 spectroscopically confirmed YSOs) to plot the mass distribution, which ranges from 2.7 $M_\odot$ to 35 $M_\odot$. The distribution peaks at ~ 8 $M_\odot$, emphasizing that the majority of YSOs are in the high mass range. Thus, we miss the low mass stars, and hence we adopted the Kroupa IMF (described in Section 1.2.4) to fit it to the peak of our distribution, extrapolated it to lower masses, and estimated the total embedded stellar population in the CMZ. The Kroupa IMF for different mass ranges are defined in Equations 1.13, 1.14 and 1.15. We follow the method described in Immer et al. (2012) and fit our mass distribution histogram with a curve of the form as in Equation 1.13 by non-linear least squares fitting routine. The fitting results in a value of A = 7339, which we used to obtain $\zeta(M)$ at M = 0.5 $M_\odot$ assuming a continuous IMF and thus estimate B = 14677 from Equation 1.14. We carried out the same exercise to estimate C = 183464. Figure 4.13 shows the mass distribution histogram and the

fit we performed on the distribution. Finally, we estimate the total mass of YSOs to be ~ 35000 $M_\odot$ in the CMZ using

$$M_{tot} = \int_{0.01}^{120} M\zeta(M)dM. \tag{4.5}$$

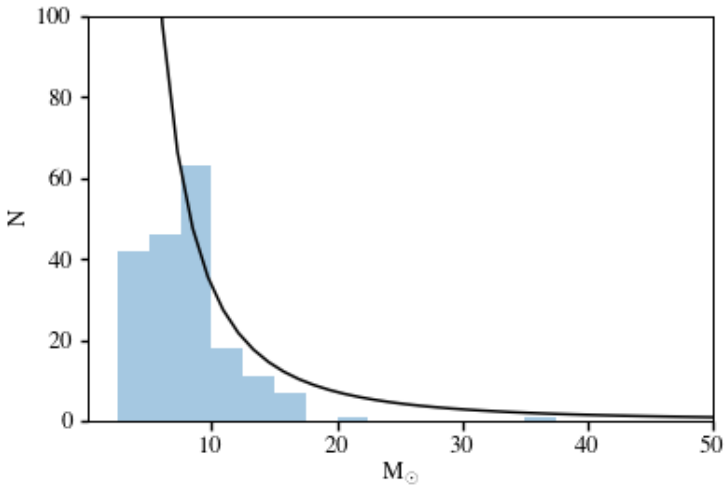

Figure 4.13: Mass distribution histogram (filled blue bars) of YSOs. These YSOs were selected using our new photometric colour-colour criteria from the SIRIUS catalogue within |l| < 1°.5 and |b|<0°.5. Masses are determined approximately using the YSO parameters from SED fits and pre-main sequence tracks of Bernasconi and Maeder (1996). The black curve represents the Kroupa IMF (Kroupa, 2001) fitted to the peak of the distribution. We estimate the mass of the underlying YSO population from the area under the curve from 0.01 $M_\odot$ to 120 $M_\odot$

Assuming all YSOs that constitute our sample have an average age of 0.75 ± 0.25 Myr, we estimated the average SFR to be ~ 0.046 $M_\odot yr^{-1}$. If we assume a different IMF (e.g. Salpeter) and change the integration limits in the mass range in addition to including the mass uncertainties from the individual SED fitting (see Table 4.3) and the uncertainty in the assumed age, our estimated error in the derived SFR is of the order of ± 0.026 $M_\odot yr^{-1}$. We also changed our colour criterion by reducing the H-K_S cut to 1.0 instead of 1.5 to account for the variability in extinction across CMZ and the estimated SFR is still within the uncertainty limit of +0.026 $M_\odot yr^{-1}$.

Our SFR estimate is lower than values from previous studies of YHA09, An11, and Immer et al. (2012). YHA09 and Immer et al. (2012) applied the YSO counting method of photometrically identified YSOs to calculate SFR of ~ 0.14 $M_\odot yr^{-1}$ (YSO lifetime ~ 0.1 Myr) and ~ 0.08 $M_\odot yr^{-1}$ (YSO lifetime ~ 1 Myr), respectively. An11 carried out a spectroscopic identification of YSOs among sources in common with YHA09 and derived a value of 0.07 $M_\odot yr^{-1}$ based on the 50% contamination they found. Based on the re-examination of YHA09 sample using radiative transfer models and realistic synthetic observations, Koepferl et al. (2015) estimated the SFR to be lower by a factor of three or more.

In addition to the YSO counting method, there have been studies that have employed the infrared luminosity-SFR relation, free-free emission from the ionised gas (i.e. bremsstrahlung radiation) at cm wavelengths to estimate the mass of the underlying YSO population, column density threshold, and volumetric star forming relations to estimate and predict, in turn, the SFR in the CMZ (Longmore et al. 2013a; Barnes et al. 2017). Longmore et al. (2013a) estimated the SFR in the |l|<1°.0, |b|<0°.5 to be ~ 0.015 $M_{\odot}yr^{-1}$ based on the free–free emission contribution to the 33 GHz flux using Wilkinson Microwave Anisotropy Probe (WMAP) data. But the predictions from the column density threshold and volumetric star formation relations exceed the observed SFR with estimates of 0.78 $M_{\odot}yr^{-1}$ and 0.41 $M_{\odot}yr^{-1}$, respectively. Given that predictions from these star formation relations and models are largely dependent on the mass of dense gas, it is important to make sure that different tracers of the dense gas are reliable probes. For example, Mills and Battersby (2017) have shown that HNCO might be a better cloud mass probe than HCN 1-0 in the Galactic centre environment.

Table 4.4: Details of the SFR estimated using different methods in the literature. The method used to estimate the SFR, the region of the CMZ covered, estimated SFR, and corresponding references are listed.

Method	Region covered	SFR ($M_{\odot}yr^{-1}$)	Reference
YSO counting (photometric criterion)	$\|l\| < 1.^{\circ}3$, $\|b\| < 0.^{\circ}17$	0.14[a]	YHA09
YSO counting (spectroscopic criterion)	...	0.07[a]	An11
YSO counting (photometric criterion)	$\|l\| < 1.^{\circ}5$, $\|b\| < 0.^{\circ}5$	0.08[b]	Immer et al. (2012)
Free–free emission – SFR	$\|l\| < 1.^{\circ}0$, $\|b\| < 0.^{\circ}5$	0.015	Longmore et al. (2013a)
	$\|l\| < 1.^{\circ}0$, $\|b\| < 1.^{\circ}0$	0.06	Longmore et al. (2013a)
Column density threshold	$\|l\| < 1.^{\circ}0$, $\|b\| < 0.^{\circ}5$	0.78	Longmore et al. (2013a)
Volumetric SF relations	$\|l\| < 1.^{\circ}0$, $\|b\| < 0.^{\circ}5$	0.41	Longmore et al. (2013a)
Infrared luminosity–SFR	$\|l\| < 1.^{\circ}0$, $\|b\| < 0.^{\circ}5$	0.09±0.02	Barnes et al. (2017)
YSO counting	$\|l\| < 1.^{\circ}5$, $\|b\| < 0.^{\circ}5$	0.046 ± 0.026	This work

[a] Assumed age of YSOs ~ 0.1 Myr
[b] Assumed age of YSOs ~ 1 Myr

Barnes et al. (2017) found an average global SFR of ~ 0.09±0.02 $M_{\odot}yr^{-1}$ in the same l, b range from the luminosity-SFR relations using 24 μm, 70 μm, and total infrared bolometric luminosity. Based on the observational evidence that the individual clouds and clusters are connected along a coherent velocity structure in position-position-velocity (PPV) space (Henshaw et al., 2016), Barnes et al. (2017) determined the SFR of individual clouds in the CMZ using the dynamical orbit model of Kruijssen et al. (2015) assuming that star forma-

tion within these clouds is tidally triggered at the pericentre of the orbit (Longmore et al., 2013b). These authors find the total SFR within these clouds to be 0.03 to 0.071 $M_{\odot}yr^{-1}$. Table 4.4 lists the details of the SFR estimated in the CMZ using various methods based on past studies.

Thus, the SFR estimate in the CMZ from different methods (including our estimate) all point to a lower value than expected given the large reservoir of dense gas available. There are several physical explanations attributed to this dearth of star formation in the CMZ. Longmore et al. (2013a) suggested that the additional turbulent energy in the gas, as indicated by the larger internal cloud velocity dispersion, could be providing support against gravitational collapse. The other explanations include episodic star formation in the CMZ due to spiral instabilities, high turbulent pressure in the CMZ, and that the gas is not self-gravitating as discussed in detail in Kruijssen et al. (2014).

4.8 Summary and conclusions

With the aim of estimating the SFR in the CMZ using spectroscopic identification of YSOs, we prepared a detailed observation of 22 fields using KMOS. From the 8 fields we observed, we extracted clean spectra for 91 sources. Based on the CO absorption found in cool, late-type stars and Brγ emission seen in YSOs, we were able to clearly separate YSOs from cool, late-type stars in the EW(CO) versus EW(Brγ) diagram. We plotted our spectroscopically classified YSOs and late-type stars in the colour-colour and colour-magnitude diagrams used in the literature to classify YSOs. We found that various criteria used to classify YSOs in such diagrams were not able to remove contaminants. We suggest a new criterion in the H-$K_{\rm S}$ versus H-[8.0] colour-colour diagram wherein we see a clear separation of YSOs and late-type stars.

We used the new and improved version of SED models for YSOs in R17 to fit the observed photometry in the wavelength range of 1.25–24 μm for 8 YSOs. From the radii and temperatures we obtained from the SED fit, we estimated their masses to be greater than 8 $M_{\odot}$. Since we needed a bigger sample to estimate the SFR in the CMZ, we searched for sources within |l| < 1°.5 and |b| < 0°.5 with valid photometry in H, $K_{\rm S}$ (IRSF catalogue), 8.0 μm (Ramírez et al., 2008) and 15μm (ISOGAL PSC), or 24 μm (Gutermuth and Heyer, 2015) bands. We identified 334 YSOs based on the criterion we defined in the H-$K_{\rm S}$ versus H-[8.0] diagram. We performed SED fits for these sources using R17 models resulting in 190 sources with a good fit, and their estimated masses range from 2.7 to 35 $M_{\odot}$, peaking at ~ 8 $M_{\odot}$. The total mass of YSOs in the CMZ was then estimated to be ~ 35000 $M_{\odot}$ by extrapolating to lower masses using a Kroupa IMF between 0.01 and 120 $M_{\odot}$. Assuming an average age of 0.75 ± 0.25 Myr for YSOs, we estimate the SFR to be ~ 0.046 ± 0.026 $M_{\odot}yr^{-1}$, that is slightly lower than found in previous studies.

It is necessary to carry out follow-up spectroscopic infrared observations to obtain a statistically significant YSO sample to further constrain our colour-colour criterion to identify YSOs. This will help us accurately determine the SFR, which is an important ingredient in the chemical evolution models of the Galaxy, as well as to understand star formation of

the Galactic centre and to serve as a template for circumnuclear star formation in the other galactic nuclei.

Chapter 5

Conclusions and future works

Contents

As mentioned in the chapter 1, the study on the structure, formation and evolution of the Milky Way, i.e., Galactic archaeology, relies extensively on the data from large scale photometric as well as spectroscopic surveys. Such Galactic archaeology surveys make use of dedicated telescopes, man power and computational facilities to carry out observations, develop tools and pipelines for data reduction and analysis. In addition, there are small scale observations carried out using public access observing facilities (e.g. ESO) based on science proposals submitted by astronomers. Thus there have been great increase in terms of the quality as well as quantity of the data from observations that have contributed to the advancements in this field. To understand and interpret these data, different types of models are in use (see sections 1.2.3 and 1.2.4), that predict various structural, chemical, and dynamical scenarios of how the Milky Way formed and evolved. Validation of such scenarios as well as improvements in these models require backing of observations. The works presented in this thesis made use of data from spectroscopic surveys as well as individual small scale spectroscopic observations using ESO telescopes to obtain results that will give us headway in the field of Galactic archaeology, especially in the dust enshrouded inner Milky Way.

At the end of each of the chapters 2, 3 and 4, I had summarised the results obtained in each work and given their respective conclusions. Here I will mention the important results and conclusions from each work, followed by my perspectives about the possible improvements or works to be done in the future.

5.1 Selection function effects

While large scale spectroscopic surveys provide the fundamental stellar parameters and elemental abundances for stars that numbers in the order of 10^5 – 10^6, it is important to understand the effect of the selection function in their derived parameters when interpreting the

results obtained using their data. It is also important to understand the measurement offsets in the derived parameters for common stars observed by each survey due to the difference in the observed wavelength range, spectral resolution as well as due to different stellar atmosphere models, linelists and other tools used in the analysis pipelines. With the increase in the number of these large scale surveys, it is thus important to compare and validate their common results as well to check the possibility of combining the fields commonly observed by them that will also improve the number statistics.

In the chapter 2, I addressed the above mentioned issues by using fundamental stellar parameters from the fields of the surveys APOGEE, GES, RAVE and LAMOST that are observed along the same lines of sight. I have shown that there are systematic offsets in the metallicity measurements for common stars between surveys. To investigate the possibility of combining common fields in order to improve the number statistics, I also studied the selection function effects on MDF and metallicity gradients in the case of each survey. The lack of common fields between all four surveys resulted in two cases for this study : APOGEE-GES-RAVE (AGR) and APOGEE-LAMOST-RAVE (ALR), resulting in a localised sample within $7 \leq R \leq 9$ kpc and $|Z| \leq 2$ kpc. For this, I used CMD as the main tool, wherein the colour and magnitude target selection cuts in each field were used, and divided into smaller bins to calculate the selection fraction by including the respective input photometric catalog used by each survey. Further, I generated mock data along similar lines of sights from stellar population synthesis models, Galaxia and TRILEGAL, and implemented these selection cuts on the mock CMDs to create mock observed sample as well as underlying parent population. This enabled to check the quality of these models and the assumptions used in them by comparing the observed MDF and vertical metallicity gradients with that of the mock ones. Both models were unable to replicate the observed trends, especially in the case of vertical metallicity gradients. I found negligible selection function effect on the MDF in the case of APOGEE, RAVE and LAMOST using quartiles as a quantitative parameter, and putting constrain on the quartile differences between the mock observed and mock parent sample MDFs. More importantly, upon scaling the metallicity values in RAVE and LAMOST to that in APOGEE, the estimated vertical metallicity gradient for each survey is consistent within 1-σ indicating the negligible effect of selection function. This result also confirmed the idea that it is indeed possible to combine the common fields of the surveys once they are put on the same metallicity scale and if the selection effects are negligible.

5.1.1 Future works

Using the common fields of three surveys limited the sample size of our study. In the future, I plan to carry out a similar study using common fields of two surveys, that will improve the sample size. There are also new data releases for each survey, wherein new observed fields are added in some surveys and analysis pipelines are improved to correct the errors in the previous data releases. Also in this work, I have not been able to include the radial metallicity gradient due to the concentration of the field center distributions in the vertical direction. With the use of only two surveys, it should be possible to include the radial metallicity gradient. This will also enable to use many other derived elements (alpha elements,

iron peak elements etc.) in these surveys to study the selection function effect on their trends and distributions. In Section 1.2.4, I have mentioned the significance of the [α/Fe] vs[Fe/H] trends and location of the knee in the interpretation of the SFR as well as IMF. Thus the comparison of [α/Fe] vs[Fe/H] trends using stars from the common fields of these surveys after proper scaling corrections will enable in understanding the consistency of the knee position in different surveys. In addition, I also plan to add new surveys like GALAH, the second data release of which have been released in April 2018, in this study. There are many upcoming surveys like WEAVE, 4MOST (see Section 1.2.2) that will improve the number statistics for the selection function effect study, also enabling to extend the study to regions outside the solar neighbourhood. This will also help in separating the individual Milky Way components, which was not possible in the work presented in this thesis. Improvement in distance estimation for nearby stars is already possible with the *Gaia* DR2 astrometric information. *Gaia* DR3 will provide the BP/RP spectra and/or RVS spectra along with the stellar parameters derived using them. This will open up more opportunities to exercise our study by including *Gaia* fields and compare their derived stellar parameters with those from other spectroscopic surveys.

My study also revealed that both Galaxia and Trilegal were unable to reproduce the observed metallicity distribution as well as vertical metallicity gradients. This is a major concern, considering that stellar population synthesis models are commonly used to understand the expected biases from selection functions while designing a spectroscopic survey. Thus stellar population synthesis models need to be updated to account for the observed trends in the chemical abundances and structure of different Milky Way components.

5.2 Galactic archaeology in the Inner Milky Way

The high dust extinction combined with the ~8 kpc distance from the Sun makes the inner Milky Way a very difficult region to observe and get good quality data. This also limits accurate predictions from population synthesis and chemical evolution models that decipher the structure, formation and evolution of this region. In the chapters 3 and 4, I used spectroscopic data from observations in this region to shed some light on the chemical abundance trends of late types stars in the inner Galactic bulge and star formation rate in the central molecular zone, respectively.

5.2.1 Inner Galactic Bulge

Using surveys like GIBS and BRAVA, the chemical abundances and kinematics for stars in the outer bulge ($|b| \geq 4^\circ$) are being investigated, producing mean metallicity and velocity maps of the outer bulge. Meanwhile, as mentioned in the Chapter 3, there have been limited number of observations and studies in the inner bulge region, especially at positive latitudes. The check for consistency/inconsistency in the chemical and kinematic trends in the inner bulge compared to that in the outer bulge is needed to understand the formation and evolution of the whole bulge. Another issue is the symmetry about the Galactic mid plane that have been assumed while constructing the velocity maps as well as in the models of the

bulge. The symmetry in mean velocity was validated for stars in the inner bulge fields along the bulge minor axis (Valenti et al., 2018). I carried out this work with the aim of investigating any North-South symmetries/asymmetries in the metallicity distribution function and composition, and comparing them to the outer bulge fields.

I carried out the data reduction and chemical abundance analysis of 71 M giant stars that are located along the bulge minor axis at l = 0°, b = ±0°, ±1°, ±2° and +3°. I was able to detect a bimodal MDF with a metal-rich peak at $\sim +0.3\,\mathrm{dex}$ and a metal-poor peak at $\sim -0.5\,\mathrm{dex}$, and only one star was found to have a metallicity exceeding 0.5 dex. The Galactic center field stars were found to be mainly metal-rich population with a mean metallicity of $+0.3\,\mathrm{dex}$. I also find symmetry in the MDF along the ±1°, ±2° fields. From the derived α abundances (Si and Mg), I found the [α/Fe] vs [Fe/H] trends to be consistent with that seen in the outer bulge fields. The decreasing trend in [α/Fe] for the supersolar metallicity stars are as expected from chemical evolution models. Thus with the caveat of a relatively small sample, I did not find significant differences in the chemical abundances between the Northern and the Southern fields, thus confirming the symmetry in chemistry between North and South of the inner Galactic bulge.

5.2.1.1 Future works

The results of bimodal MDF and chemical abundance trends are consistent with that found in outer bulge fields. The next step is to explore various formation and evolution scenarios of the bulge that leads to the observed MDF bimodality and α abundance trends. The debate on the bulge formation from the two proposed scenarios : secular evolution of disc or dissipational collapse, relies on such results to come to an agreement. N-body simulations can be used to predict the chemo-morphological characteristics of this region, as had already been implemented by Fragkoudi et al. (2018) for the Milky Way bulge. The α abundance trend that I obtained can also be used to constrain the star formation rate and IMF by making use of chemical evolution models (e.g. Grieco et al. 2015). In this work, I have compared the [α/Fe] vs [Fe/H] trends in the inner bulge to that in the outer bulge. Since there is a debate on the contribution of thin and thick discs to the bulge formation and evolution, comparison with the trends of stars in thick and thin discs will help reveal their contribution. For this, I will have to obtain similar high resolution spectra (using same instrument) of stars in both both bulge as well as thin and thick discs. More importantly, I will have to carry out the analysis in a consistent manner for all stars, as I did in this work for North and South field stars, to ensure that there is negligible measurement offset.

More high resolution spectroscopic observations need to be carried out in the inner bulge regions, especially at positive latitudes and covering a range of longitudes, to have a large enough sample size to confirm the results. With the current and upcoming *Gaia* data releases providing accurate astrometric information, it will be possible to efficiently get rid of foreground stars while selecting targets for our observations. The absence of sub solar metallicity stars in the Galactic center field also needs to be investigated as there were only 9 observed stars in this field. I also collaborate with groups that have carried out observations in the Galactic center and nuclear cluster using the Gemini/IGRINS and Keck II/NIRSPEC,

which can help improve the sample size as well as the K band wavelength coverage when combined with the CRIRES spectra. The CRIRES update project, CRIRES+ (Dorn et al., 2014), extends the wavelength coverage of CRIRES by a factor of ten, including the Y, J, H, L and M bands in addition to the already existing K band. The extension in wavelength coverage will provide the opportunity to extract the abundances for more elements. The C and N abundances extracted from CO and CN molecular lines can be used to estimate ages for red giant stars by relying on the mass - [C/N] relation (Martig et al., 2016). This relation is based on the first dredge-up process, as the star arrives on the giant branch following the CNO cycle (converting H to He), that brings up stellar materials from the core tho the surface. I also plan to derive the abundances of other tracers of age like the s-process neutron capture element, yttrium, that has been shown to have a tight relation with age (da Silva et al., 2012; Nissen, 2015).

The deep K band photometry of the VVV survey is shedding light on the structural details of the region in addition to being used as input photometric catalog for spectroscopic observations. In addition, the MOONS survey (mentioned in Section 1.2.2) will be able to provide accurate radial velocities, metallicities and chemical abundances for bulge stars in highly extincted regions, thus enabling to shed light on the chemo-dynamical characteristics of the bulge.

The Japan Astrometry Satellite Mission for Infrared Exploration (JASMINE) is a space based astrometric survey developed by the National Astronomical Observatory of Japan, that makes use of a series of three spacecrafts with telescopes of increasing size and capability, i.e., Nano-JASMINE : 5 cm (2019-2021), small-JASMINE : 30 cm (2022-2024), JASMINE : 80 cm (late 2020's). Among these, small-JASMINE will operate in determine Hw-band (1.1 ~ 1.7 μm) to determine positions and parallaxes accurate to 10~50 μarcseconds for stars (brighter than Hw = 11.5 mag) in a 3°×3°region around the Galactic center. JASMINE will be an extended version of small-JASMINE observing in Kw-band (1.5 ~ 2.5 μm) towards the Galactic bulge (20°× 10°) region around the Galactic center and determine the positions and parallaxes to an accuracy of up to 10 μarcseconds (for stars brighter than Kw = 11 mag). The main science goal will be to understand the formation of the Galactic bulge, star formation histories around the Galactic center, and the evolution of the super massive black hole (Gouda, 2012). Thus in the future, this survey will provide distances and tangential velocities of stars in the Galactic bulge, complementing the radial velocity and chemical abundance measurements from spectroscopic surveys (APOGEE, BRAVA, GIBS, MOONS etc.) and individual observations.

5.2.2 SFR in the CMZ

The low star formation rate in the central molecular zone, estimated by observational means, is a matter of concern as it is not expected from the presence of a large reservoir of dense molecular gas. Various star formation models that takes into account the mass of dense gas predict an order of magnitude higher rate of star formation in the CMZ. Most of the star formation rate (SFR) estimates towards the CMZ comes from studies of young stellar objects (YSOs) using infrared photometry. But their status as a YSO has to be confirmed by

spectroscopic observations, which makes the current observed SFR estimates in the CMZ a matter of debate.

I have carried out near-IR spectroscopic observations of photometrically selected YSOs in the CMZ using the mid-resolution K-band Multi Object Spectrograph (KMOS). I separated the evolved stars from YSOs based mainly on the absence or presence (respectively) of the CO absorption band at ~2.3 μm as well as the Br-ν line. In addition, I have found a new photometric criterion to separate YSOs and evolved stars in the color-color diagram using a combination of H, K and 8 μm photometric magnitudes. I used this criteria on the CMZ sources with high resolution near infrared photometry from Nishiyama et al. (2009) to identify possible YSO candidates in the CMZ. By modelling the spectral energy distributions for these YSOs using the latest Robitaille (2017) SED models, I calculated their approximate masses from the model fit parameters. Assuming the Kroupa IMF to our mass distribution and extrapolating to lower masses, I estimated the SFR in CMZ to be $\sim 0.046 \pm 0.026\,M_{\odot}yr^{-1}$ M⊙/Yr. This is slightly lower than the previous SFR estimates in the literature (0.07-0.14 M⊙/Yr) and an order of magnitude lower than the rates predicted by different star formation prescriptions.

5.2.2.1 Future works

Only 8 fields out of 22 fields in the observing proposal could be observed due to bad weather, reducing the sample size as well as the observed area drastically. The proposed criterion to separate YSOs from late type stars needs to be validated by observing and obtaining K band spectra of more stars in the region. I will submit an updated proposal in this term to observe more stars using KMOS. Another concern is regarding the mass estimation that depends on the fitting of photometric SED using Robitaille (2017) models. There are degeneracies in these models that can bias the derived parameters like bolometric luminosities and $T_{\rm eff}$ that are used in combination with the isochrone tracks of Bernasconi and Maeder (1996) to estimate the masses of identified YSOs. I still need to find better methods to encounter these issues. I would like to make use of cm wavelength high spatial resolution observations of VLA to confirm the YSOs in the CMZ identified by our new proposed criterion. Another future project involves the measuring of the SFR in the CMZ using different methods involving cm, mm as well as mid IR wavelength observations (see Section 4.1) and comparing these different SFR estimates. This will help us understand the bias, if any, in the SFR estimates from different tracers of star formation. The ultimate goal will be to trace the SFR and in turn the SFH in the Galactic center region, which is yet to be determined accurately.

I also plan to use the KMOS spectra of late type stars to determine their $T_{\rm eff}$ from the $T_{\rm eff}$ -CO equivalent width relation of Schultheis et al. (2015), their metallicities and radial velocities. Feldmeier-Krause et al. (2017) have used a spectral fitting method to estimate metallicities of late type stars from the low resolution KMOS spectra. This technique can be used to estimate metallicties of the late type stars from the observed spectra, especially using those in the three fields close to the Galactic center. This will also help in obtaining an upper limit of metallicity in the Galactic center, where I had high resolution spectra of only 9 stars.

The Enhanced Resolution Imager and Spectrograph (ERIS; Amico et al. 2012), a planned

instrument (first light in 2020) onboard the UT4 (VLT), will provide IR imaging using near to mid IR camera and J-K band spectroscopy using an integral field spectrograph with a powerful adaptive optics (AO) system. The spectral resolution of 8000 (higher than KMOS) will enable in obtaining deep spectra for YSOs and late type stars towards the star forming regions in the Galactic center. ERIS would be the ideal instrument to get deep and complete near infrared spectra as well as photometry of stars which will enable us to derive the SFH in the inner Milky Way.

Finally, considering that YSO counting is a commonly used method to estimate SFR in the CMZ as well as other individual star forming regions of the Milky Way, a dedicated imaging + spectroscopic survey (preferably in near to mid IR range) to detect YSOs in star forming regions will benefit the community focusing on young pre-main sequence stars and SFR estimation.

List of Figures

List of Tables

Bibliography

Abadi, M. G., Navarro, J. F., Steinmetz, M., and Eke, V. R. (2003). Simulations of Galaxy Formation in a Λ Cold Dark Matter Universe. II. The Fine Structure of Simulated Galactic Disks. ApJ, 597:21–34. (Cited in page 9.)

Adams, F. C., Lada, C. J., and Shu, F. H. (1987). Spectral evolution of young stellar objects. ApJ, 312:788–806. (Cited in page 97.)

Ak, S., Bilir, S., Karaali, S., Buser, R., and Cabrera-Lavers, A. (2007). The metallicity distributions in high-latitudes with SDSS. New A, 12:605–612. (Cited in page 58.)

Alam, S., Albareti, F. D., Allende Prieto, C., Anders, F., Anderson, S. F., Anderton, T., Andrews, B. H., Armengaud, E., Aubourg, É., Bailey, S., and et al. (2015). The Eleventh and Twelfth Data Releases of the Sloan Digital Sky Survey: Final Data from SDSS-III. ApJS, 219:12. (Cited in page 39.)

Albareti, F. D., Allende Prieto, C., Almeida, A., Anders, F., Anderson, S., Andrews, B. H., Aragón-Salamanca, A., Argudo-Fernández, M., Armengaud, E., Aubourg, E., and et al. (2017). The 13th Data Release of the Sloan Digital Sky Survey: First Spectroscopic Data from the SDSS-IV Survey Mapping Nearby Galaxies at Apache Point Observatory. ApJS, 233:25. (Cited in pages 35 and 40.)

Allen, L. E., Calvet, N., D'Alessio, P., Merin, B., Hartmann, L., Megeath, S. T., Gutermuth, R. A., Muzerolle, J., Pipher, J. L., Myers, P. C., and Fazio, G. G. (2004). Infrared Array Camera (IRAC) Colors of Young Stellar Objects. ApJS, 154:363–366. (Cited in pages 98, 99, 110 and 134.)

Allende Prieto, C., Beers, T. C., Wilhelm, R., Newberg, H. J., Rockosi, C. M., Yanny, B., and Lee, Y. S. (2006). A Spectroscopic Study of the Ancient Milky Way: F- and G-Type Stars in the Third Data Release of the Sloan Digital Sky Survey. ApJ, 636:804–820. (Cited in page 15.)

Allende Prieto, C., Sivarani, T., Beers, T. C., Lee, Y. S., Koesterke, L., Shetrone, M., Sneden, C., Lambert, D. L., Wilhelm, R., Rockosi, C. M., Lai, D. K., Yanny, B., Ivans, I. I., Johnson, J. A., Aoki, W., Bailer-Jones, C. A. L., and Re Fiorentin, P. (2008). The SEGUE Stellar Parameter Pipeline. III. Comparison with High-Resolution Spectroscopy of SDSS/SEGUE Field Stars. AJ, 136:2070–2082. (Cited in page 39.)

Amico, P., Marchetti, E., Pedichini, F., Baruffolo, A., Delabre, B., Duchateau, M., Ekinci, M., Fantinel, D., Fedrigo, E., Finger, G., Frank, C., Hofmann, R., Jolley, P., Lizon, J. L., Le Louarn, M., Madec, P.-Y., Soenke, C., and Weisz, H. (2012). The design of ERIS for the VLT. In *Ground-based and Airborne Instrumentation for Astronomy IV*, volume 8446 of Proc. SPIE, page 844620. (Cited in page 126.)

An, D., Ramírez, S. V., Sellgren, K., Arendt, R. G., Adwin Boogert, A. C., Robitaille, T. P., Schultheis, M., Cotera, A. S., Smith, H. A., and Stolovy, S. R. (2011). Massive Young Stellar Objects in the Galactic Center. I. Spectroscopic Identification from Spitzer Infrared Spectrograph Observations. ApJ, 736:133. (Cited in pages 100 and 109.)

Anders, F., Chiappini, C., Rodrigues, T. S., Piffl, T., Mosser, B., Miglio, A., Montalbán, J., Girardi, L., Minchev, I., Valentini, M., and Steinmetz, M. (2016). Galactic Archaeology with CoRoT and APOGEE: Creating mock observations from a chemodynamical model. *Astronomische Nachrichten*, 337:926. (Cited in page 33.)

Anstee, S. D. and O'Mara, B. J. (1991). An investigation of Brueckner's theory of line broadening with application to the sodium D lines. MNRAS, 253:549–560. (Cited in page 74.)

Athanassoula, E. (2005). On the nature of bulges in general and of box/peanut bulges in particular: input from N-body simulations. MNRAS, 358:1477–1488. (Cited in page 7.)

Athanassoula, E., Rodionov, S. A., Peschken, N., and Lambert, J. C. (2016). Forming Disk Galaxies in Wet Major Mergers. I. Three Fiducial Examples. ApJ, 821:90. (Cited in page 8.)

Babusiaux, C. (2016). Correlations between Kinematics and Metallicity in the Galactic Bulge: A Review. PASA, 33:e026. (Cited in page 90.)

Babusiaux, C., Katz, D., Hill, V., Royer, F., Gómez, A., Arenou, F., Combes, F., Di Matteo, P., Gilmore, G., Haywood, M., Robin, A. C., Rodriguez-Fernandez, N., Sartoretti, P., and Schultheis, M. (2014). Metallicity and kinematics of the bar in situ. A&A, 563:A15. (Cited in pages 62, 65, 86, 89 and 90.)

Bahcall, J. N. (1986). Star counts and galactic structure. ARA&A, 24:577–611. (Cited in page 18.)

Balick, B. and Brown, R. L. (1974). Intense sub-arcsecond structure in the galactic center. ApJ, 194:265–270. (Cited in page 24.)

Bally, J., Stark, A. A., Wilson, R. W., and Henkel, C. (1988). Galactic center molecular clouds. II - Distribution and kinematics. ApJ, 324:223–247. (Cited in page 116.)

Bania, T. M. (1977). Carbon monoxide in the inner Galaxy. ApJ, 216:381–403. (Cited in page 116.)

Barklem, P. S. and O'Mara, B. J. (1998). The broadening of strong lines of Caˆ+, Mgˆ+ and Baˆ+ by collisions with neutral hydrogen atoms. MNRAS, 300:863–871. (Cited in page 74.)

Barklem, P. S., Piskunov, N., and O'Mara, B. J. (2000). A list of data for the broadening of metallic lines by neutral hydrogen collisions. *A&AS*, 142:467–473. (Cited in page 74.)

Barnes, A. T., Longmore, S. N., Battersby, C., Bally, J., Kruijssen, J. M. D., Henshaw, J. D., and Walker, D. L. (2017). Star formation rates and efficiencies in the Galactic Centre. MNRAS, 469:2263–2285. (Cited in pages 96, 97, 102 and 118.)

Bastian, N., Covey, K. R., and Meyer, M. R. (2010). A Universal Stellar Initial Mass Function? A Critical Look at Variations. ARA&A, 48:339–389. (Cited in page 23.)

Battersby, C., Bally, J., Ginsburg, A., Bernard, J.-P., Brunt, C., Fuller, G. A., Martin, P., Molinari, S., Mottram, J., Peretto, N., Testi, L., and Thompson, M. A. (2011). Characterizing precursors to stellar clusters with Herschel. A&A, 535:A128. (Cited in page 96.)

Becklin, E. E. and Neugebauer, G. (1968). Infrared Observations of the Galactic Center. ApJ, 151:145. (Cited in page 26.)

Bell, E. F., Zucker, D. B., Belokurov, V., Sharma, S., Johnston, K. V., Bullock, J. S., Hogg, D. W., Jahnke, K., de Jong, J. T. A., Beers, T. C., Evans, N. W., Grebel, E. K., Ivezić, Ž., Koposov, S. E., Rix, H.-W., Schneider, D. P., Steinmetz, M., and Zolotov, A. (2008). The Accretion Origin of the Milky Way's Stellar Halo. ApJ, 680:295–311. (Cited in pages 6 and 7.)

Benjamin, R. A., Churchwell, E., Babler, B. L., Bania, T. M., Clemens, D. P., Cohen, M., Dickey, J. M., Indebetouw, R., Jackson, J. M., Kobulnicky, H. A., Lazarian, A., Marston, A. P., Mathis, J. S., Meade, M. R., Seager, S., Stolovy, S. R., Watson, C., Whitney, B. A., Wolff, M. J., and Wolfire, M. G. (2003). GLIMPSE. I. An SIRTF Legacy Project to Map the Inner Galaxy. PASP, 115:953–964. (Cited in page 34.)

Bennett, C. L., Halpern, M., Hinshaw, G., Jarosik, N., Kogut, A., Limon, M., Meyer, S. S., Page, L., Spergel, D. N., Tucker, G. S., Wollack, E., Wright, E. L., Barnes, C., Greason, M. R., Hill, R. S., Komatsu, E., Nolta, M. R., Odegard, N., Peiris, H. V., Verde, L., and Weiland, J. L. (2003). First-Year Wilkinson Microwave Anisotropy Probe (WMAP) Observations: Preliminary Maps and Basic Results. ApJS, 148:1–27. (Cited in page 4.)

Bensby, T., Feltzing, S., Lundström, I., and Ilyin, I. (2005). α-, r-, and s-process element trends in the Galactic thin and thick disks. A&A, 433:185–203. (Cited in page 8.)

Bensby, T., Yee, J. C., Feltzing, S., et al. (2013). Chemical evolution of the Galactic bulge as traced by microlensed dwarf and subgiant stars. V. Evidence for a wide age distribution and a complex MDF. A&A, 549:A147. (Cited in pages 88, 89 and 133.)

Bernard, E. J., Schultheis, M., Di Matteo, P., Hill, V., Haywood, M., and Calamida, A. (2018). Star formation history of the Galactic bulge from deep HST imaging of low reddening windows. *ArXiv e-prints*. (Cited in pages 7 and 23.)

Bernasconi, P. A. and Maeder, A. (1996). About the absence of a proper zero age main sequence for massive stars. A&A, 307:829–839. (Cited in pages 112, 114, 117, 126, 135 and 136.)

Bik, A., Kaper, L., and Waters, L. B. F. M. (2006). VLT K-band spectroscopy of massive young stellar objects in (ultra-)compact HII regions. A&A, 455:561–576. (Cited in pages 100, 105 and 107.)

Bland-Hawthorn, J. and Gerhard, O. (2016). The Galaxy in Context: Structural, Kinematic, and Integrated Properties. ARA&A, 54:529–596. (Cited in pages 5, 8 and 24.)

Blum, R. D., Ramírez, S. V., Sellgren, K., and Olsen, K. (2003). Really Cool Stars and the Star Formation History at the Galactic Center. ApJ, 597:323–346. (Cited in page 74.)

Boeche, C., Siebert, A., Piffl, T., Just, A., Steinmetz, M., Grebel, E. K., Sharma, S., Kordopatis, G., Gilmore, G., Chiappini, C., Freeman, K., Gibson, B. K., Munari, U., Siviero, A., Bienaymé, O., Navarro, J. F., Parker, Q. A., Reid, W., Seabroke, G. M., Watson, F. G., Wyse, R. F. G., and Zwitter, T. (2014). Chemical gradients in the Milky Way from the RAVE data. II. Giant stars. A&A, 568:A71. (Cited in page 57.)

Boeche, C., Siebert, A., Piffl, T., Just, A., Steinmetz, M., Sharma, S., Kordopatis, G., Gilmore, G., Chiappini, C., Williams, M., Grebel, E. K., Bland-Hawthorn, J., Gibson, B. K., Munari, U., Siviero, A., Bienaymé, O., Navarro, J. F., Parker, Q. A., Reid, W., Seabroke, G. M., Watson, F. G., Wyse, R. F. G., and Zwitter, T. (2013). Chemical gradients in the Milky Way from the RAVE data. I. Dwarf stars. A&A, 559:A59. (Cited in page 20.)

Boehle, A., Ghez, A. M., Schödel, R., Meyer, L., Yelda, S., Albers, S., Martinez, G. D., Becklin, E. E., Do, T., Lu, J. R., Matthews, K., Morris, M. R., Sitarski, B., and Witzel, G. (2016). An Improved Distance and Mass Estimate for Sgr A* from a Multistar Orbit Analysis. ApJ, 830:17. (Cited in page 5.)

Bonifacio, P., Dalton, G., Trager, S., Aguerri, A. L., Carrasco, E., Vallenari, A., Abrams, D. C., Middleton, K., and Sayède, F. (2016). WEAVE an overview and status update. In Reylé, C., Richard, J., Cambrésy, L., Deleuil, M., Pécontal, E., Tresse, L., and Vauglin, I., editors, *SF2A-2016: Proceedings of the Annual meeting of the French Society of Astronomy and Astrophysics*, pages 267–270. (Cited in page 17.)

Borkova, T. V. and Marsakov, V. A. (2003). Two populations among the metal-poor field RR Lyrae stars. A&A, 398:133–139. (Cited in page 58.)

Bournaud, F., Elmegreen, B. G., and Martig, M. (2009). The Thick Disks of Spiral Galaxies as Relics from Gas-rich, Turbulent, Clumpy Disks at High Redshift. ApJ, 707:L1–L5. (Cited in page 9.)

Bovy, J., Nidever, D. L., Rix, H.-W., Girardi, L., Zasowski, G., Chojnowski, S. D., Holtzman, J., Epstein, C., Frinchaboy, P. M., Hayden, M. R., Rodrigues, T. S., Majewski, S. R., Johnson, J. A., Pinsonneault, M. H., Stello, D., Allende Prieto, C., Andrews, B., Basu, S., Beers, T. C., Bizyaev, D., Burton, A., Chaplin, W. J., Cunha, K., Elsworth, Y., García, R. A., García-Herńandez, D. A., García Pérez, A. E., Hearty, F. R., Hekker, S., Kallinger, T., Kinemuchi, K., Koesterke, L., Mészáros, S., Mosser, B., O'Connell, R. W., Oravetz,

D., Pan, K., Robin, A. C., Schiavon, R. P., Schneider, D. P., Schultheis, M., Serenelli, A., Shetrone, M., Silva Aguirre, V., Simmons, A., Skrutskie, M., Smith, V. V., Stassun, K., Weinberg, D. H., Wilson, J. C., and Zamora, O. (2014). The APOGEE Red-clump Catalog: Precise Distances, Velocities, and High-resolution Elemental Abundances over a Large Area of the Milky Way's Disk. ApJ, 790:127. (Cited in page 32.)

Bovy, J., Rix, H.-W., Liu, C., Hogg, D. W., Beers, T. C., and Lee, Y. S. (2012). The Spatial Structure of Mono-abundance Sub-populations of the Milky Way Disk. ApJ, 753:148. (Cited in pages 8 and 32.)

Bressan, A., Marigo, P., Girardi, L., Salasnich, B., Dal Cero, C., Rubele, S., and Nanni, A. (2012). PARSEC: stellar tracks and isochrones with the PAdova and TRieste Stellar Evolution Code. MNRAS, 427:127–145. (Cited in pages 44 and 70.)

Brook, C. B., Kawata, D., Gibson, B. K., and Freeman, K. C. (2004). The Emergence of the Thick Disk in a Cold Dark Matter Universe. ApJ, 612:894–899. (Cited in page 9.)

Buder, S., Asplund, M., Duong, L., Kos, J., Lind, K., Ness, M. K., Sharma, S., Bland-Hawthorn, J., Casey, A. R., De Silva, G. M., D'Orazi, V., Freeman, K. C., Lewis, G. F., Lin, J., Martell, S. L., Schlesinger, K. J., Simpson, J. D., Zucker, D. B., Zwitter, T., Amarsi, A. M., Anguiano, B., Carollo, D., Cotar, K., Cottrell, P. L., Da Costa, G., Gao, X. D., Hayden, M. R., Horner, J., Ireland, M. J., Kafle, P. R., Munari, U., Nataf, D. M., Nordlander, T., Stello, D., Ting, Y.-S., Traven, G., Watson, F., Wittenmyer, R. A., Wyse, R. F. G., Yong, D., Zinn, J. C., and Zerjal, M. (2018). The GALAH Survey: Second Data Release. *ArXiv e-prints*. (Cited in page 16.)

Carey, S. J., Noriega-Crespo, A., Mizuno, D. R., Shenoy, S., Paladini, R., Kraemer, K. E., Price, S. D., Flagey, N., Ryan, E., Ingalls, J. G., Kuchar, T. A., Pinheiro Gonçalves, D., Indebetouw, R., Billot, N., Marleau, F. R., Padgett, D. L., Rebull, L. M., Bressert, E., Ali, B., Molinari, S., Martin, P. G., Berriman, G. B., Boulanger, F., Latter, W. B., Miville-Deschenes, M. A., Shipman, R., and Testi, L. (2009). MIPSGAL: A Survey of the Inner Galactic Plane at 24 and 70 μm. PASP, 121:76–97. (Cited in pages 12 and 96.)

Carlin, J. L., Lépine, S., Newberg, H. J., Deng, L.-C., Beers, T. C., Chen, Y.-Q., Christlieb, N., Fu, X.-T., Gao, S., Grillmair, C. J., Guhathakurta, P., Han, Z.-W., Hou, J.-L., Lee, H.-T., Li, J., Liu, C., Liu, X.-W., Pan, K.-K., Sellwood, J. A., Wang, H.-C., Yang, F., Yanny, B., Zhang, Y.-Y., Zheng, Z., and Zhu, Z. (2012). An algorithm for preferential selection of spectroscopic targets in LEGUE. *RAA*, 12:755–771. (Cited in pages 33 and 38.)

Carollo, D., Beers, T. C., Lee, Y. S., Chiba, M., Norris, J. E., Wilhelm, R., Sivarani, T., Marsteller, B., Munn, J. A., Bailer-Jones, C. A. L., Fiorentin, P. R., and York, D. G. (2007). Two stellar components in the halo of the Milky Way. Nature, 450:1020–1025. (Cited in page 6.)

Carollo, D., Beers, T. C., Placco, V. M., Santucci, R. M., Denissenkov, P., Tissera, P. B., Lentner, G., Rossi, S., Lee, Y. S., and Tumlinson, J. (2016). The age structure of the Milky Way's halo. *Nature Physics*, 12:1170–1176. (Cited in page 7.)

Carr, J. S. (1989). Near-infrared CO emission in young stellar objects. ApJ, 345:522–535. (Cited in page 100.)

Carr, J. S., Sellgren, K., and Balachandran, S. C. (2000). The First Stellar Abundance Measurements in the Galactic Center: The M Supergiant IRS 7. ApJ, 530:307–322. (Cited in page 62.)

Carrell, K., Chen, Y., and Zhao, G. (2012). Metallicity Gradients of Thick Disk Dwarf Stars. AJ, 144:185. (Cited in page 58.)

Casey, A. R., Hawkins, K., Hogg, D. W., Ness, M., Rix, H.-W., Kordopatis, G., Kunder, A., Steinmetz, M., Koposov, S., Enke, H., Sanders, J., Gilmore, G., Zwitter, T., Freeman, K. C., Casagrande, L., Matijevič, G., Seabroke, G., Bienaymé, O., Bland-Hawthorn, J., Gibson, B. K., Grebel, E. K., Helmi, A., Munari, U., Navarro, J. F., Reid, W., Siebert, A., and Wyse, R. (2017). The RAVE-on Catalog of Stellar Atmospheric Parameters and Chemical Abundances for Chemo-dynamic Studies in the Gaia Era. ApJ, 840:59. (Cited in page 40.)

Chabrier, G. (2001). The Galactic Disk Mass Budget. I. Stellar Mass Function and Density. ApJ, 554:1274–1281. (Cited in page 18.)

Chabrier, G. (2003). Galactic Stellar and Substellar Initial Mass Function. PASP, 115:763–795. (Cited in page 23.)

Chen, L., Hou, J. L., and Wang, J. J. (2003). On the Galactic Disk Metallicity Distribution from Open Clusters. I. New Catalogs and Abundance Gradient. AJ, 125:1397–1406. (Cited in page 58.)

Chen, Y. Q., Zhao, G., Carrell, K., and Zhao, J. K. (2011). The Metallicity Gradient of the Thick Disk Based on Red Horizontal-branch Stars from SDSS DR8. AJ, 142:184. (Cited in page 58.)

Chen, Y.-Q., Zhao, G., Liu, C., Ren, J., Jia, Y.-P., Zhao, J.-K., Luo, A.-L., Wu, Y., Zhang, Y., Hou, Y.-H., Wang, Y.-F., and Yang, M. (2015). A comparison of stellar atmospheric parameters from the LAMOST and APOGEE datasets. *RAA*, 15:1125. (Cited in page 39.)

Cheng, J. Y., Rockosi, C. M., Morrison, H. L., Schönrich, R. A., Lee, Y. S., Beers, T. C., Bizyaev, D., Pan, K., and Schneider, D. P. (2012). Metallicity Gradients in the Milky Way Disk as Observed by the SEGUE Survey. ApJ, 746:149. (Cited in page 32.)

Chiappini, C., Matteucci, F., and Gratton, R. (1997). The Chemical Evolution of the Galaxy: The Two-Infall Model. ApJ, 477:765–780. (Cited in page 22.)

Churchwell, E., Babler, B. L., Meade, M. R., Whitney, B. A., Benjamin, R., Indebetouw, R., Cyganowski, C., Robitaille, T. P., Povich, M., Watson, C., and Bracker, S. (2009a). The Spitzer/GLIMPSE Surveys: A New View of the Milky Way. PASP, 121:213. (Cited in pages 12 and 96.)

Churchwell, E., Babler, B. L., Meade, M. R., Whitney, B. A., Benjamin, R., Indebetouw, R., Cyganowski, C., Robitaille, T. P., Povich, M., Watson, C., and Bracker, S. (2009b). The Spitzer/GLIMPSE Surveys: A New View of the Milky Way. PASP, 121:213. (Cited in page 34.)

Cirasuolo, M., Afonso, J., Carollo, M., Flores, H., Maiolino, R., Oliva, E., Paltani, S., Vanzi, L., Evans, C., Abreu, M., Atkinson, D., Babusiaux, C., Beard, S., Bauer, F., Bellazzini, M., Bender, R., Best, P., Bezawada, N., Bonifacio, P., Bragaglia, A., Bryson, I., Busher, D., Cabral, A., Caputi, K., Centrone, M., Chemla, F., Cimatti, A., Cioni, M.-R., Clementini, G., Coelho, J., Crnojevic, D., Daddi, E., Dunlop, J., Eales, S., Feltzing, S., Ferguson, A., Fisher, M., Fontana, A., Fynbo, J., Garilli, B., Gilmore, G., Glauser, A., Guinouard, I., Hammer, F., Hastings, P., Hess, A., Ivison, R., Jagourel, P., Jarvis, M., Kaper, L., Kauffman, G., Kitching, A. T., Lawrence, A., Lee, D., Lemasle, B., Licausi, G., Lilly, S., Lorenzetti, D., Lunney, D., Maiolino, R., Mannucci, F., McLure, R., Minniti, D., Montgomery, D., Muschielok, B., Nandra, K., Navarro, R., Norberg, P., Oliver, S., Origlia, L., Padilla, N., Peacock, J., Pedichini, F., Peng, J., Pentericci, L., Pragt, J., Puech, M., Randich, S., Rees, P., Renzini, A., Ryde, N., Rodrigues, M., Roseboom, I., Royer, F., Saglia, R., Sanchez, A., Schiavon, R., Schnetler, H., Sobral, D., Speziali, R., Sun, D., Stuik, R., Taylor, A., Taylor, W., Todd, S., Tolstoy, E., Torres, M., Tosi, M., Vanzella, E., Venema, L., Vitali, F., Wegner, M., Wells, M., Wild, V., Wright, G., Zamorani, G., and Zoccali, M. (2014). MOONS: the Multi-Object Optical and Near-infrared Spectrograph for the VLT. In *Ground-based and Airborne Instrumentation for Astronomy V*, volume 9147 of Proc. SPIE, page 91470N. (Cited in page 17.)

Civiš, S., Ferus, M., Chernov, V. E., and Zanozina, E. M. (2013). Infrared transitions and oscillator strengths of Ca and Mg. A&A, 554:A24. (Cited in page 73.)

Clarkson, W., Sahu, K., Anderson, J., Smith, T. E., Brown, T. M., Rich, R. M., Casertano, S., Bond, H. E., Livio, M., Minniti, D., Panagia, N., Renzini, A., Valenti, J., and Zoccali, M. (2008). Stellar Proper Motions in the Galactic Bulge from Deep Hubble Space Telescope ACS WFC Photometry. ApJ, 684:1110–1142. (Cited in page 7.)

Combes, F. and Sanders, R. H. (1981). Formation and properties of persisting stellar bars. A&A, 96:164–173. (Cited in page 7.)

Cooper, H. D. B., Lumsden, S. L., Oudmaijer, R. D., Hoare, M. G., Clarke, A. J., Urquhart, J. S., Mottram, J. C., Moore, T. J. T., and Davies, B. (2013). The RMS survey: near-IR spectroscopy of massive young stellar objects. MNRAS, 430:1125–1157. (Cited in pages 105 and 107.)

Cui, X.-Q., Zhao, Y.-H., Chu, Y.-Q., Li, G.-P., Li, Q., Zhang, L.-P., Su, H.-J., Yao, Z.-Q., Wang, Y.-N., Xing, X.-Z., Li, X.-N., Zhu, Y.-T., Wang, G., Gu, B.-Z., Luo, A.-L., Xu, X.-Q., Zhang, Z.-C., Liu, G.-R., Zhang, H.-T., Yang, D.-H., Cao, S.-Y., Chen, H.-Y., Chen, J.-J., Chen, K.-X., Chen, Y., Chu, J.-R., Feng, L., Gong, X.-F., Hou, Y.-H., Hu, H.-Z., Hu, N.-S., Hu, Z.-W., Jia, L., Jiang, F.-H., Jiang, X., Jiang, Z.-B., Jin, G., Li, A.-H., Li, Y., Li,

Y.-P., Liu, G.-Q., Liu, Z.-G., Lu, W.-Z., Mao, Y.-D., Men, L., Qi, Y.-J., Qi, Z.-X., Shi, H.-M., Tang, Z.-H., Tao, Q.-S., Wang, D.-Q., Wang, D., Wang, G.-M., Wang, H., Wang, J.-N., Wang, J., Wang, J.-L., Wang, J.-P., Wang, L., Wang, S.-Q., Wang, Y., Wang, Y.-F., Xu, L.-Z., Xu, Y., Yang, S.-H., Yu, Y., Yuan, H., Yuan, X.-Y., Zhai, C., Zhang, J., Zhang, Y.-X., Zhang, Y., Zhao, M., Zhou, F., Zhou, G.-H., Zhu, J., and Zou, S.-C. (2012). The Large Sky Area Multi-Object Fiber Spectroscopic Telescope (LAMOST). *RAA*, 12:1197–1242. (Cited in page 15.)

Cunha, K., Sellgren, K., Smith, V. V., Ramirez, S. V., Blum, R. D., and Terndrup, D. M. (2007). Chemical Abundances of Luminous Cool Stars in the Galactic Center from High-Resolution Infrared Spectroscopy. ApJ, 669:1011–1023. (Cited in page 62.)

da Silva, R., Porto de Mello, G. F., Milone, A. C., da Silva, L., Ribeiro, L. S., and Rocha-Pinto, H. J. (2012). Accurate and homogeneous abundance patterns in solar-type stars of the solar neighbourhood: a chemo-chronological analysis. A&A, 542:A84. (Cited in page 125.)

Das, P., Williams, A., and Binney, J. (2016). Characterizing stellar halo populations II: the age gradient in blue horizontal-branch stars. MNRAS, 463:3169–3185. (Cited in page 7.)

de Jong, R. S., Barden, S. C., Bellido-Tirado, O., Brynnel, J. G., Frey, S., Giannone, D., Haynes, R., Johl, D., Phillips, D., Schnurr, O., Walcher, J. C., Winkler, R., Ansorge, W. R., Feltzing, S., McMahon, R. G., Baker, G., Caillier, P., Dwelly, T., Gaessler, W., Iwert, O., Mandel, H. G., Piskunov, N. A., Pragt, J. H., Walton, N. A., Bensby, T., Bergemann, M., Chiappini, C., Christlieb, N., Cioni, M.-R. L., Driver, S., Finoguenov, A., Helmi, A., Irwin, M. J., Kitaura, F.-S., Kneib, J.-P., Liske, J., Merloni, A., Minchev, I., Richard, J., and Starkenburg, E. (2016). 4MOST: the 4-metre Multi-Object Spectroscopic Telescope project at preliminary design review. In *Ground-based and Airborne Instrumentation for Astronomy VI*, volume 9908 of Proc. SPIE, page 99081O. (Cited in page 17.)

De Silva, G. M., Freeman, K. C., Bland-Hawthorn, J., Martell, S., de Boer, E. W., Asplund, M., Keller, S., Sharma, S., Zucker, D. B., Zwitter, T., Anguiano, B., Bacigalupo, C., Bayliss, D., Beavis, M. A., Bergemann, M., Campbell, S., Cannon, R., Carollo, D., Casagrande, L., Casey, A. R., Da Costa, G., D'Orazi, V., Dotter, A., Duong, L., Heger, A., Ireland, M. J., Kafle, P. R., Kos, J., Lattanzio, J., Lewis, G. F., Lin, J., Lind, K., Munari, U., Nataf, D. M., O'Toole, S., Parker, Q., Reid, W., Schlesinger, K. J., Sheinis, A., Simpson, J. D., Stello, D., Ting, Y.-S., Traven, G., Watson, F., Wittenmyer, R., Yong, D., and Žerjal, M. (2015). The GALAH survey: scientific motivation. MNRAS, 449:2604–2617. (Cited in page 16.)

de Vaucouleurs, G. (1959). General Physical Properties of External Galaxies. *Handbuch der Physik*, 53:311. (Cited in page 19.)

Deason, A. J., Belokurov, V., and Evans, N. W. (2011). The Milky Way stellar halo out to 40 kpc: squashed, broken but smooth. MNRAS, 416:2903–2915. (Cited in page 7.)

Debattista, V. P., Ness, M., Gonzalez, O. A., Freeman, K., Zoccali, M., and Minniti, D. (2017). Separation of stellar populations by an evolving bar: implications for the bulge of the Milky Way. MNRAS, 469:1587–1611. (Cited in page 8.)

Demarque, P., Woo, J.-H., Kim, Y.-C., and Yi, S. K. (2004). Y^2 Isochrones with an Improved Core Overshoot Treatment. ApJS, 155:667–674. (Cited in pages 78, 79 and 132.)

Deng, L.-C., Newberg, H. J., Liu, C., Carlin, J. L., Beers, T. C., Chen, L., Chen, Y.-Q., Christlieb, N., Grillmair, C. J., Guhathakurta, P., Han, Z.-W., Hou, J.-L., Lee, H.-T., Lépine, S., Li, J., Liu, X.-W., Pan, K.-K., Sellwood, J. A., Wang, B., Wang, H.-C., Yang, F., Yanny, B., Zhang, H.-T., Zhang, Y.-Y., Zheng, Z., and Zhu, Z. (2012). LAMOST Experiment for Galactic Understanding and Exploration (LEGUE) The survey's science plan. *RAA*, 12:735–754. (Cited in page 15.)

DENIS Consortium (2005). VizieR Online Data Catalog: The DENIS database (DENIS Consortium, 2005). *VizieR Online Data Catalog*, 2263. (Cited in page 37.)

Di Matteo, P. (2016). The Disc Origin of the Milky Way Bulge. PASA, 33:e027. (Cited in page 7.)

Di Matteo, P., Gómez, A., Haywood, M., Combes, F., Lehnert, M. D., Ness, M., Snaith, O. N., Katz, D., and Semelin, B. (2015). Why the Milky Way's bulge is not only a bar formed from a cold thin disk. *Astronomy and Astrophysics*, 577:A1. (Cited in page 7.)

Di Matteo, P., Haywood, M., Gómez, A., van Damme, L., Combes, F., Halle, A., Semelin, B., Lehnert, M. D., and Katz, D. (2014). Mapping a stellar disk into a boxy bulge: The outside-in part of the Milky Way bulge formation. *Astronomy and Astrophysics*, 567:A122. (Cited in page 7.)

Dicke, R. H., Peebles, P. J. E., Roll, P. G., and Wilkinson, D. T. (1965). Cosmic Black-Body Radiation. ApJ, 142:414–419. (Cited in page 4.)

Do, T., Kerzendorf, W., Winsor, N., Støstad, M., Morris, M. R., Lu, J. R., and Ghez, A. M. (2015). Discovery of Low-metallicity Stars in the Central Parsec of the Milky Way. ApJ, 809:143. (Cited in pages 87 and 88.)

Dong, H., Mauerhan, J., Morris, M. R., Wang, Q. D., and Cotera, A. (2015). Origins of massive field stars in the Galactic Centre: a spectroscopic study. MNRAS, 446:842–856. (Cited in pages 107 and 109.)

Dopita, M. A. and Ryder, S. D. (1994). On the law of star formation in disk galaxies. ApJ, 430:163–178. (Cited in page 22.)

Dorn, R. J., Anglada-Escude, G., Baade, D., Bristow, P., Follert, R., Gojak, D., Grunhut, J., Hatzes, A., Heiter, U., Hilker, M., Ives, D. J., Jung, Y., Käufl, H.-U., Kerber, F., Klein, B., Lizon, J.-L., Lockhart, M., Löwinger, T., Marquart, T., Oliva, E., Origlia, L., Pasquini, L., Paufique, J., Piskunov, N., Pozna, E., Reiners, A., Smette, A., Smoker, J., Seemann,

U., Stempels, E., and Valenti, E. (2014). CRIRES+: Exploring the Cold Universe at High Spectral Resolution. *The Messenger*, 156:7–11. (Cited in page 125.)

Doroshkevich, A. G., Zeldovich, Y. B., Syunyaev, R. A., and Khlopov, M. Y. (1980a). Astrophysical Implications of the Neutrino Rest Mass - Part Three - Nonlinear Growth of Perturbations and the Missing Mass. *Soviet Astronomy Letters*, 6:257. (Cited in page 4.)

Doroshkevich, A. G., Zeldovich, Y. B., Syunyaev, R. A., and Khlopov, M. Y. (1980b). Astrophysical Implications of the Neutrino Rest Mass - Part Two - the Density Perturbation Spectrum and Small-Scale Fluctuations in the MICROWAVE_ Background. *Soviet Astronomy Letters*, 6:252–259. (Cited in page 4.)

Drimmel, R., Cabrera-Lavers, A., and López-Corredoira, M. (2003). A three-dimensional Galactic extinction model. A&A, 409:205–215. (Cited in page 20.)

Duong, L., Freeman, K. C., Asplund, M., Casagrande, L., Buder, S., Lind, K., Ness, M., Bland-Hawthorn, J., De Silva, G. M., D'Orazi, V., Kos, J., Lewis, G. F., Lin, J., Martell, S. L., Schlesinger, K., Sharma, S., Simpson, J. D., Zucker, D. B., Zwitter, T., Anguiano, B., Da Costa, G. S., Hyde, E., Horner, J., Kafle, P. R., Nataf, D. M., Reid, W., Stello, D., Ting, Y.-S., and Wyse, R. F. G. (2018). The GALAH survey: properties of the Galactic disc(s) in the solar neighbourhood. MNRAS, 476:5216–5232. (Cited in page 58.)

Dutra, C. M. and Bica, E. (2001). New infrared star clusters and candidates in the Galaxy detected with 2MASS. A&A, 376:434–440. (Cited in page 103.)

Eggen, O. J., Lynden-Bell, D., and Sandage, A. R. (1962). Evidence from the motions of old stars that the Galaxy collapsed. ApJ, 136:748. (Cited in page 6.)

Eisenstein, D. J., Weinberg, D. H., Agol, E., Aihara, H., Allende Prieto, C., Anderson, S. F., Arns, J. A., Aubourg, É., Bailey, S., Balbinot, E., and et al. (2011). SDSS-III: Massive Spectroscopic Surveys of the Distant Universe, the Milky Way, and Extra-Solar Planetary Systems. AJ, 142:72. (Cited in page 13.)

Epchtein, N., de Batz, B., Capoani, L., Chevallier, L., Copet, E., Fouqué, P., Lacombe, P., Le Bertre, T., Pau, S., Rouan, D., Ruphy, S., Simon, G., Tiphène, D., Burton, W., Bertin, E., Deul, E., Habing, H., Borsenberger, J., Dennefeld, M., Guglielmo, F., Loup, C., Mamon, G., Ng, Y., Omont, A., Provost, L., Renault, J.-C., Tanguy, F., Kimeswenger, S., Kienel, C., Garzon, F., Persi, P., Ferrari-Toniolo, M., Robin, A., Paturel, G., Vauglin, I., Forveille, T., Delfosse, X., Hron, J., Schultheis, M., Appenzeller, I., Wagner, S., Balazs, L., Holl, A., Lépine, J., Boscolo, P., Picazzio, E., Duc, P.-A., and Mennessier, M.-O. (1997). The deep near-infrared southern sky survey (DENIS). *The Messenger*, 87:27–34. (Cited in page 36.)

Fatuzzo, M. and Melia, F. (2009). Star Formation at the Galactic Center. PASP, 121:585–590. (Cited in page 26.)

Fazio, G. G., Hora, J. L., Allen, L. E., Ashby, M. L. N., Barmby, P., Deutsch, L. K., Huang, J.-S., Kleiner, S., Marengo, M., Megeath, S. T., Melnick, G. J., Pahre, M. A., Patten, B. M.,

Polizotti, J., Smith, H. A., Taylor, R. S., Wang, Z., Willner, S. P., Hoffmann, W. F., Pipher, J. L., Forrest, W. J., McMurty, C. W., McCreight, C. R., McKelvey, M. E., McMurray, R. E., Koch, D. G., Moseley, S. H., Arendt, R. G., Mentzell, J. E., Marx, C. T., Losch, P., Mayman, P., Eichhorn, W., Krebs, D., Jhabvala, M., Gezari, D. Y., Fixsen, D. J., Flores, J., Shakoorzadeh, K., Jungo, R., Hakun, C., Workman, L., Karpati, G., Kichak, R., Whitley, R., Mann, S., Tollestrup, E. V., Eisenhardt, P., Stern, D., Gorjian, V., Bhattacharya, B., Carey, S., Nelson, B. O., Glaccum, W. J., Lacy, M., Lowrance, P. J., Laine, S., Reach, W. T., Stauffer, J. A., Surace, J. A., Wilson, G., Wright, E. L., Hoffman, A., Domingo, G., and Cohen, M. (2004). The Infrared Array Camera (IRAC) for the Spitzer Space Telescope. ApJS, 154:10–17. (Cited in page 12.)

Feldmeier, A., Neumayer, N., Seth, A., Schödel, R., Lützgendorf, N., de Zeeuw, P. T., Kissler-Patig, M., Nishiyama, S., and Walcher, C. J. (2014). Large scale kinematics and dynamical modelling of the Milky Way nuclear star cluster. A&A, 570:A2. (Cited in page 26.)

Feldmeier-Krause, A., Kerzendorf, W., Neumayer, N., Schödel, R., Nogueras-Lara, F., Do, T., de Zeeuw, P. T., and Kuntschner, H. (2017). KMOS view of the Galactic Centre - II. Metallicity distribution of late-type stars. MNRAS, 464:194–209. (Cited in pages 87 and 126.)

Feldmeier-Krause, A., Neumayer, N., Schödel, R., Seth, A., Hilker, M., de Zeeuw, P. T., Kuntschner, H., Walcher, C. J., Lützgendorf, N., and Kissler-Patig, M. (2015). KMOS view of the Galactic centre. I. Young stars are centrally concentrated. A&A, 584:A2. (Cited in page 26.)

Felli, M., Comoretto, G., Testi, L., Omont, A., and Schuller, F. (2000). The search for YSOs from ISOGAL data. Application to the l = +45 field. A&A, 362:199–214. (Cited in pages 101 and 134.)

Felli, M., Testi, L., Schuller, F., and Omont, A. (2002). Young massive stars in the ISOGAL survey. II. The catalogue of bright YSO candidates. A&A, 392:971–990. (Cited in pages 98, 101 and 134.)

Fernández-Alvar, E., Allende Prieto, C., Schlesinger, K. J., Beers, T. C., Robin, A. C., Schneider, D. P., Lee, Y. S., Bizyaev, D., Ebelke, G., Malanushenko, E., Malanushenko, V., Oravetz, D., Pan, K., and Simmons, A. (2015). Deep SDSS optical spectroscopy of distant halo stars. II. Iron, calcium, and magnesium abundances. A&A, 577:A81. (Cited in page 6.)

Fragkoudi, F., Di Matteo, P., Haywood, M., Gómez, A., Combes, F., Katz, D., and Semelin, B. (2017). Bars and boxy/peanut bulges in thin and thick discs. I. Morphology and line-of-sight velocities of a fiducial model. A&A, 606:A47. (Cited in page 8.)

Fragkoudi, F., Di Matteo, P., Haywood, M., Schultheis, M., Khoperskov, S., Gómez, A., and Combes, F. (2018). The disc origin of the Milky Way bulge: II. Dissecting the chemo-

morphological relations using N-body simulations and APOGEE. *ArXiv e-prints*. (Cited in pages 63 and 124.)

Freeman, K. and Bland-Hawthorn, J. (2002). The New Galaxy: Signatures of Its Formation. ARA&A, 40:487–537. (Cited in page 9.)

Freudling, W., Romaniello, M., Bramich, D. M., Ballester, P., Forchi, V., García-Dabló, C. E., Moehler, S., and Neeser, M. J. (2013). Automated data reduction workflows for astronomy. The ESO Reflex environment. A&A, 559:A96. (Cited in page 104.)

Frogel, J. A., Tiede, G. P., and Kuchinski, L. E. (1999). The Metallicity and Reddening of Stars in the Inner Galactic Bulge. AJ, 117:2296–2307. (Cited in page 62.)

Gao, S., Just, A., and Grebel, E. K. (2013). Detailed comparison of Milky Way models based on stellar population synthesis and SDSS star counts at the north Galactic pole. A&A, 549:A20. (Cited in page 19.)

García Pérez, A. E., Allende Prieto, C., Holtzman, J. A., Shetrone, M., Mészáros, S., Bizyaev, D., Carrera, R., Cunha, K., García-Hernández, D. A., Johnson, J. A., Majewski, S. R., Nidever, D. L., Schiavon, R. P., Shane, N., Smith, V. V., Sobeck, J., Troup, N., Zamora, O., Weinberg, D. H., Bovy, J., Eisenstein, D. J., Feuillet, D., Frinchaboy, P. M., Hayden, M. R., Hearty, F. R., Nguyen, D. C., O'Connell, R. W., Pinsonneault, M. H., Wilson, J. C., and Zasowski, G. (2016). ASPCAP: The APOGEE Stellar Parameter and Chemical Abundances Pipeline. AJ, 151:144. (Cited in page 13.)

García Pérez, A. E., Ness, M., Robin, A. C., Martinez-Valpuesta, I., Sobeck, J., Zasowski, G., Majewski, S. R., Bovy, J., Allende Prieto, C., Cunha, K., Girardi, L., Mészáros, S., Nidever, D., Schiavon, R. P., Schultheis, M., Shetrone, M., and Smith, V. V. (2018). The Bulge Metallicity Distribution from the APOGEE Survey. ApJ, 852:91. (Cited in page 63.)

Gardner, E., Debattista, V. P., Robin, A. C., Vásquez, S., and Zoccali, M. (2014). N-body simulation insights into the X-shaped bulge of the Milky Way: kinematics and distance to the Galactic Centre. MNRAS, 438:3275–3290. (Cited in page 7.)

Geballe, T. R. and Persson, S. E. (1987). Emission from CO band heads in young stellar objects. ApJ, 312:297–302. (Cited in page 100.)

Gillessen, S., Plewa, P. M., Eisenhauer, F., Sari, R., Waisberg, I., Habibi, M., Pfuhl, O., George, E., Dexter, J., von Fellenberg, S., Ott, T., and Genzel, R. (2017). An Update on Monitoring Stellar Orbits in the Galactic Center. ApJ, 837:30. (Cited in page 5.)

Gilmore, G., Randich, S., Asplund, M., Binney, J., Bonifacio, P., Drew, J., Feltzing, S., Ferguson, A., Jeffries, R., Micela, G., and et al. (2012). The Gaia-ESO Public Spectroscopic Survey. *The Messenger*, 147:25–31. (Cited in page 15.)

Gilmore, G. and Reid, N. (1983). New light on faint stars. III - Galactic structure towards the South Pole and the Galactic thick disc. MNRAS, 202:1025–1047. (Cited in pages 8 and 19.)

Gilmore, G., Wyse, R. F. G., and Norris, J. E. (2002). Deciphering the Last Major Invasion of the Milky Way. ApJ, 574:L39–L42. (Cited in page 8.)

Girardi, L., Groenewegen, M. A. T., Hatziminaoglou, E., and da Costa, L. (2005). Star counts in the Galaxy. Simulating from very deep to very shallow photometric surveys with the TRILEGAL code. A&A, 436:895–915. (Cited in pages 18, 19 and 45.)

Glass, I. S., Matsumoto, S., Carter, B. S., and Sekiguchi, K. (2001). Large-amplitude variables near the Galactic Centre. MNRAS, 321:77–95. (Cited in pages 101, 107, 109 and 134.)

Gonzalez, O. A., Rejkuba, M., Zoccali, M., Hill, V., Battaglia, G., Babusiaux, C., Minniti, D., Barbuy, B., Alves-Brito, A., Renzini, A., Gomez, A., and Ortolani, S. (2011). Alpha element abundances and gradients in the Milky Way bulge from FLAMES-GIRAFFE spectra of 650 K giants. A&A, 530:A54. (Cited in pages 7 and 88.)

Gonzalez, O. A., Rejkuba, M., Zoccali, M., Valenti, E., Minniti, D., Schultheis, M., Tobar, R., and Chen, B. (2012). Reddening and metallicity maps of the Milky Way bulge from VVV and 2MASS. II. The complete high resolution extinction map and implications for Galactic bulge studies. A&A, 543:A13. (Cited in pages 26, 28, 64, 74, 130 and 132.)

Gonzalez, O. A., Zoccali, M., Debattista, V. P., Alonso-García, J., Valenti, E., and Minniti, D. (2015a). Reinforcing the link between the double red clump and the X-shaped bulge of the Milky Way. A&A, 583:L5. (Cited in page 7.)

Gonzalez, O. A., Zoccali, M., Vasquez, S., Hill, V., Rejkuba, M., Valenti, E., Rojas-Arriagada, A., Renzini, A., Babusiaux, C., Minniti, D., and Brown, T. M. (2015b). The GIRAFFE Inner Bulge Survey (GIBS). II. Metallicity distributions and alpha element abundances at fixed Galactic latitude. A&A, 584:A46. (Cited in page 16.)

Gouda, N. (2012). Infrared Space Astrometry Missions
JASMINE Missions
. In Aoki, W., Ishigaki, M., Suda, T., Tsujimoto, T., and Arimoto, N., editors, *Galactic Archaeology: Near-Field Cosmology and the Formation of the Milky Way*, volume 458 of *Astronomical Society of the Pacific Conference Series*, page 417. (Cited in page 125.)

Greene, T. P. and Lada, C. J. (1996). Near-Infrared Spectra and the Evolutionary Status of Young Stellar Objects: Results of a 1.1-2.4 (??) Survey. AJ, 112:2184. (Cited in page 105.)

Grevesse, N., Asplund, M., and Sauval, A. J. (2007). The Solar Chemical Composition. Space Sci. Rev., 130:105–114. (Cited in page 83.)

Grieco, V., Matteucci, F., Ryde, N., Schultheis, M., and Uttenthaler, S. (2015). Chemical evolution of the Galactic Centre. MNRAS, 450:2094–2103. (Cited in pages 63 and 124.)

Gustafsson, B., Edvardsson, B., Eriksson, K., et al. (2008). A grid of MARCS model atmospheres for late-type stars. I. Methods and general properties. A&A, 486:951. (Cited in page 72.)

Gutermuth, R. A. and Heyer, M. (2015). A 24μm Point Source Catalog of the Galactic Plane from Spitzer/MIPSGAL. AJ, 149:64. (Cited in pages 110, 112, 115, 116, 119 and 136.)

Hambly, N. C., Davenhall, A. C., Irwin, M. J., and MacGillivray, H. T. (2001). The SuperCOSMOS Sky Survey - III. Astrometry. MNRAS, 326:1315–1327. (Cited in page 36.)

Hanson, M. M., Howarth, I. D., and Conti, P. S. (1997). The Young Massive Stellar Objects of M17. ApJ, 489:698–718. (Cited in page 100.)

Hayden, M. R., Bovy, J., Holtzman, J. A., Nidever, D. L., Bird, J. C., Weinberg, D. H., Andrews, B. H., Majewski, S. R., Allende Prieto, C., Anders, F., Beers, T. C., Bizyaev, D., Chiappini, C., Cunha, K., Frinchaboy, P., García-Herńandez, D. A., García Pérez, A. E., Girardi, L., Harding, P., Hearty, F. R., Johnson, J. A., Mészáros, S., Minchev, I., O'Connell, R., Pan, K., Robin, A. C., Schiavon, R. P., Schneider, D. P., Schultheis, M., Shetrone, M., Skrutskie, M., Steinmetz, M., Smith, V., Wilson, J. C., Zamora, O., and Zasowski, G. (2015). Chemical Cartography with APOGEE: Metallicity Distribution Functions and the Chemical Structure of the Milky Way Disk. ApJ, 808:132. (Cited in pages 8 and 46.)

Hayden, M. R., Holtzman, J. A., Bovy, J., Majewski, S. R., Johnson, J. A., Allende Prieto, C., Beers, T. C., Cunha, K., Frinchaboy, P. M., García Pérez, A. E., Girardi, L., Hearty, F. R., Lee, Y. S., Nidever, D., Schiavon, R. P., Schlesinger, K. J., Schneider, D. P., Schultheis, M., Shetrone, M., Smith, V. V., Zasowski, G., Bizyaev, D., Feuillet, D., Hasselquist, S., Kinemuchi, K., Malanushenko, E., Malanushenko, V., O'Connell, R., Pan, K., and Stassun, K. (2014). Chemical Cartography with APOGEE: Large-scale Mean Metallicity Maps of the Milky Way Disk. AJ, 147:116. (Cited in pages 56 and 57.)

Hayden, M. R., Recio-Blanco, A., de Laverny, P., Mikolaitis, S., and Worley, C. C. (2017). The AMBRE project: The thick thin disk and thin thick disk of the Milky Way. A&A, 608:L1. (Cited in page 8.)

Haywood, M. (2008). Radial mixing and the transition between the thick and thin Galactic discs. MNRAS, 388:1175–1184. (Cited in page 8.)

Haywood, M., Di Matteo, P., Lehnert, M. D., Katz, D., and Gómez, A. (2013). The age structure of stellar populations in the solar vicinity. Clues of a two-phase formation history of the Milky Way disk. A&A, 560:A109. (Cited in page 9.)

Helmi, A. (2008). The stellar halo of the Galaxy. A&A Rev., 15:145–188. (Cited in page 6.)

Henshaw, J. D., Longmore, S. N., Kruijssen, J. M. D., Davies, B., Bally, J., Barnes, A., Battersby, C., Burton, M., Cunningham, M. R., Dale, J. E., Ginsburg, A., Immer, K., Jones, P. A., Kendrew, S., Mills, E. A. C., Molinari, S., Moore, T. J. T., Ott, J., Pillai, T., Rathborne, J., Schilke, P., Schmiedeke, A., Testi, L., Walker, D., Walsh, A., and Zhang, Q. (2016). Molecular gas kinematics within the central 250 pc of the Milky Way. MNRAS, 457:2675–2702. (Cited in page 118.)

Hill, V., Lecureur, A., Gómez, A., Zoccali, M., Schultheis, M., Babusiaux, C., Royer, F., Barbuy, B., Arenou, F., Minniti, D., and Ortolani, S. (2011). The metallicity distribution of bulge clump giants in Baade's window. A&A, 534:A80. (Cited in page 86.)

Ho, A. Y. Q., Ness, M. K., Hogg, D. W., Rix, H.-W., Liu, C., Yang, F., Zhang, Y., Hou, Y., and Wang, Y. (2017). Label Transfer from APOGEE to LAMOST: Precise Stellar Parameters for 450,000 LAMOST Giants. ApJ, 836:5. (Cited in page 39.)

Høg, E., Fabricius, C., Makarov, V. V., Urban, S., Corbin, T., Wycoff, G., Bastian, U., Schwekendiek, P., and Wicenec, A. (2000). The Tycho-2 catalogue of the 2.5 million brightest stars. A&A, 355:L27–L30. (Cited in page 36.)

Holtzman, J. A., Shetrone, M., Johnson, J. A., Allende Prieto, C., Anders, F., Andrews, B., Beers, T. C., Bizyaev, D., Blanton, M. R., Bovy, J., Carrera, R., Chojnowski, S. D., Cunha, K., Eisenstein, D. J., Feuillet, D., Frinchaboy, P. M., Galbraith-Frew, J., García Pérez, A. E., García-Hernández, D. A., Hasselquist, S., Hayden, M. R., Hearty, F. R., Ivans, I., Majewski, S. R., Martell, S., Meszaros, S., Muna, D., Nidever, D., Nguyen, D. C., O'Connell, R. W., Pan, K., Pinsonneault, M., Robin, A. C., Schiavon, R. P., Shane, N., Sobeck, J., Smith, V. V., Troup, N., Weinberg, D. H., Wilson, J. C., Wood-Vasey, W. M., Zamora, O., and Zasowski, G. (2015). Abundances, Stellar Parameters, and Spectra from the SDSS-III/APOGEE Survey. AJ, 150:148. (Cited in page 41.)

Houdashelt, M. L., Bell, R. A., and Sweigart, A. V. (2000). Improved Color-Temperature Relations and Bolometric Corrections for Cool Stars. AJ, 119:1448–1469. (Cited in page 74.)

Howard, C. D., Rich, R. M., Reitzel, D. B., Koch, A., De Propris, R., and Zhao, H. (2008). The Bulge Radial Velocity Assay (BRAVA). I. Sample Selection and a Rotation Curve. ApJ, 688:1060–1077. (Cited in pages 89, 90 and 93.)

Huang, Y., Liu, X.-W., Zhang, H.-W., Yuan, H.-B., Xiang, M.-S., Chen, B.-Q., Ren, J.-J., Sun, N.-C., Wang, C., Zhang, Y., Hou, Y.-H., Wang, Y.-F., and Yang, M. (2015). On the metallicity gradients of the Galactic disk as revealed by LSS-GAC red clump stars. *RAA*, 15:1240. (Cited in page 58.)

Hubble, E. (1929). A Relation between Distance and Radial Velocity among Extra-Galactic Nebulae. *Proceedings of the National Academy of Science*, 15:168–173. (Cited in page 3.)

Hubble, E. P. (1936). *Realm of the Nebulae*. (Cited in page 5.)

Huber, D., Bryson, S. T., Haas, M. R., Barclay, T., Barentsen, G., Howell, S. B., Sharma, S., Stello, D., and Thompson, S. E. (2016). VizieR Online Data Catalog: K2 EPIC stellar properties for 138600 targets (Huber+, 2016). *VizieR Online Data Catalog*, 222. (Cited in page 40.)

Immer, K., Schuller, F., Omont, A., and Menten, K. M. (2012). Recent star formation in the inner Galactic bulge seen by ISOGAL. II. The central molecular zone. A&A, 537:A121. (Cited in pages 100, 116, 117 and 118.)

Johnson, C. I., Rich, R. M., Kobayashi, C., Kunder, A., and Koch, A. (2014). LIGHT, ALPHA, AND Fe-PEAK ELEMENT ABUNDANCES IN THE GALACTIC BULGE. *THE ASTRONOMICAL JOURNAL*, 148(4):67. (Cited in pages 88, 89 and 133.)

Jurić, M., Ivezić, Ž., Brooks, A., Lupton, R. H., Schlegel, D., Finkbeiner, D., Padmanabhan, N., Bond, N., Sesar, B., Rockosi, C. M., Knapp, G. R., Gunn, J. E., Sumi, T., Schneider, D. P., Barentine, J. C., Brewington, H. J., Brinkmann, J., Fukugita, M., Harvanek, M., Kleinman, S. J., Krzesinski, J., Long, D., Neilsen, Jr., E. H., Nitta, A., Snedden, S. A., and York, D. G. (2008). The Milky Way Tomography with SDSS. I. Stellar Number Density Distribution. ApJ, 673:864–914. (Cited in page 8.)

Kafle, P. R., Sharma, S., Lewis, G. F., and Bland-Hawthorn, J. (2014). On the Shoulders of Giants: Properties of the Stellar Halo and the Milky Way Mass Distribution. ApJ, 794:59. (Cited in page 8.)

Karim, M. T. and Mamajek, E. E. (2017). Revised geometric estimates of the North Galactic Pole and the Sun's height above the Galactic mid-plane. MNRAS, 465:472–481. (Cited in page 91.)

Käufl, H. U., Amico, P., Ballester, P., et al. (2006). Good Vibrations: Report from the Commissioning of CRIRES. *The Messenger*, 126:32. (Cited in page 65.)

Käufl, H.-U., Ballester, P., Biereichel, P., et al. (2004). CRIRES: a high-resolution infrared spectrograph for ESO's VLT. In Moorwood, A. F. M. and Iye, M., editors, *Society of Photo-Optical Instrumentation Engineers (SPIE) Conference Series*, volume 5492 of *Presented at the Society of Photo-Optical Instrumentation Engineers (SPIE) Conference*, pages 1218–1227. (Cited in page 65.)

Kaulakys, B. (1985). Analytical expressions for cross sections of rydberg-neutral inelastic collisions. *Journal of Physics B: Atomic and Molecular Physics*, 18(6):L167. (Cited in page 74.)

Kaulakys, B. (1991). Free electron model for collisional angular momentum mixing of high rydberg atoms. *Journal of Physics B: Atomic, Molecular and Optical Physics*, 24(5):L127. (Cited in page 74.)

Kennicutt, Jr., R. C. (1989). The star formation law in galactic disks. ApJ, 344:685–703. (Cited in page 22.)

Kennicutt, Jr., R. C. (1998). The Global Schmidt Law in Star-forming Galaxies. ApJ, 498:541–552. (Cited in page 23.)

Klein Gebbinck, M., , and Sforna, D. (2012). *VERY LARGE TELESCOPE: Gasgano Userâs Manual*. (Cited in page 71.)

Klypin, A., Kravtsov, A. V., Valenzuela, O., and Prada, F. (1999). Where Are the Missing Galactic Satellites? ApJ, 522:82–92. (Cited in page 4.)

Koepferl, C. M. and Robitaille, T. P. (2017). The FluxCompensator: Making Radiative Transfer Models of Hydrodynamical Simulations Directly Comparable to Real Observations. ApJ, 849:3. (Cited in page 100.)

Koepferl, C. M., Robitaille, T. P., Morales, E. F. E., and Johnston, K. G. (2015). Main-sequence Stars Masquerading as Young Stellar Objects in the Central Molecular Zone. ApJ, 799:53. (Cited in pages 100 and 117.)

Kordopatis, G. (2014). RAVE: Results and Updates from Data Release 4. In Ballet, J., Martins, F., Bournaud, F., Monier, R., and Reylé, C., editors, *SF2A-2014: Proceedings of the Annual meeting of the French Society of Astronomy and Astrophysics*, pages 431–435. (Cited in page 14.)

Kordopatis, G., Gilmore, G., Wyse, R. F. G., Steinmetz, M., Siebert, A., Bienaymé, O., McMillan, P. J., Minchev, I., Zwitter, T., Gibson, B. K., Seabroke, G., Grebel, E. K., Bland-Hawthorn, J., Boeche, C., Freeman, K. C., Munari, U., Navarro, J. F., Parker, Q., Reid, W. A., and Siviero, A. (2013). In the thick of it: metal-poor disc stars in RAVE. MNRAS, 436:3231–3246. (Cited in pages 8, 14, 36, 39 and 45.)

Kordopatis, G., Recio-Blanco, A., de Laverny, P., Bijaoui, A., Hill, V., Gilmore, G., Wyse, R. F. G., and Ordenovic, C. (2011). Automatic stellar spectra parameterisation in the IR Ca ii triplet region. A&A, 535:A106. (Cited in pages 14, 41 and 58.)

Kroupa, P. (2001). On the variation of the initial mass function. MNRAS, 322:231–246. (Cited in pages 24, 117 and 136.)

Kruijssen, J. M. D., Dale, J. E., and Longmore, S. N. (2015). The dynamical evolution of molecular clouds near the Galactic Centre - I. Orbital structure and evolutionary timeline. MNRAS, 447:1059–1079. (Cited in page 118.)

Kruijssen, J. M. D., Longmore, S. N., Elmegreen, B. G., Murray, N., Bally, J., Testi, L., and Kennicutt, R. C. (2014). What controls star formation in the central 500 pc of the Galaxy? MNRAS, 440:3370–3391. (Cited in page 119.)

Kunder, A., Koch, A., Rich, R. M., de Propris, R., Howard, C. D., Stubbs, S. A., Johnson, C. I., Shen, J., Wang, Y., Robin, A. C., Kormendy, J., Soto, M., Frinchaboy, P., Reitzel, D. B., Zhao, H., and Origlia, L. (2012). The Bulge Radial Velocity Assay (BRAVA). II. Complete Sample and Data Release. AJ, 143:57. (Cited in pages 7 and 89.)

Kunder, A., Kordopatis, G., Steinmetz, M., Zwitter, T., McMillan, P. J., Casagrande, L., Enke, H., Wojno, J., Valentini, M., Chiappini, C., Matijevič, G., Siviero, A., de Laverny, P., Recio-Blanco, A., Bijaoui, A., Wyse, R. F. G., Binney, J., Grebel, E. K., Helmi, A., Jofre, P., Antoja, T., Gilmore, G., Siebert, A., Famaey, B., Bienaymé, O., Gibson, B. K., Freeman, K. C., Navarro, J. F., Munari, U., Seabroke, G., Anguiano, B., Žerjal, M., Minchev, I., Reid, W., Bland-Hawthorn, J., Kos, J., Sharma, S., Watson, F., Parker, Q. A., Scholz, R.-D., Burton, D., Cass, P., Hartley, M., Fiegert, K., Stupar, M., Ritter, A., Hawkins, K., Gerhard, O., Chaplin, W. J., Davies, G. R., Elsworth, Y. P., Lund, M. N., Miglio, A., and

Mosser, B. (2017). The Radial Velocity Experiment (RAVE): Fifth Data Release. AJ, 153:75. (Cited in pages 37, 39 and 41.)

Kupka, F., Piskunov, N., Ryabchikova, T. A., Stempels, H. C., and Weiss, W. W. (1999). VALD-2: Progress of the Vienna Atomic Line Data Base. A&AS, 138:119–133. (Cited in page 73.)

Kupka, F. G., Ryabchikova, T. A., Piskunov, N. E., Stempels, H. C., and Weiss, W. W. (2000). VALD-2 – The New Vienna Atomic Line Database. *Baltic Astronomy*, 9:590–594. (Cited in page 73.)

Lada, C. J. (1987). Star formation - From OB associations to protostars. In Peimbert, M. and Jugaku, J., editors, *Star Forming Regions*, volume 115 of *IAU Symposium*, pages 1–17. (Cited in page 97.)

Launhardt, R., Zylka, R., and Mezger, P. G. (2002). The nuclear bulge of the Galaxy. III. Large-scale physical characteristics of stars and interstellar matter. A&A, 384:112–139. (Cited in pages 24, 25, 26 and 129.)

Lawrence, A., Warren, S. J., Almaini, O., Edge, A. C., Hambly, N. C., Jameson, R. F., Lucas, P., Casali, M., Adamson, A., Dye, S., Emerson, J. P., Foucaud, S., Hewett, P., Hirst, P., Hodgkin, S. T., Irwin, M. J., Lodieu, N., McMahon, R. G., Simpson, C., Smail, I., Mortlock, D., and Folger, M. (2013). UKIDSS-DR9 LAS, GCS and DXS Surveys (Lawrence+ 2012). *VizieR Online Data Catalog*, 2319:0. (Cited in pages 71 and 132.)

Lee, Y. S., Beers, T. C., Allende Prieto, C., Lai, D. K., Rockosi, C. M., Morrison, H. L., Johnson, J. A., An, D., Sivarani, T., and Yanny, B. (2011). The SEGUE Stellar Parameter Pipeline. V. Estimation of Alpha-element Abundance Ratios from Low-resolution SDSS/SEGUE Stellar Spectra. AJ, 141:90. (Cited in page 39.)

Lee, Y. S., Beers, T. C., Carlin, J. L., Newberg, H. J., Hou, Y., Li, G., Luo, A.-L., Wu, Y., Yang, M., Zhang, H., Zhang, W., and Zhang, Y. (2015). Application of the Segue Stellar Parameter Pipeline To Lamost Stellar Spectra. AJ, 150(6):187. (Cited in page 39.)

Lee, Y. S., Beers, T. C., Sivarani, T., Allende Prieto, C., Koesterke, L., Wilhelm, R., Re Fiorentin, P., Bailer-Jones, C. A. L., Norris, J. E., Rockosi, C. M., Yanny, B., Newberg, H. J., Covey, K. R., Zhang, H.-T., and Luo, A.-L. (2008a). The SEGUE Stellar Parameter Pipeline. I. Description and Comparison of Individual Methods. AJ, 136:2022–2049. (Cited in page 39.)

Lee, Y. S., Beers, T. C., Sivarani, T., Johnson, J. A., An, D., Wilhelm, R., Allende Prieto, C., Koesterke, L., Re Fiorentin, P., Bailer-Jones, C. A. L., Norris, J. E., Yanny, B., Rockosi, C., Newberg, H. J., Cudworth, K. M., and Pan, K. (2008b). The SEGUE Stellar Parameter Pipeline. II. Validation with Galactic Globular and Open Clusters. AJ, 136:2050–2069. (Cited in page 39.)

Lemaître, G. (1931). The Beginning of the World from the Point of View of Quantum Theory. Nature, 127:706. (Cited in page 3.)

Liu, C., Xu, Y., Wan, J.-C., Wang, H.-F., Carlin, J. L., Deng, L.-C., Newberg, H. J., Cao, Z.-H., Hou, Y.-H., Wang, Y.-F., and Zhang, Y. (2017). Mapping the Milky Way with LAMOST I: method and overview. *Research in Astronomy and Astrophysics*, 17:096. (Cited in page 38.)

Liu, X.-W., Zhao, G., and Hou, J.-L. (2015). Preface: The LAMOST Galactic surveys and early results. *Research in Astronomy and Astrophysics*, 15:1089. (Cited in page 16.)

Livingston, W. and Wallace, L. (1991). *An atlas of the solar spectrum in the infrared from 1850 to 9000 cm-1 (1.1 to 5.4 micrometer)*. NSO Technical Report, Tucson: National Solar Observatory, National Optical Astronomy Observatory, 1991. (Cited in page 73.)

Longair, M. S. (2008). *Galaxy Formation*. (Cited in pages 2 and 129.)

Longmore, S. N., Bally, J., Testi, L., Purcell, C. R., Walsh, A. J., Bressert, E., Pestalozzi, M., Molinari, S., Ott, J., Cortese, L., Battersby, C., Murray, N., Lee, E., Kruijssen, J. M. D., Schisano, E., and Elia, D. (2013a). Variations in the Galactic star formation rate and density thresholds for star formation. MNRAS, 429:987–1000. (Cited in pages 100, 118 and 119.)

Longmore, S. N., Kruijssen, J. M. D., Bally, J., Ott, J., Testi, L., Rathborne, J., Bastian, N., Bressert, E., Molinari, S., Battersby, C., and Walsh, A. J. (2013b). Candidate super star cluster progenitor gas clouds possibly triggered by close passage to Sgr A*. MNRAS, 433:L15–L19. (Cited in page 119.)

Majewski, S. R., APOGEE Team, and APOGEE-2 Team (2016). The Apache Point Observatory Galactic Evolution Experiment (APOGEE) and its successor, APOGEE-2. *Astronomische Nachrichten*, 337:863. (Cited in page 14.)

Majewski, S. R., Schiavon, R. P., Frinchaboy, P. M., Allende Prieto, C., Barkhouser, R., Bizyaev, D., Blank, B., Brunner, S., Burton, A., Carrera, R., Chojnowski, S. D., Cunha, K., Epstein, C., Fitzgerald, G., García Pérez, A. E., Hearty, F. R., Henderson, C., Holtzman, J. A., Johnson, J. A., Lam, C. R., Lawler, J. E., Maseman, P., Mészáros, S., Nelson, M., Nguyen, D. C., Nidever, D. L., Pinsonneault, M., Shetrone, M., Smee, S., Smith, V. V., Stolberg, T., Skrutskie, M. F., Walker, E., Wilson, J. C., Zasowski, G., Anders, F., Basu, S., Beland, S., Blanton, M. R., Bovy, J., Brownstein, J. R., Carlberg, J., Chaplin, W., Chiappini, C., Eisenstein, D. J., Elsworth, Y., Feuillet, D., Fleming, S. W., Galbraith-Frew, J., García, R. A., García-Hernández, D. A., Gillespie, B. A., Girardi, L., Gunn, J. E., Hasselquist, S., Hayden, M. R., Hekker, S., Ivans, I., Kinemuchi, K., Klaene, M., Mahadevan, S., Mathur, S., Mosser, B., Muna, D., Munn, J. A., Nichol, R. C., O'Connell, R. W., Parejko, J. K., Robin, A. C., Rocha-Pinto, H., Schultheis, M., Serenelli, A. M., Shane, N., Silva Aguirre, V., Sobeck, J. S., Thompson, B., Troup, N. W., Weinberg, D. H., and Zamora, O. (2017). The Apache Point Observatory Galactic Evolution Experiment (APOGEE). AJ, 154:94. (Cited in pages 13 and 62.)

Majewski, S. R., Zasowski, G., and Nidever, D. L. (2011). Lifting the Dusty Veil with Near- and Mid-infrared Photometry. I. Description and Applications of the Rayleigh-Jeans Color Excess Method. ApJ, 739:25. (Cited in page 34.)

Marigo, P., Girardi, L., Bressan, A., Groenewegen, M. A. T., Silva, L., and Granato, G. L. (2008). Evolution of asymptotic giant branch stars. II. Optical to far-infrared isochrones with improved TP-AGB models. A&A, 482:883–905. (Cited in page 20.)

Martig, M., Fouesneau, M., Rix, H.-W., Ness, M., Mészáros, S., García-Hernández, D. A., Pinsonneault, M., Serenelli, A., Silva Aguirre, V., and Zamora, O. (2016). Red giant masses and ages derived from carbon and nitrogen abundances. MNRAS, 456:3655–3670. (Cited in page 125.)

Martin, C. L., Walsh, W. M., Xiao, K., Lane, A. P., Walker, C. K., and Stark, A. A. (2004). The AST/RO Survey of the Galactic Center Region. I. The Inner 3 Degrees. ApJS, 150:239–262. (Cited in page 26.)

Martinez-Valpuesta, I. and Gerhard, O. (2011). Unifying A Boxy Bulge and Planar Long Bar in the Milky Way. ApJ, 734:L20. (Cited in page 7.)

Matsunaga, N., Kawadu, T., Nishiyama, S., Nagayama, T., Hatano, H., Tamura, M., Glass, I. S., and Nagata, T. (2009). A near-infrared survey of Miras and the distance to the Galactic Centre. MNRAS, 399:1709–1729. (Cited in pages 107 and 109.)

Matteucci, F. (2014). Chemical Evolution of the Milky Way and Its Satellites. *The Origin of the Galaxy and Local Group, Saas-Fee Advanced Course, Volume 37. ISBN 978-3-642-41719-1. Springer-Verlag Berlin Heidelberg, 2014, p. 145*, 37:145. (Cited in page 21.)

Matteucci, F. and Francois, P. (1989). Galactic chemical evolution - Abundance gradients of individual elements. MNRAS, 239:885–904. (Cited in page 22.)

Matteucci, F. and Francois, P. (1992). Oxygen abundances in halo stars as tests of galaxy formation. A&A, 262:L1–L4. (Cited in page 22.)

Mauerhan, J. C., Cotera, A., Dong, H., Morris, M. R., Wang, Q. D., Stolovy, S. R., and Lang, C. (2010a). Isolated Wolf-Rayet Stars and O Supergiants in the Galactic Center Region Identified Via Paschen-α Excess. ApJ, 725:188–199. (Cited in pages 105, 107 and 109.)

Mauerhan, J. C., Muno, M. P., Morris, M. R., Stolovy, S. R., and Cotera, A. (2010b). Near-infrared Counterparts to Chandra X-ray Sources Toward the Galactic Center. II. Discovery of Wolf-Rayet Stars and O Supergiants. ApJ, 710:706–728. (Cited in page 107.)

McKee, C. F. and Williams, J. P. (1997). The Luminosity Function of OB Associations in the Galaxy. ApJ, 476:144–165. (Cited in page 96.)

McMahon, R. G., Banerji, M., Gonzalez, E., Koposov, S. E., Bejar, V. J., Lodieu, N., Rebolo, R., and VHS Collaboration (2013). First Scientific Results from the VISTA Hemisphere Survey (VHS). *The Messenger*, 154:35–37. (Cited in page 12.)

McWilliam, A. and Rich, R. M. (1994). The first detailed abundance analysis of Galactic bulge K giants in Baade's window. ApJS, 91:749–791. (Cited in page 7.)

Megeath, S. T., Allen, L. E., Gutermuth, R. A., Pipher, J. L., Myers, P. C., Calvet, N., Hartmann, L., Muzerolle, J., and Fazio, G. G. (2004). Initial Results from the Spitzer Young Stellar Cluster Survey. ApJS, 154:367–373. (Cited in pages 99 and 134.)

Mezger, P. O. (1978). The Galactic Extended Low-density HII Region and Its Relation to Star Formation and Diffuse IR Emission. A&A, 70:565. (Cited in page 96.)

Miglio, A., Chiappini, C., Morel, T., Barbieri, M., Chaplin, W. J., Girardi, L., Montalbán, J., Valentini, M., Mosser, B., Baudin, F., Casagrande, L., Fossati, L., Silva Aguirre, V., and Baglin, A. (2013). Galactic archaeology: mapping and dating stellar populations with asteroseismology of red-giant stars. MNRAS, 429:423–428. (Cited in page 19.)

Mikolaitis, Š., Hill, V., Recio-Blanco, A., de Laverny, P., Allende Prieto, C., Kordopatis, G., Tautvaišiene, G., Romano, D., Gilmore, G., Randich, S., Feltzing, S., Micela, G., Vallenari, A., Alfaro, E. J., Bensby, T., Bragaglia, A., Flaccomio, E., Lanzafame, A. C., Pancino, E., Smiljanic, R., Bergemann, M., Carraro, G., Costado, M. T., Damiani, F., Hourihane, A., Jofré, P., Lardo, C., Magrini, L., Maiorca, E., Morbidelli, L., Sbordone, L., Sousa, S. G., Worley, C. C., and Zaggia, S. (2014). The Gaia-ESO Survey: the chemical structure of the Galactic discs from the first internal data release. A&A, 572:A33. (Cited in page 58.)

Mills, E. A. C. and Battersby, C. (2017). Origins of Scatter in the Relationship between HCN 1-0 and Dense Gas Mass in the Galactic Center. ApJ, 835:76. (Cited in page 118.)

Minniti, D., Lucas, P. W., Emerson, J. P., Saito, R. K., Hempel, M., Pietrukowicz, P., Ahumada, A. V., Alonso, M. V., Alonso-Garcia, J., Arias, J. I., Bandyopadhyay, R. M., Barbá, R. H., Barbuy, B., Bedin, L. R., Bica, E., Borissova, J., Bronfman, L., Carraro, G., Catelan, M., Clariá, J. J., Cross, N., de Grijs, R., Dékány, I., Drew, J. E., Fariña, C., Feinstein, C., Fernández Lajús, E., Gamen, R. C., Geisler, D., Gieren, W., Goldman, B., Gonzalez, O. A., Gunthardt, G., Gurovich, S., Hambly, N. C., Irwin, M. J., Ivanov, V. D., Jordán, A., Kerins, E., Kinemuchi, K., Kurtev, R., López-Corredoira, M., Maccarone, T., Masetti, N., Merlo, D., Messineo, M., Mirabel, I. F., Monaco, L., Morelli, L., Padilla, N., Palma, T., Parisi, M. C., Pignata, G., Rejkuba, M., Roman-Lopes, A., Sale, S. E., Schreiber, M. R., Schröder, A. C., Smith, M., , Jr., L. S., Soto, M., Tamura, M., Tappert, C., Thompson, M. A., Toledo, I., Zoccali, M., and Pietrzynski, G. (2010). VISTA Variables in the Via Lactea (VVV): The public ESO near-IR variability survey of the Milky Way. New A, 15:433–443. (Cited in page 12.)

Molinari, S., Swinyard, B., Bally, J., Barlow, M., Bernard, J.-P., Martin, P., Moore, T., Noriega-Crespo, A., Plume, R., Testi, L., Zavagno, A., Abergel, A., Ali, B., André, P., Baluteau, J.-P., Benedettini, M., Berné, O., Billot, N. P., Blommaert, J., Bontemps, S., Boulanger, F., Brand, J., Brunt, C., Burton, M., Campeggio, L., Carey, S., Caselli, P., Cesaroni, R., Cernicharo, J., Chakrabarti, S., Chrysostomou, A., Codella, C., Cohen, M.,

Compiegne, M., Davis, C. J., de Bernardis, P., de Gasperis, G., Di Francesco, J., di Giorgio, A. M., Elia, D., Faustini, F., Fischera, J. F., Fukui, Y., Fuller, G. A., Ganga, K., Garcia-Lario, P., Giard, M., Giardino, G., Glenn, J. ., Goldsmith, P., Griffin, M., Hoare, M., Huang, M., Jiang, B., Joblin, C., Joncas, G., Juvela, M., Kirk, J., Lagache, G., Li, J. Z., Lim, T. L., Lord, S. D., Lucas, P. W., Maiolo, B., Marengo, M., Marshall, D., Masi, S., Massi, F., Matsuura, M., Meny, C., Minier, V., Miville-Deschênes, M.-A., Montier, L., Motte, F., Müller, T. G., Natoli, P., Neves, J., Olmi, L., Paladini, R., Paradis, D., Pestalozzi, M., Pezzuto, S., Piacentini, F., Pomarès, M., Popescu, C. C., Reach, W. T., Richer, J., Ristorcelli, I., Roy, A., Royer, P., Russeil, D., Saraceno, P., Sauvage, M., Schilke, P., Schneider-Bontemps, N., Schuller, F., Schultz, B., Shepherd, D. S., Sibthorpe, B., Smith, H. A., Smith, M. D., Spinoglio, L., Stamatellos, D., Strafella, F., Stringfellow, G., Sturm, E., Taylor, R., Thompson, M. A., Tuffs, R. J., Umana, G., Valenziano, L., Vavrek, R., Viti, S., Waelkens, C., Ward-Thompson, D., White, G., Wyrowski, F., Yorke, H. W., and Zhang, Q. (2010). Hi-GAL: The Herschel Infrared Galactic Plane Survey. PASP, 122:314–325. (Cited in page 96.)

Moorwood, A. (2005). CRIRES: Context and Status. In Käufl, H. U., Siebenmorgen, R., and Moorwood, A. F. M., editors, *High Resolution Infrared Spectroscopy in Astronomy*, page 15. (Cited in page 65.)

Moorwood, A., Cuby, J.-G., Biereichel, P., Brynnel, J., Delabre, B., Devillard, N., van Dijsseldonk, A., Finger, G., Gemperlein, H., Gilmozzi, R., Herlin, T., Huster, G., Knudstrup, J., Lidman, C., Lizon, J.-L., Mehrgan, H., Meyer, M., Nicolini, G., Petr, M., Spyromilio, J., and Stegmeier, J. (1998a). ISAAC sees first light at the VLT. *The Messenger*, 94:7–9. (Cited in page 65.)

Moorwood, A., Cuby, J.-G., and Lidman, C. (1998b). SOFI sees first light at the NTT. *The Messenger*, 91:9–13. (Cited in page 65.)

Morris, M. and Serabyn, E. (1996). The Galactic Center Environment. ARA&A, 34:645–702. (Cited in pages 26 and 116.)

Muno, M. P., Baganoff, F. K., Bautz, M. W., Brandt, W. N., Garmire, G. P., and Ricker, G. R. (2003). X-Ray Sources with Periodic Variability in a Deep Chandra Image of the Galactic Center. ApJ, 599:465–474. (Cited in pages 107 and 109.)

Murray, N. and Rahman, M. (2010). Star Formation in Massive Clusters Via the Wilkinson Microwave Anisotropy Probe and the Spitzer Glimpse Survey. ApJ, 709:424–435. (Cited in page 96.)

Nagashima, C., Nagayama, T., Nakajima, Y., Tamura, M., Sugitani, K., Nagata, T., Hirao, T., Nakaya, H., Yanagisawa, K., and Sato, S. (1999). Development of SIRIUS — A Simultaneous-Color InfraRed Imager for Unbiased Survey. In Nakamoto, T., editor, *Star Formation 1999*, pages 397–398. (Cited in pages 116 and 136.)

Nagayama, T., Nagashima, C., Nakajima, Y., Nagata, T., Sato, S., Nakaya, H., Yamamuro, T., Sugitani, K., and Tamura, M. (2003). SIRUS: a near infrared simultaneous three-band

camera. In Iye, M. and Moorwood, A. F. M., editors, *Instrument Design and Performance for Optical/Infrared Ground-based Telescopes*, volume 4841 of Proc. SPIE, pages 459–464. (Cited in pages 116 and 136.)

Nataf, D. M., Udalski, A., Gould, A., Fouqué, P., and Stanek, K. Z. (2010). The Split Red Clump of the Galactic Bulge from OGLE-III. ApJ, 721:L28–L32. (Cited in page 7.)

Ness, M. and Freeman, K. (2016). The Metallicity Distribution of the Milky Way Bulge. PASA, 33:e022. (Cited in page 7.)

Ness, M., Freeman, K., Athanassoula, E., Wylie-de-Boer, E., Bland-Hawthorn, J., Asplund, M., Lewis, G. F., Yong, D., Lane, R. R., and Kiss, L. L. (2013a). ARGOS - III. Stellar populations in the Galactic bulge of the Milky Way. MNRAS, 430:836–857. (Cited in pages 7 and 88.)

Ness, M., Freeman, K., Athanassoula, E., Wylie-de-Boer, E., Bland-Hawthorn, J., Asplund, M., Lewis, G. F., Yong, D., Lane, R. R., Kiss, L. L., and Ibata, R. (2013b). ARGOS - IV. The kinematics of the Milky Way bulge. MNRAS, 432:2092–2103. (Cited in pages 7, 86, 89 and 91.)

Ness, M., Freeman, K., Athanassoula, E., Wylie-De-Boer, E., Bland-Hawthorn, J., Lewis, G. F., Yong, D., Asplund, M., Lane, R. R., Kiss, L. L., and Ibata, R. (2012). The Origin of the Split Red Clump in the Galactic Bulge of the Milky Way. ApJ, 756:22. (Cited in page 7.)

Ness, M., Hogg, D. W., Rix, H.-W., Ho, A. Y. Q., and Zasowski, G. (2015). The Cannon: A data-driven approach to Stellar Label Determination. ApJ, 808:16. (Cited in page 39.)

Nidever, D. L., Bovy, J., Bird, J. C., Andrews, B. H., Hayden, M., Holtzman, J., Majewski, S. R., Smith, V., Robin, A. C., García Pérez, A. E., Cunha, K., Allende Prieto, C., Zasowski, G., Schiavon, R. P., Johnson, J. A., Weinberg, D. H., Feuillet, D., Schneider, D. P., Shetrone, M., Sobeck, J., García-Hernández, D. A., Zamora, O., Rix, H.-W., Beers, T. C., Wilson, J. C., O'Connell, R. W., Minchev, I., Chiappini, C., Anders, F., Bizyaev, D., Brewington, H., Ebelke, G., Frinchaboy, P. M., Ge, J., Kinemuchi, K., Malanushenko, E., Malanushenko, V., Marchante, M., Mészáros, S., Oravetz, D., Pan, K., Simmons, A., and Skrutskie, M. F. (2014). Tracing Chemical Evolution over the Extent of the Milky Way's Disk with APOGEE Red Clump Stars. ApJ, 796:38. (Cited in page 32.)

Nishiyama, S., Nagata, T., Kusakabe, N., Matsunaga, N., Naoi, T., Kato, D., Nagashima, C., Sugitani, K., Tamura, M., Tanabé, T., and Sato, S. (2006). Interstellar Extinction Law in the J, H, and K_s Bands toward the Galactic Center. ApJ, 638:839–846. (Cited in page 103.)

Nishiyama, S., Tamura, M., Hatano, H., Kato, D., Tanabé, T., Sugitani, K., and Nagata, T. (2009). Interstellar Extinction Law Toward the Galactic Center III: J, H, K_S Bands in the 2MASS and the MKO Systems, and 3.6, 4.5, 5.8, 8.0 μm in the Spitzer/IRAC System. ApJ, 696:1407–1417. (Cited in pages 26, 28, 64, 65, 108, 110, 111, 126, 130, 132 and 135.)

Nissen, P. E. (2015). High-precision abundances of elements in solar twin stars. Trends with stellar age and elemental condensation temperature. A&A, 579:A52. (Cited in page 125.)

Nordström, B., Mayor, M., Andersen, J., Holmberg, J., Pont, F., Jørgensen, B. R., Olsen, E. H., Udry, S., and Mowlavi, N. (2004). The Geneva-Copenhagen survey of the Solar neighbourhood. Ages, metallicities, and kinematic properties of 14 000 F and G dwarfs. A&A, 418:989–1019. (Cited in page 32.)

Oka, T., Geballe, T. R., Goto, M., Usuda, T., and McCall, B. J. (2005). Hot and Diffuse Clouds near the Galactic Center Probed by Metastable $H^+_3 1$,. ApJ, 632:882–893. (Cited in pages 26 and 116.)

Omont, A., Gilmore, G. F., Alard, C., Aracil, B., August, T., Baliyan, K., Beaulieu, S., Bégon, S., Bertou, X., Blommaert, J. A. D. L., Borsenberger, J., Burgdorf, M., Caillaud, B., Cesarsky, C., Chitre, A., Copet, E., de Batz, B., Egan, M. P., Egret, D., Epchtein, N., Felli, M., Fouqué, P., Ganesh, S., Genzel, R., Glass, I. S., Gredel, R., Groenewegen, M. A. T., Guglielmo, F., Habing, H. J., Hennebelle, P., Jiang, B., Joshi, U. C., Kimeswenger, S., Messineo, M., Miville-Deschênes, M. A., Moneti, A., Morris, M., Ojha, D. K., Ortiz, R., Ott, S., Parthasarathy, M., Pérault, M., Price, S. D., Robin, A. C., Schultheis, M., Schuller, F., Simon, G., Soive, A., Testi, L., Teyssier, D., Tiphène, D., Unavane, M., van Loon, J. T., and Wyse, R. (2003a). ISOGAL: A deep survey of the obscured inner Milky Way with ISO at 7 mu m and 15 mu m and with DENIS in the near-infrared. A&A, 403:975–992. (Cited in pages 65 and 112.)

Omont, A., Gilmore, G. F., Alard, C., Aracil, B., August, T., Baliyan, K., Beaulieu, S., Begon, S., Bertou, X., Blommaert, J. A. D. L., Borsenberger, J., Burgdorf, M., Caillaud, B., Cesarsky, C., Chitre, A., Copet, E., de Batz, B., Egan, M. P., Egret, D., Epchtein, N., Felli, M., Fouque, P., Ganesh, S., Genzel, R., Glass, I. S., Gredel, R., Groenewegen, M. A. T., Guglielmo, F., Habing, H. J., Hennebelle, P., Jiang, B., Joshi, U. C., Kimeswenger, S., Messineo, M., Miville-Deschenes, M. A., Moneti, A., Morris, M., Ojha, D. K., Ortiz, R., Ott, S., Parthasarathy, M., Perault, M., Price, S. D., Robin, A. C., Schultheis, M., Schuller, F., Simon, G., Soive, A., Testi, L., Teyssier, D., Tiphene, D., Unavane, M., van Loon, J. T., and Wyse, R. (2003b). VizieR Online Data Catalog: The ISOGAL Point Source Catalogue - IGPSC (Omont+ 2003). *VizieR Online Data Catalog*, 2243. (Cited in page 112.)

Origlia, L. (2014). A review of the chemical abundances and kinematics of the Galactic bulge. In Feltzing, S., Zhao, G., Walton, N. A., and Whitelock, P., editors, *Setting the scene for Gaia and LAMOST*, volume 298 of *IAU Symposium*, pages 28–39. (Cited in page 7.)

Ortolani, S., Renzini, A., Gilmozzi, R., Marconi, G., Barbuy, B., Bica, E., and Rich, R. M. (1995). Near-coeval formation of the Galactic bulge and halo inferred from globular cluster ages. Nature, 377:701–704. (Cited in page 7.)

Osorio, Y., Barklem, P. S., Lind, K., Belyaev, A. K., Spielfiedel, A., Guitou, M., and

Feautrier, N. (2015). Mg line formation in late-type stellar atmospheres. I. The model atom. A&A, 579:A53. (Cited in page 74.)

Pardi, M. C., Ferrini, F., and Matteucci, F. (1995). Evolution of spiral galaxies. 4: The thick disk in the solar region as an intermediate collapse phase. ApJ, 444:207–221. (Cited in page 22.)

Pasquini, L., Avila, G., Blecha, A., Cacciari, C., Cayatte, V., Colless, M., Damiani, F., de Propris, R., Dekker, H., di Marcantonio, P., Farrell, T., Gillingham, P., Guinouard, I., Hammer, F., Kaufer, A., Hill, V., Marteaud, M., Modigliani, A., Mulas, G., North, P., Popovic, D., Rossetti, E., Royer, F., Santin, P., Schmutzer, R., Simond, G., Vola, P., Waller, L., and Zoccali, M. (2002). Installation and commissioning of FLAMES, the VLT Multifibre Facility. *The Messenger*, 110:1–9. (Cited in page 15.)

Pehlivan Rhodin, A., Hartman, H., Nilsson, H., and Jönsson, P. (2017). Experimental and theoretical oscillator strengths of Mg i for accurate abundance analysis. A&A, 598:A102. (Cited in page 73.)

Penzias, A. A. and Wilson, R. W. (1965). A Measurement of Excess Antenna Temperature at 4080 Mc/s. ApJ, 142:419–421. (Cited in page 4.)

Perlmutter, S., Aldering, G., Goldhaber, G., Knop, R. A., Nugent, P., Castro, P. G., Deustua, S., Fabbro, S., Goobar, A., Groom, D. E., Hook, I. M., Kim, A. G., Kim, M. Y., Lee, J. C., Nunes, N. J., Pain, R., Pennypacker, C. R., Quimby, R., Lidman, C., Ellis, R. S., Irwin, M., McMahon, R. G., Ruiz-Lapuente, P., Walton, N., Schaefer, B., Boyle, B. J., Filippenko, A. V., Matheson, T., Fruchter, A. S., Panagia, N., Newberg, H. J. M., Couch, W. J., and Project, T. S. C. (1999). Measurements of Ω and Λ from 42 High-Redshift Supernovae. ApJ, 517:565–586. (Cited in page 4.)

Persson, S. E., West, S. C., Carr, D. M., Sivaramakrishnan, A., and Murphy, D. C. (1992). A near-infrared camera for Las Campanas Observatory. PASP, 104:204–214. (Cited in page 62.)

Piddington, J. H. and Minnett, H. C. (1951). Observations of Galactic Radiation at Frequencies of 1200 and 3000 Mc/s. *Australian Journal of Scientific Research A Physical Sciences*, 4:459. (Cited in page 24.)

Piffl, T., Binney, J., McMillan, P. J., Steinmetz, M., Helmi, A., Wyse, R. F. G., Bienaymé, O., Bland-Hawthorn, J., Freeman, K., Gibson, B., Gilmore, G., Grebel, E. K., Kordopatis, G., Navarro, J. F., Parker, Q., Reid, W. A., Seabroke, G., Siebert, A., Watson, F., and Zwitter, T. (2014a). Constraining the Galaxy's dark halo with RAVE stars. MNRAS, 445:3133–3151. (Cited in page 14.)

Piffl, T., Scannapieco, C., Binney, J., Steinmetz, M., Scholz, R.-D., Williams, M. E. K., de Jong, R. S., Kordopatis, G., Matijevič, G., Bienaymé, O., Bland-Hawthorn, J., Boeche, C., Freeman, K., Gibson, B., Gilmore, G., Grebel, E. K., Helmi, A., Munari, U., Navarro, J. F., Parker, Q., Reid, W. A., Seabroke, G., Watson, F., Wyse, R. F. G., and Zwitter, T.

(2014b). The RAVE survey: the Galactic escape speed and the mass of the Milky Way. A&A, 562:A91. (Cited in page 14.)

Piskunov, N. and Valenti, J. A. (2017). Spectroscopy Made Easy: Evolution. A&A, 597:A16. (Cited in page 72.)

Piskunov, N. E., Kupka, F., Ryabchikova, T. A., Weiss, W. W., and Jeffery, C. S. (1995). Vald: The vienna atomic line data base. 112:525. (Cited in page 73.)

Planck Collaboration, Ade, P. A. R., Aghanim, N., Arnaud, M., Ashdown, M., Aumont, J., Baccigalupi, C., Banday, A. J., Barreiro, R. B., Bartlett, J. G., and et al. (2016). Planck 2015 results. XIII. Cosmological parameters. A&A, 594:A13. (Cited in page 4.)

Portail, M., Wegg, C., Gerhard, O., and Martinez-Valpuesta, I. (2015). Made-to-measure models of the Galactic box/peanut bulge: stellar and total mass in the bulge region. MNRAS, 448:713–731. (Cited in page 7.)

Quinn, P. J., Hernquist, L., and Fullagar, D. P. (1993). Heating of galactic disks by mergers. ApJ, 403:74–93. (Cited in page 9.)

Ramírez, S. V., Arendt, R. G., Sellgren, K., Stolovy, S. R., Cotera, A., Smith, H. A., and Yusef-Zadeh, F. (2008). Point Sources from a Spitzer IRAC Survey of the Galactic Center. ApJS, 175:147–164. (Cited in pages 100, 103, 109, 112, 115, 116, 119 and 136.)

Ramirez, S. V., Depoy, D. L., Frogel, J. A., Sellgren, K., and Blum, R. D. (1997). Luminosity and Temperature from Near-Infrared Spectra of Late-Type Giant Stars. AJ, 113:1411–1420. (Cited in page 70.)

Ramírez, S. V., Sellgren, K., Carr, J. S., Balachandran, S. C., Blum, R., Terndrup, D. M., and Steed, A. (2000a). Stellar Iron Abundances at the Galactic Center. ApJ, 537:205–220. (Cited in pages 62, 69, 105 and 132.)

Ramírez, S. V., Stephens, A. W., Frogel, J. A., and DePoy, D. L. (2000b). Metallicity of Red Giants in the Galactic Bulge from Near-Infrared Spectroscopy. 120:833–844. (Cited in pages 62, 65 and 70.)

Recio-Blanco, A., Bijaoui, A., and de Laverny, P. (2006). Automated derivation of stellar atmospheric parameters and chemical abundances: the MATISSE algorithm. MNRAS, 370:141–150. (Cited in page 14.)

Recio-Blanco, A., de Laverny, P., Kordopatis, G., Helmi, A., Hill, V., Gilmore, G., Wyse, R., Adibekyan, V., Randich, S., Asplund, M., Feltzing, S., Jeffries, R., Micela, G., Vallenari, A., Alfaro, E., Allende Prieto, C., Bensby, T., Bragaglia, A., Flaccomio, E., Koposov, S. E., Korn, A., Lanzafame, A., Pancino, E., Smiljanic, R., Jackson, R., Lewis, J., Magrini, L., Morbidelli, L., Prisinzano, L., Sacco, G., Worley, C. C., Hourihane, A., Bergemann, M., Costado, M. T., Heiter, U., Joffre, P., Lardo, C., Lind, K., and Maiorca, E. (2014). The Gaia-ESO Survey: the Galactic thick to thin disc transition. A&A, 567:A5. (Cited in page 8.)

Reddy, B. E., Lambert, D. L., and Allende Prieto, C. (2006). Elemental abundance survey of the Galactic thick disc. MNRAS, 367:1329–1366. (Cited in page 8.)

Reid, M. J. and Brunthaler, A. (2004). The Proper Motion of Sagittarius A*. II. The Mass of Sagittarius A*. ApJ, 616:872–884. (Cited in page 24.)

Rich, R. M. (2013). *The Galactic Bulge*, page 271. (Cited in page 7.)

Rich, R. M., Origlia, L., and Valenti, E. (2007). The First Detailed Abundances for M Giants in the Inner Bulge from Infrared Spectroscopy. ApJ, 665:L119–L122. (Cited in pages 62 and 86.)

Rich, R. M., Origlia, L., and Valenti, E. (2012). Detailed Abundances for M Giants in Two Inner Bulge Fields from Infrared Spectroscopy. ApJ, 746:59. (Cited in pages 62, 86 and 88.)

Rich, R. M., Ryde, N., Thorsbro, B., Fritz, T. K., Schultheis, M., Origlia, L., and Jönsson, H. (2017). Detailed Abundances for the Old Population near the Galactic Center. I. Metallicity Distribution of the Nuclear Star Cluster. AJ, 154:239. (Cited in pages 65, 74, 78 and 79.)

Rieke, G. H., Young, E. T., Engelbracht, C. W., Kelly, D. M., Low, F. J., Haller, E. E., Beeman, J. W., Gordon, K. D., Stansberry, J. A., Misselt, K. A., Cadien, J., Morrison, J. E., Rivlis, G., Latter, W. B., Noriega-Crespo, A., Padgett, D. L., Stapelfeldt, K. R., Hines, D. C., Egami, E., Muzerolle, J., Alonso-Herrero, A., Blaylock, M., Dole, H., Hinz, J. L., Le Floc'h, E., Papovich, C., Pérez-González, P. G., Smith, P. S., Su, K. Y. L., Bennett, L., Frayer, D. T., Henderson, D., Lu, N., Masci, F., Pesenson, M., Rebull, L., Rho, J., Keene, J., Stolovy, S., Wachter, S., Wheaton, W., Werner, M. W., and Richards, P. L. (2004). The Multiband Imaging Photometer for Spitzer (MIPS). ApJS, 154:25–29. (Cited in page 12.)

Riess, A. G., Filippenko, A. V., Challis, P., Clocchiatti, A., Diercks, A., Garnavich, P. M., Gilliland, R. L., Hogan, C. J., Jha, S., Kirshner, R. P., Leibundgut, B., Phillips, M. M., Reiss, D., Schmidt, B. P., Schommer, R. A., Smith, R. C., Spyromilio, J., Stubbs, C., Suntzeff, N. B., and Tonry, J. (1998). Observational Evidence from Supernovae for an Accelerating Universe and a Cosmological Constant. AJ, 116:1009–1038. (Cited in page 4.)

Rix, H.-W. and Bovy, J. (2013). The Milky Way's stellar disk. Mapping and modeling the Galactic disk. A&A Rev., 21:61. (Cited in pages 10, 11 and 129.)

Robin, A. C., Marshall, D. J., Schultheis, M., and Reylé, C. (2012). Stellar populations in the Milky Way bulge region: towards solving the Galactic bulge and bar shapes using 2MASS data. A&A, 538:A106. (Cited in page 20.)

Robin, A. C., Reylé, C., Derrière, S., and Picaud, S. (2003). A synthetic view on structure and evolution of the Milky Way. A&A, 409:523–540. (Cited in pages 18 and 20.)

Robitaille, T. P. (2011). HYPERION: an open-source parallelized three-dimensional dust continuum radiative transfer code. A&A, 536:A79. (Cited in page 100.)

Robitaille, T. P. (2017). A modular set of synthetic spectral energy distributions for young stellar objects. A&A, 600:A11. (Cited in pages 111 and 126.)

Robitaille, T. P., Whitney, B. A., Indebetouw, R., and Wood, K. (2007). Interpreting Spectral Energy Distributions from Young Stellar Objects. II. Fitting Observed SEDs Using a Large Grid of Precomputed Models. ApJS, 169:328–352. (Cited in pages 111 and 115.)

Robitaille, T. P., Whitney, B. A., Indebetouw, R., Wood, K., and Denzmore, P. (2006). Interpreting Spectral Energy Distributions from Young Stellar Objects. I. A Grid of 200,000 YSO Model SEDs. ApJS, 167:256–285. (Cited in pages 97, 108, 110, 111 and 135.)

Rojas-Arriagada, A., Recio-Blanco, A., de Laverny, P., Mikolaitis, Š., Matteucci, F., Spitoni, E., Schultheis, M., Hayden, M., Hill, V., Zoccali, M., Minniti, D., Gonzalez, O. A., Gilmore, G., Randich, S., Feltzing, S., Alfaro, E. J., Babusiaux, C., Bensby, T., Bragaglia, A., Flaccomio, E., Koposov, S. E., Pancino, E., Bayo, A., Carraro, G., Casey, A. R., Costado, M. T., Damiani, F., Donati, P., Franciosini, E., Hourihane, A., Jofré, P., Lardo, C., Lewis, J., Lind, K., Magrini, L., Morbidelli, L., Sacco, G. G., Worley, C. C., and Zaggia, S. (2017). The Gaia-ESO Survey: Exploring the complex nature and origins of the Galactic bulge populations. A&A, 601:A140. (Cited in pages 7, 42, 44, 47, 86 and 87.)

Rojas-Arriagada, A., Recio-Blanco, A., Hill, V., de Laverny, P., Schultheis, M., Babusiaux, C., Zoccali, M., Minniti, D., Gonzalez, O. A., Feltzing, S., Gilmore, G., Randich, S., Vallenari, A., Alfaro, E. J., Bensby, T., Bragaglia, A., Flaccomio, E., Lanzafame, A. C., Pancino, E., Smiljanic, R., Bergemann, M., Costado, M. T., Damiani, F., Hourihane, A., Jofré, P., Lardo, C., Magrini, L., Maiorca, E., Morbidelli, L., Sbordone, L., Worley, C. C., Zaggia, S., and Wyse, R. (2014). The Gaia-ESO Survey: metallicity and kinematic trends in the Milky Way bulge. A&A, 569:A103. (Cited in pages 69, 70 and 132.)

Rubele, S., Girardi, L., Kerber, L., Cioni, M.-R. L., Piatti, A. E., Zaggia, S., Bekki, K., Bressan, A., Clementini, G., de Grijs, R., Emerson, J. P., Groenewegen, M. A. T., Ivanov, V. D., Marconi, M., Marigo, P., Moretti, M.-I., Ripepi, V., Subramanian, S., Tatton, B. L., and van Loon, J. T. (2015). The VMC survey - XIV. First results on the look-back time star formation rate tomography of the Small Magellanic Cloud. MNRAS, 449:639–661. (Cited in page 19.)

Rubele, S., Kerber, L., Girardi, L., Cioni, M.-R., Marigo, P., Zaggia, S., Bekki, K., de Grijs, R., Emerson, J., Groenewegen, M. A. T., Gullieuszik, M., Ivanov, V., Miszalski, B., Oliveira, J. M., Tatton, B., and van Loon, J. T. (2012). The VMC survey. IV. The LMC star formation history and disk geometry from four VMC tiles. A&A, 537:A106. (Cited in page 19.)

Rubin, V. C. and Ford, Jr., W. K. (1970). Rotation of the Andromeda Nebula from a Spectroscopic Survey of Emission Regions. ApJ, 159:379. (Cited in page 4.)

Ryabchikova, T., Piskunov, N., Kurucz, R. L., Stempels, H. C., Heiter, U., Pakhomov, Y., and Barklem, P. S. (2015). A major upgrade of the VALD database. Phys. Scr, 90(5):054005. (Cited in page 73.)

Ryabchikova, T. A., Piskunov, N. E., Kupka, F., and Weiss, W. W. (1997). The Vienna Atomic Line Database : Present State and Future Development. *Baltic Astronomy*, 6:244–247. (Cited in page 73.)

Ryan, S. G. and Norris, J. E. (1991). Subdwarf Studies. III. The Halo Metallicity Distribution. AJ, 101:1865–1878. (Cited in page 6.)

Ryde, N., Fritz, T. K., Rich, R. M., Thorsbro, B., Schultheis, M., Origlia, L., and Chatzopoulos, S. (2016a). Detailed Abundance Analysis of a Metal-poor Giant in the Galactic Center. ApJ, 831:40. (Cited in pages 63 and 65.)

Ryde, N. and Schultheis, M. (2015). Chemical abundances of M giants in the Galactic centre: A single metal-rich population with low [α/Fe]. A&A, 573:A14. (Cited in pages 62, 65 and 82.)

Ryde, N., Schultheis, M., Grieco, V., Matteucci, F., Rich, R. M., and Uttenthaler, S. (2016b). Chemical Evolution of the Inner 2 Degrees of the Milky Way Bulge: [α/Fe] Trends and Metallicity Gradients. *AJ*, 151:1. (Cited in pages 65, 74, 78 and 82.)

Saito, R. K., Hempel, M., Minniti, D., Lucas, P. W., Rejkuba, M., Toledo, I., Gonzalez, O. A., Alonso-García, J., Irwin, M. J., Gonzalez-Solares, E., Hodgkin, S. T., Lewis, J. R., Cross, N., Ivanov, V. D., Kerins, E., Emerson, J. P., Soto, M., Amôres, E. B., Gurovich, S., Dékány, I., Angeloni, R., Beamin, J. C., Catelan, M., Padilla, N., Zoccali, M., Pietrukowicz, P., Moni Bidin, C., Mauro, F., Geisler, D., Folkes, S. L., Sale, S. E., Borissova, J., Kurtev, R., Ahumada, A. V., Alonso, M. V., Adamson, A., Arias, J. I., Bandyopadhyay, R. M., Barbá, R. H., Barbuy, B., Baume, G. L., Bedin, L. R., Bellini, A., Benjamin, R., Bica, E., Bonatto, C., Bronfman, L., Carraro, G., Chenè, A. N., Clariá, J. J., Clarke, J. R. A., Contreras, C., Corvillón, A., de Grijs, R., Dias, B., Drew, J. E., Fariña, C., Feinstein, C., Fernández-Lajús, E., Gamen, R. C., Gieren, W., Goldman, B., González-Fernández, C., Grand, R. J. J., Gunthardt, G., Hambly, N. C., Hanson, M. M., Hełminiak, K. G., Hoare, M. G., Huckvale, L., Jordán, A., Kinemuchi, K., Longmore, A., López-Corredoira, M., Maccarone, T., Majaess, D., Martín, E. L., Masetti, N., Mennickent, R. E., Mirabel, I. F., Monaco, L., Morelli, L., Motta, V., Palma, T., Parisi, M. C., Parker, Q., Peñaloza, F., Pietrzyński, G., Pignata, G., Popescu, B., Read, M. A., Rojas, A., Roman-Lopes, A., Ruiz, M. T., Saviane, I., Schreiber, M. R., Schröder, A. C., Sharma, S., Smith, M. D., Sodré, L., Stead, J., Stephens, A. W., Tamura, M., Tappert, C., Thompson, M. A., Valenti, E., Vanzi, L., Walton, N. A., Weidmann, W., and Zijlstra, A. (2012). VVV DR1: The first data release of the Milky Way bulge and southern plane from the near-infrared ESO public survey VISTA variables in the Vía Láctea. A&A, 537:A107. (Cited in page 12.)

Salpeter, E. E. (1955). The Luminosity Function and Stellar Evolution. ApJ, 121:161. (Cited in page 23.)

Santucci, R. M., Beers, T. C., Placco, V. M., Carollo, D., Rossi, S., Lee, Y. S., Denissenkov,

P., Tumlinson, J., and Tissera, P. B. (2015). Chronography of the Milky Way's Halo System with Field Blue Horizontal-branch Stars. ApJ, 813:L16. (Cited in page 7.)

Schlegel, D. J., Finkbeiner, D. P., and Davis, M. (1998). Maps of Dust Infrared Emission for Use in Estimation of Reddening and Cosmic Microwave Background Radiation Foregrounds. ApJ, 500:525–553. (Cited in pages 20 and 36.)

Schlesinger, K. J., Johnson, J. A., Rockosi, C. M., Lee, Y. S., Beers, T. C., Harding, P., Allende Prieto, C., Bird, J. C., Schönrich, R., Yanny, B., Schneider, D. P., Weaver, B. A., and Brinkmann, J. (2014). The Vertical Metallicity Gradient of the Milky Way Disk: Transitions in [α/Fe] Populations. ApJ, 791:112. (Cited in page 58.)

Schlesinger, K. J., Johnson, J. A., Rockosi, C. M., Lee, Y. S., Morrison, H. L., Schönrich, R., Allende Prieto, C., Beers, T. C., Yanny, B., Harding, P., Schneider, D. P., Chiappini, C., da Costa, L. N., Maia, M. A. G., Minchev, I., Rocha-Pinto, H., and Santiago, B. X. (2012). The Metallicity Distribution Functions of SEGUE G and K Dwarfs: Constraints for Disk Chemical Evolution and Formation. ApJ, 761:160. (Cited in page 32.)

Schmidt, M. (1959). The Rate of Star Formation. ApJ, 129:243. (Cited in page 22.)

Schödel, R., Feldmeier, A., Kunneriath, D., Stolovy, S., Neumayer, N., Amaro-Seoane, P., and Nishiyama, S. (2014). Surface brightness profile of the Milky Way's nuclear star cluster. A&A, 566:A47. (Cited in page 26.)

Schödel, R., Najarro, F., Muzic, K., and Eckart, A. (2010). Peering through the veil: near-infrared photometry and extinction for the Galactic nuclear star cluster. Accurate near infrared H, Ks, and L' photometry and the near-infrared extinction-law toward the central parsec of the Galaxy. A&A, 511:A18. (Cited in page 110.)

Schönrich, R. and Binney, J. (2009). Chemical evolution with radial mixing. MNRAS, 396:203–222. (Cited in page 9.)

Schuller, F., Menten, K. M., Contreras, Y., Wyrowski, F., Schilke, P., Bronfman, L., Henning, T., Walmsley, C. M., Beuther, H., Bontemps, S., Cesaroni, R., Deharveng, L., Garay, G., Herpin, F., Lefloch, B., Linz, H., Mardones, D., Minier, V., Molinari, S., Motte, F., Nyman, L.-Å., Reveret, V., Risacher, C., Russeil, D., Schneider, N., Testi, L., Troost, T., Vasyunina, T., Wienen, M., Zavagno, A., Kovacs, A., Kreysa, E., Siringo, G., and Weiß, A. (2009). ATLASGAL - The APEX telescope large area survey of the galaxy at 870 μm. A&A, 504:415–427. (Cited in page 96.)

Schuller, F., Omont, A., Glass, I. S., Schultheis, M., Egan, M. P., and Price, S. D. (2006). Recent star formation in the inner Galactic Bulge seen by ISOGAL. I. Classification of bright mid-IR sources in a test field. A&A, 453:535–545. (Cited in pages 98 and 100.)

Schultheis, M., Chen, B. Q., Jiang, B. W., Gonzalez, O. A., Enokiya, R., Fukui, Y., Torii, K., Rejkuba, M., and Minniti, D. (2014). Mapping the Milky Way bulge at high resolution: the 3D dust extinction, CO, and X factor maps. *ArXiv e-prints*. (Cited in page 65.)

Schultheis, M., Kordopatis, G., Recio-Blanco, A., de Laverny, P., Hill, V., Gilmore, G., Alfaro, E. J., Costado, M. T., Bensby, T., Damiani, F., Feltzing, S., Flaccomio, E., Lardo, C., Jofre, P., Prisinzano, L., Zaggia, S., Jimenez-Esteban, F., Morbidelli, L., Lanzafame, A. C., Hourihane, A., Worley, C., and Francois, P. (2015). The Gaia-ESO Survey: Tracing interstellar extinction. A&A, 577:A77. (Cited in pages 46, 62, 87, 88 and 126.)

Schultheis, M., Lançon, A., Omont, A., Schuller, F., and Ojha, D. K. (2003). Near-IR spectra of ISOGAL sources in the inner Galactic Bulge. A&A, 405:531–550. (Cited in pages 100, 101 and 134.)

Schultheis, M., Rojas-Arriagada, A., García Pérez, A. E., Jönsson, H., Hayden, M., Nandakumar, G., Cunha, K., Allende Prieto, C., Holtzman, J. A., Beers, T. C., Bizyaev, D., Brinkmann, J., Carrera, R., Cohen, R. E., Geisler, D., Hearty, F. R., Fernandez-Tricado, J. G., Maraston, C., Minnitti, D., Nitschelm, C., Roman-Lopes, A., Schneider, D. P., Tang, B., Villanova, S., Zasowski, G., and Majewski, S. R. (2017). Baade's window and APOGEE. Metallicities, ages, and chemical abundances. A&A, 600:A14. (Cited in pages 39, 69, 70, 83, 86 and 132.)

Schultheis, M., Ryde, N., and Nandakumar, G. (2016). Temperatures and metallicities of M giants in the Galactic bulge from low-resolution K-band spectra. A&A, 590:A6. (Cited in pages 65 and 74.)

Schultheis, M., Sellgren, K., Ramírez, S., Stolovy, S., Ganesh, S., Glass, I. S., and Girardi, L. (2009). Interstellar extinction and long-period variables in the Galactic centre. A&A, 495:157–168. (Cited in pages 98, 110, 112, 114, 115 and 138.)

Searle, L. and Zinn, R. (1978). Compositions of halo clusters and the formation of the galactic halo. ApJ, 225:357–379. (Cited in pages 6 and 7.)

Sellwood, J. A. and Binney, J. J. (2002). Radial mixing in galactic discs. MNRAS, 336:785–796. (Cited in page 9.)

Serabyn, E. and Morris, M. (1996). Sustained star formation in the central stellar cluster of the Milky Way. Nature, 382:602–604. (Cited in page 26.)

Sharma, S., Bland-Hawthorn, J., Binney, J., Freeman, K. C., Steinmetz, M., Boeche, C., Bienaymé, O., Gibson, B. K., Gilmore, G. F., Grebel, E. K., Helmi, A., Kordopatis, G., Munari, U., Navarro, J. F., Parker, Q. A., Reid, W. A., Seabroke, G. M., Siebert, A., Watson, F., Williams, M. E. K., Wyse, R. F. G., and Zwitter, T. (2014). Kinematic Modeling of the Milky Way Using the RAVE and GCS Stellar Surveys. ApJ, 793:51. (Cited in page 32.)

Sharma, S., Bland-Hawthorn, J., Johnston, K. V., and Binney, J. (2011). Galaxia: A Code to Generate a Synthetic Survey of the Milky Way. ApJ, 730:3. (Cited in pages 18, 19, 33, 45 and 55.)

Sharples, R., Bender, R., Agudo Berbel, A., Bezawada, N., Castillo, R., Cirasuolo, M., Davidson, G., Davies, R., Dubbeldam, M., Fairley, A., Finger, G., Förster Schreiber, N.,

Gonte, F., Hess, A., Jung, I., Lewis, I., Lizon, J.-L., Muschielok, B., Pasquini, L., Pirard, J., Popovic, D., Ramsay, S., Rees, P., Richter, J., Riquelme, M., Rodrigues, M., Saviane, I., Schlichter, J., Schmidtobreick, L., Segovia, A., Smette, A., Szeifert, T., van Kesteren, A., Wegner, M., and Wiezorrek, E. (2013). First Light for the KMOS Multi-Object Integral-Field Spectrometer. *The Messenger*, 151:21–23. (Cited in page 102.)

Shen, J., Rich, R. M., Kormendy, J., Howard, C. D., De Propris, R., and Kunder, A. (2010). Our Milky Way as a Pure-disk GalaxyA Challenge for Galaxy Formation. ApJ, 720:L72–L76. (Cited in page 7.)

Skrutskie, M. F., Cutri, R. M., Stiening, R., Weinberg, M. D., Schneider, S., Carpenter, J. M., Beichman, C., Capps, R., Chester, T., Elias, J., Huchra, J., Liebert, J., Lonsdale, C., Monet, D. G., Price, S., Seitzer, P., Jarrett, T., Kirkpatrick, J. D., Gizis, J. E., Howard, E., Evans, T., Fowler, J., Fullmer, L., Hurt, R., Light, R., Kopan, E. L., Marsh, K. A., McCallon, H. L., Tam, R., Van Dyk, S., and Wheelock, S. (2006). The Two Micron All Sky Survey (2MASS). AJ, 131:1163–1183. (Cited in page 11.)

Smith, M. C., Okamoto, S., Yuan, H.-B., and Liu, X.-W. (2012). The assembly of the Milky Way and its satellite galaxies. *RAA*, 12:1021–1043. (Cited in page 15.)

Smith, V. V., Cunha, K., Shetrone, M. D., Meszaros, S., Allende Prieto, C., Bizyaev, D., Garcìa Pèrez, A., Majewski, S. R., Schiavon, R., Holtzman, J., and Johnson, J. A. (2013). Chemical Abundances in Field Red Giants from High-resolution H-band Spectra Using the APOGEE Spectral Linelist. ApJ, 765:16. (Cited in pages 74 and 78.)

Smoker, J. (2007). *Very Large Telescope Paranal Science Operations CRIRES User Manual*. (Cited in page 70.)

Smoker, J., Valenti, E., Asmus, D., Birstow, P., Smette, A., Hilker, M., Wolff, B., and Jung, Y. (2012). *Very Large Telescope Paranal Science Operations CRIRES data reduction cookbook*. (Cited in page 71.)

Smolinski, J. P., Lee, Y. S., Beers, T. C., An, D., Bickerton, S. J., Johnson, J. A., Loomis, C. P., Rockosi, C. M., Sivarani, T., and Yanny, B. (2011). The SEGUE Stellar Parameter Pipeline. IV. Validation with an Extended Sample of Galactic Globular and Open Clusters. AJ, 141:89. (Cited in page 39.)

Snaith, O., Haywood, M., Di Matteo, P., Lehnert, M. D., Combes, F., Katz, D., and Gómez, A. (2015). Reconstructing the star formation history of the Milky Way disc(s) from chemical abundances. A&A, 578:A87. (Cited in page 23.)

Sneden, C., Lucatello, S., Ram, R. S., Brooke, J. S. A., and Bernath, P. (2014). Line Lists for the A $^2\Pi$-X $^2\Sigma^+$ (Red) and B $^2\Sigma^+$-X $^2\Sigma^+$ (Violet) Systems of CN, $^{13}C^{14}N$, and $^{12}C^{15}N$, and Application to Astronomical Spectra. ApJS, 214:26. (Cited in pages 74, 84 and 133.)

Soubiran, C., Bienaymé, O., Mishenina, T. V., and Kovtyukh, V. V. (2008). Vertical distribution of Galactic disk stars. IV. AMR and AVR from clump giants. A&A, 480:91–101. (Cited in page 58.)

Spergel, D. N., Verde, L., Peiris, H. V., Komatsu, E., Nolta, M. R., Bennett, C. L., Halpern, M., Hinshaw, G., Jarosik, N., Kogut, A., Limon, M., Meyer, S. S., Page, L., Tucker, G. S., Weiland, J. L., Wollack, E., and Wright, E. L. (2003). First-Year Wilkinson Microwave Anisotropy Probe (WMAP) Observations: Determination of Cosmological Parameters. ApJS, 148:175–194. (Cited in page 4.)

Statler, T. S. (1988). Orbital decay in aspherical galaxies. I - Oblate systems. ApJ, 331:71–101. (Cited in page 9.)

Steinmetz, M., Zwitter, T., Siebert, A., Watson, F. G., Freeman, K. C., Munari, U., Campbell, R., Williams, M., Seabroke, G. M., Wyse, R. F. G., Parker, Q. A., Bienaymé, O., Roeser, S., Gibson, B. K., Gilmore, G., Grebel, E. K., Helmi, A., Navarro, J. F., Burton, D., Cass, C. J. P., Dawe, J. A., Fiegert, K., Hartley, M., Russell, K. S., Saunders, W., Enke, H., Bailin, J., Binney, J., Bland-Hawthorn, J., Boeche, C., Dehnen, W., Eisenstein, D. J., Evans, N. W., Fiorucci, M., Fulbright, J. P., Gerhard, O., Jauregi, U., Kelz, A., Mijović, L., Minchev, I., Parmentier, G., Peñarrubia, J., Quillen, A. C., Read, M. A., Ruchti, G., Scholz, R.-D., Siviero, A., Smith, M. C., Sordo, R., Veltz, L., Vidrih, S., von Berlepsch, R., Boyle, B. J., and Schilbach, E. (2006). The Radial Velocity Experiment (RAVE): First Data Release. AJ, 132:1645–1668. (Cited in page 14.)

Stolovy, S., Ramirez, S., Arendt, R. G., Cotera, A., Yusef-Zadeh, F., Law, C., Gezari, D., Sellgren, K., Karr, J., Moseley, H., and Smith, H. A. (2006). A mid-infrared survey of the inner 2 $\times 1.5 degrees of the Galaxy with Spitzer/IRAC. In Schdel, R., Bower, G. C., Muno, M. P., Nayakshin,$ –182. ($Cited in pages\ 102 and\ 134.$)

Stonkutė, E., Koposov, S. E., Howes, L. M., Feltzing, S., Worley, C. C., Gilmore, G., Ruchti, G. R., Kordopatis, G., Randich, S., Zwitter, T., Bensby, T., Bragaglia, A., Smiljanic, R., Costado, M. T., Tautvaišienė, G., Casey, A. R., Korn, A. J., Lanzafame, A. C., Pancino, E., Franciosini, E., Hourihane, A., Jofré, P., Lardo, C., Lewis, J., Magrini, L., Monaco, L., Morbidelli, L., Sacco, G. G., and Sbordone, L. (2016). The Gaia-ESO Survey: the selection function of the Milky Way field stars. MNRAS, 460:1131–1146. (Cited in pages 33, 35 and 36.)

Støstad, M., Do, T., Murray, N., Lu, J. R., Yelda, S., and Ghez, A. (2015). Mapping the Outer Edge of the Young Stellar Cluster in the Galactic Center. ApJ, 808:106. (Cited in page 26.)

Stoughton, C., Lupton, R. H., Bernardi, M., Blanton, M. R., Burles, S., Castander, F. J., Connolly, A. J., Eisenstein, D. J., Frieman, J. A., Hennessy, G. S., Hindsley, R. B., Ivezić, Ž., Kent, S., Kunszt, P. Z., Lee, B. C., Meiksin, A., Munn, J. A., Newberg, H. J., Nichol, R. C., Nicinski, T., Pier, J. R., Richards, G. T., Richmond, M. W., Schlegel, D. J., Smith, J. A., Strauss, M. A., SubbaRao, M., Szalay, A. S., Thakar, A. R., Tucker, D. L., Vanden Berk, D. E., Yanny, B., Adelman, J. K., Anderson, Jr., J. E., Anderson, S. F., Annis, J., Bahcall, N. A., Bakken, J. A., Bartelmann, M., Bastian, S., Bauer, A., Berman, E., Böhringer,

H., Boroski, W. N., Bracker, S., Briegel, C., Briggs, J. W., Brinkmann, J., Brunner, R., Carey, L., Carr, M. A., Chen, B., Christian, D., Colestock, P. L., Crocker, J. H., Csabai, I., Czarapata, P. C., Dalcanton, J., Davidsen, A. F., Davis, J. E., Dehnen, W., Dodelson, S., Doi, M., Dombeck, T., Donahue, M., Ellman, N., Elms, B. R., Evans, M. L., Eyer, L., Fan, X., Federwitz, G. R., Friedman, S., Fukugita, M., Gal, R., Gillespie, B., Glazebrook, K., Gray, J., Grebel, E. K., Greenawalt, B., Greene, G., Gunn, J. E., de Haas, E., Haiman, Z., Haldeman, M., Hall, P. B., Hamabe, M., Hansen, B., Harris, F. H., Harris, H., Harvanek, M., Hawley, S. L., Hayes, J. J. E., Heckman, T. M., Helmi, A., Henden, A., Hogan, C. J., Hogg, D. W., Holmgren, D. J., Holtzman, J., Huang, C.-H., Hull, C., Ichikawa, S.-I., Ichikawa, T., Johnston, D. E., Kauffmann, G., Kim, R. S. J., Kimball, T., Kinney, E., Klaene, M., Kleinman, S. J., Klypin, A., Knapp, G. R., Korienek, J., Krolik, J., Kron, R. G., Krzesiński, J., Lamb, D. Q., Leger, R. F., Limmongkol, S., Lindenmeyer, C., Long, D. C., Loomis, C., Loveday, J., MacKinnon, B., Mannery, E. J., Mantsch, P. M., Margon, B., McGehee, P., McKay, T. A., McLean, B., Menou, K., Merelli, A., Mo, H. J., Monet, D. G., Nakamura, O., Narayanan, V. K., Nash, T., Neilsen, Jr., E. H., Newman, P. R., Nitta, A., Odenkirchen, M., Okada, N., Okamura, S., Ostriker, J. P., Owen, R., Pauls, A. G., Peoples, J., Peterson, R. S., Petravick, D., Pope, A., Pordes, R., Postman, M., Prosapio, A., Quinn, T. R., Rechenmacher, R., Rivetta, C. H., Rix, H.-W., Rockosi, C. M., Rosner, R., Ruthmansdorfer, K., Sandford, D., Schneider, D. P., Scranton, R., Sekiguchi, M., Sergey, G., Sheth, R., Shimasaku, K., Smee, S., Snedden, S. A., Stebbins, A., Stubbs, C., Szapudi, I., Szkody, P., Szokoly, G. P., Tabachnik, S., Tsvetanov, Z., Uomoto, A., Vogeley, M. S., Voges, W., Waddell, P., Walterbos, R., Wang, S.-i., Watanabe, M., Weinberg, D. H., White, R. L., White, S. D. M., Wilhite, B., Wolfe, D., Yasuda, N., York, D. G., Zehavi, I., and Zheng, W. (2002). Sloan Digital Sky Survey: Early Data Release. AJ, 123:485–548. (Cited in page 11.)

Sunyaev, R. A. and Zeldovich, Y. B. (1970). Small-Scale Fluctuations of Relic Radiation. Ap&SS, 7:3–19. (Cited in page 4.)

Tody, D. (1993). IRAF in the Nineties. In Hanisch, R. J., Brissenden, R. J. V., and Barnes, J., editors, *ASP Conf. Ser. 52: Astronomical Data Analysis Software and Systems II*, page 173. (Cited in page 71.)

Tonry, J. L., Stubbs, C. W., Lykke, K. R., Doherty, P., Shivvers, I. S., Burgett, W. S., Chambers, K. C., Hodapp, K. W., Kaiser, N., Kudritzki, R.-P., Magnier, E. A., Morgan, J. S., Price, P. A., and Wainscoat, R. J. (2012). The Pan-STARRS1 Photometric System. ApJ, 750:99. (Cited in page 38.)

Valenti, E., Zoccali, M., Gonzalez, O. A., Minniti, D., Alonso-García, J., Marchetti, E., Hempel, M., Renzini, A., and Rejkuba, M. (2016). Stellar density profile and mass of the Milky Way bulge from VVV data. A&A, 587:L6. (Cited in pages 7 and 91.)

Valenti, E., Zoccali, M., Mucciarelli, A., Gonzalez, O. A., Surot Madrid, F., Minniti, D., Rejkuba, M., Pasquini, L., Fiorentino, G., Bono, G., Rich, R. M., and Soto, M. (2018).

The central velocity dispersion of the Milky Way bulge. *ArXiv e-prints*. (Cited in pages 90 and 124.)

Valenti, J. A. and Piskunov, N. (1996). Spectroscopy made easy: A new tool for fitting observations with synthetic spectra. A&AS, 118:595–603. (Cited in pages 15 and 72.)

Valenti, J. A. and Piskunov, N. (2012). SME: Spectroscopy Made Easy. Astrophysics Source Code Library. (Cited in page 72.)

van Dokkum, P. G. (2001). Cosmic-Ray Rejection by Laplacian Edge Detection. PASP, 113:1420–1427. (Cited in page 104.)

van Loon, J. T., Gilmore, G. F., Omont, A., Blommaert, J. A. D. L., Glass, I. S., Messineo, M., Schuller, F., Schultheis, M., Yamamura, I., and Zhao, H. S. (2003). Infrared stellar populations in the central parts of the Milky Way galaxy. MNRAS, 338:857–879. (Cited in page 65.)

Vanhollebeke, E., Groenewegen, M. A. T., and Girardi, L. (2009). Stellar populations in the Galactic bulge. Modelling the Galactic bulge with TRILEGAL. A&A, 498:95–107. (Cited in page 19.)

Villalobos, Á. and Helmi, A. (2008). Simulations of minor mergers - I. General properties of thick discs. MNRAS, 391:1806–1827. (Cited in page 9.)

Ward-Thompson, D. and Robson, E. I. (1990). Dust around H II regions. II - W49A. MNRAS, 244:458–464. (Cited in page 96.)

Wegg, C. and Gerhard, O. (2013). Mapping the three-dimensional density of the Galactic bulge with VVV red clump stars. MNRAS, 435:1874–1887. (Cited in page 7.)

Weiland, J. L., Arendt, R. G., Berriman, G. B., Dwek, E., Freudenreich, H. T., Hauser, M. G., Kelsall, T., Lisse, C. M., Mitra, M., Moseley, S. H., Odegard, N. P., Silverberg, R. F., Sodroski, T. J., Spiesman, W. J., and Stemwedel, S. W. (1994). COBE diffuse infrared background experiment observations of the galactic bulge. ApJ, 425:L81–L84. (Cited in pages 7, 26, 28, 64, 130 and 132.)

Werner, M. W., Roellig, T. L., Low, F. J., Rieke, G. H., Rieke, M., Hoffmann, W. F., Young, E., Houck, J. R., Brandl, B., Fazio, G. G., Hora, J. L., Gehrz, R. D., Helou, G., Soifer, B. T., Stauffer, J., Keene, J., Eisenhardt, P., Gallagher, D., Gautier, T. N., Irace, W., Lawrence, C. R., Simmons, L., Van Cleve, J. E., Jura, M., Wright, E. L., and Cruikshank, D. P. (2004). The Spitzer Space Telescope Mission. ApJS, 154:1–9. (Cited in page 12.)

Whitney, B. A., Wood, K., Bjorkman, J. E., and Cohen, M. (2003). Two-dimensional Radiative Transfer in Protostellar Envelopes. II. An Evolutionary Sequence. ApJ, 598:1079–1099. (Cited in page 98.)

Williams, M. E. K., Steinmetz, M., Sharma, S., Bland-Hawthorn, J., de Jong, R. S., Seabroke, G. M., Helmi, A., Freeman, K. C., Binney, J., Minchev, I., Bienaymé, O., Campbell, R.,

Fulbright, J. P., Gibson, B. K., Gilmore, G. F., Grebel, E. K., Munari, U., Navarro, J. F., Parker, Q. A., Reid, W., Siebert, A., Siviero, A., Watson, F. G., Wyse, R. F. G., and Zwitter, T. (2011). The Dawning of the Stream of Aquarius in RAVE. ApJ, 728:102. (Cited in page 20.)

Wojno, J., Kordopatis, G., Piffl, T., Binney, J., Steinmetz, M., Matijevič, G., Bland-Hawthorn, J., Sharma, S., McMillan, P., Watson, F., Reid, W., Kunder, A., Enke, H., Grebel, E. K., Seabroke, G., Wyse, R. F. G., Zwitter, T., Bienaymé, O., Freeman, K. C., Gibson, B. K., Gilmore, G., Helmi, A., Munari, U., Navarro, J. F., Parker, Q. A., and Siebert, A. (2017). The selection function of the RAVE survey. MNRAS, 468:3368–3380. (Cited in pages 32, 33, 37, 48, 54 and 55.)

Wojno, J., Kordopatis, G., Steinmetz, M., McMillan, P., Matijevič, G., Binney, J., Wyse, R. F. G., Boeche, C., Just, A., Grebel, E. K., Siebert, A., Bienaymé, O., Gibson, B. K., Zwitter, T., Bland-Hawthorn, J., Navarro, J. F., Parker, Q. A., Reid, W., Seabroke, G., and Watson, F. (2016). Chemical separation of disc components using RAVE. MNRAS, 461:4246–4255. (Cited in page 14.)

Wood, P. R., Habing, H. J., and McGregor, P. J. (1998). Infrared monitoring of OH/IR stars near the Galactic Center. A&A, 336:925–941. (Cited in pages 101 and 134.)

Wright, E. L., Eisenhardt, P. R. M., Mainzer, A. K., Ressler, M. E., Cutri, R. M., Jarrett, T., Kirkpatrick, J. D., Padgett, D., McMillan, R. S., Skrutskie, M., Stanford, S. A., Cohen, M., Walker, R. G., Mather, J. C., Leisawitz, D., Gautier, III, T. N., McLean, I., Benford, D., Lonsdale, C. J., Blain, A., Mendez, B., Irace, W. R., Duval, V., Liu, F., Royer, D., Heinrichsen, I., Howard, J., Shannon, M., Kendall, M., Walsh, A. L., Larsen, M., Cardon, J. G., Schick, S., Schwalm, M., Abid, M., Fabinsky, B., Naes, L., and Tsai, C.-W. (2010). The Wide-field Infrared Survey Explorer (WISE): Mission Description and Initial On-orbit Performance. AJ, 140:1868–1881. (Cited in page 34.)

Wu, Y., Luo, A.-L., Li, H.-N., Shi, J.-R., Prugniel, P., Liang, Y.-C., Zhao, Y.-H., Zhang, J.-N., Bai, Z.-R., Wei, P., Dong, W.-X., Zhang, H.-T., and Chen, J.-J. (2011). Automatic determination of stellar atmospheric parameters and construction of stellar spectral templates of the Guoshoujing Telescope (LAMOST). *Research in Astronomy and Astrophysics*, 11:924–946. (Cited in pages 16 and 39.)

Wyse, R. F. G. (2016). Galactic Archaeology: Current Surveys and Instrumentation. In Skillen, I., Barcells, M., and Trager, S., editors, *Multi-Object Spectroscopy in the Next Decade: Big Questions, Large Surveys, and Wide Fields*, volume 507 of *Astronomical Society of the Pacific Conference Series*, page 13. (Cited in page 32.)

Xiang, M.-S., Liu, X.-W., Yuan, H.-B., Huang, Y., Wang, C., Ren, J.-J., Chen, B.-Q., Sun, N.-C., Zhang, H.-W., Huo, Z.-Y., and Rebassa-Mansergas, A. (2015). The evolution of stellar metallicity gradients of the Milky Way disk from LSS-GAC main sequence turn-off stars: a two-phase disk formation history? *RAA*, 15:1209. (Cited in page 58.)

York, D. G., Adelman, J., Anderson, Jr., J. E., Anderson, S. F., Annis, J., Bahcall, N. A., Bakken, J. A., Barkhouser, R., Bastian, S., Berman, E., Boroski, W. N., Bracker, S., Briegel, C., Briggs, J. W., Brinkmann, J., Brunner, R., Burles, S., Carey, L., Carr, M. A., Castander, F. J., Chen, B., Colestock, P. L., Connolly, A. J., Crocker, J. H., Csabai, I., Czarapata, P. C., Davis, J. E., Doi, M., Dombeck, T., Eisenstein, D., Ellman, N., Elms, B. R., Evans, M. L., Fan, X., Federwitz, G. R., Fiscelli, L., Friedman, S., Frieman, J. A., Fukugita, M., Gillespie, B., Gunn, J. E., Gurbani, V. K., de Haas, E., Haldeman, M., Harris, F. H., Hayes, J., Heckman, T. M., Hennessy, G. S., Hindsley, R. B., Holm, S., Holmgren, D. J., Huang, C.-h., Hull, C., Husby, D., Ichikawa, S.-I., Ichikawa, T., Ivezić, Ž., Kent, S., Kim, R. S. J., Kinney, E., Klaene, M., Kleinman, A. N., Kleinman, S., Knapp, G. R., Korienek, J., Kron, R. G., Kunszt, P. Z., Lamb, D. Q., Lee, B., Leger, R. F., Limmongkol, S., Lindenmeyer, C., Long, D. C., Loomis, C., Loveday, J., Lucinio, R., Lupton, R. H., MacKinnon, B., Mannery, E. J., Mantsch, P. M., Margon, B., McGehee, P., McKay, T. A., Meiksin, A., Merelli, A., Monet, D. G., Munn, J. A., Narayanan, V. K., Nash, T., Neilsen, E., Neswold, R., Newberg, H. J., Nichol, R. C., Nicinski, T., Nonino, M., Okada, N., Okamura, S., Ostriker, J. P., Owen, R., Pauls, A. G., Peoples, J., Peterson, R. L., Petravick, D., Pier, J. R., Pope, A., Pordes, R., Prosapio, A., Rechenmacher, R., Quinn, T. R., Richards, G. T., Richmond, M. W., Rivetta, C. H., Rockosi, C. M., Ruthmansdorfer, K., Sandford, D., Schlegel, D. J., Schneider, D. P., Sekiguchi, M., Sergey, G., Shimasaku, K., Siegmund, W. A., Smee, S., Smith, J. A., Snedden, S., Stone, R., Stoughton, C., Strauss, M. A., Stubbs, C., SubbaRao, M., Szalay, A. S., Szapudi, I., Szokoly, G. P., Thakar, A. R., Tremonti, C., Tucker, D. L., Uomoto, A., Vanden Berk, D., Vogeley, M. S., Waddell, P., Wang, S.-i., Watanabe, M., Weinberg, D. H., Yanny, B., Yasuda, N., and SDSS Collaboration (2000). The Sloan Digital Sky Survey: Technical Summary. AJ, 120:1579–1587. (Cited in page 11.)

Yoshii, Y. (1982). Density Distribution of Faint Stars in the Direction of the North Galactic Pole. PASJ, 34:365. (Cited in page 8.)

Yuan, H.-B., Liu, X.-W., Huo, Z.-Y., Xiang, M.-S., Huang, Y., Chen, B.-Q., Zhang, H.-H., Sun, N.-C., Wang, C., Zhang, H.-W., Zhao, Y.-H., Luo, A.-L., Shi, J.-R., Li, G.-P., Yuan, H.-L., Dong, Y.-Q., Li, G.-W., Hou, Y.-H., and Zhang, Y. (2015). LAMOST Spectroscopic Survey of the Galactic Anticentre (LSS-GAC): target selection and the first release of value-added catalogues. MNRAS, 448:855–894. (Cited in page 33.)

Yusef-Zadeh, F., Hewitt, J. W., Arendt, R. G., Whitney, B., Rieke, G., Wardle, M., Hinz, J. L., Stolovy, S., Lang, C. C., Burton, M. G., and Ramirez, S. (2009). Star Formation in the Central 400 pc of the Milky Way: Evidence for a Population of Massive Young Stellar Objects. ApJ, 702:178–225. (Cited in pages 26, 27, 98, 99, 109, 129 and 134.)

Zacharias, N., Finch, C. T., Girard, T. M., Henden, A., Bartlett, J. L., Monet, D. G., and Zacharias, M. I. (2013). The Fourth US Naval Observatory CCD Astrograph Catalog (UCAC4). AJ, 145:44. (Cited in page 38.)

Zasowski, G., Johnson, J. A., Frinchaboy, P. M., Majewski, S. R., Nidever, D. L., Rocha

Pinto, H. J., Girardi, L., Andrews, B., Chojnowski, S. D., Cudworth, K. M., Jackson, K., Munn, J., Skrutskie, M. F., Beaton, R. L., Blake, C. H., Covey, K., Deshpande, R., Epstein, C., Fabbian, D., Fleming, S. W., Garcia Hernandez, D. A., Herrero, A., Mahadevan, S., Mészáros, S., Schultheis, M., Sellgren, K., Terrien, R., van Saders, J., Allende Prieto, C., Bizyaev, D., Burton, A., Cunha, K., da Costa, L. N., Hasselquist, S., Hearty, F., Holtzman, J., García Pérez, A. E., Maia, M. A. G., O'Connell, R. W., O'Donnell, C., Pinsonneault, M., Santiago, B. X., Schiavon, R. P., Shetrone, M., Smith, V., and Wilson, J. C. (2013). Target Selection for the Apache Point Observatory Galactic Evolution Experiment (APOGEE). AJ, 146:81. (Cited in pages 13, 19, 32 and 34.)

Zhao, G., Zhao, Y.-H., Chu, Y.-Q., Jing, Y.-P., and Deng, L.-C. (2012). LAMOST spectral survey An overview. *RAA*, 12:723–734. (Cited in page 15.)

Zinnecker, H. and Yorke, H. W. (2007). Toward Understanding Massive Star Formation. ARA&A, 45:481–563. (Cited in page 97.)

Zoccali, M., Gonzalez, O. A., Vasquez, S., Hill, V., Rejkuba, M., Valenti, E., Renzini, A., Rojas-Arriagada, A., Martinez-Valpuesta, I., Babusiaux, C., Brown, T., Minniti, D., and McWilliam, A. (2014). The GIRAFFE Inner Bulge Survey (GIBS). I. Survey description and a kinematical map of the Milky Way bulge. A&A, 562:A66. (Cited in pages 7, 16, 89, 90 and 91.)

Zoccali, M., Hill, V., Lecureur, A., Barbuy, B., Renzini, A., Minniti, D., Gómez, A., and Ortolani, S. (2008a). The metal content of bulge field stars from FLAMES-GIRAFFE spectra. I. Stellar parameters and iron abundances. A&A, 486:177–189. (Cited in page 88.)

Zoccali, M., Hill, V., Lecureur, A., et al. (2008b). The metal content of bulge field stars from FLAMES-GIRAFFE spectra. I. Stellar parameters and iron abundances. A&A, 486:177–189. (Cited in page 7.)

Zoccali, M. and Valenti, E. (2016). The 3D Structure of the Galactic Bulge. PASA, 33:e025. (Cited in page 7.)

Zoccali, M., Vasquez, S., Gonzalez, O. A., Valenti, E., Rojas-Arriagada, A., Minniti, J., Rejkuba, M., Minniti, D., McWilliam, A., Babusiaux, C., Hill, V., and Renzini, A. (2017). The GIRAFFE Inner Bulge Survey (GIBS). III. Metallicity distributions and kinematics of 26 Galactic bulge fields. A&A, 599:A12. (Cited in pages 7, 16, 63, 86 and 91.)

Zwitter, T., Matijevič, G., Breddels, M. A., Smith, M. C., Helmi, A., Munari, U., Bienaymé, O., Binney, J., Bland-Hawthorn, J., Boeche, C., Brown, A. G. A., Campbell, R., Freeman, K. C., Fulbright, J., Gibson, B., Gilmore, G., Grebel, E. K., Navarro, J. F., Parker, Q. A., Seabroke, G. M., Siebert, A., Siviero, A., Steinmetz, M., Watson, F. G., Williams, M., and Wyse, R. F. G. (2010). Distance determination for RAVE stars using stellar models . II. Most likely values assuming a standard stellar evolution scenario. A&A, 522:A54. (Cited in page 42.)